UNIVERSITAT POLITÈCNICA DE VALÈNCIA
DEPARTAMENTO DE MÁQUINAS Y MOTORES TÉRMICOS

A comprehensive methodology to analyse the Global Energy Balance in Reciprocating Internal Combustion Engines

D O C T O R A L T H E S I S

Presented by:

Mr. Ricardo Carreño Arango

Supervised by:

Dr. Jaime Martín Díaz

Valencia, September 2016

DOCTORAL THESIS

A COMPREHENSIVE METHODOLOGY TO ANALYSE THE GLOBAL ENERGY BALANCE IN RECIPROCATING INTERNAL COMBUSTION ENGINES

presented by

RICARDO CARREÑO ARANGO

in the

DEPARTAMENTO DE MÁQUINAS Y MOTORES TÉRMICOS of the UNIVERSITAT POLITÈCNICA DE VALÈNCIA

in fulfilment of the requirements for the degree of

Doctor of Philosophy

Valencia, September 2016

DOCTORAL THESIS

A COMPREHENSIVE METHODOLOGY TO ANALYSE THE GLOBAL ENERGY BALANCE IN RECIPROCATING INTERNAL COMBUSTION ENGINES

Presented by: Mr. Ricardo Carreño Arango
Supervised by: Dr. Jaime Martín Díaz

EXAMINING BOARD:

President:	Dr. José M. Desantes
Secretary:	Dr. Octavio Armas
Vocal:	Dr. Angelo Onorati

REVIEWING BOARD:

Reviewer 1:	Dr. Angelo Onorati
Reviewer 2:	Dr. Carlo Beatrice
Reviewer 3:	Dr. Juan J. Hernandez

Valencia, September 2016

Abstract

The main objective of this doctoral thesis is the development of a comprehensive methodology to perform and analyse the thermal balance of reciprocating engines, based on experimental and theoretical techniques. Starting from previous works carried out in the research group, which are related to combustion diagnosis and thermal management, a methodology to analyse the thermal balance from two points of view was proposed: on the one hand, the external point of view, mainly based on experimental measurements, and on the other hand, the internal point of view, based on modelling. The combination of both approaches allows the necessary model adjustment, along with a detailed characterization of the different energy flows.

Apart from the thermal balance methodology, several proposals to model some internal processes have been provided, being noteworthy the sub-models for heat transfer to the chamber walls, the ports and between the oil and coolant, besides, a detailed mechanical losses model was also developed. With the aim of ensuring the models reliability and robustness, an integral uncertainty adjustment methodology is proposed, which allows determining some parameters affecting the thermodynamic properties within the chamber and the sub-models adjustment.

The analysis and calibration methodology is flexible enough to be applied in different types of engines and combustion modes, thus ensuring its generality. To demonstrate the methodology potential, it is finally applied to analyse specific parametric studies in two engines, showing its usefulness for both diagnostic and predictive applications.

Resumen

El objetivo principal de la presente tesis doctoral es el desarrollo de una metodología integral que permita analizar el balance de energía en motores de combustión interna alternativos, mediante la combinación de diferentes técnicas experimentales y teóricas. Para ello, partiendo de varios trabajos previos realizados en el grupo de investigación en temas relacionados con diagnóstico de la combustión y gestión térmica del motor, se ha propuesto una separación del análisis energético en dos puntos de vista: exterior, basado principalmente en medidas experimentales e interior, fundamentalmente basado en modelado. La combinación de ambos enfoques permite el necesario ajuste de los modelos, así como la caracterización completa y fiable de los flujos de energía en el motor.

Junto a la metodología del balance energético, se han aportado una serie de propuestas para el modelado de diferentes procesos internos, entre los que destacan los modelos de transmisión de calor a las paredes de la cámara de combustión, a las pipas y entre el aceite y el refrigerante, así como un modelo detallado de pérdidas mecánicas. Con el fin de garantizar la robustez y fiabilidad de dichos modelos, se ha propuesto una metodología de ajuste de incertidumbres que permite obtener el valor de varios parámetros que afectan al cálculo de las condiciones termodinámicas en la cámara, así como el ajuste de los diferentes modelos propuestos.

La metodología de análisis y calibración es suficientemente flexible para ser aplicada a motores de características y modos de combustión diferentes, asegurando así la generalidad de la herramienta. Para mostrar su potencial, se ha aplicado a dos motores en estudios paramétricos específicos, verificándose su utilidad como herramienta tanto de diagnóstico como para su uso en aplicaciones predictivas.

Resum

L'objectiu principal de la present tesi doctoral és el desenrotllament d'una metodologia integral que permeta analitzar el balanç d'energia en motors de combustió interna alternatius, per mitjà de la combinació de diferents tècniques experimentals i teòriques. Per a això, partint de diversos treballs previs realitzats en el grup d'investigació en temes relacionats amb diagnòstic de la combustió i gestió tèrmica del motor, s'ha proposat una separació de l'anàlisi energètica en dos punts de vista: exterior, basat principalment en mesures experimentals i interior, fonamentalment basat en modelatge. La combinació d'ambdós enfocaments permet el necessari ajust dels models, així com la caracterització detallada dels diferents fluxos energètics.

Junt amb la metodologia del balanç energètic, s'han aportat una sèrie de propostes per al modelatge de diferents processos interns, entre els que destaquen els models de transmissió de calor a les parets de la cambra de combustió, a les pipes i entre l'oli i el refrigerant, així com un model detallat de pèrdues mecàniques. A fi de garantir la robustesa i fiabilitat dels dits models, s'ha proposat una metodologia integral d'ajust d'incerteses que permet obtindre el valor de diversos paràmetres que afecten el càlcul de les condicions termodinàmiques en la cambra, així com l'ajust dels diferents models proposats.

La metodologia d'anàlisi i calibratge és prou flexible per a ser aplicada a motors de característiques i modes de combustió diferents, assegurant així la generalitat de la ferramenta. Per a mostrar el seu potencial, finalment s'ha aplicat a dos motors en estudis paramètrics específics, verificant la seua utilitat tant com a ferramenta de diagnòstic com en aplicacions predictives.

A mi papá

Agradecimientos

Esta tesis no estaría finalizada si no me detuviera unos instantes para agradecer a todas aquellas personas que de una u otra manera me han brindado su apoyo durante esta etapa de mi vida. En primer lugar, quisiera expresar mis más afectuosos agradecimientos a mi director de tesis, Jaime Martín; gracias Xaume por tu dedicación más allá de las obligaciones, si pudiera volver a elegir, te elegiría nuevamente como mi director de tesis y amigo.

Quisiera expresar mi gratitud a Francisco Payri por sus invaluables consejos y su dirección durante el análisis de los resultados de esta tesis. Gracias por alentarnos a buscar más respuestas y a profundizar en los análisis. Quisiera extender este agradecimiento a los responsables del departamento, es también gracias a su gestión que ha sido posible el desarrollo de esta tesis. Del mismo modo, me gustaría incluir a todo el personal de secretaría e informática y al personal técnico por toda la ayuda brindada.

A Ricardo Novella le debo mi gratitud por sus acertados consejos y su vocación por ayudar. Rixi, gracias especialmente por tu amistad, más importante que el trabajo mismo. A Pablo Olmeda quisiera darle las gracias por haber estado siempre disponible y próximo cada vez que lo hemos necesitado y por los ratos de tertulia al final de la jornada. De igual manera quisiera agradecer a José M. García y a Antonio García, ya que cuando toqué su puerta en busca de apoyo me lo brindaron sin dudar. Del mismo modo, quisiera extender este agradecimiento a todos los compañeros CMT que siempre estuvieron prestos a resolver mis dudas y tenderme una mano.

Quisiera agradecer a Norma Molina por su soporte en todo lo relacionado con CALMEC, por su paciencia y buena energía que hacían mucho más ameno el trabajo. A Víctor, José Luis, Dani, Santi, Roger, Juan y a todos los PFC, TFG y TFM que de una u otra manera aportaron su grano de arena en la elaboración de esta tesis, quisiera agradecerles por su esfuerzo y manifestarles que este ha hecho posible el llevar este trabajo a buen puerto.

I would like to express my gratitude to the Institute for Combustion Engines of the RWTH Aachen University for welcoming me in their laboratories and give me all the support during the internship. Especially, I sincerely appreciate the advice of Mr. Benedikt Heuser and Dr. Florian Kremer during my stay in Aachen.

I also would like to thank Donna Fields for helping me to improve my language skills. Donna, thank you for your sincerity, your commitment, and especially, your friendship.

También quiero expresar mi gratitud a todos los amigos CMT: a Marcos Carreres, José Pedro García, Juan Ramón Llobet, Daniel Estepa, Daniel Vaquerizo, Diego Blanco y todos aquellos con los que en mayor o menor medida tuve la oportunidad de compartir durante los años de doctorado. Han sido ustedes los que me han hecho sentir parte de todo esto. A mi amigo Guillermo Ferro, quiero agradecerle el estar siempre cerca aun en la distancia. A mi amigo Jordi Chulia por soportar las largas conversaciones CMT y por encontrar siempre el comentario audaz e hilarante. A todos los buenos amigos que he tenido la fortuna de encontrar durante esta etapa de mi vida, nunca serán *incognitos* para mí.

Me gustaría expresar mi más profunda gratitud a Miguel y a Concha, y a toda la familia Cerdá Durán, por haberme acogido como uno más de la familia y haber hecho de Valencia (¡y Moraira!) un hogar más para mí. *Moltes gràcies per la seua acollida.* También debo agradecer a toda mi familia (Carreño y Arango) por su apoyo y afecto. En especial quiero agradecer a mi tío Wilson y a Sandrita por estar al pie del cañón en el momento más difícil de mi vida.

Quiero agradecer especialmente a mis hermanos, Oscar y Diana, con quienes he luchado hombro a hombro por progresar y con los que sé que puedo contar ahora y siempre; mis logros son nuestros logros. A mis sobrinas Mariana y Antonia, gracias por recordarme que son las cosas más pequeñas las que más nos llenan de alegría. A mi mamá, quien con su sacrificio y abnegación es tan artífice de esta tesis; gracias por dedicar tu vida a impulsarme a conseguir mis sueños y por ser el motor de la familia. A mi papá, hombre sin parangón, quiero agradecerle el haberme inculcado su visión; de ti he aprendido lo más importante, allá donde estés, espero que te sientas orgulloso.

Gracias a ti Belén por tu infinita paciencia y comprensión, por estar junto a mí en los buenos y en los malos momentos. Gracias por contagiarme con tu fuerza y tu sonrisa cuando más lo necesito. Gracias por enseñarme, entre muchas otras cosas, que no solo se ha de planear, se ha de hacer. ¡Lo hemos logrado!

Gracias a Dios.

This research has been partially funded by FEDER and Spanish Ministerio de Economía y Competitividad through project TRA2013-41348-R

"Hay hombres que luchan un día y son buenos. Hay otros que luchan un año y son mejores. Hay quienes luchan muchos años, y son muy buenos. Pero hay los que luchan toda la vida, esos son los imprescindibles"

Bertolt Brecht

Contents

Symbols, subscripts and abbreviations

Symbols

Latin

A	Area	$[m]$
a	Acceleration	$[m/s^2]$
$bmep$	Brake mean effective pressure	$[bar]$
c	Clearance	$[m]$
c_m	Mean piston speed	$[m/s]$
c_p	Specific heat at constant pressure	$[J/kgK]$
D	Diameter	$[m]$
e	Eccentricity	$[m]$
F	Force	$[N]$
h	Heat transfer coefficient	$[W/m^2K]$
$\dot{H}_{bb}$	Net sensible enthalpy flow	$[kW]$
H_v	Lower heating value	$[kW]$
$imep$	Indicated mean effective pressure	$[bar]$
k	Thermal conductivity	$[W/mK]$
$\dot{m}$	Mass flow rate	$[kg/s]$
N	Power	$[kW]$
n	Speed, polytropic exponent	[rpm], [-]
p	In-cylinder pressure	$[bar]$
$\dot{Q}$	Heat transfer	$[kW]$
T	Temperature	$[K]$ or $[^\circ C]$

V	Volume	$[m^3]$
$\dot{V}$	Volumetric flow	$[m^3/s]$
v	Velocity	$[m/s]$
z	Number of cylinders	$[-]$

Greek

α	Crank angle	$[^\circ]$
α_c	Pressure viscosity coefficient	$[m^2/N]$
$\Delta\alpha$	Angular interval	$[^\circ]$
γ	Adiabatic index	$[-]$
ε	Uncertainty	$[\%]$
ζ	Asperities radius of curvature	$[\mu m]$
η	Efficiency	$[-]$
κ	Rate of change of shear stress with pressure	$[-]$
λ	Separation parameter	$[-]$
μ	Viscosity	$[P_a s]$
ρ	Density	$[kg/m^3]$
ϱ	Asperity density	$[\mu m^{-2}]$
σ	Composite surface roughness parameter	$[\mu m]$
τ	Shear stress	$[MPa]$
ω	Angular speed	$[rad/s]$

Subscript

0	Initial, motoring
a	air
atm	atmospheric
b	burned products
bb	blow-by
c	In-cylinder charge
ch	cylinder head
CFD	calculated from CFD
CO	relative to carbon monoxide
$conv$	convective
$crank$	crankcase

$crit$	critical
cyl	cylinder
d	displaced
eff	effective
en	relative to engine
ev	evaporated
EVO	relative to exhaust valve opening
ex	external
f	Final, fuel
g	gas
HC	relative to hydrocarbon
i	node i, cylinder i
in	internal
inj	injected
int	calculated at Intake
IVC	relative to intake valve closing
IVO	relative to intake valve opening
l	liquid, fluid
lin	liner
max	maximum
n	polytropic exponent
nb	unburned
pis	piston
ri	piston rings
s	stoichiometric
$soot$	relative to soot emission
t	relative to tumble model
vap	vaporization
w	relative to Woschni model

Abbreviations

BSFC	Brake Specific Fuel Consumption
CDC	Conventional Diesel Combustion
CI	Compression Ignition
CGC	Conventional Gasoline Combustion

CNG	Compressed Natural Gas
CR	Compression Ratio
DI	Direct Injection
EGR	Exhaust Gases Recirculation
ETM	Engine Thermal Management
EVC	Exhaust Valve Closing
EVO	Exhaust Valve Opening
GDI	Gasoline Direct Injection
GEB	Global Energy Balance
GTDI	Gasoline Turbocharged Direct Injection
HCCI	Homogeneous Charge Compression Ignition
HT	Heat Transfer
IGR	Internal Gas Recirculation
IVC	Intake Valve Closing
LHRE	Low Heat Rejection Engines
LPG	Liquid Petroleum Gas
MLR	Multi-variable Linear Regression
MSN	Mean Swirl Number
PID	Proportional-Integral-Derivative controller
PM	Particulate Matter
PPC	Partially Premixed Combustion
RCCI	Reactivity Controlled Compression Ignition
RICE	Reciprocating Internal Combustion Engines
RTD	Resistance Temperature Detector
SoE	Start of Energizing
SI	Spark Ignition
SoI	Start of Injection
SN	Swirl Number
TDI	Diesel Turbocharged Direct Injection

Chapter 1

Introduction

Contents

1.1 Background

Since its development, the Reciprocating Internal Combustion Engine (RICE) has brought several benefits to mankind, being especially remarkable in the transportation sector but also in domestic and industrial applications. It is partly responsible for the fast growing and evolution of cities and has moulded the present society lifestyle. As a consequence, the use of RICEs has increased over the last decades, giving place to two major concerns:

1. The combustion process of conventional RICEs leads to pollutants emissions that are released to the ambient as part of the exhaust gases. In normal operation, NO_x and Particulate Matter (PM) are main issues in Diesel engines, whilst gasoline engines produce higher concentration of CO and HC emissions. These pollutants are reported to have harmful

effects on human health [1–3], thus becoming a major issue in modern cities.

2. Fossil fuels are the main source of energy in transportation applications. However, as can be seen in Figure 1.1, the oil reserves are progressively running out whilst the demand of energy rises. Thereby, the use of gas and oil extraction methods that are more aggressive with the environment (for example the *fracking*[1] [4–6]) are becoming a common practice. As a consequence, the awareness towards the preservation of the non-renewable sources and the protection of the environment has increased; therefore, the development of more efficient powertrains is gaining importance.

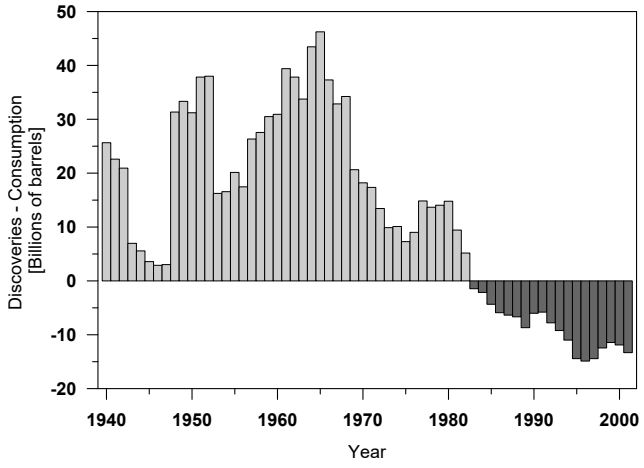

Figure 1.1. *Annual balance of new barrels discovered versus consumed. Source: [7].*

As the harmful inmissions in the ambient have reached alarming levels, current legislations are focused on reducing RICE tailpipe emissions levels. In this sense, the European Union defined the *European emission standards* (Euro 1 to 6) that new vehicles sold in the European territory must comply. In Figure 1.2 it is possible to see the evolution of the increasingly stringent

[1] *Fracking* consist on the hydraulic fracturing of rocks by means of a pressurized liquid. This technique can be responsible of several environmental impacts ranging from the potential to cause earthquakes to the contamination of water supplies.

normative restrictions since the Euro 1 comes into the scene. It is possible to see how the allowed NO_x emissions level has been reduced about 84%, the PM about 96% and the HC and CO more than 80% with respect to Euro 1 limits.

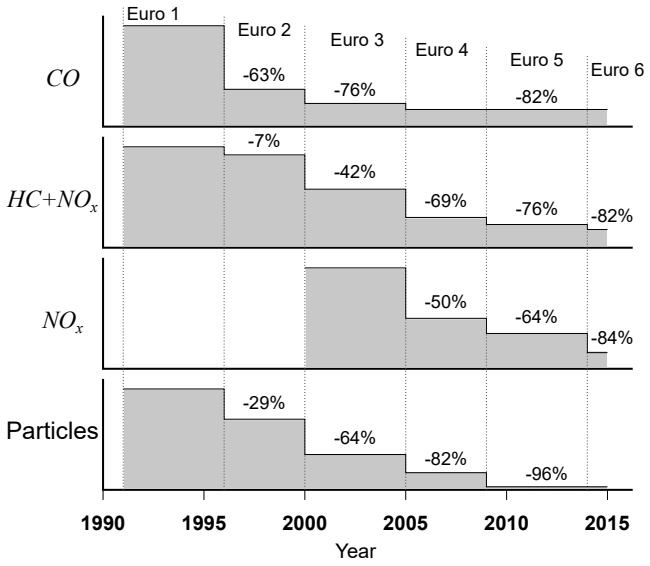

Figure 1.2. *Euro normative evolution.*

With the purpose of meeting those regulations, during the last two decades the engine research have been mainly focused on reducing these pollutants, mostly by means of active techniques oriented to limit their formation during the combustion process. As a result, current RICE technology has reached a development level in which further emissions reduction is barely attainable through these active methodologies; therefore, aftertreatment systems have become a very common solution.

Recently, the climatic change consequence of green house gases emissions such as CO_2, along with the decrease of fossil fuel storages, have moved the research interest towards optimization of RICE operation with the aim of reaching the maximum efficiency possible. In this frame, two ruling tendencies can be identified as the principal responsible of this revitalized interest:

1. Since the signing of the Kyoto protocol in 1998, the industrialized countries have been committed to binding green house gases emission reduction targets, thus, current international legislation set the new research

lines, in which the reduction of CO_2 is one of the most important objectives. According to the new European regulation [8], the CO_2 emissions must be increasingly reduced in the upcoming years, putting even more pressure over the automotive industry.

2. As mentioned, the task of attaining lower NO_x, HC, CO and PM emissions only with in-cylinder techniques seems to be hardly achievable, which has led to the generalized use of aftertreatment systems. Such systems reduce effectively the emissions but penalize the fuel consumption as a consequence of the gas flow restriction through the exhaust, which increase the pumping work. In addition, they often require regeneration processes that are achieved by using post injection strategies.

Taking into account that reducing fuel consumption leads to lower CO_2 emissions, efforts have been made on developing innovative engine strategies that allow reaching higher efficiency with low penalty in emissions. Therefore, new developments requires comprehensive analysis methodologies that allow assessing their benefits and drawbacks. In this framework, the diagnosis and evaluation tools plays a vital role to assess the real thermal improvement reached with a determined technology. One common evaluation approach consist on performing the engine thermal balance, which allows determining the energy splitting in several terms such as heat rejection, exhaust gas energy losses and effective work. This process allows assessing the energy usage and identifying the main energy waste sources and their recovery potential.

Whit this aim, a comprehensive methodology to perform and analyse the engine energy balance is proposed in this thesis. One remarkable innovation of this work consists on the combined use of experimental and modelling tools, thus providing a complete insight of the RICE thermal behaviour.

1.2 Previous works

The work presented in this doctoral thesis was possible thanks to previous theses related with combustion diagnosis and thermal management, in which the main thermodynamic model, along with some sub-models, were developed. Following, the timeline of the reference works and a brief description of their main subject is presented:

- 1986: Tinaut [9] propose the base thermodynamic model to perform the combustion diagnosis of Direct Injection (DI) Diesel engines.
- 1998: Armas [10] implements a combustion diagnosis model for DI Diesel engines, in which several sub-models necessary to accurately determine the heat release were developed. This work also includes comprehensive sensitivity analysis of different terms involved in the combustion diagnosis, and propose a methodology for the uncertainties adjustment.
- 2007: Degraeuwe [11] develops a thermal management methodology for DI Diesel engines, in which specific heat rejection to different engine components is determined. This work provides a lumped conductance model for the detailed calculation of heat rejection to different engine sub-systems (i.e. cooling and lubricating).
- 2007: Martín [12][2] updated and improved some of the models previously proposed by Armas, being remarkable the efforts made in the heat transfer and the filling and emptying models. This work set the basis for a general engine thermal characterization, including information of the complete cycle.
- 2016: García [13] propose the bases of a detailed mechanical losses model. This works include several sub-models to determine the friction between engine elements with relative motion as well as to calculate the engine pumps power. Starting from this work, an improved mechanical losses model, suitable to be applied in different types of engines can be proposed.

Owing to these previous efforts, the basis for an integral engine thermal characterization, which includes accurate combustion diagnosis, is established. The present thesis goes further in the thermal evaluation tools improvement, taking advantage of the potential of these previous works, and making efforts to upgrade the current models and developing *state of art* new ones.

[2]Note that the cited reference corresponds to a later published book (2012). This is the final published form of Martín's thesis, which is used in this work.

1.3 Objectives

The main objective of this doctoral thesis is **the development of a comprehensive methodology to perform and analyse the engine energy repartition**, based on the combination of experimental measurements (in-cylinder pressure and some mean variables) and some models. To comply with the main objective, some particular objectives have to be satisfied:

1. *Proposing a comprehensive thermal balance methodology that allows determining and analysing all the energy terms.* The methodology proposed must consider all the energy interactions occurring in RICEs. Besides, it should takes into account the difficulty of experimental measurements, thus introducing a complementary modelling point of view to complete the analysis.

2. *Developing the necessary sub-models to complete a comprehensive thermal balance.* Efforts will be focused on improving existing heat transfer and mechanical losses sub-models, and developing new ones, in order to have a complete description of all the significant phenomena in different engine configurations. Accomplishing this objective will increase the methodology robustness and generality, thus allowing its application on different types of RICEs.

3. *Proposing a methodology for the calibration of the sub-models.* The method must describe the step by step process to combine the available experimental data to adjust the sub-models. Therefore, the specific engine characteristics and the limitation of experimental measurements must be considered.

4. *Showing the potential of the calibrated sub-models and the energy balance methodology through their application on different engines.* The analysis will include the characterization of the energy repartition in some parametric studies and the application in predictive analysis.

Meeting these objectives will result in a global analysis methodology tested in a set of engines with different characteristics. Besides, conclusions regarding the experimental and modelling work as well as the results obtained in different engines will be attained. To get these objectives, the methodology presented in the next section will be followed.

1.4 Methodology

The methodology followed to achieve the objectives is shown in Figure 1.3. As can be seen, this work consist of five main tasks, organized in several chapters.

Chapter 2 deals with the literature survey of current strategies to optimize engine efficiency. In this sense, a comprehensive review is performed to understand the engine research background over the last 2 decades. The trade-off between emissions and efficiency, along with the potential of thermal balance for engine evaluation is discussed in this chapter. An extensive amount of works dealing with RICE thermal balances is used for the discussion, where the importance of establishing a comprehensive methodology for its analysis is evidenced.

Chapter 3 shows a complete description of the experimental installations and the reference thermodynamic model, including:

- Details of the instrumentation required to perform the experimental work.
- A description of the different sub-models included in CALMEC and SiCiclo (0D thermodynamic tools), detailing which of them need to be further upgraded as done in the following sections.

Based on the experimental and modelled information available, **Chapter 4** introduces an integral experimental and modelling methodology to perform the thermal balance, called *Global Energy Balance* (GEB). This methodology considers 2 main points of view, on the one hand the *External GEB*, which considers the engine as a black box and whose terms are obtained mainly through experimental techniques; and on the other hand the *Internal GEB*, which takes into account all the internal energy degradation phenomena due to thermal and mechanical processes (e.g. heat rejection and friction). For the sake of completeness, the relationship between internal, and internal-external terms will be also detailed in this chapter. Special analysis of some heat rejection terms used for the calibration and validation stages will be provided, along with an experimental uncertainty analysis.

Taking into account the description of the energy terms provided in Chapter 4, the improvement of some reference sub-models and the proposal

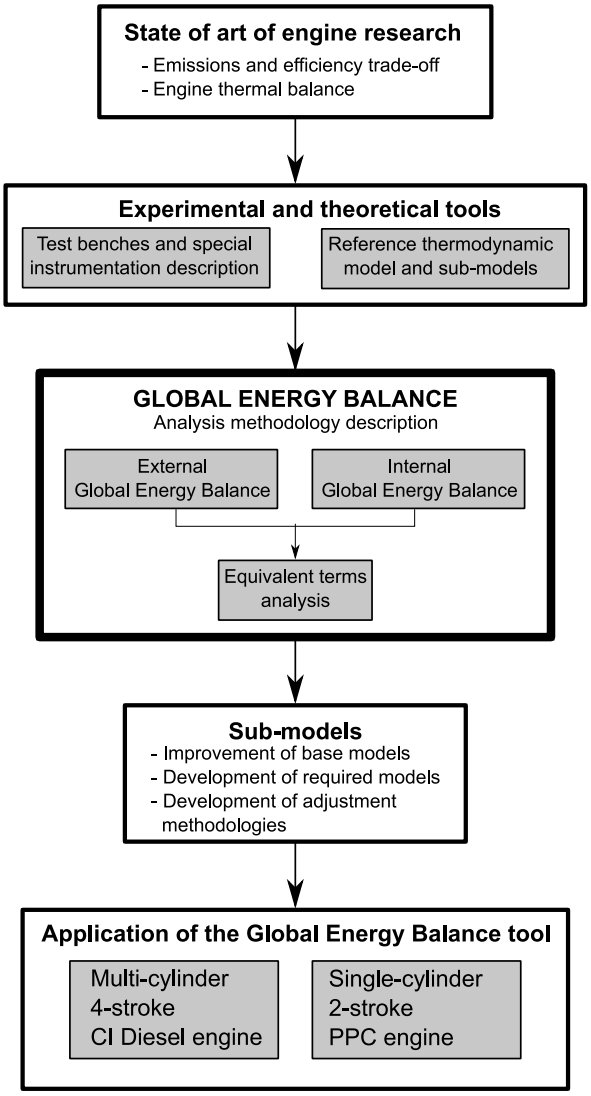

Figure 1.3. *Thesis methodology.*

of new ones will be necessary. Therefore, **Chapter 5** is dedicated to the development and validation of specific heat transfer and mechanical losses sub-models, along with a comprehensive uncertainties adjustment process.

To asses the potential of the methodology developed in this work, **Chapter 6** describes the use of the GEB in two different engines: one conventional

multi-cylinder 4-stroke Diesel engine, and a research single-cylinder engine. The work presented in this section is divided in 2 steps:

1. Description of the sub-models calibration methodology based on the equivalent heat transfer terms presented in Chapter 4, along with the uncertainties tuning described in Chapter 5.

2. Performing the GEB analysis in some parametric variations, aimed at the integral energy characterization of the studied engines, along with an example of the use of the calibrated sub-models and GEB for predictive applications (using a 0D thermodynamic model).

Finally, **Chapter 7** summarises the work performed and shows the main conclusions regarding its contributions. In addition, some proposals for future works are lastly discussed.

For convenience, besides each chapter bibliography, at the end of this document all the references cited are organized in alphabetic order, indicating the pages where they are cited.

Bibliography

[1] Health Effects Institute. "Diesel Exhaust: A Critical Analysis of Emissions, Exposure, and Health Effects". *A Special Report of the Institute's Diesel Working Group*, 1995.

[2] Pope C. and Dockery D. "Health Effects of Fine Particulate Air Pollution: Lines that Connect". *Journal of the Air & Waste Management Association*, Vol. 56 n^o 6, pp. 709–742, 2006.

[3] Oberdörster G. and Utell M.J. "Ultrafine particles in the urban air: to the respiratory tract–and beyond?". *Environmental health perspectives*, Vol. 110 n^o 8, pp. A440–A441, 2002.

[4] UNEP. "Gas fracking: can we safely squeeze the rocks?". *Environmental Development*, Vol. 6, pp. 86–99, apr 2013.

[5] Davies R., Foulger G., Bindley A. and Styles P. "Induced seismicity and hydraulic fracturing for the recovery of hydrocarbons". *Marine and Petroleum Geology*, Vol. 45, pp. 171–185, aug 2013.

[6] Goodman P., Galatioto F., Thorpe N., Namdeo A., Davies R. and Bird R. "Investigating the traffic-related environmental impacts of hydraulic-fracturing (fracking) operations.". *Environment international*, Vol. 89, pp. 248–260, feb 2016.

[7] Aleklett K. and Campbell C. "The Peak and Decline of World Oil and Gas Production". *Minerals & Energy - Raw Materials Report*, Vol. 18 n^o 1, pp. 5–20, 2003.

[8] European Parliament. "Regulation (EU) No 333/2014 of the European Parliament and of the Council of 11 March 2014 amending Regulation (EC) No 443/2009 to define the modalities for reaching the 2020 target to reduce CO2 emissions from new passenger cars". *Official Journal of the European Union*, Vol. L103 Vol 5, pp. 15–21, 2014.

[9] Tinaut F. *Contribución al estudio del proceso de combustión en motores de encendido por compresión de inyección directa*. Ph.D. Thesis, Universidad Politécnica de Valencia, 1986.

[10] Armas O. *Diagnóstico experimental del proceso de combustión en motores Diesel de inyección directa*. Servicio de Publicaciones UPV, ISBN 84-7721-772-X, Valencia, 1999.

[11] Degraeuwe B. *Contribution to the thermal management of DI Diesel engines.* Ph.D. Thesis, Universidad Politécnica de Valencia, 2007.

[12] Martín J. *Diagnóstico de la combustión en motores de Diesel de inyección directa.* Reverté, ISBN 978-84-291-4717-9, Barcelona, 2012.

[13] García D. *Aportación al modelado de emisiones y consumo basado en la señal de presión en el cilindro en motores Diesel.* Ph.D. Thesis, Universidad Politécnica de Valencia, 2016.

Chapter 2

Methodologies to improve engine efficiency

Contents

2.1 Introduction

As seen in Chapter 1, the evolution of the RICE during last years have been framed by stringent emissions regulations; thereby, it is interesting to analyse the **trade-off between consumption and emissions** before dealing with the methodologies to improve the RICE efficiency. Thus, next section starts with a brief review of the strategies used to reduce emissions and their effect on the engine consumption.

The **methodologies aimed at achieving better RICE efficiencies** involve both, the development of more efficient combustion processes and the global improvement of engine sub-systems. Some examples of these efforts are the study of new combustion modes helpful to increase the indicated efficiency, the use of better turbocharging and turbocompounding systems to enhance the air management, the design of new chamber configurations to improve the air-fuel mixing process and the optimized management of the cooling and lubricating systems. Alternatively, advanced engine concepts such as Downsizing and hybridization are gaining a place in the research focus and the current market.

Defining a **methodology to evaluate the advantages and disadvantages of each technique** or engine concept is an important topic, thereby, performing the engine thermal balance has come into scene as an integral strategy to determine the energy usage. In this sense, the thermal balance consist on determining how the fuel energy is distributed or degraded

up to becoming mechanical power. Therefore, a comprehensive literature review of works dealing with RICE thermal balances is presented, remarking the importance of the accurate determination and analysis of each energy term. Finally, a discussion about the relevance that the thermal balance has had as an evaluation tool of the mentioned techniques, and the need for a detailed and comprehensive thermal balance methodology is presented.

2.2 Combustion and emissions trade-off

The emissions regulations imposed the last 25 years have progressively become more stringent, thus establishing the boundaries of what the automotive researchers can explore, maintaining the fuel consumption as low as possible. The main challenge has been then, to achieve the highest engine efficiency while keeping the emission below allowed levels.

Taking into account the current state of the automotive research, in this section the most common techniques used to optimize consumption and emissions trade-off are briefly described.

2.2.1 Air management

The development of sophisticated injection systems requires a proper air management, considering that the maximum power delivered by the engine is limited by the fuel that can be burned, which depends on the amount of intake air. The main drawback of increasing the air mass in the chamber is a higher combustion temperature and O_2 concentration, which leads to higher NO_x formation. On the other hand, burning the fuel in stratified condition (usually occurring in DI engines) produces high PM emissions. NO_x emissions can be mitigated by using part of the burned gases of the previous cycle in the mixture; however, this has an important effect on soot production.

The principal air management strategies used to optimize consumption and emissions trade-off in current engines are:

- **Turbocharging:** the use of turbochargers enhance the intake process by taking advantage of the exhaust energy to compress the air, thus leading to densities above the ambient [1] and achieving better engine efficiency [2, 3]. Moreover, turbocharging leads to lower fuel/air ratio, thus improving the combustion and reducing CO emissions [4] and

PM [5]. However, high boost pressure usually leads to higher in-cylinder temperature; in Conventional Diesel Combustion (CDC), this high temperature increases NO_x formation [2], while in Conventional Gasoline Combustion (CGC) increases knocking risk [6–9]. These effects can be reduced by using air intercooler [10], optimized injection settings or new combustion modes such as HCCI, in which the gas temperature is lower than in conventional Diesel and gasoline combustion, thus the higher boost pressure does not imply an important increase in NO_x [3] and reduce the knocking risks [9].

- **Exhaust gas recirculation:** a common practice to reduce the combustion temperature, and hence the NO_x formation, consist on the use of Exhaust Gas Recirculation (EGR). The use of EGR in CDC has the drawback of reducing the engine efficiency and increasing the PM emissions [11], since lower temperature in the chamber tends to increase the combustion duration and reduce the combustion efficiency [5]. Moreover, increasing the EGR has a great impact on the turbocharger operation, specially in high pressure EGR engines, where the gas flow through the turbine diminishes, thus affecting the turbine efficiency and the pumping losses. To optimize the NO_x-PM trade-off, Maiboom and Tauzia [12] combines the use of water in Diesel emulsion and EGR, achieving reduction of both when compared with CDC; however, these method have some problems regarding cold-start, long term emulsion stability and injection system components.

- **Internal Gas Recirculation:** the Internal Gas Recirculation (IGR) consist on retain a fraction of burned mass during exhaust process by means of appropriate valve timing [13]. The effect of IGR on emissions is similar as those of EGR, thus reducing NO_x formation. However, since the IGR cannot be cooled, high temperature at IVC and during compression is reached, thus affecting the combustion phasing and duration, and in gasoline Direct Injection engines (GDI), increases the knocking sensitivity [14]. Therefore, in CDC it is common to use only EGR due to its better effect in emissions reduction [12, 13]; however, in premixed combustion [15], specially of low reactivity fuels [16], combined IGR and EGR strategies are used to achieve both, low emissions and high efficiency, thanks to the higher temperature of IGR, which increases the charge reactivity [16] and helps to reduce the HC and CO emissions [15] as a result of higher combustion completion.

2.2.2 In-cylinder processes

The combustion process and its control is one of the most important issues regarding emissions reduction, since the formation (and in some cases the reduction) of the species mainly depends on the combustion strategies employed and the in-cylinder conditions. Several studies dealing with the control of parameters affecting the injection/combustion process, as well as their effect on engine efficiency and emissions can be found in the literature [17].

The most important parameters to control fuel injection and fuel/air mixing processes, oriented at optimizing consumption and emissions trade-off are:

- **Injection pressure:** the spray mixing properties are improved by higher injection pressure. In CI engines, the penetration length increase at higher injection pressure, determining the fuel-air mixing rate and the air utilization [17]. Currently, Diesel injection pressure ranges between 200 bar and 2500 bar, but the benefits of increase the pressure over 3000 bar have been also evaluated [18, 19]. In general, faster fuel injection leads to faster combustion, with a subsequent increase in the indicated and brake efficiencies, along with a reduction in the PM formation [20]; however, higher injection pressure leads also to an increase in NO_x formation [21] due to an enhancement of the combustion process, and hence higher gas temperature. It is interesting to highlight that very high injection pressure can also penalize the Brake Specific Fuel Consumption (BSFC) [22], due to higher power requirements of the injection pump; moreover, working at high pressure increase the wear of the injection system. In the case of GDI engines, there is also a trend to use higher injection pressures; however, gasoline injection pressure is about 10 times lower than Diesel (reaching pressures up to 200 bar [23]).

- **Injection timing:** it affects combustion phasing and Rate of Heat Release (RoHR) shape, through the change in the premixed/diffusion repartition. Thus, the ignition delay is affected by the injection timing as a result of changes in the air pressure and temperature near TDC. Advancing the Start of Injection (SoI) use to produce higher in-cylinder pressure evolution and increases the indicated efficiency; however, the higher temperature peaks lead to more NO_x formation. Delaying the SoI helps to

control NO_x formation, but usually has a penalty on PM formation [24] and brake efficiency [25], this last due to indicated efficiency worsening.

- **Multiple injections:** The modern injection system technology gives place to more complex and precise injection control, allowing the use of multiple injection strategies. Pilot injections are useful to reduce noise and NO_x emissions with low effect on engine performance [26, 27]. On the other hand, coupled post injections with high pressure are useful to complete the combustion of the PM, and a later post injection helps to the regeneration of the particulate filter and the NO_x adsorption catalyst [17]. However, these strategies use to have negative effects on consumption, since late combustion is not useful from the indicated efficiency point of view.

- **Air motion within the chamber:** to improve the air-fuel mixing process and achieve faster burning rates, the modern RICE are designed to generate high vorticity and turbulence in the combustion chamber. The main rotative macro structures that can be found in RICE are the swirl and tumble, being differentiated by their rotary axis (swirl rotates in the cylinder axis and tumble in the diametrical axis). Both are generated during the intake process and evolve in compression-expansion strokes thanks to the engine geometry (particularly ports and combustion chamber configuration). The swirl movement is prompted by chamber configurations consisting of a shallow bowl engraved into the piston crown [1], whilst the tumble movement is enhanced by pentroof combustion chambers [28–30]. Numerical studies shows that high swirl ratios increase NO_x levels but reduce the PM emissions [31]. On the counterpart, high tumble ratios combined with optimal air management and injection setting results in good emission-performance trade-off [13].

- **Injection rate shaping:** the NO_x thermal formation mechanism (responsible for most NO_x emissions) takes place at high temperature, which are dependent on RoHR. At the same time, the RoHR depends on the injection rate shaping. Some authors propose to inject low quantities of fuel at the beginning of injection to reduce NO_x formation [17], which can be achieved using pilot injections or boot shaped injections [32].

  Nishimura *et al.* [32] studied the effects of fuel injection rate on combustion and emission in a DI Diesel engine. They found that pilot injection helps to simultaneously reduce NO_x and noise, with a slight increase in

PM emission. With the use of boot shaped injection rates, they achieve an important reduction in both, PM and combustion noise. Their results emphasize the benefits of using injection rate control as a key strategy to reduce emissions. Since the injection rate is highly dependent on the injection pressure, Kohketsu *et al.* [33] examined the feasibility of using a variable pressure injection system, based on two common rails. They reproduced a boot shaped injection rate, and found that the use of this system improves the fuel consumption as well as NO_x and PM emissions trade-off. According to these authors, it seems that boot injection rate effects are more important at high speed and load operating points than at medium speed and load operating points [34, 35].

2.2.3 Other strategies

Apart of improving the air management and in-cylinder processes as described in previous sections, alternative strategies can be used to optimize the consumption and emissions trade-off. The use of aftertreatment systems and cleaner fuels are examples of alternatives widely studied.

Following, a brief introduction of the effect on emissions and consumption of these solutions is presented:

- **Aftertreatment systems**: to comply with the current emissions normative, the use of aftertreatment systems has become necessary. Several types of systems based on chemical and mechanical operating principles can be found [5]. A brief description of the most common aftertreatment systems is following presented:

  Catalytic converter: it accelerates oxidation/reduction reactions of exhaust gases that have not reached equilibrium. The most used are the 3-way catalytic converters, since they can reduce simultaneously NO_x, HC and CO emissions [36].

  Selective catalytic reduction: it is used to reduce NO_x through chemical reaction with ammonia, obtained from the injection of urea in an hydrolysis catalyst[1]. The selective catalytic reduction is usually accompanied by an oxidation catalyst to reduce CO and HC [5] emissions and improve NO_x oxidation [37]. Modern systems allows reducing 90% of

[1] It is done to avoid the direct use of the more toxic ammonia.

NO_x; however, it has been reported that they increase the amount of nano particles emission and fuel consumption [38].

NO_x storage-reduction: this chemical filters store NO_x during lean mixture operation; therefore they require regeneration. This is done by means of post injection strategies, which means increasing fuel consumption [39].

Diesel particulate filters: they are located at the exhaust line and help to reduce about 99% the PM emissions [40]. The DPF is usually placed after the turbine [41]; however, Bermúdez *et al.* [42] evaluate the possibility of using a pre-turbo aftertreatment placement. They reported an increase in the amount of NO_2 converted from NO and a reduction in emitted CO at low load.

Since all these aftertreatment techniques implies the use of elements which restrain the gas flow through the exhaust, and some of them also requires a regeneration process achieved through post injection, all of them penalize the fuel consumption as can be confirmed in the stated references.

- **Cleaner fuels**: the use of these fuels to improve both, consumption and emissions, has opened a complete research field. Thus, several works devoted to analyse the benefits and drawbacks can be found in the literature survey. Rakopoulos *et al.* [43] found that the use of biodiesel could lead to higher BSFC; however, the main agreement is that the indicated efficiency is not affected [44]. In the same line, Lapuerta *et al.* [45] presented a comprehensive literature review, concluding that the use of biodiesel reduces significantly the PM emissions but increase the NO_x emissions. Verhelst [46] performs a review about the possibilities of using hydrogen as a fuel for RICE. In spite of the benefits of using hydrogen in terms of performance and emissions, it has important drawbacks regarding the production, transportation and storage [47].

2.3 Consumption optimization methodologies

Taking into account that better RICEs efficiency leads to lower CO_2 emissions, and aftertreatment generalization has given room to the efficiency-oriented optimization of the engine operation, engine consumption has become a major issue.

Several strategies to reduce fuel consumption can be found in the literature. In the next sections, these methodologies are grouped depending on the research topic addressed.

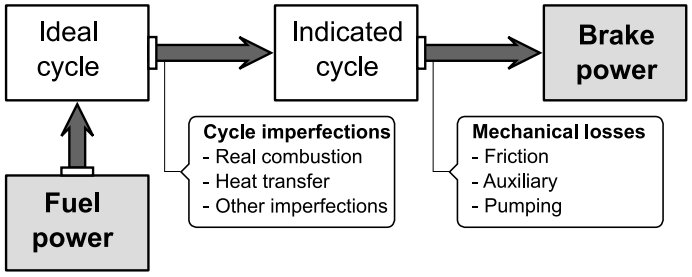

Figure 2.1. *RICE efficiency degradation.*

A simplified schema of the efficiency degradation[2] is presented in Figure 2.1. The ideal-to-indicate power ratio is mainly affected, on the one hand, by combustion imperfections inherent to the real combustion process (e.g. RoHR shape, phasing and duration) and on the other hand, by the HT between hot gases and chamber walls. Besides, other imperfections related with valve timing effect on the gas properties (changes of adiabatic index, γ, due to composition and temperature), blow-by losses, incomplete combustion, etc., also reduce the ideal-to-indicate power ratio; nevertheless, they use to have a minor effect or are indirectly affected by other engine parameters (for example, increasing EGR reduces γ but its use is mandatory to control NO_x emissions). Similarly, the indicated-to-brake power ratio is degraded by mechanical losses (i.e. pumping work, friction and auxiliary systems energy consumption).

Taking into account Figure 2.1 and the stated comments, the following lines for RICE efficiency improvement have been considered:

1. Indicated cycle optimization

[2]The energy degradation will be thoroughly dealt with at Chapter 4.

2. Air management
3. Heat transfer reduction
4. Mechanical losses reduction
5. Other strategies

For the sake of rigour, some comments must be done regarding the previous classification:

- The reduction of the HT losses helps to improve the indicated cycle [48]; however, the engine thermal management to speed up the engine heating at cold-start and the optimal engine cooling to reduce temperature gradients are also important to reduce the mechanical losses (lower energy required by the coolant pump and lower friction) [49]. Due to the essential role of HT in the engine operation, both topics will be dealt with in detail, independently of the indicated cycle optimization.
- The valve timing [50] and gas properties (temperature and composition) [51] affects the ideal-to-indicated power ratio, whilst pumping work affects the indicated-to-brake power ratio [1]. Therefore, the air management affects different engine degradation processes during engine operation and it is analysed separately.

2.3.1 Indicated cycle optimization

The $p - V$ diagram is usually referred as indicated cycle, from which the gross indicated work and the pumping work are obtained[3]. Improving the engine thermodynamic processes to increase the net indicated power (by increasing the gross indicated power and reducing the pumping power) is known as *indicated cycle optimization*. It includes the proper management of fuel injection, fuel/air mixing and combustion processes, along with the control of the gas thermodynamic conditions inside the chamber (temperature and composition) [52, 53].

In general, better indicated efficiency is reached with faster combustion (after proper combustion phasing), which in turn are favoured by high pressure and temperature [1]. In this sense, the flexibility of the CDC and CGC

[3]More details of these terms and their determination can be found in Chapter 4.2.2.

is limited by their intrinsic combustion process and mechanical and thermal limitations, but mainly by the emissions formation. Therefore, new injection/combustion strategies are being developed in order to improve the indicated cycle while keeping acceptable emissions. As an example, the injection control technologies allows deactivating cylinders [54] to reduce the power output when it is not required.

2.3.1.1 Alternative combustion modes

The combustion process has evolved thanks to the introduction of sophisticated and reliable injection systems, which allow using Direct Injection (DI) strategies. This has led to improve the classic CDC [55, 56] and CGC [57], increasing the indicated efficiency and reducing the emissions [17, 20]. To reach both higher efficiencies and lower NO_x and PM emissions, the optimization of the fuel/air mixing process is mandatory to attain high burning rates while keeping low combustion temperature. Several years ago, one of the most promising combustion modes was the Homogeneous Charge Compression Ignition (HCCI), in which an homogeneous premixed charge of air, fuel and residual gases is burned by autoignition, allowing a combustion with lower temperature and lower fuel/air ratios than in CDC. This combustion mode, mainly oriented to NO_x and PM control also showed some potential to reduce consumption thanks to the fast RoHR and lower HT (due to the lower gas temperature) [58].

The benefits of using HCCI concepts have been widely reported [58–61]; however, the precise control of pressure and temperature required for a proper autoignition, besides the complex homogeneous charge preparation, limit the HCCI strategy to a narrow operating range and result in long warm-up periods and high HC and CO emissions levels [62, 63]. To overcome these issues, several variations of the HCCI concept have been proposed, such as: premixed charge compression ignition [64, 65], active radical combustion [66], modulate kinetics [67] and partially premixed combustion [16, 68] among others. In these concepts, new air management strategies, fuel injection and mixture formation are used to extend the operating range [69] and to reduce preignition, knocking [70] and HC emissions [67] while achieving high indicated efficiency [71].

The premixed methods before commented have in common that they try to reduce the charge reactivity through the reduction of the mixture temperature, thus slowing down the chemical reactions and delaying the autoigni-

tion [72, 73]. The control of the charge reactivity by blending or separately injecting low and high reactivity fuels to achieve reactivity stratification along the chamber, called Reactivity Controlled Compression Ignition (RCCI), has been studied as a solution of most of the problems presented by the previous modes, while achieving high engine efficiency [74, 75]. The benefits of the RCCI concept regarding NO_x and PM emissions reduction have been broadly reported [76–78]. However, RCCI strategy has the drawback of low combustion efficiency (high HC and CO emissions) when compared with CDC and CGC. This is mainly explained by the unburned fuel trapped in crevices and flame quenching near the walls [78, 79]. It has been reported that, with the proper design of the combustion chamber (piston shape optimization and crevice reduction), the combustion efficiency can be significantly improved [80], reaching indicated efficiencies higher than $50\%\dot{m}_f H_v$ in light-duty engines [81] and $55\%\dot{m}_f H_v$ in high-duty engines [82].

2.3.2 Air management

The improvement of the injection/combustion systems has made necessary the development of advanced air management strategies to comply with the higher air flow required. Furthermore, the mixing process is enhanced through adequate air motion within the chamber. These processes can be improved by means of a proper intake/exhaust lines design, since the filling and emptying process depends on the fluid dynamic configuration. For this purpose, computational simulation tools such as 1D modelling [83] and CFD [84], allow performing dedicated studies of the fluid gas motion, thus optimizing the RICE intake/exhaust geometry to enhance the gases flux through the chamber and improving the fuel/air mixing process.

The design of the intake/exhaust manifolds can be optimized to take advantage of pulsating waves in order to enhance the corresponding processes for the most relevant operating conditions [5, 85]. Moreover, the use of technologies such as **variable valve timing** allows modifying the valves timing and lift to optimize the intake/exhaust process, thus increasing the volumetric efficiency and/or reducing the pumping losses [50].

To ensure a proper intake process in a wider range of the engine map, additional approaches such as **supercharging** have become usual in current engines to ensure the required amount of air in the cylinder. Supercharging increases the air density at intake, thus leading to higher air mass trapped, more fuel injection at same fuel/air ratio and hence higher power output for a

fixed engine size [1]. Moreover, supercharging benefits the fuel/air mixing process and hence the combustion and engine performance [86]. Supercharging is done by means of compressors, which can be driven by the engine crankshaft, an external source or a turbine located in the exhausts. This last is known as *turbocharging*, being the most usual supercharging method [5] whose benefits on engine performance has been widely demonstrated with one-stage [87], two-stage [88] and three-stages [89] turbocharging systems. In general, this increase of air and fuel amounts allows working at high indicated mean effective pressure (*imep*) operating conditions, which are the zones of the engine map with the highest brake efficiency [25]. Besides, the use of turbocharging systems allows reducing the engine size and increasing the specific power, and hence reduces the BSFC. This is the main idea behind Downsizing, which is analysed in Section 2.3.5.1.

Increasing the boost pressure also increases the air temperature, which reduce the air density at intake when compared with the isothermal process. For this reason, the use of exchangers after the compressor is a common practice. These exchangers consist on air-air or air-water heat exchangers, known as *intercoolers*. **Cooling the air** increases the air density, and reduces the temperature evolution within the chamber, which leads to less HT and hence increases the indicated efficiency [25] (with an additional reduction of NO_x). The intercooler efficiency is higher at high air temperatures [5], thus the improvements of intercooling are more important at highly turbocharged operating conditions [10].

The **air movement within the chamber** also has an important effect on engine efficiency. The induction of vortex increase the fuel/air mixing process and combustion development, thus modern RICEs are designed to generate high vorticity and turbulence in the combustion chamber. As explained in Section 2.2.2, the main rotative macro structures found in RICEs are the swirl and tumble. Both can be enhanced by using an appropriate port and combustion chamber design [13, 90] or by means of guide vanes in the intake line [90, 91]. The effect of swirl in consumption is not clear; depending on the engine design and the operating condition evaluated, the efficiency can be improved as a result of an enhanced combustion process [92–94]; however, the increase of HT and pumping work can lead to lower efficiency values [92, 93]. On the counterpart, the use of tumble increase the turbulence before the ignition, thus accelerating the burn rates, stabilizing the combustion, and extending the dilution limit [95]. Some works on new engine concepts shows

that high tumble ratios combined with optimal air management and injection setting results in good emission-performance trade-off [13].

The interest on reducing NO_x emissions has led to the extended use of **EGR** (see section 2.2.1), which is a challenge in order to attain an adequate air management. The EGR can be supplied to the engine by mixing the intake fresh air with a fraction of the exhaust gases taken from the exhaust line at low or high pressure, i.e. after or before their expansion in the turbine respectively [51]. The EGR have two main consequences in terms of air management: on the one hand, it requires the use of several valves along the intake/exhaust lines, thus generating pressure drops and hence energy losses; on the other hand, it changes the chemical properties of the charge and modifies its thermodynamic conditions at intake, thus reducing the O_2 concentration with a negative effect on combustion efficiency. To diminish these negative effects, some alternatives can be used: cooling the EGR helps to maintain the air density, thus increasing trapped O_2, and combinations of low and high pressure EGR are useful to reduce losses in the intake/exhaust lines [96, 97].

Finally, the **IGR** strategy improves CDC and CGC efficiency during the warm-up period as a consequence of two main effects, on the one hand, replacing some air with IGR leads to near to stoichiometric mixtures, and hence higher combustion temperatures are reached. On the other hand, the gas temperature evolution increases as consequence of higher gas temperature at IVC. The commented effects speed-up the engine warm-up, reducing friction and emissions (see section 2.2.1). In premixed combustions, the IGR used is also extended to low load operating conditions, since it increases the charge reactivity, thus providing more combustion control, improving the combustion efficiency and hence reducing consumption [15, 16].

Summarizing, with proper air management several benefits on the indicated cycle can be achieved, leading to better efficiency along with low emissions level and good cylinder filling at a wide operating conditions range. Finally, it allows increasing the power output or reducing the engine size (Downsizing), with clear additional benefits on consumption.

2.3.3 Heat transfer reduction

The Heat Transfer (HT) accounts for about 15-35%$\dot{m}_f H_v$ of the total fuel energy [98] depending on the operating condition. Therefore, several authors have made important efforts to improve the engine efficiency by means

of reducing the heat losses in the chamber, either by setting appropriate engine operating parameters or by improving the engine architecture, materials and sub-systems. Taking into account that injection and air management settings in current engines are mainly oriented to control emissions, this section is focused on HT optimization from two different points of view: the smart design and operation of engine cooling sub-systems to achieve optimal cooling and warm-up processes, known as *engine thermal management*, and using combustion chamber coatings to reduce the walls thermal conductivity, known as *low heat rejection engines*.

2.3.3.1 Engine thermal management

Engine thermal management (ETM) can be defined as the adequate control of all the thermal fluxes of the engine in order to reduce emission or consumption [99]. The most important thermal fluxes are those associated with the cooling of hot metallic parts, aimed at reducing thermal stresses. However, the lubrication system also requires an appropriate cooling to avoid oil degradation, while oil temperature has a direct effect on consumption. The smart design and operation of all these sub-systems and their interactions have positioned the ETM as an interesting alternative to increase the engine efficiency; thus, it have been subject of several researches [100–102].

Traditionally, the cooling systems are designed to ensure the engine integrity at the most unfavourable operating conditions [99], being the natural consequence an inefficient operation in a broad range of the engine map, and hence lower engine efficiency. The ETM is aimed at using the adequate coolant flux and temperature to keep the cooled part or fluid at the optimal thermal condition within the material resistance limits, being this specially interesting at low load, where less heat has to be evacuated [103]. In the case of the combustion chamber, if the coolant temperature increases, the HT is sightly reduced due to the temperature gradient reduction, which will also lead to higher gas temperature, as can be seen in Figure 2.2. This higher gas temperature results in shorter ignition delay, short pre-mixed combustion and fast combustion completion [5], thus it can be stated that high coolant temperatures are beneficial for improving the engine efficiency. In steady state, the influence of coolant temperature on performance depends on the load, having moderate impact at low load, and small at medium and high load [99].

The conventional engine cooling system consists on a mechanical pump driven by the engine, where the volumetric flow is proportional to the engine

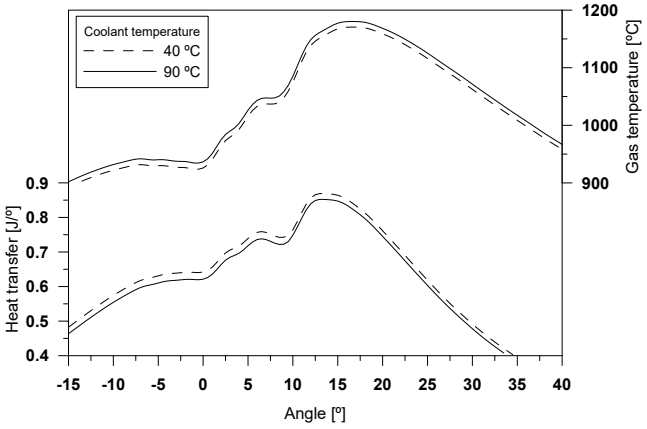

Figure 2.2. *Coolant temperature influence on the gas temperature and HT.*

speed. The cooling capacity is selected to overcome the thermal requirements at maximum engine power, leading to overcooling the engine and increasing the fuel consumption and energy wasting [104]. A clear example is the cold-start, where the indicated efficiency is significantly low, thus high thermal loads are desirables [105] to reach the optimal engine operation temperature, reducing in this way the heat losses and friction [106]. According to Torregrosa *et al.* [99], reductions about 20% in the warm-up time reduce the HC and CO emissions about 16% and 12%, and the BSFC about 1.6% with a reduced effect on NO_x and PM. The right management of the coolant flow as function of the thermal requirements can be achieved, on the one hand by performing modifications on the pumping system, and on the other hand by modifying the flow repartition along the circuit to account for the cooling specific requirements. In this direction, the development of sophisticated electronic control devices [107] is shown as an important tool to re-design the usual cooling systems. Some of the ETM methods found in the literature are the following:

- The use of **electric valves** at the coolant pump outlet is the easiest way to control the coolant flow in a classic system [100]. The coolant flow is kept low at cold-start and low power operating conditions, thus reducing the thermal capacity of the coolant and hence speeding-up the warm-up process. This has a positive effect in terms of emissions and

friction reduction, explained by the oil heating and its subsequent low viscosity.

- The substitution of the mechanical pump for an **electric pump**, allows adjusting the coolant flow to the instantaneous engine thermal requirements independently of the engine speed [49]. This benefits the warm-up process at low power operating conditions; however, the efficiency of the mechanical-electric energy transformation results in higher fuel consumption at high power conditions. Considering that engines operate at low load the 90% of its life-time [5], the overall balance results in a global BSFC reduction.

- **Electric thermostats** allow a better temperature control than the traditional thermostats, thanks to their short-time response and higher temperature resistance. The maximum coolant temperature allowed in traditional thermostats is limited by the wax temperature fusion (between 85°C and 90°C) [107], whilst the electric thermostats allow reaching higher temperatures, leading also to higher oil temperature and hence reducing the friction losses [105]. Taking into account that the higher coolant temperature increases the HT rate in the radiator, and hence increasing its efficiency, smaller and more lightweight radiators can be used [108].

- The advances in numerical calculations along with the electrical systems previously described, allow performing **better design of cooling systems**, centring the cooling capacity in places with higher thermal gradients. It is achieved by higher local coolant speed and by producing coolant streams in the critical surfaces, e.g. the valves seat. This is known as precision cooling and is defined as the minimum cooling necessary to achieve an optimised temperature distribution [109]. The main characteristics of this procedure are: low temperature difference between cylinders or equivalent points, higher operation temperatures within thermal resistance limits, enhanced lubrication and smaller cooling system.

- The **evaporative cooling** consists on evaporates the coolant using the heat from the engine, and condenses it in the radiator. The main advantage of this cooling mode is the higher heat power that a phase transition is able to evacuate. For a given coolant flow rate, it could be hundred times the power exchanged by convection. Thus, the mass flow rate

necessary to cool the engine is significantly lower thanks to the increase in the HT coefficient [110]. However, this method has some issues that makes difficult its implementation: it requires a high capacity radiator to condensate the vapour; the vapour bubbles can block the flux producing pressure drops, and hence changes the density of the coolant in its gas state, which makes necessary the use of bigger cooling systems [111].

As presented, the use of sophisticated elements along with the proper design, yields in optimized cooling systems instead of the oversized ones that are traditionally used. This results in additional efficiency benefits by reducing the energy consumption of the engine sub-systems (smaller pumps and coolers). The electronic control and the understanding of the engine thermal processes are key points to find the adequate ETM configurations.

2.3.3.2 Low heat rejection engines

Theoretically, the reduction of the HT to the combustion chamber walls results in the indicated efficiency improvement [1]. By means of thermal barrier coating, the HT can be effectively reduced. It consist of applying a layer of a low thermal conductivity material over an area exposed to high thermal gradients. The normal configuration of a coating system consists on a bond coat applied on the combustion chamber surface, followed by a coating layer. The bond coat consist usually on a $MCrAlY$ alloy and some similar variations [112]. This layer works as protection against the oxidation and corrosion, and relaxes the thermal stresses due to the mismatch of the coefficient of thermal expansion between the coating layer and the combustion chamber surface [113].

Different materials such as Al_2O_3, TiO_2, mullite, $CaO/MgO + ZrO_2$, yttria-stabilized zirconia, etc. can be used as engine coating materials [114–116]. This materials have some properties which makes them suitable for this application, i.e. low thermal conductivity, no phase transformation in the in-cylinder temperature range, high melting point, chemical inertness, same thermal expansion coefficient as the combustion chamber surface material, good adherence in the combustion chamber surface and low sintering rate of porous micro structures [117]. The coating layer is deposited on the combustion chamber walls by means of a thermal spraying process as shown in Figure 2.3, in which the powder coating material is fed to a source of heat (a fuel gas/oxygen flame or a plasma jet) inside or outside of the spray apparatus.

The coating material is melted superficially or completely, or it is heated until it is sufficiently soft to adhere to the surface, then a spray gas stream propels the particles towards the combustion chamber surface. Since the process is performed at high temperature, the surface is subject to moderate thermal stress without melting [118].

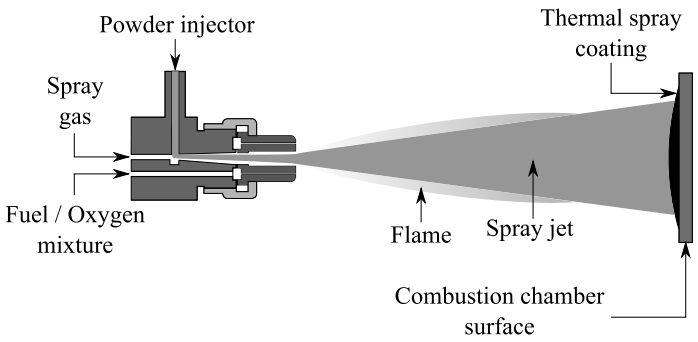

Figure 2.3. *Thermal spraying process.*

An engine with this kind of coatings is commonly referred as Low Heat Rejection Engine (LHRE). The main combustion difference between LHREs compared with CDC is: higher fuel evaporation rate due to higher temperature, which decreases the pre-mixed burning phase and shortens the combustion delay, leading to longer diffusion burning phase [119, 120]. In general, LHREs depict better performance and lower consumption than CDC; however, there is some discussion regarding the improvements and viability of their extended use, and also different points of view regarding engine power, BSFC, brake efficiency, air management and emissions can be found when compared LHREs with conventional Diesel engines:

– The use of coatings produces a chain of favourable effects that increase the engine efficiency [121–123]: reducing HT implies higher temperature and pressure, thus reaching higher *imep* and hence higher torque and power [121, 123]. This HT reduction also increases the energy availability at exhaust [124], which can be used in organic Rankine cycles [125] or turbocharging and turbocompounding systems [126], leading up to 15% lower consumption with these configurations [127, 128]. Some further benefits of using LHREs have also been reported when operating with alternative fuels (e.g. vegetable oils and alcohol blends), after performing an injection setting optimization [129].

– Few authors reported increases in BSFC [127, 128]: LHREs can have longer combustion duration [130, 131], leading to lower indicated efficiency. In naturally aspirated engines, the volumetric efficiency reduction as consequence of higher residuals temperature and lower air density (as air gets heated by the insulated components of the engine) can lead up to 10% higher consumption [127, 128].

Apart from the discussion regarding efficiency implications, one of the main LHREs drawbacks is the increase of NO_x emissions, due to the higher combustion temperatures and longer combustion durations [128]. However, the HC, CO and PM emissions are lower due to high in-cylinder gas and wall temperatures, which help the oxidation reactions to proceed close to completion [48, 122].

2.3.4 Friction and auxiliary losses reduction

The mechanical losses of an engine are understood as those which reduce the gross indicated-to-brake power ratio. These are the pumping losses, the friction losses and the auxiliary activation energy. The pumping losses are taken into account in the indicated cycle by calculating the net indicated power; therefore, the optimization of the pumping work has already been discussed in Section 2.3.1. This section deals with the mechanical losses which lead to energy degradation from the net indicated power to the brake power.

Friction and auxiliary losses accounts for up to $12\%\dot{m}_f H_v$ of the total fuel energy [25]. Regarding the relative importance of each engine sub-system in the total mechanical losses, a wide variation range can be found in the literature [132, 133], thus the pumping work ranges between 15% and 30% of the total mechanical losses, friction between 45% and 65% and auxiliary between 15 and 25%. At the same time, the friction weight of each engine part is also variable depending on the source: piston rings and skirt accounts for about 40% and 75% of total friction, bearings between 20% and 40%, and the camshaft ranges between 7% and 30%. The reduction of friction and auxiliary losses directly leads to more brake power output, thus in the following sections, some methods proposed in the literature to reduce them are presented.

2.3.4.1 Friction losses reduction

The friction between metallic parts with relative movement reduces the final power availability at the crankshaft. Therefore, the friction level depends on the contact surfaces and lubricating oil properties. Some of the techniques used to reduce the friction are:

- **Smooth surfaces** (low roughness surfaces) are essential to decrease the friction coefficient. It can be achieved by means of the appropriate manufacturing process or surface treatment. By using coatings in the liner, the brake efficiency can be increased. An example is the work of Morawitz *et al.* [134], in which a reduction of the BSFC between 1% and 2% in a New European Driving Cycle test (NEDC) is reported.

- The use of **high oil temperature** reduces the oil viscosity and hence increases the engine efficiency [135]. The main problem of this technique is the oil overheating, which could lead to faster oil film degradation and hence direct contact between metallic parts, thus strongly increasing the friction and wear.

- By using **Low Viscosity Oil** (LVO), reductions on BSFC about 2% at low load and 1.7% in a NEDC have been reported [136]. In general, LVOs are better in normal city driving conditions and shortens the warm-up periods; however, in high load operating points, the BSFC can increase due to deterioration of the oil film between parts due to the oil heating, and hence the viscosity reduction.

- The **optimization of components design** helps to reduce friction, i.e. reducing sizes and weights of the piston, bearings and camshaft elements [137], better refinement of the piston rigs surface [138], decreasing the sealing force of the rings [139], using cam roller followers [140], decreasing the loads of valve springs [141] and substituting multiple belts for conventional V-belts [137]. All this changes are restricted by the engine operating requirements and the materials resistance, e.g. lower rings sealing forces reduce the friction between them and liner but can increase the blow-by leakage and the flow of oil from the crankcase to the combustion chamber.

- **Reducing turbocharger friction** is also interesting to increase the engine efficiency, since the capacity of the turbocharger to transform

exhaust energy in mechanical energy to increase the compression work gives place to a better intake process, with the benefits explained in Section 2.3.2. Different methodologies to asses the mechanical losses in the turbocharger can be found in the literature, ranging from experimental [142] or modelling processes [143].

2.3.4.2 Auxiliary systems improvement

The auxiliary systems of the engine are those necessary to the appropriate and safe engine operation, i.e. cooling, lubricating and injection systems. The coolant, oil and fuel pumps are usually driven by the engine crankshaft, thus the improvement of these components is key to increase the engine mechanical efficiency. Besides, high performance of auxiliary systems allows using specific engine strategies, e.g. high injection pressure by using high pressure fuel pump, fast warm-up by deactivating coolant flow, etc.

The mechanically activated pumps are designed to comply with the high power requirements, which makes them inefficient at low power operating conditions. The new auxiliary systems incorporates electric pumps, valves, thermostats and optimized circuits to allow a smart thermal management that led to additional improvements, as already discussed in section 2.3.3.1. Similarly, new oil pumps have been developed: Lasecki and Cousineau [144] asses the use of an electric oil pump and a dual pump system (mechanical and electrical), Meira *et al.* [145] propose the use of variable flow pumps to adapt the oil flow depending on the operating conditions. Arata *et al.* [146] present a two-stage variable displacement vane pump to increase the oil flow at low speed and avoid unnecessary pumping work at medium and high speed.

Finally, the fuel pumping systems usually consist on a low pressure feeding pump and a high pressure volumetric displacement pump. This volumetric pump has an important energy loss due to the high injection pressure requirement (up to 2000 bar in modern systems) and the relative small amount of injected fuel at low load operating points. The use of fuel metering (i.e. inlet throttling) by a solenoid valve at the pump inlet, allows pumping the fuel according to the engine requirement. The control of the fuel flow from the feeding pump to the high pressure volumetric pump results in liquid-vapour mixture compression, reducing the compression power requirement but also increasing the fluctuations in the pump discharge and hence in the rail-pressure [147]. The use of electric low pressure pumps also help to reduce the energy consumption. In this case, only the fuel required for the engine and for lubricating the

high pressure pump is comprised in the low pressure pump [148], avoiding unnecessary energy consumption.

2.3.5 Other strategies

Reaching significant efficiency improvements in conventional RICEs seems to be more difficult day after day. In some cases, the engine evolutions discussed in previous sections are more expensive than the benefits obtained. For this reason, the optimization of the current RICE efficiency can benefit from the development of new powertrain technologies. One interesting concept is the Downsizing, in which a conventional engine is reduced in size and is operated at high load, where the engine efficiency is higher. Other growing tendency is the use of hybrid engines, in which a RICE and an electric motor are combined, achieving lower emissions and higher efficiency.

2.3.5.1 Downsizing

The advances in turbocharging and injection technologies allow reducing the RICE displacement while keeping its performance [149, 150]. This is generally known as engine Downsizing. One of the main advantages of Downsizing is that the engine works in engine map regions at high load, which have better indicated and mechanical efficiency [25]. Despite the advantages of this technique, there is a number of limitations, which impose a minimum characteristic size for the RICE displacement [151]. This is due to three main thermo-fluid-dynamic issues:

1. The difficulties imposed by the intrinsic nature of the processes with well-defined space and time scales, such as injection and combustion, and all their related basic processes (spray break-up and atomization, air entrainment, evaporation, mixing, etc.) [152], when it is tried to adapt them to small sizes (small combustion chambers) and short times (high engine speeds).

2. Some limits are related with the air management in relation with turbocharging, due to the efficiency drop when decreasing the turbine size. Moreover, the highly pulsating flow in engines with low number of cylinders implies a different fluid dynamic process with considerable uncertainties regarding its impact on turbine performance [153].

3. The increase in the surface-to-volume ratio leads to performance degradation as a result of higher HT [154]. As the specific HT highly increases when the engine size is reduced, it has been suggested by some authors that HT may limit the engine size [155].

The high reduction of the engine size, known as *extremely Downsizing*, theoretically should improve the specific power; however, as commented, it faces some technical problems related with turbocharging systems [87, 156] along with issues regarding with thermo-mechanical resistance, high pressure injection systems [157] and elevated powertrain noise, vibrations and harshness [158].

2.3.5.2 Hybrid powertrains

The electric powertrain has an interesting potential due to its zero local emissions and low noise; however, the battery electric vehicle has not gain widespread acceptance due to its limited operating range, long recharge time and poor efficiency [159]. The hybrid electric vehicle raises as a solution for these issues, as it has the advantages of both, combustion engines and electric motors, in terms of efficiency and emissions when compared with conventional RICEs. The hybrids can directly drive the rear axis or can work as a generator, transforming the mechanical energy from the engine and vehicle deceleration into electrical energy, and storing it in the energy buffer. In this sense, several works are devoted to improve power batteries [160, 161].

In spite of the promising future for the electric vehicle, the RICE is still the most widespread transportation solution, either as a conventional or hybrid powertrain, thus the introduction of hybrids opens a new field for conventional RICEs, since the benefits obtained can increase importantly the efficiency while remaining at low emissions level.

2.4 Thermal balance in reciprocating internal combustion engines

Thermal balance is a methodology to assess the use of the energy in RICEs. The main objective is to evaluate the efficiency with which the chemical energy of fuel is transformed into mechanical energy (brake power) by means of the detailed analysis of the rest of energy flows. Therefore, the determination of the process inefficiencies is done by tracking these secondary energy flows, e.g. heat rejection, exhaust energy, friction, etc.

Thermal balance is a useful tool to evaluate specific engine strategies aimed at reducing fuel consumption, such as those described in previous sections (LHREs[4], highly turbocharged engines, alternative fuels, Downsizing, etc.). Determining the paths followed by the fuel energy until reaching the final destinations allows identifying the energy waste and the mechanisms that produce those losses. The comprehensive understanding of the energy degradation is vital to optimize different processes inherent to RICE operation such as: cooling, lubricating, fuel injection, friction reduction and air management. Therefore, the suitability of a specific engine concept, strategy or system can be established by means of the thermal balance.

Depending on the information available and the specific research interest, the terms involved in the thermal balance are differently defined among authors, and in consequence, the level of detail can vary significantly between works. Figure 2.4 shows the most general approach, in which the simplified thermal analysis includes the brake power, the heat rejection (HT to coolant and oil together), the exhaust gases energy and other minor losses that are usually difficult to estimate, e.g. HT to the ambient, blow-by enthalpy loss and unburned fuel.

The determination of each energy term can be performed through experimental or modelled information. The experimental measurements are usually employed to assess the performance of a new engine concept or strategy, whilst modelling results are commonly used to perform a prior determination of the energy degradation. To broaden the understanding of thermal balances and its potential as analysis tool, its *state of the art* in a wide range of RICE applications is presented in the following sections.

[4]Note that LHRE is the abbreviation defined for *low heat rejection engine*.

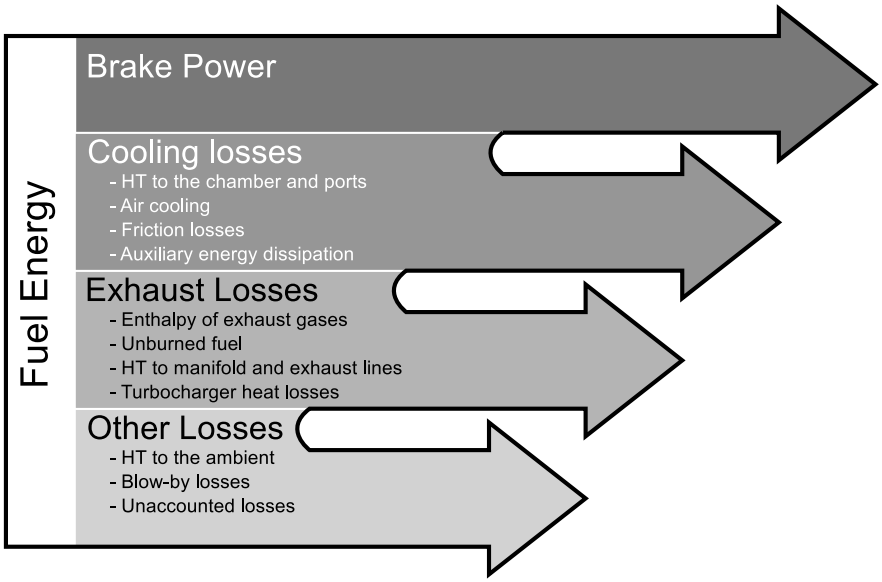

Figure 2.4. *Main terms of the thermal balance.*

2.4.1 Thermal balance in conventional engines

The most widespread RICE technologies, i.e. CI Diesel engines and SI gasoline engines, are referred in this work as the conventional RICEs. The extended use of these powertrains make them the natural reference to appraise the performance of new RICE concepts. Therefore, the determination of the thermal balance and the understanding of the thermal processes and energy transformations in conventional RICEs, becomes the first step to identify the improvement paths.

There is a vast amount of works dealing with the thermal balance for both, CI [162–170] and SI [171–173] engines. In both cases, the thermal balance is highly dependent on the injection and air management technologies, engine size, application and operating condition evaluated.

As examples of simplified thermal balances in conventional RICEs, Tables 2.1 and 2.2 show the typical values of the indicated parameters and mechanical losses (top), along with the thermal balance (bottom) of a light-duty Turbocharged Direct Injection Diesel engine (TDI) and a light-duty Tur-

bocharged Direct Injection Gasoline engine (GTDI). [5] Taking into account the reference values presented, the following observations can be stated:

Term \ Range	LS/LL	LS/HL	HS/LL	HS/HL
Indicated efficiency	40-43	41-42	47-49	45-47
Pumping power	1-2	<1	7-10	5-6
Friction and auxiliary	5-7	3-4	8-13	6-7
Brake efficiency	34-35	**36-37**	26-32	32-35
Heat rejection	**34-40**	27-30	29-35	24-25
Exhaust enthalpy	27-28	29-33	37-40	**39-42**
Unburned fuel	1-2	**1-3**	<1	<1

Note 1: LS(Low speed), LL(Low load), HS(High speed), HL(High load)
Note 2: Energy terms values in percentage of fuel energy ($\%\dot{m}_f H_v$)

Table 2.1. *Thermal balance of a conventional 1.6l TDI.*

Term \ Range	LS/LL	LS/HL	HS/LL	HS/HL
Indicated efficiency	30-38	33-36	37-40	30-36
Pumping power	2-4	<1	4-7	2-3
Friction and auxiliary	4-6	2-3	5-7	3-4
Brake efficiency	27-30	**29-33**	26-30	24-28
Heat rejection	**25-31**	15-27	24-30	15-20
Exhaust enthalpy	35-40	**37-44**	37-38	38-40
Unburned fuel	1-2	1-2	2-10	**5-20**

Note 1: LS(Low speed), LL(Low load), HS(High speed), HL(High load)
Note 2: Energy terms values in percentage of fuel energy ($\%\dot{m}_f H_v$)

Table 2.2. *Thermal balance of a conventional 2.3l GTDI.*

- The **brake efficiency** is higher at high load [165, 171] despite the indicated efficiency is slightly higher at low load. This is easily explained taking into account that at low load an important part of the indicated

[5] For the sake of completeness, Table 2.3 at the end of this chapter shows a summary of the literature review regarding thermal balances in RICEs.

power is used to beat the friction and activate the auxiliary elements. In the case of TDI, the same trends are observed at high and low speed; however, GTDI has lower indicated and brake efficiencies at high speed and load due to the high unburned fuel losses, as explained later.

The indicated and brake efficiencies are better in TDI engines, which is explained by the better indicated cycle of Diesel combustion, as shown in Figure 2.5. The difference in the peak pressure due to the different compression ratio is the key parameter to determine the indicated efficiency. Taking into account that the mechanical losses have similar level[6], the resulting brake efficiency is also higher in TDI engines.

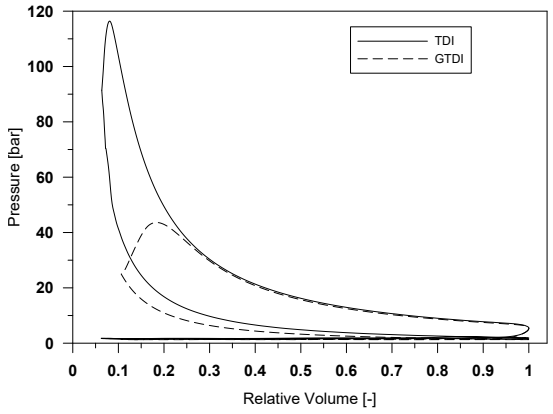

Figure 2.5. *Indicated cycles of TDI and GTDI engines (3m/s mean piston speed and 75% load).*

- The **heat rejection** refers to all the HT to the coolant and oil, i.e. HT from chamber and ports, friction (which is dissipated as heat to the coolant and oil), air cooling losses (for air-coolant intercoolers) and auxiliary activation energy (which is somehow dissipated in the pumped fluid). The higher cooling losses in the TDI engines are mainly due to the higher HT in the chamber, produced by the higher operating pressure and temperatures when compared with the GTDI engines. Part of the energy going to the coolant is lost as heat rejection to the ambient, being

[6]The slightly higher mechanical losses observed in TDI engines is partially due to the higher injection pressure, taking into account that the Diesel is injected at pressures up to 2000 bar [19], whilst DI gasoline engines work with pressures lower than 200 bar [23].

this specially important in TDI engines at low speed and load, where it can reach values higher than $20\%\dot{m}_f H_v$ as reported by Smith *et al.* [165].

- The exhaust losses depend on the definition assumed, since it can include the unburned fuel, the HT from exhaust manifold to the ambient and the HT from the turbine case. In some works, the unburned fuel is accounted independently [53, 104, 171], the HT from the turbocharger case to the ambient is measured [165], or all these terms are grouped in a miscellaneous or unaccounted energy term [163, 168]. For the sake of clarity, the exhaust enthalpy presented in Tables 2.1 and 2.2 correspond to the net enthalpy variation between intake and exhaust ports, where the unburned fuel was not included.

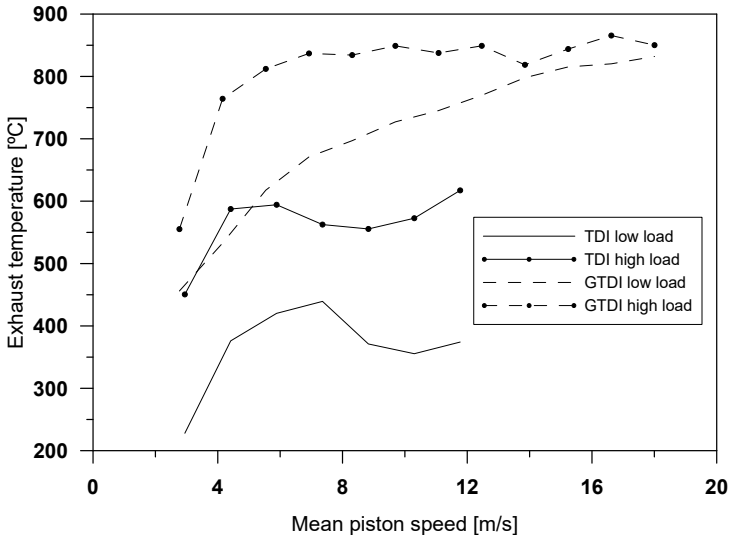

Figure 2.6. *Exhaust temperature comparison between TDI and GTDI engines.*

At low load and up to mid-speed, the **exhaust enthalpy** is higher in GTDI engines due to the higher exhaust temperatures, as can be seen in Figure 2.6, which is explained by its stoichiometric fuel/air equivalence ratio. However, at high speed, the exhaust losses weight is lower in GTDI engines as a consequence of the high unburned fuel. In naturally aspirated SI engines, the exhaust losses tend to increase with speed and load [173] and should be higher than CI engines at comparable

conditions, taking into account that the combustion efficiency is similar [1]. Some authors consider the unburned fuel as energy lost in the exhaust [174]; therefore, by adding the unburned fuel and the exhaust losses at high speed in Table 2.2, these reach higher values than those of TDI engines.

- The energy losses due to **unburned fuel** lie about 1-3%$\dot{m}_f H_v$ in the whole TDI engine map and in the case of GTDI engines operating at low load. Increasing the speed of GTDI engines leads to high gas temperature, which increases the risk of knocking[7] and can lead to exhaust elements damage [175, 176]. To reduce this temperature, a common technique is to work with fuel-rich mixtures (high fuel/air ratio) [176, 177]; thereby, the heating of the unburned fuel reduces the gas temperature. For this reason, unburned fuels of GTDI engines at high speed reach values between 5-20%$\dot{m}_f H_v$ or even higher [174].

Performing the thermal balance in steady state operation is interesting to accurately determine the effects of specifics parameters in the engine thermal behaviour, which allows adjusting dedicated models or assessing engine strategies. With these goals, some examples are the works of Boulahlib *et al.* [164], who evaluate the effects of various engine loads and climatic conditions on the thermal balance, Tauzia and Maiboom [53] perform thermal balances in a stoichiometric Diesel combustion, analysing the effect of using different injection settings and intake strategies, Durgun and Şahin [166] analyse and compare the thermal balance on naturally aspirated and turbocharged Diesel engines, and Smith *et al.* [165] and Caton *et al.* [171] analyse the engine speed and load impact on the heat rejection and engine efficiency in Diesel and gasoline engines respectively.

One interesting application of the thermal balance in conventional RICEs is the evaluation of the energy degradation during the warm-up period. The reported engine efficiency at this stage is low [178–181] due to coolant heating until reaching operation temperature, high friction due to high oil viscosity (because of low oil temperature), and high heat losses due to metal thermal storage capacity. One of the problems of performing the thermal balance during transient operation is the difficulty to accurately measure the data

[7] In SI engines, knocking is an abnormal combustion phenomenon, consisting in the autoignition of a portion of the charge ahead of the advancing flame, producing a fast release of fuel energy characterized for very high pressure gradients and sharp metallic noise.

necessary to compute the energy terms, which can lead to high experimental uncertainty as reported by Romero *et al.* [178], who performed an experimental thermal balance during warm-up period, and found that the unaccounted losses reach important values due to the effect of the metal thermal storage capacity and the experimental uncertainty. To overcome these issues, Donn *et al.* [179] performed controlled measurements in climactic chambers, which can be used to develop accurate thermal engine simulation models, Jarrier *et al.* [180] simulated the HT from gases to each part of engine by means of a lumped capacity model, and proposed empirical correlations to calculate the friction losses distribution. Finally, Jung *et al.* [181] developed an engine thermal management predictive model validated with steady state measurements.

2.4.2 Thermal balance application on alternative combustion modes, alternative fuels and fuel blends

As analysed in Section 2.3.1.1, the optimization of the air-fuel mixing process to attain high burning rates while keeping low temperature combustion can be achieved through premixed combustions (e.g. HCCI, PPC and RCCI). Since there are some drawbacks regarding premixed combustion of conventional Diesel or gasoline fuels, some works are focused on applying these new combustion concepts with alternative fuels and fuel blends [60, 78].

Different works can be found in the literature, where the use of fuel blends such as Diesel-gasoline [75], and alternative fuels such as biodiesel [128], natural gas [182] and hydrogen [46] are reported. These fuels and combustion modes are evaluated, on the one hand to reduce emissions, and on the other hand to assess the benefits of using renewable fuels (biodiesel and hydrogen).

Although, there are some technical problems regarding the production, storage and transportation of such alternative fuels [183], the benefits of biodiesel [45], alcohol [184, 185] and hydrogen [186] blends with the conventional Diesel and gasoline to overcome these issues have been widely documented. Beyond the emissions and efficiency, the energy distribution analysis due to the use of alternative fuels and fuel blends is helpful to understand the paths to improve the engine thermodynamic processes. Running an engine with alternative fuels not always leads to better efficiency and emissions levels [187], this can be explained by several factors such as the type of fuel used, unsuitable engine design and non-optimized operation settings. The thermal balance provides some guidelines to optimize the engine operation and to perform changes in the baseline design through assessment of energy wasting. The

main tendencies of the energy repartition obtained by using different fuels are summarized as follows:

- **Diesel-gasoline blends:** this blend is usually achieved by in-cylinder mixture of DI Diesel and Port fuel Injected (PFI) gasoline fuels, thus achieving reactivity stratification along the chamber (RCCI mode). Diesel-gasoline RCCI is characterized by low combustion and gas temperatures, therefore leading to important reduction of HT and exhaust losses while achieving high efficiency [75]. In spite of the efficiency improvement, the unburned fuel losses are high due to quenching and incomplete combustion in crevices [80].

- **Biodiesel:** depending on the biodiesel used, the thermal balance results can differ among authors. Few works reported lower brake efficiency when compared with CDC, whilst most of the works reported low effect [44, 121, 188] or even a slight increase [189]. The higher combustion temperature of the biodiesel leads to higher HT [190] and lower exhaust energy losses. Therefore, a combination of a LHRE with fuel blends is reported as a useful strategy to reduce HT losses [128, 189], thus increasing the exhaust gases energy and hence the energy availability at exhaust.

- **Alcohol-Diesel blends:** despite these blends can lead to lower brake efficiency in some operating conditions [191], several authors reported increases in the brake efficiency thanks to the ethanol's cooling effect and its higher combustion efficiency in comparison with conventional Diesel, leading also to lower HT and exhaust energy losses [77, 78, 192]. Alasfour [193] found that in an engine fuelled with a butanol-gasoline blend the heat loss to the cooling water remained constant. At lean operation, the exhaust losses were lower because the exhaust temperature also decreased. At richer operation, the exhaust energy remained constant for both, pure gasoline and butanol-gasoline blend. Caton [194] performed a thermal balance study on different alcohol blends, finding similar HT and exhaust losses between them, being the higher brake efficiency that of the Methanol and Ethanol. Benajes et al. [77] performed simplified thermal balances to assess the effect of ethanol ratio in a Ethanol/Gasoline-Diesel blend. They compared different blending ratios and operating parameters (injection settings and EGR rate), reporting high indicated efficiency as consequence of unburned fuel losses

reduction (through reducing the reactivity gradient in the chamber), while the HT and exhaust losses were kept constant.

- **Gaseous fuels:** the gaseous fuels have some common characteristics such as no fuel cooling effect, advanced spark timing (in SI engines), lower flame speed and longer combustion than CGC. These features explain the thermal balance results obtained from different gas fuelled engines. In comparison with the CGC, the gaseous fuels have lower brake power; however, they have higher brake efficiency and lower HT and exhausts losses. Depending on the specific fuel or blend, and the operating conditions, different combustion efficiencies and energy distributions to coolant and exhausts can be found.

  Özcan and Söylemez [195] assessed the performance of a SI engine fuelled with **Liquid petroleum gas** (LPG) and water addition. They found that water addition improves the brake power and reduces the heat and exhaust losses. This is explained by the cooling effect of the water, which reduces the temperature within the chamber. However, the unburned fuel losses are higher because the longer combustion process and the lower flame speed.

  The **Compressed Natural Gas** (CNG) has been also studied as a fuel choice for SI engines. Gharehghani *et al.* [196] performed a thermal balance in a SI gasoline engine. They found an increment in the brake efficiency about $4.5\%\dot{m}_f H_v$ when compared with CGC. Javaheri *et al.* [197] evaluated the CR and the air-fuel ratio effect on the thermal balance, finding better efficiency when both were increased. Similar works and results have also been reported for different gaseous fuels such as biogas [198].

- **Hydrogen blends:** Yüksel and Ceviz [186] performed a thermal balance to asses the effect of hydrogen-gasoline blends in terms of efficiency. They used three different levels of hydrogen, and found an increase in the engine efficiency but a decrease in the engine brake power. They found also a reduction in the HT to coolant and lower unaccounted losses (mainly unburned fuel and HT to ambient). The Exhaust gases energy was almost the same for both, CGC and hydrogen-gasoline blends. Dimopoulos *et al.* [199] optimized a passenger car fuelled with an hydrogen-CNG blend, using high EGR rates in the major part of the engine map. By means of experimental results and theoretical analysis, they obtained information of the real and theoretical combustion processes, and found

increases in the engine efficiency when compared with a pure CNG fuelled engine.

- **Other fuels and blends:** the wide range of alternative fuels and blends makes difficult to analyse in detail all of them; besides, it is out of the scope of this work. However, some examples where thermal balances are applied are the following: Orbaiz *et al.* [200, 201] performed experimental and simulation studies of a SI engine running with CNG, hydrogen and two different synthesis gases. Mistry [202] carried out a comparative assessment of performance using CNG, LPG and gasoline. Finally, Caton [194] performed thermal balances for 8 different alternative fuels. In all those studies, a simplified thermal balance has been used as evaluation tool to compare the global behaviour of each alternative, obtaining valuable information of each waste source.

2.4.3 Thermal balance on low heat rejection engines and engine thermal management

As explained in section 2.3.3.2, reducing the chamber HT theoretically improves the engine efficiency; however, it seems that the efficiency improvements achieved up to date are low. In this sense, thermal balances are specially useful to determine where the fuel energy really goes. The main agreement is that most of the energy saved by reducing the HT is lost as exhaust energy [126, 203, 204], whilst small increases in the brake efficiency are attained. Different experimental and modelling applications of LHREs can be found in the literature:

- Woods *et al.* [203] analysed the thermal balance for three different single-cylinder LHREs, providing detailed energy repartition to the coolant, taking into account the HT contributions from the combustion chamber, the intercooler and the turbocharger separately.

- Taymaz *et al.* [126, 204] compared the energy repartition of the conventional Diesel engine with its LHRE version.

- Modi *et al.* [189] performed an experimental study to assess the performance of a LHRE fuelled with biodiesel blends.

On the other hand, ETM[8] also requires a well understanding of the energy degradation, placing the thermal balance as a valuable tool for the analysis of new engine cooling technologies:

- Kang *et al.* [104] performed an energy balance to improve the ETM analysis of a double-loop coolant circuit, in which separated cooling lines for the head and block were used. They developed a complete engine thermal model validated with experimental data, aimed at identifying the features of the proposed system.
- Xin and Zheng [205] analysed the effect of the HT to the ambient (i.e. convective and radiative HT from exhaust manifold, turbocharger and engine block). Their model was validated with experimental HT to the coolant.
- Franco and Martorano [206] highlighted the importance of considering the energy transformation in the engine, and proposed predictive methods validated with experimental data, aimed at calculating the engine thermal load.
- Rabeau and Magand [207] developed an ETM simulation platform, aimed at modelling the fluids temperatures and some energy terms. They compared different powertrain architectures to determine the benefit of different cooling strategies for downsized and hybrid engines.

2.4.4 Exhaust energy recovery

Once the energy usage has been thoroughly analysed, the natural next step is to address the recovery methodologies. Considering that some engine concepts such as LHRE [126, 204], some alternative fuels [188] or combinations of both [189] lead to higher exhaust energy, a large number of works dealing with the evaluation of the second law of thermodynamics to determine the engine exergy can be found in the literature [208]. Moreover, the analysis of the exhaust losses is a necessary step to determine the feasibility of using a recovery system, and hence, the further implementation of the thermal balance is necessary to validate the predictions of the second law analysis [208].

Several authors dealt with the determination of the energy waste and availability in organic regenerative cycles for Diesel [162, 163, 167, 169, 170]

[8]Note that ETM is the abbreviation defined for *engine thermal management*.

and gasoline [172, 173] engines. In these works, experimental and modelled energy and exergy analysis are used to assess the feasibility and improvements of using organic regenerative cycles. The effects of efficiency-improvement strategies such as cylinder deactivation, use of advanced materials and improved insulation to limit the HT, turbocompounding [163, 167] and high and low pressure loop EGR systems [170] are taken into account in the thermal balance and the exergy balance to determine the most promissory strategies [209].

2.4.5 Summary

As presented in this section, the thermal balance has been widely used to evaluate the RICE performance and thermal behaviour. In recent years, it has been used to determine the feasibility and benefits of new engine technologies and strategies, aimed at reducing emissions and increasing the engine efficiency. In Table 2.3, the summary of the *state of the art* of RICEs thermal balance is presented. The following conclusions can be highlighted:

- The identification of the energy losses is interesting to evaluate new engine strategies and technologies. Thus, the thermal analysis of the engine allows quantifying the effect of using a specific methodology.
- The thermal balance has been widely used to assess the thermal behaviour of engines fuelled with alternative fuels and fuel blends. The normal procedure is to compare with the same engine fuelled with conventional Diesel or gasoline. The thermal balance allows also identifying the improvement paths, taking into account that in most works, conventional Diesel or gasoline engines are used without optimization for the alternative fuel.
- In spite of the theoretical efficiency increase due to reducing the chamber HT, main agreement shows that the effect in the exhaust energy is higher than the effect in the brake efficiency.
- An important research field is the determination of the engine exergy. Several works deal with the thermal balance to determine the exhaust energy and its availability. A common practice is to develop robust models to evaluate the effect of operating parameters or engine technologies in the exhaust energy availability, therefore reducing the experimental work.

- In spite of the benefits of using thermal balances and their widespread application, in most works the analysis is performed taking into account a very simple approach, that is, considering only the brake efficiency, global cooling and exhaust losses; however, detailed distribution or internal interactions are not usually taken into account.

Ref.	Year	Combustion (Fuel)	z (Vol [l/cyl])	Technology	Operating Condition	Brake eff. (Indicated eff.)	Cooling	Oil	Exhaust	Friction	Turbo	Intercooler	EGR	Ambient	Unburned	Residual
[1]*	1988	SI (Gasoline)	-		Max. Power	25-28	17-26	-	34-45	-	-	-	-	-	2-5	-
		CI (Diesel)	-		Max. Power	34-38	16-35	-	22-35	-	-	-	-	-	1-2	-
[203]	1992	CI (Diesel)	1 (2.3)		Rated Power	36	20	-	41	-	(0.9)	(8)	-	3	-	-
		CI (Diesel)	1 (2.3)	LHRE + Air cooling	Rated Power	35	17	-	46	-	(0.9)	(9)	-	3	-	-
		CI (Diesel)	1 (2.3)	LHRE	Rated Power	34	10	-	53	-	(1.5)	-	-	3	-	-
[210]	1997	CI (Diesel)	6 (16.6)		Max. Speed, Full load	38 (43)	28	-	29	5	-	-	-	-	-	-
[193]	1997	SI (Butanol-Gasoline)	1 (0.45)		0.9 Fuel/Air ratio	29	24	-	29	7	-	-	-	-	-	11
[192]	2000	CI (Diesel)	1 (1.1)		Max. Load	29	18	19	19	-	-	-	-	-	-	16
		CI (5% Ethanol-Diesel)	1 (1.1)		Max. Load	29	18	15	17	-	-	-	-	-	-	22
		CI (20% Ethanol-Diesel)	1 (1.1)		Max. Load	33	17	12	15	-	-	-	-	-	-	22
[171]	2000	SI (Gasoline)	8 (0.7)		Low speed, Low load	18 (25)	40	-	34	(7)	-	-	-	-	0.67	-
		SI (Gasoline)	8 (0.7)		High speed, High load	31 (36)	19	-	44	(5)	-	-	-	-	0.67	-
[191]	2002	CI (No 2 Diesel)	6 (1.4)		Max. Speed, High load	41-37	20-15	-	30-36	-	-	6-8	-	-	-	-
		CI (10% Ethanol-Diesel)	6 (1.4)		Max. Speed, High load	41-35	20-15	-	30-35	-	-	6-8	-	-	-	-
[186]	2003	SI (Gasoline)	4 (0.45)		Near Max. Throttle, Speed sweep	32-40	12-18	-	17-31	-	-	-	-	-	-	39
		SI (Hydrogen-Gasoline)	4 (0.45)		Near Max. Throttle, Speed sweep	36-48	10-14	-	20-32	-	-	-	-	-	-	34-12
[195]	2006	SI (Gasoline)	4 (0.32)		max load, speed sweep	25-31	11-18	-	17-29	-	-	-	-	-	-	47
		SI (50% Water-LPG)	4 (0.32)		max load, speed sweep	28-34	10-16	-	15-27	-	-	-	-	-	-	47
[126]	2006	CI (Diesel)	6 (0.99)		Low and High Load	26-37	49-27	-	24-29	-	-	-	-	-	-	1-7
		CI (Diesel)	6 (0.99)	LHRE	Low and High Load	26-38	49-23	-	27-37	-	-	-	-	-	-	1
[162]	2007	CI (Diesel)	-		max load	32	19	-	31	-	-	6	9	-	-	4
[163]	2008	CI (Diesel)	4 (0.425)		Max. Efficiency	39-41	36-31	-	17	2	1	3-7	1	-	-	1
[164]	2009	CI (Diesel)	4 (0.94)		Full Load	33-36	26	-	37-29	-	-	-	-	-	-	3-9
		CI (Diesel)	4 (0.94)	Air cooling	Full Load (2300rpm)	33-35	25.00	-	39-34	-	-	-	-	-	-	3-7
[166]	2009	CI (Diesel)	-		Speed sweep	33-36 (42-44)	23-32	-	36-25	9-8	-	-	-	-	-	-
		CI (7.5% Gasoline-Diesel)	-		Const. Speed (1500rpm)	35 (42)	27	-	30	6.7	-	-	-	-	-	-
[165]*	2009	CI (Diesel)	4 (0.5)		Engine map	22-40	13-18	3-9	25-36	-	-	0.4-6	-	7	-	3
[194]	2010	SI (Isooctane)	8 (0.7)		MBT	25	25	-	43	6	-	-	-	-	0.67	-
		SI (Methanol)	8 (0.7)		MBT	26	26	-	41	6	-	-	-	-	0.67	-
		SI (Hydrogen)	8 (0.7)		MBT	24	25	-	44	6	-	-	-	-	0.67	-
[167]	2010	CI (Diesel)	4 (0.475)		Road Load and Max. Efficiency	24-44	23-20	-	29-27	14-2	-	2-7	8–	-	-	-
		CI (Diesel)	4 (0.475)	LHRE + Turbocompounding	Road Load and Max. Efficiency	26-45	5-11	-	48-34	14-2	1	2-7	4–	-	-	-
[168]*	2010	CI (Diesel)	-		Max Indicated efficiency	40-42	17-19	-	19-21	-	-	8-10	10-12	-	-	1-3
[172]*	2011	SI (Gasoline)	4 (0.33)		Max. Load	35	21-35	-	20-36	-	-	-	-	-	-	10
[179]	2011	CI (Diesel)	6 (0.49)	Split cooling	Map	27-39	38-21	(3-5)	12-32	-	-	0.5-5	(3-0)	19-3	-	4
[75]	2011	CI (Diesel-Gasoline)	1 (2.44)	RCCI	Load sweep (1300rpm)	(50-56)	20-30	-	23-12	-	-	-	-	-	8-3	-
[211]	2012	CI (Biodiesel- Diesel)	4 (0.5)		Low and High Load	28-34	50-30	-	19-29	-	-	-	-	-	-	0.3
		CI (Biodiesel- Diesel)	4 (0.5)	LHRE	Low and High Load	27-37	48-23	-	24-38	-	-	-	-	-	-	0.1
[196]*	2013	SI (CNG)	4 (0.425)		Full and Half load	29-37	18-29	-	23-47	-	-	-	-	-	-	-
[173]*	2013	SI (Gasoline)	4 (0.3)		Map	13-32	50-22	-	17-34	-	-	-	-	-	-	-
[169]	2013	CI (Diesel)	4 (0.3)		Load sweep (2000rpm)	13-36	66-39	-	16-19	-	-	-	-	-	-	6
[53]	2013	CI (Diesel)	4 (0.5)		Low and High Power	33-38	34-31	-	26-27	7-2	-	-	-	-	0.5-0.1	-
		CI (Diesel)	4 (0.5)		Low and High Power (Stoich.)	29-34	40-31	-	20-26	7-2	-	-	-	-	4	-
[181]	2013	CI (Diesel)	4 (0.6)		Mid-high speed, high torque	36-39	31-22	-	28-33	3-4	-	-	-	-	2	-
[128]*	2014	CI (Biodiesel)	4 (0.625)		Max. Load (2000rpm)	24-25	21-25	18-21	21-26	-	-	-	-	-	-	8-11
[197]	2014	SI (CNG)	1 (0.5)	Variable CR	High Power, Fuel/Air ratio sweep	(35-45)	26-32	-	16-27	-	-	-	-	-	20	-
[201]*	2014	SI (CNG)	6 (0.66)		Fuel/Air ratio sweep, Rich mixture	16-27	30-49	-	17-21	-	-	-	-	-	3	-
		SI (Synthetic gas)	6 (0.66)		Fuel/Air ratio sweep, Rich mixture	25-29	39-52	-	18-20	-	-	-	-	-	15-45	-
		SI (Hydrogen)	6 (0.66)		Fuel/Air ratio sweep, Rich mixture	20-30	40-50	-	18	-	-	-	-	-	0-20	-
[198]	2014	SI (Biogas)	6 (2.15)	Variable CR	87.5% Load	28	32	-	40	-	-	-	-	-	-	1.4
[207]	2014	CI (Diesel)	4 (0.4)		NEDC	24	43	-	21	12	-	-	-	-	-	-
		CI (Diesel)	2 (0.465)	Downsized	NEDC	30	36	-	27	7	-	-	-	-	-	-
[170]	2015	CI (Diesel)	6 (1.75)	High Boosted	Max load	42-43	12-9	-	39-38	5-8	-	-	-	-	-	1-2
		CI (Diesel)	6 (1.75)	High Boosted + Rankine	Max. Load	43-44	12-9	-	38-37	5-8	-	-	-	-	-	1-2
[104]	2015	CI (Diesel)	6 (0.98)		Half load	36	16	-	37	9	-	-	-	-	2	-
		CI (Diesel)	6 (0.98)	Smart cooling	Half load	37	15	-	39	8	-	-	-	-	2	-
[77]	2015	CI (10%Ethanol/Gasoline-Diesel)	1 (1.806)	RCCI	Low load (1200rpm) 59% PFI	(48)	30	-	20	-	-	-	-	-	2	-
		CI (20%Ethanol/Gasoline-Diesel)	1 (1.806)	RCCI	Low load (1200rpm) 59% PFI	(48)	30	-	20	-	-	-	-	-	2	-
		CI (85%Ethanol/Gasoline-Diesel)	1 (1.806)	RCCI	Low load (1200rpm) 59% PFI	(44)	29	-	19	-	-	-	-	-	8	-

Note 1: In the references marked with *, variation ranges are presented, thus the addition of all terms differs from $100\%\dot{m}_f H_v$

Note 2: The values in brackets are not directly considered in the thermal balance addition

Table 2.3. *State of the art of thermal balance, energy terms in* $\%\dot{m}_f H_v$.

2.5 Conclusions

In this chapter, a comprehensive *state of the art* about the methodologies to improve RICE efficiency has been presented. The analysis was focused on three main aspects: the **consumption and emissions trade-off** to describe the background of engine research in last years, the **consumption optimization methodologies** to explain the main strategies used to increase the engine efficiency, and finally, the analysis of **thermal balances in RICEs** as an evaluation tool used in an extensive amount of works.

During the last decades, the RICE development efforts have been mainly focused on the reduction of in-cylinder emissions formation rather than fuel consumption optimization, thus establishing a trade-off between them. Some techniques used to optimize this trade-off are:

- Turbocharging: it increases engine efficiency and reduce CO and PM emissions; however, it increase NO_x levels due to higher in-cylinder temperature.
- EGR and IGR: they reduce combustion temperature and hence NO_x formation; however, in CDC and CGC they worsen the combustion and increase fuel consumption.
- Injection setting: it control the emissions formation, therefore, the optimization of the injection setting is usually aimed at minimizing emissions (with penalty in consumption).
- Air motion within the chamber: the enhancement of the mixing process increases the engine efficiency and reduces PM emissions; however, it can lead to higher NO_x levels due to higher combustion temperature.

As a consequence of the in-cylinder processes optimization to minimize emissions, current RICE technology has reached a development level in which further emissions reduction is barely attainable through these active methodologies; therefore, the use of aftertreatment systems and cleaner fuels have become widely studied solutions .

The generalized use of aftertreatment systems and the increasing awareness due to climatic change, consequence of green house gases emissions, are shifting the interest of the research towards the optimization of the RICE operation to improve its efficiency. This can be achieved by using strategies such as:

- **Indicated cycle optimization:** the use of new combustion modes such as HCCI, PPC, RCCI, etc., allows reaching higher engine efficiency than CDC and CGC, while keeping low combustion temperature and hence low NO_x emissions. Through improvement of the combustion efficiency by means of optimal engine design and operation, an important reduction of HC, CO and PM can be also achieved.

- **Air management optimization:** several strategies such as variable valve timing, EGR and IGR (to control the mixture reactivity), turbocharging, air cooling and enhanced air movement within the chamber are used to improve the intake and mixing processes and to control the charge properties (temperature, γ and reactivity), thus providing flexibility to optimize the engine efficiency at different operating settings and combustion modes.

- **Heat transfer reduction:** reducing the HT leads in general to higher engine efficiency. This can be achieved, on the one hand, through ETM, which allows shortening the warm-up process and managing the cooling capacity accordingly to the engine requirements, thereby reducing the HT and the cooling systems energy consumption. On the other hand, thermal barrier coatings reduce the HT, which leads to lower fuel consumption, higher *imep* and higher energy availability at the exhaust.

- **Friction and auxiliary losses reduction:** the reduction of friction losses and auxiliary systems consumption increases the brake efficiency. Friction can be reduced by using smooth surfaces and low viscosity oils (or high oil temperature), and auxiliary systems requirements can be minimized through replacement of mechanical components to electrical ones, which can be controlled more efficiently. The reduction of these losses influences positively the engine brake efficiency as a consequence of higher mechanical efficiency.

- **Other strategies:** the design of optimal powertrains, which operate at high-efficient engine map regions, is a promising solution to reduce fuel consumption while keeping high engine performance. This is the main idea behind *downsizing* and *hybridization*. On the one hand, downsizing is achieved thanks to high turbocharging, engine displacement reduction and high load engine operation, where the engine efficiency is higher. On the other hand, hybridization is achieved by coupling a RICE with

an electric motor and optimizing their operation accordingly with the specific requirements.

As can be seen, the development and implementation of new technologies to improve engine efficiency involve a comprehensive understanding of different thermal processes occurring during the RICE operation. In this regard, performing simplified thermal balances has been widely use to evaluate current and new RICE technologies:

- **Conventional TDI and GTDI engines:** in general, TDI engines have higher brake efficiency than GTDI engines due to the more efficient indicated cycle; however, the HT is also higher as a consequence of the higher in-cylinder pressure. On the counterpart, GTDI engines reach higher temperature at exhaust that leads to higher exhaust losses.
- **Alternative combustion modes, fuels and fuel blends:** the premixed combustion modes reach higher indicated efficiency than CDC and CGC, whilst the HT and exhaust losses are lower thanks to the low temperature combustion operation; however, the unburned fuel losses are higher due to unburned fuel trapped in crevices and flame quenching near the walls. Among the premixed modes, the RCCI is one of the most efficient.

  To increase the efficiency of conventional and premixed combustion modes, while maintaining low emissions level, several alternative fuels and fuel blends have been studied. The thermal balance is highly related with the combustion mode, fuel properties and engine features; therefore, different results have been reported.
- **LHRE and ETM:** the HT of LHREs is lower than in the reference baseline engines, thereby increasing both engine efficiency and exhaust losses. Moreover, the use of coatings also reduces unburned fuel due to higher in-cylinder and walls temperatures.

  ETM methodologies allow faster warm-up trough increasing HT from chamber. In stationary operation, they allow reducing HT (increasing the exhaust losses) by means of flexible coolant flow control. In both cases, the HT management leads to higher engine efficiency.

Most of these thermal balances works take into account the main terms (brake efficiency, heat rejection and exhaust losses), and in some of them the

unburned fuel and unaccounted losses are also included. The simplicity of these thermal balances is due, on the one hand, to the complexity of the experimental measurement of the required variables, and on the other hand, to the difficulty of modelling and calibrating accurate models to determine detailed energy distribution. As a consequence, most of the works found are addressed to either, experimental or modelling determination of the thermal balance, thus limiting and simplifying the analysis. In fact, **there is a lack of works proposing a global methodology to perform and analyse the thermal balance**, in which experimental and modelling techniques can be used to obtain the detailed and accurate energy split. For this reason, **the development of a global strategy to perform a comprehensive analysis of the energy balance, taking into account different information sources (experimental and modelled) seems to be worth and interesting.**

Bibliography

[1] Heywood J.B. *Internal Combustion Engines Fundamentals*. McGraw-Hill, ISBN 978-0-07-028637-5, New York, 1988.

[2] Rakopoulos C.D., Dimaratos A.M., Giakoumis E.G. and Rakopoulos D.C. "Evaluation of the effect of engine, load and turbocharger parameters on transient emissions of diesel engine". *Energy Conversion and Management*, Vol. 50 n^o 9, pp. 2381–2393, September 2009.

[3] Canakci M. "Combustion characteristics of a DI-HCCI gasoline engine running at different boost pressures". *Fuel*, Vol. 96, pp. 546–555, June 2012.

[4] Karabektas M. "The effects of turbocharger on the performance and exhaust emissions of a diesel engine fuelled with biodiesel". *Renewable Energy*, Vol. 34 n^o 4, pp. 989–993, apr 2009.

[5] Payri F. and J.M. Desantes. *Motores de combustión interna alternativos*. Reverté, ISBN 978-84-291-4802-2, Barcelona, 2011.

[6] Zhen X., Wang Y., Xu S., Zhu Y., Tao C., Xu T. and Song M. "The engine knock analysis - An overview". *Applied Energy*, Vol. 92, pp. 628–636, apr 2012.

[7] Galloni E., Fontana G. and Staccone S. "Numerical and experimental characterization of knock occurrence in a turbo-charged spark-ignition engine". *Energy Conversion and Management*, Vol. 85, pp. 417–424, sep 2014.

[8] De Bellis V. "Performance optimization of a spark-ignition turbocharged VVA engine under knock limited operation". *Applied Energy*, Vol. 164, pp. 162–174, feb 2016.

[9] Yang Y., Dec J.E., Sjöberg M. and Ji C. "Understanding fuel anti-knock performances in modern SI engines using fundamental HCCI experiments". *Combustion and Flame*, Vol. 162 n^o 10, pp. 4008–4015, oct 2015.

[10] Payri F., Martín J., Garcia A. and Carreño R. "Experimental and Theoretical Analysis of the Energy Balance in a DI Diesel Engine". *SAE Technical Paper 2015-01-1651*, 2015.

[11] Abd-Alla G.H. and Abdalla G. "Using exhaust gas recirculation in internal combustion engines: a review". *Energy Conversion and Management*, Vol. 43 n^o 8, pp. 1027–1042, 2002.

[12] Maiboom A. and Tauzia X. "NOx and PM emissions reduction on an automotive HSDI Diesel engine with water-in-diesel emulsion and EGR: An experimental study". *Fuel*, Vol. 90 n^o 11, pp. 3179–3192, November 2011.

[13] Benajes J., Novella R., De Lima D., Tribotté P., Quechon N., Obernesser P. and Dugue V. "Analysis of the combustion process, pollutant emissions and efficiency of an innovative 2-stroke HSDI engine designed for automotive applications". *Applied Thermal Engineering*, Vol. 58 n^o 1-2, pp. 181–193, September 2013.

[14] Bourhis G., Chauvin J., Gautrot X. and de Francqueville L. "LP EGR and IGR Compromise on a GDI Engine at Middle Load". *SAE Int. J. Engines*, Vol. 6 n^o 1, pp. 67–77, 2013.

[15] Bression G., Soleri D., Savy S., Dehoux S., Azoulay D., Hamouda H., Doradoux L., Guerrassi N. and Lawrence N. "A Study of Methods to Lower HC and CO Emissions in Diesel HCCI". *SAE Int. J. Fuels Lubr.*, Vol. 1 n^o 1, pp. 37–49, 2009.

[16] Benajes J., Martín J., Novella R. and Thein K. "Understanding the performance of the multiple injection gasoline partially premixed combustion concept implemented in a 2-Stroke high speed direct injection compression ignition engine". *Applied Energy*, Vol. 161, pp. 465–475, jan 2016.

[17] Mohan B., Yang W. and Chou S.K. "Fuel injection strategies for performance improvement and emissions reduction in compression ignition engines - A Review". *Renewable and Sustainable Energy Reviews*, Vol. 28, pp. 664–676, December 2013.

[18] Wloka J.A., Pflaum S. and Wachtmeister G. "Potential and Challenges of a 3000 Bar Common-Rail Injection System Considering Engine Behavior and Emission Level". *SAE Int. J. Engines*, Vol. 3 n^o 1, pp. 801–813, 2010.

[19] Wang X., Huang Z., Zhang W., Kuti O.A. and Nishida K. "Effects of ultra-high injection pressure and micro-hole nozzle on flame structure

and soot formation of impinging diesel spray". *Applied Energy*, Vol. 88 n^o 5, pp. 1620–1628, May 2011.

[20] Pickett L.M. and Siebers D.L. "Soot in diesel fuel jets: effects of ambient temperature, ambient density, and injection pressure". *Combustion and Flame*, Vol. 138 n^o 1-2, pp. 114–135, July 2004.

[21] Su T., Chang C., Reitz R., Farrell P., Pierpont A. and Tow T. "Effects of Injection Pressure and Nozzle Geometry on Spray SMD and D.I. Emissions". *SAE Technical Paper 952360*, 1995.

[22] Dogde L.G., Simescu S., Neely G.D., Maymar M.J., Dickey D.W. and Savonen C.L. "Effect of Small Holes and High Injection Pressures on Diesel Engine Combustion". *SAE Technical Paper 2002-01-0494*, 2002.

[23] Mitroglou N., Nouri J.M., Gavaises M. and Arcoumanis C. "Spray Characteristics of a Multi-hole Injector for Direct-Injection Gasoline Engines". *International Journal of Engine Research*, Vol. 7 n^o 3, pp. 255–270, 2006.

[24] Agarwal A.K., Srivastava D.K., Dhar A., Maurya R.K., Shukla P.C. and Singh A.P. "Effect of fuel injection timing and pressure on combustion, emissions and performance characteristics of a single cylinder diesel engine". *Fuel*, Vol. 111, pp. 374–383, September 2013.

[25] Payri F., Olmeda P., Martín J. and Carreño R. "Experimental analysis of the global energy balance in a DI diesel engine". *Applied Thermal Engineering*, Vol. 89, pp. 545–557, October 2015.

[26] Badami M., Mallamo F., Millo F. and Rossi E.E. "Influence of Multiple Injection Strategies on Emissions , Combustion Noise and BSFC of a DI Common Rail Diesel Engine". *SAE Technical Paper 2002-01-0503*, 2002.

[27] Hiwase S.D., Moorthy S., Prasad H., Dumpa M. and Metkar R.M. "Multidimensional Modeling of Direct Injection Diesel Engine with Split Multiple Stage Fuel Injections". *Procedia Engineering*, Vol. 51, pp. 670–675, January 2013.

[28] Achuth M. and Mehta P.S. "Predictions of tumble and turbulence in four-valve pentroof spark ignition engines". *International Journal of Engine Research*, Vol. 2 n^o 3, pp. 209–227, January 2001.

[29] Huang R.F., Huang C.W., Chang S.B., Yang H.S., Lin T.W. and Hsu W.Y. "Topological flow evolutions in cylinder of a motored engine during intake and compression strokes". *Journal of Fluids and Structures*, Vol. 20 n^o 1, pp. 105–127, January 2005.

[30] Maharudrppa Mallikarjuna J. "Effect of Manifold Orientation on Non-Reacting In-Cylinder Tumble Flows in an IC Engine with Pentroof Piston - An Investigation Using PIV". *SAE Technical Paper 2010-01-0956*, 2010.

[31] Wei S., Wang F., Leng X., Liu X. and Ji K. "Numerical analysis on the effect of swirl ratios on swirl chamber combustion system of DI diesel engines". *Energy Conversion and Management*, Vol. 75, pp. 184–190, November 2013.

[32] Nishimura T., Satoh K., Takahashi S. and Yokota K. "Effects of Fuel Injection Rate on Combustion and Emission in a DI Diesel Engine". *SAE Technical Paper 981929*, 1998.

[33] Kohketsu S., Tanabe K. and Mori K. "Flexibly controlled injection rate shape with next generation common rail system for heavy duty DI diesel engines". *SAE Technical Paper 2000-01-0705*, 2000.

[34] Desantes J.M., Benajes J., Molina S. and González C.A. "The modification of the fuel injection rate in heavy-duty diesel engines. Part 1: Effects on engine performance and emissions". *Applied Thermal Engineering*, Vol. 24 n^o 17-18, pp. 2701–2714, December 2004.

[35] Desantes J.M., Benajes J., Molina S. and González C.A. "The modification of the fuel injection rate in heavy-duty diesel engines. Part 2: Effects on combustion". *Applied Thermal Engineering*, Vol. 24 n^o 17-18, pp. 2715–2726, December 2004.

[36] Michel P., Charlet A., Colin G., Chamaillard Y., Bloch G. and Nouillant C. "Optimizing fuel consumption and pollutant emissions of gasoline-HEV with catalytic converter". *Control Engineering Practice*, dec 2015.

[37] Ummel D. and Price K. "Performance and Sulfur Effect Evaluation of Tier 4 DOC+SCR Systems for Vanadia, Iron, and Copper SCR". *SAE International J. Engines*, Vol. 7 n^o 3, pp. 1244–1251, 2014.

[38] Pietikäinen M., Väliheikki A., Oravisjärvi K., Kolli T., Huuhtanen M., Niemi S., Virtanen S., Karhu T. and Keiski R.L. "Particle and NOx emissions of a non-road diesel engine with an SCR unit: The effect of fuel". *Renewable Energy*, Vol. 77, pp. 377–385, may 2015.

[39] Tsumagari I., Hirabayashi H., Takenaka Y., Hosoya M. and Shimoda M. "Study of 2-LEG NOx Storage-Reduction Catalyst System for HD Diesel Engine". *SAE Techinical Paper 2006-01-0211*, 2006.

[40] Konstandopoulos A.G., Kostoglou M., Vlachos N. and Kladopoulou E. "Advances in the science and technology of diesel particulate filter simulation". *Advances in Chemical Engineering*, Vol. 33, pp. 213–275,284–294, 2007.

[41] Beatrice C., Di Iorio S., Guido C. and Napolitano P. "Detailed characterization of particulate emissions of an automotive catalyzed DPF using actual regeneration strategies". *Experimental Thermal and Fluid Science*, Vol. 39, pp. 45–53, May 2012.

[42] Bermúdez V., Luján J.M., Piqueras P. and Campos D. "Pollutants emission and particle behavior in a pre-turbo aftertreatment light-duty diesel engine". *Energy*, Vol. 66, pp. 509–522, March 2014.

[43] Rakopoulos C.D., Hountalas D.T., Zannis T.C. and Levendis Y.A. "Operational and Environmental Evaluation of Diesel Engine Burning Oxygan-Enriched Intake Air or Oxygen-Enriched Fuels: A Review". *SAE Techinical Paper 2004-01-2924*, 2004.

[44] Senatore A., Cardone M., Rocco V. and Prati M.V. "A Comparative Analysis of Combustion Process in D.I. Diesel Engine Fueled with Biodiesel and Diesel Fuel". *SAE Techinical Paper 2000-01-0691*, 2000.

[45] Lapuerta M., Armas O. and Rodríguez-Fernández J. "Effect of biodiesel fuels on diesel engine emissions". *Progress in Energy and Combustion Science*, Vol. 34 n^o 2, pp. 198–223, 2008.

[46] Verhelst S. "Recent progress in the use of hydrogen as a fuel for internal combustion engines". *International Journal of Hydrogen Energy*, Vol. 39 n^o 2, pp. 1071–1085, 2014.

[47] Shelef M. and Kukkonen C.A. "Prospects of hydrogen-fueled vehicles". *Progress in Energy and Combustion Science*, Vol. 20 n^o 2, pp. 139–148, January 1994.

[48] Parlak A., Yasar H. and Sahin B. "Performance and exhaust emission characteristics of a lower compression ratio LHR Diesel engine". *Energy Conversion and Management*, Vol. 44 n^o 1, pp. 163–175, January 2003.

[49] Pang H.H. and Brace C.J. "Review of engine cooling technologies for modern engines". *Proc. Inst. Mech. Engrs.*, Vol. 218 n^o 11, pp. 1209–1215, 2004.

[50] Parvate-Patil G.B., Hong H. and Gordon B. "An assessment of intake and exhaust philosophies for variable valve timing". *SAE Technical Paper 2003-32-0078*, 2003.

[51] Park Y. and Bae C. "Experimental study on the effects of high/low pressure EGR proportion in a passenger car diesel engine". *Applied Energy*, Vol. 133, pp. 308–316, November 2014.

[52] Osada H., Uchida N., Shimada K. and Aoyagi Y. "Reexamination of Multiple Fuel Injections for Improving the Thermal Efficiency of a Heavy-Duty Diesel Engine". *SAE Technical Paper 2013-01-0909*, apr 2013.

[53] Tauzia X. and Maiboom A. "Experimental study of an automotive Diesel engine efficiency when running under stoichiometric conditions". *Applied Energy*, Vol. 105, pp. 116–124, May 2013.

[54] Flierl R., Lauer F., Breuer M. and Hannibal W. "Cylinder Deactivation with Mechanically Fully Variable Valve Train". *SAE Int. J. Engines*, Vol. 5 n^o 2, pp. 207–215, 2012.

[55] Uyehara O.A. "Factors that Affect BSFC and Emissions for Diesel Engines : Part 1 - Presentation of Concepts". *SAE Techinical Paper 870343*, 1987.

[56] Beck N.J. and Uyehara O.A. "Factors That Affect BSFC and Emissions for Diesel Engines : Part II Experimental Confirmation of Concepts Presented in Part I". *SAE Techinical Paper 870344*, 1987.

[57] Wang C., Xu H., Herreros J.M., Wang J. and Cracknell R. "Impact of fuel and injection system on particle emissions from a GDI engine". *Applied Energy*, Vol. 132, pp. 178–191, November 2014.

[58] Stanglmaier R.H. and Roberts C.E. "(HCCI): Benefits , Compromises , and Future Engine Applications". *SAE Techinical Paper 1999-01-3682*, 1999.

[59] Hardy A.J. J. and Heywood J.B. "Fuel economy benefits and aftertreatment requirements of a naturally aspirated HCCI-SI engine system". *SAE International Journal of Engines*, Vol. 1 n^o 1, pp. 1263–1277, 2009.

[60] Zheng M., Han X., Asad U. and Wang J. "Investigation of butanol-fuelled HCCI combustion on a high efficiency diesel engine". *Energy Conversion and Management*, Vol. 98, pp. 215–224, July 2015.

[61] Caton J.A. "Thermodynamic Advantages of Low Temperature Combustion (LTC) Engines Using Low Heat Rejection (LHR) Concepts". *SAE Techinical Paper 2011-01-0312*, 2011.

[62] Bendu H. and Murugan S. "Homogeneous charge compression ignition (HCCI) combustion: Mixture preparation and control strategies in diesel engines". *Renewable and Sustainable Energy Reviews*, Vol. 38, pp. 732–746, October 2014.

[63] Alkidas A.C. "Combustion advancements in gasoline engines". *Energy Conversion and Management*, Vol. 48 n^o 11, pp. 2751–2761, November 2007.

[64] Neely G.D., Sasaki S. and Leet J.A. "Experimental Investigation of PCCI-DI Combustion on Emissions in a Light-Duty Diesel Engine". *SAE Techinical Paper 2004-01-0121*, 2004.

[65] Aoyama T., Hattori Y., Mizuta J. and Sato Y. "An Experimental Study on Premixed-Charge Compression Ignition Gasoline Engine". *SAE Techinical Paper 960081*, 1996.

[66] Ishibashi Y. and Asai M. "Improving the Exhaust Emissions of Two-Stroke Engines by Applying the Activated Radical Combustion". *SAE Techinical Paper 960742*, 1996.

[67] Kimura S., Aoki O., Kitahara Y. and Aiyoshizawa E. "Ultra-Clean Combustion Technology Combining a Low-Temperature and Premixed Combustion Concept for Meeting Future Emission Standards". *SAE Technical Paper 2001-01-0200*, 2001.

[68] Benajes J., Molina S., Novella R. and De Lima D. "Implementation of the Partially Premixed Combustion concept in a 2-stroke HSDI diesel engine fueled with gasoline". *Applied Energy*, Vol. 122, pp. 94–111, jun 2014.

[69] Bedoya I.D., Saxena S., Cadavid F.J., Dibble R.W. and Wissink M. "Experimental evaluation of strategies to increase the operating range of a biogas-fueled HCCI engine for power generation". *Applied Energy*, Vol. 97, pp. 618–629, September 2012.

[70] Palma A., Del Core D. and Esposito C. "The HCCI Concept and Control , Performed with MultiAir Technology on Gasoline Engines". *SAE Techinical Paper 2011-24-0026*, 2011.

[71] Dec J.E. and Yang Y. "Boosted HCCI for High Power without Engine Knock and with Ultra-Low NOx Emissions - using Conventional Gasoline". *SAE Int. J. Engines*, Vol. 3 n^o 1, pp. 750–767, 2010.

[72] Desantes J.M., Benajes J., García A. and Monsalve-Serrano J. "The role of the in-cylinder gas temperature and oxygen concentration over low load reactivity controlled compression ignition combustion efficiency". *Energy*, Vol. 78, pp. 854–868, dec 2014.

[73] Benajes J., Molina S., García A., Belarte E. and Vanvolsem M. "An investigation on RCCI combustion in a heavy duty diesel engine using in-cylinder blending of diesel and gasoline fuels". *Applied Thermal Engineering*, Vol. 63 n^o 1, pp. 66–76, feb 2014.

[74] Benajes J., Molina S., García A. and Monsalve-Serrano J. "Effects of direct injection timing and blending ratio on RCCI combustion with different low reactivity fuels". *Energy Conversion and Management*, Vol. 99, pp. 193–209, jul 2015.

[75] Kokjohn S.L., Hanson R.M., Splitter D.A. and Reitz R.D. "Fuel reactivity controlled compression ignition (RCCI): a pathway to controlled high-efficiency clean combustion". *International Journal of Engine Research*, Vol. 12 n^o 3, pp. 209–226, 2011.

[76] Benajes J., Pastor J.V., García A. and Monsalve-Serrano J. "The potential of RCCI concept to meet EURO VI NOx limitation and ultra-low soot emissions in a heavy-duty engine over the whole engine map". *Fuel*, Vol. 159, pp. 952–961, nov 2015.

[77] Benajes J., Molina S., García A. and Monsalve-Serrano J. "Effects of low reactivity fuel characteristics and blending ratio on low load RCCI (reactivity controlled compression ignition) performance and emissions in a heavy-duty diesel engine". *Energy*, Vol. 90, pp. 1261–1271, oct 2015.

[78] Heuser B., Kremer F., Pischinger S., Rohs H., Holderbaum B. and Körfer T. "An experimental investigation of dual-fuel combustion in a light duty Diesel engine by in-cylinder blending of ethanol and Diesel". *SAE Int. J. Engines*, Vol. 9 n^o 1, pp. 11–25, 2015.

[79] Belarte E. *Estudio del proceso de combustión premezclada controlada por la reactividad del combustible en un motor de encendido por compresión.* Ph.D. Thesis, Universitat Politècnica de València, 2015.

[80] Benajes J., Pastor J.V., García A. and Monsalve-Serrano J. "An experimental investigation on the influence of piston bowl geometry on RCCI performance and emissions in a heavy-duty engine". *Energy Conversion and Management*, Vol. 103, pp. 1019–1030, oct 2015.

[81] Dempsey A.B., Walker N.R. and Reitz R.D. "Effect of Piston Bowl Geometry on Dual Fuel Reactivity Controlled Compression Ignition (RCCI) in a Light-Duty Engine Operated with Gasoline/Diesel and Methanol/Diesel". *SAE Int. J. Engines*, Vol. 6 n^o 1, pp. 78–100, 2013.

[82] Kokjohn S.L. and Reitz R.D. "Reactivity Controlled Compression Ignition and Conventional Diesel Combustion: A Comparison of Methods to Meet Light-Duty NOx and Fuel Economy Targets". *International Journal of Engine Research*, Vol. 0 n^o 0, pp. 1–17, 2013.

[83] Payri F., Benajes J., Galindo J. and Serrano J.R. "Modelling of turbocharged diesel engines in transient operation. Part 2: Wave action models for calculating the transient operation in a high speed direct injection engine". *Proc. IMechE, Part D: Journal of Automobile Engineering*, Vol. 216 n^o 6, pp. 479–493, 2002.

[84] Gil A. *Modelado tridimensional del flujo de aire en el cilindro de motores Diesel de inyección directa.* Reverté, ISBN 978-84-291-4711-7, Barcelona, 2007.

[85] Malkhede D.N. and Khalane H. "Maximizing Volumetric Efficiency of IC Engine through Intake Manifold Tuning". *SAE Techinical Paper 2015-01-1738*, 2015.

[86] Zhang L., Takatsuki T. and Yokota K. "An Observation and Analysis of the Combustion Under Supercharging on a DI Diesel Engine". *SAE Techinical Paper 940844*, 1994.

[87] Petitjean D., Bernardini L., Middlemass C. and Shahed S.M. "Advanced gasoline engine turbocharging technology for fuel economy improvements". *SAE Technical Paper 2004-01-0988*, 2004.

[88] Galindo J., Serrano J.R., Climent H. and Varnier O. "Impact of two-stage turbocharging architectures on pumping losses of automotive engines based on an analytical model". *Energy Conversion and Management*, Vol. 51 n^o 10, pp. 1958–1969, October 2010.

[89] Nitta J., Minato A. and Shimazaki N. "Performance Evaluation of Three-Stage Turbocharging System for Heavy-Duty Diesel Engine". *SAE Technical Paper 2011-01-0374*, 2011.

[90] Kawashima J. "Research on a variable swirl intake port for high-speed 4-valve DI diesel engine". *JSAE Review*, Vol. 20 n^o 3, pp. 421–424, July 1999.

[91] Bari S. and Saad I. "CFD modelling of the effect of guide vane swirl and tumble device to generate better in-cylinder air flow in a CI engine fuelled by biodiesel". *Computers & Fluids*, Vol. 84, pp. 262–269, September 2013.

[92] Benajes J., Molina S., Garcia J.M. and Riesco J.M. "The effect of swirl on combustion and exhaust emissions in heavy-duty diesel engines". *Proceedings of the Institution of Mechanical Engineers, Part D: Journal of Automobile Engineering*, Vol. 218 n^o 10, pp. 1141–1148, 2004.

[93] Fridriksson H.S., Tuner M., Andersson O., Sunden B., Persson H. and Ljungqvist M. "Effect of Piston Bowl Shape and Swirl Ratio on Engine Heat Transfer in a Light-Duty Diesel Engine". *SAE Techinical Paper 2014-01-1141*, 2014.

[94] Miles P.C. "The Influence of Swirl on HSDI Diesel Combustion at Moderate Speed and Load". *SAE Techinical Paper 2000-01-1829*, 2000.

[95] He Y., Selamet A., Reese R.A., Vick R.K. and Amer A.A. "Impact of Tumble on Combustion in SI Engines: Correlation between Flow and Engine Experiments". *SAE paper 2007-01-4003*, 2007.

[96] Vítek O., Macek J., Polášek M., Schmerbeck S. and Kammerdiener T. "Comparison of Different EGR Solutions". *SAE Techinical Paper 2008-01-0206*, 2008.

[97] Millo F., Giacominetto P.F. and Bernardi M.G. "Analysis of different exhaust gas recirculation architectures for passenger car Diesel engines". *Applied Energy*, Vol. 98, pp. 79–91, October 2012.

[98] Payri F., Olmeda P., Martín J. and Carreño R. "A New Tool to Perform Global Energy Balances in DI Diesel Engines". *SAE Int. J. Engines*, Vol. 7 n^o 1, pp. 43–59, 2014.

[99] Torregrosa A.J., Broatch A., Olmeda P. and Romero C. "Assessment of the influence of different cooling system configurations on engine warm-up, emissions and fuel consumption". *International Journal of Automotive Technology*, Vol. 9 n^o 4, pp. 447–458, 2008.

[100] Allen D.J. and Lasecki M.P. "Thermal Management Evolution and Controlled Coolant Flow". *SAE Techinical Paper 2001-01-1732*, 2001.

[101] Chastain J.H. and Wagner J.R. "Advanced Thermal Management for Internal Combustion Engines - Valve Design , Component Testing and Block Redesign". *SAE Techinical Paper 2006-01-1232*, 2006.

[102] Zhou B., Lan X., Xu X. and Liang X. "Numerical model and control strategies for the advanced thermal management system of diesel engine". *Applied Thermal Engineering*, Vol. 82, pp. 368–379, May 2015.

[103] Degraeuwe B. *Contribution to the thermal management of DI Diesel engines*. Ph.D. Thesis, Universidad Politécnica de Valencia, 2007.

[104] Kang H., Ahn H. and Min K. "Smart cooling system of the double loop coolant structure with engine thermal management modeling". *Applied Thermal Engineering*, Vol. 79, pp. 124–131, 2015.

[105] Andrews G., Ounzain A., Li H., Bell M., Tate J. and Ropkins K. "The Use of a Water/Lube Oil Heat Exchanger and Enhanced Cooling Water Heating to Increase Water and Lube Oil Heating Rates in Passenger Cars for Reduced Fuel Consumption and CO2 Emissions During Cold Start". *SAE Techinical Paper 2007-01-2067*, 2007.

[106] Roberts A., Brooks R. and Shipway P. "Internal combustion engine cold-start efficiency: A review of the problem, causes and potential solutions". *Energy Conversion and Management*, Vol. 82, pp. 327–350, June 2014.

[107] Choukroun A. and Chanfreau M. "Automatic Control of Electronic Actuators for an Optimized Engine Cooling Thermal Management". *SAE Techinical Paper 2001-01-1758*, 2001.

[108] Hughes C.A.V. and Wiseman M.W. "Feasibility of Intelligent Control Strategies to Reduce Cooling System Size". *SAE Techinical Paper 2001-01-1759*, 2001.

[109] Robinson K., Hawley J.G., Campbell N.A.F. and Tilley D.G. "A Review of Precision Engine Cooling". *SAE Techinical Paper 1999-01-0578*, 1999.

[110] Porot P.A., Ménégazzi P. and Ap N.S. "Understanding and Improving Evaporative Engine Cooling at High Load , High Speed by Engine Tests and 3D Calculations". *SAE Techinical Paper 971792*, 1997.

[111] Harrison H. "Evaporative Cooling". *SAE Techinical Paper 260015*, 1926.

[112] Karaoglanli A.C., Dikici H. and Kucuk Y. "Effects of heat treatment on adhesion strength of thermal barrier coating systems". *Engineering Failure Analysis*, Vol. 32, pp. 16–22, September 2013.

[113] Waki H., Nishikawa I., Kobayashi A. and Ishii N. "Sensitivity to experimental errors in evaluating the thermal expansion coefficient of a thermal barrier coating by using coating system specimens". *Vacuum*, Vol. 88, pp. 93–97, February 2013.

[114] Cao X.Q., Vassen R. and Stoever D. "Ceramic materials for thermal barrier coatings". *Journal of the European Ceramic Society*, Vol. 24 n^o 1, pp. 1–10, January 2004.

[115] Lima C.R.C. and Guilemany J.M. "Adhesion improvements of Thermal Barrier Coatings with HVOF thermally sprayed bond coats". *Surface and Coatings Technology*, Vol. 201 n^o 8, pp. 4694–4701, January 2007.

[116] Hejwowski T. "Comparative study of thermal barrier coatings for internal combustion engine". *Vacuum*, Vol. 85 n^o 5, pp. 610–616, November 2010.

[117] Cernuschi F., Bianchi P., Leoni M. and Scardi P. "Thermal Diffusivity/Microstructure Relationship in Y-PSZ Thermal Barrier Coatings". *Journal of Thermal Spray Technology*, Vol. 8 n^o 1, pp. 102–109, 1999.

[118] Babiak Z., Wenz T. and Engl L. "Fundamentals of Thermal Spraying , Flame and Arc Spraying". In Bach F., Laarmann A. and Thomas W., editors, *Modern Surface Technology*, chapter 8, pp. 119–136. Wiley-VCH Verlag GmbH & Co. KGaA, ISBN 978-3-527-31532-1, Weinheim, 2006.

[119] Sun X., Wang W.G., Bata R.M. and Gao X. "Performance Evaluation of Low Heat Rejection Engines". *ASME. J. Eng. Gas Turbines Power*, Vol. 116 n^o 4, pp. 758–764, 1994.

[120] İşcan B. and Aydın H. "Improving the usability of vegetable oils as a fuel in a low heat rejection diesel engine". *Fuel Processing Technology*, Vol. 98, pp. 59–64, June 2012.

[121] Hazar H. "Effects of biodiesel on a low heat loss diesel engine". *Renewable Energy*, Vol. 34 n^o 6, pp. 1533–1537, June 2009.

[122] MohamedMusthafa M., Sivapirakasam S.P. and Udayakumar M. "Comparative studies on fly ash coated low heat rejection diesel engine on performance and emission characteristics fueled by rice bran and pongamia methyl ester and their blend with diesel". *Energy*, Vol. 36 n^o 5, pp. 2343–2351, May 2011.

[123] Chan S.H. "Performance and emissions characteristics of a partially insulated gasoline engine". *International Journal of Thermal Sciences*, Vol. 40 n^o 3, pp. 255–261, March 2001.

[124] Parlak A. "The effect of heat transfer on performance of the Diesel cycle and exergy of the exhaust gas stream in a LHR Diesel engine at the optimum injection timing". *Energy Conversion and Management*, Vol. 46 n^o 2, pp. 167–179, January 2005.

[125] Macián V., Serrano J.R., Dolz V. and Sánchez J.P. "Methodology to design a bottoming Rankine cycle, as a waste energy recovering system in vehicles. Study in a HDD engine". *Applied Energy*, Vol. 104, pp. 758–771, apr 2013.

[126] Taymaz I. "An experimental study of energy balance in low heat rejection diesel engine". *Energy*, Vol. 31 n^o 2-3, pp. 364–371, February 2006.

[127] Jaichandar S. and Tamilporai P. "Low Heat Rejection Engines - An Overview". *SAE Technical Paper 2003-01-0405*, 2003.

[128] Abedin M.J., Masjuki H.H., Kalam M.A., Sanjid A. and Ashraful A.M. "Combustion, performance, and emission characteristics of low heat rejection engine operating on various biodiesels and vegetable oils". *Energy Conversion and Management*, Vol. 85, pp. 173–189, September 2014.

[129] Krishna M.V.S.M., Rao V.V.R.S., Reddy T.K.K. and Murthy P.V.K. "Comparative studies on performance evaluation of DI diesel engine with high grade low heat rejection combustion chamber with carbureted alcohols and crude jatropha oil". *Renewable and Sustainable Energy Reviews*, Vol. 36, pp. 1–19, August 2014.

[130] Cheng W., Wong V. and Gao F. "Heat Transfer Measurement Comparisons in Insulated and Non-Insulated Diesel Engines". *SAE Technical Paper 890570*, 1989.

[131] Dickey D. "The Effect of Insulated Combustion Chamber Surfaces on Direct-Injected Diesel Engine Performance, Emissions and Combustion". *SAE Technical Paper 890292*, 1989.

[132] Taraza D. and Henein N. "Friction Losses in Multi-Cylinder Diesel Engines". *SAE Technical Paper 2000-01-0921*, 2000.

[133] Holmberg K., Andersson P. and Erdemir A. "Global energy consumption due to friction in passenger cars". *Tribology International*, Vol. 47, pp. 221–234, March 2012.

[134] Morawitz U., Mehring J. and Schramm L. "Benefits of Thermal Spray Coatings in Internal Combustion Engines, with Specific View on Friction Reduction and Thermal Management". *SAE Technical Paper 2013-01-0292*, April 2013.

[135] De Carvalho M.J., Seidl P., Belchior C. and Sodré J.R. "Lubricant viscosity and viscosity improver additive effects on diesel fuel economy". *Tribology International*, Vol. 43 n^o 12, pp. 2298–2302, December 2010.

[136] Macián V., Tormos B., Bermúdez V. and Ramírez L. "Assessment of the effect of low viscosity oils usage on a light duty diesel engine fuel consumption in stationary and transient conditions". *Tribology International*, Vol. 79, pp. 132–139, November 2014.

[137] Hoshi M. "Reducing friction losses in automobile engines". *Tribology International*, Vol. 17 n^o 4, pp. 185–189, August 1984.

[138] Etsion I. and Sher E. "Improving fuel efficiency with laser surface textured piston rings". *Tribology International*, Vol. 42 n^o 4, pp. 542–547, April 2009.

[139] Okamoto M. and Sakai I. "Contact Pressure Distribution of Piston Rings -Calculation Based on Piston Ring Contour -". *SAE Techinical Paper 2001-01-0571*, 2001.

[140] Korte V., Glas T., Lettmann M., Krepulat W. and Steinmetz C. "Cam Roller Follower Design for Heavy Duty Diesel Engines". *SAE Technical Paper 2000-01-0525*, 2000.

[141] Muhr T.H. "New Technologies for Engine Valve Springs". *SAE Techinical Paper 930912*, 1993.

[142] Deligant M., Podevin P. and Descombes G. "Experimental identification of turbocharger mechanical friction losses". *Energy*, Vol. 39 n^o 1, pp. 388–394, March 2012.

[143] Serrano J.R., Olmeda P., Tiseira A., García-Cuevas L.M. and Lefebvre A. "Importance of Mechanical Losses Modeling in the Performance Prediction of Radial Turbochargers under Pulsating Flow Conditions". *SAE Int. J. Engines*, Vol. 6 n^o 2, pp. 729–738, April 2013.

[144] Lasecki M.P. and Cousineau J.M. "Controllable Electric Oil Pumps in Heavy Duty Diesel Engines". *SAE Techinical Paper 2003-01-3421*, 2003.

[145] Meira J., Ribeiro E., Filho A. and Melo W. "Strategies for energy savings with use of constant and variable oil pump systems". *SAE Techinical Paper 2011-36-0150*, 2011.

[146] Arata T., Novi N., Ariga K., Yamashita A. and Armenio G. "Development of a Two-Stage Variable Displacement Vane Oil Pump". *SAE Techinical Paper 2012-01-0408*, 2012.

[147] Teng H. and McCandless J. "Performance analysis of rail-pressure supply pumps of common-rail fuel systems for diesel engines". *SAE Technical Paper 2005-01-0909*, 2005.

[148] De Cesare M., Parotto M., Covassin F. and Sgatti S. "Electric Low Pressure Fuel Pump Control for Fuel Saving". *SAE Techinical Paper 2013-01-0339*, 2013.

[149] Körfer T., Lamping M., Kolbeck A., Pischinger S., Adolph D. and Busch H. "Potential of Modern Diesel Engines with Lowest Raw Emissions - a Key Factor for Future CO2 Reduction". *SAE Technical Paper 2009-26-0025*, 2009.

[150] Thirouard M. and Pacaud P. "Increasing power density in hsdi engines as an approach for engine downsizing". *SAE Int. J. Engines*, Vol. 3 n^o 2, pp. 56–71, 2010.

[151] Turner J., Blake D., Moore J., Burke P., Pearson R., Patel R., Blundell D., Chandrashekar R., Matteucci L., Barker P. and Card C. "The Lotus Range Extender Engine". *SAE Int. J. Engines*, Vol. 3 n^o 2, pp. 318–351, 2010.

[152] Pickett L.M. and Siebers D.L. "An investigation of diesel soot formation processes using micro-orifices". *Proceedings of the Combustion Institute*, Vol. 29 n^o 1, pp. 655–662, jan 2002.

[153] Payri F., Serrano J.R., Fajardo P., Reyes-Belmonte M.A. and Gozalbo-Belles R. "A physically based methodology to extrapolate performance maps of radial turbines". *Energy Conversion and Management*, Vol. 55, pp. 149–163, mar 2012.

[154] Torregrosa A.J., Broatch A., Olmeda P. and Cornejo O. "Experiments on subcooled flow boiling in I.C. engine-like conditions at low flow velocities". *Experimental Thermal and Fluid Science*, Vol. 52, pp. 347–354, jan 2014.

[155] Aichlmayr H.T., Kittelson D.B. and Zachariah M.R. "Miniature free-piston homogeneous charge compression ignition engine-compressor concept-Part I: performance estimation and design considerations unique to small dimensions". *Chemical Engineering Science*, Vol. 57 n^o 19, pp. 4161–4171, oct 2002.

[156] Turner J., Popplewell A., Marshall D.J., Johnson T.R., Barker L., King J., Martin J., Lewis A.G.J., Akehurst S., Brace C.J. and Copeland C.D. "SuperGen on Ultraboost: Variable-Speed Centrifugal Supercharging as

an Enabling Technology for Extreme Engine Downsizing". *SAE Int. J. Engines*, Vol. 8 n^o 4, 2015.

[157] Thirouard M., Mendez S., Pacaud P., Chmielarczyk V., Ambrazas D., Lavoisier F., Garsi C. and Barbeau B. "Potential to Improve Specific Power Using Very High Injection Pressure In HSDI Diesel Engines". *SAE Technical Paper 2009-01-1524*, 2009.

[158] Brandl S., Graf B. and Rust A. "NVH Challenges and Solutions for Vehicles with Low CO2 Emission". *SAE Int. J. Passeng. Cars - Mech. Syst.*, Vol. 5 n^o 3, pp. 1084–1090, 2012.

[159] Schell A., Peng H., Tran D., Stamos E., Lin C.C. and Kim M.J. "Modelling and control strategy development for fuel cell electric vehicles". *Annual Reviews in Control*, Vol. 29 n^o 1, pp. 159–168, January 2005.

[160] Chau K.T., Wong Y.S. and Chan C.C. "An overview of energy sources for electric vehicles". *Energy Conversion and Management*, Vol. 40 n^o 10, pp. 1021–1039, July 1999.

[161] Rao Z. and Wang S. "A review of power battery thermal energy management". *Renewable and Sustainable Energy Reviews*, Vol. 15 n^o 9, pp. 4554–4571, December 2011.

[162] Teng H., Regner G. and Cowland C. "Waste Heat Recovery of Heavy-Duty Diesel Engines by Organic Rankine Cycle Part I: Hybrid System of Diesel and Rankine Engines". *SAE Technical Paper 2007-01-0537*, 2007.

[163] Edwards K.D., Wagner R.M. and Graves R.L. "Identification of Potential Efficiency Opportunities in Internal Combustion Engines Using a Detailed Thermodynamic Analysis of Engine Simulation Results". *SAE Technical Paper 2008-01-0293*, 2008.

[164] Boulahlib M.S., Boukebbab S., Gaci F. and Kholai O. "Experimental Study of Energy Balance for Air-Cooled DI Diesel Engines Operating in Hot Climates". *SAE Techinical Paper 2009-01-1974*, 2009.

[165] Smith L.A., Preston W.H., Dowd G., Taylor O. and Wilkinson K.M. "Application of a First Law Heat Balance Method to a Turbocharged Automotive Diesel Engine". *SAE Technical Paper 2009-01-2744*, 2009.

[166] Durgun O. and Şahin Z. "Theoretical investigation of heat balance in direct injection (DI) diesel engines for neat diesel fuel and gasoline fumigation". *Energy Conversion and Management*, Vol. 50 n^o 1, pp. 43–51, January 2009.

[167] Edwards K.D., Wagner R. and Briggs T. "Investigating Potential Light-duty Efficiency Improvements through Simulation of Turbocompounding and Waste-heat Recovery Systems". *SAE Techinical Paper 2010-01-2209*, 2010.

[168] Teng H. "Waste Heat Recovery Concept to Reduce Fuel Consumption and Heat Rejection from a Diesel Engine". *SAE Int. J. Commer. Veh.*, Vol. 3 n^o 1, pp. 60–68, 2010.

[169] Singh S., Garg A., Gupta A. and Permude A. "Analysis of Thermal Balance of Diesel Engine and Identification of Scope for Waste Heat Recovery". *SAE Techinical Paper 2013-01-2744*, 2013.

[170] Yamaguchi T., Aoyagi Y., Uchida N., Fukunaga A., Kobayashi M., Adachi T. and Hashimoto M. "Fundamental Study of Waste Heat Recovery in the High Boosted 6-cylinder Heavy Duty Diesel Engine". *SAE Int. J. Mater. Manf.*, Vol. 8 n^o 2, 2015.

[171] Caton J.A. "Operating Characteristics of a Spark-Ignition Engine Using the Second Law of Thermodynamics : Effects of Speed and Load". *SAE Techinical Paper 2000-01-0952*, 2000.

[172] He M., Zhang X., Zeng K. and Gao K. "A combined thermodynamic cycle used for waste heat recovery of internal combustion engine". *Energy*, Vol. 36 n^o 12, pp. 6821–6829, December 2011.

[173] Fu J., Liu J., Feng R., Yang Y., Wang L. and Wang Y. "Energy and exergy analysis on gasoline engine based on mapping characteristics experiment". *Applied Energy*, Vol. 102, pp. 622–630, February 2013.

[174] Páv K., Václav R. and Václav V. "Heat balance in modern automotive engines". *Journal of Middle European Construction and Design of Cars*, Vol. 10 n^o 2, pp. 6–13, 2013.

[175] Grandin B. and Ångström H. "Replacing Fuel Enrichment in a Turbo Charged SI Engine: Lean Burn or Cooled EGR". *SAE Technical Paper 1999-01-3505*, 1999.

[176] Nose H., Inoue T., Katagiri S., Sakai A., Kawasaki T. and Okamura M. "Fuel Enrichment Control System by Catalyst Temperature Estimation to Enable Frequent Stoichiometric Operation at High Engine Speed/Load Condition". *SAE Technical Paper 2013-01-0341*, 2013.

[177] Bermúdez V., Luján J.M., Climent H. and Campos D. "Assessment of pollutants emission and aftertreatment efficiency in a GTDi engine including cooled LP-EGR system under different steady-state operating conditions". *Applied Energy*, Vol. 158, pp. 459–473, nov 2015.

[178] Romero C.A., Torregrosa A.J., Olmeda P. and Martín J. "Energy Balance During the Warm-Up of a Diesel Engine". *SAE Techinical Paper 2014-01-0676*, 2014.

[179] Donn C., Zulehner W., Ghebru D., Spicher U. and Honzen M. "Experimental Heat Flux Analysis of an Automotive Diesel Engine in Steady-State Operation and During Warm-Up". *SAE Techinical Paper 2011-24-0067*, 2011.

[180] Jarrier L., Champoussin J.C., Yu R. and Gentile D. "Warm-Up of a D.I. Diesel Engine : Experiment and Modeling". *SAE Technical Paper 2000-01-0299*, 2000.

[181] Jung D., Yong J., Choi H., Song H. and Min K. "Analysis of engine temperature and energy flow in diesel engine using engine thermal management". *Journal of Mechanical Science and Technology*, Vol. 27 n^o 2, pp. 583–592, March 2013.

[182] Kakaee A.H., Paykani A. and Ghajar M. "The influence of fuel composition on the combustion and emission characteristics of natural gas fueled engines". *Renewable and Sustainable Energy Reviews*, Vol. 38, pp. 64–78, October 2014.

[183] Pearson R.J., Eisaman M.D., Turner J., Edwards P.P., Jiang Z., Kuznetsov V.L., Littau K.A., Di Marco L. and Taylor S.R.G. "Energy storage via carbon-neutral fuels made from CO 2, Water, and Renewable Energy". *Proceedings of the IEEE*, Vol. 100 n^o 2, pp. 440–460, 2012.

[184] Imran A., Varman M., Masjuki H.H. and Kalam M.A. "Review on alcohol fumigation on diesel engine: A viable alternative dual fuel technology

for satisfactory engine performance and reduction of environment concerning emission". *Renewable and Sustainable Energy Reviews*, Vol. 26, pp. 739–751, October 2013.

[185] Kumar S., Cho J.H., Park J. and Moon I. "Advances in diesel-alcohol blends and their effects on the performance and emissions of diesel engines". *Renewable and Sustainable Energy Reviews*, Vol. 22, pp. 46–72, June 2013.

[186] Yüksel F. and Ceviz M.A. "Thermal balance of a four stroke SI engine operating on hydrogen as a supplementary fuel". *Energy*, Vol. 28 n^o 11, pp. 1069–1080, September 2003.

[187] Abedin M.J., Masjuki H.H., Kalam M.A., Sanjid A., Rahman S.M. and Masum B.M. "Energy balance of internal combustion engines using alternative fuels". *Renewable and Sustainable Energy Reviews*, Vol. 26, pp. 20–33, October 2013.

[188] Magno A., Mancaruso E. and Vaglieco B. "Effects of a biodiesel blend on energy distribution and exhaust emissions of a small CI engine". *Energy Conversion and Management*, Vol. 96, pp. 72–80, May 2015.

[189] Modi A.J. and Gosai D.C. "Experimental study on Thermal Barrier coated diesel engine performance with Blends of diesel and Palm biodiesel". *SAE Int. J. Fuels Lubr.*, Vol. 3 n^o 2, pp. 1–16, 2010.

[190] Abedin M.J., Masjuki H.H., Kalam M.A., Varman M., Arbab M.I., Fattah I.M. and Masum B.M. "Experimental investigation of a multicylinder unmodified diesel engine performance, emission, and heat loss characteristics using different biodiesel blends: rollout of B10 in Malaysia.". *The Scientific World Journal*, Vol. 2014 n^o 349858, pp. 9 pages, January 2014.

[191] Mendoza M.C. and Woon P.V. "E-diesel Effects on Engine Component Cummins C8 . 3 Engine". *SAE Techinical Paper 2002-01-2847*, 2002.

[192] Ajav E.A., Singh B. and Bhattacharya T.K. "Thermal balance of a single cylinder diesel engine operating on alternative fuels". *Energy Conversion and Management*, Vol. 41 n^o 14, pp. 1533–1541, September 2000.

[193] Alasfour F.N. "Butanol–A single-cylinder engine study: availability analysis". *Applied Thermal Engineering*, Vol. 17 n^o 6, pp. 537–549, June 1997.

[194] Caton J.A. "Implications of fuel selection for an SI engine: Results from the first and second laws of thermodynamics". *Fuel*, Vol. 89 n^o 11, pp. 3157–3166, November 2010.

[195] Özcan H. and Söylemez M.S. "Thermal balance of a LPG fuelled, four stroke SI engine with water addition". *Energy Conversion and Management*, Vol. 47 n^o 5, pp. 570–581, March 2006.

[196] Gharehghani A., Mirsalim M. and Yusaf T. "Experimental investigation of thermal balance of a turbocharged SI engine operating on natural gas". *Applied Thermal Engineering*, Vol. 60 n^o 1-2, pp. 200–207, October 2013.

[197] Javaheri A., Esfahanian V., Salavati-Zadeh A. and Darzi M. "Energetic and exergetic analyses of a variable compression ratio spark ignition gas engine". *Energy Conversion and Management*, Vol. 88, pp. 739–748, December 2014.

[198] Yingjian L., Qi Q., Xiangzhu H. and Jiezhi L. "Energy balance and efficiency analysis for power generation in internal combustion engine sets using biogas". *Sustainable Energy Technologies and Assessments*, Vol. 6, pp. 25–33, June 2014.

[199] Dimopoulos P., Bach C., Soltic P. and Boulouchos K. "Hydrogen-natural gas blends fuelling passenger car engines: Combustion, emissions and well-to-wheels assessment". *International Journal of Hydrogen Energy*, Vol. 33 n^o 23, pp. 7224–7236, December 2008.

[200] Orbaiz P., Brear M.J., Abbasi P. and Dennis P.A. "A Comparative Study of a Spark Ignition Engine Running on Hydrogen, Synthesis Gas and Natural Gas". *SAE Int. J. Engines*, Vol. 6 n^o 1, pp. 23–44, 2013.

[201] Orbaiz P. and Brear M. "Energy Balance of a Spark Ignition Engine Running on Hydrogen, Synthesis Gas and Natural Gas". *SAE Techinical Paper 2014-01-1337*, 2014.

[202] Mistry C.S. "Comparative Assessment on Performance of Multi cylinder Engine Using CNG , LPG and Petrol as a Fuel". *SAE Techinical Paper 2005-01-1056*, 2005.

[203] Woods M., Bryzik W. and Schwarz E. "Heat Rejection from High Output Adiabatic Diesel Engine". *SAE Techinical Paper 920541*, 1992.

[204] Taymaz I., Cakir K., Gur M. and Mimaroglu A. "Experimental investigation of heat losses in a ceramic coated diesel engine". *Surface and Coatings Technology*, Vol. 169-170, pp. 168–170, June 2003.

[205] Xin Q. and Zheng J. "Theoretical Analysis of Internal Combustion Engine Miscellaneous Heat Losses". *SAE Techinical Paper 2009-01-2881*, 2009.

[206] Franco A. and Martorano L. "Methods to Evaluate In-Cylinder Heat Transfer and Thermal Load in the Small Internal Combustion Engines". *SAE Techinical Paper 1999-01-1252*, 1999.

[207] Rabeau F. and Magand S. "Modeling of a Thermal Management Platform of an Automotive D . I Diesel Engine to Predict the Impact of Downsizing and Hybridization during a Cold Start". *SAE Techinical Paper 2014-01-0657*, 2014.

[208] Rakopoulos C.D. and Giakoumis E.G. "Second-law analyses applied to internal combustion engines operation". *Progress in Energy and Combustion Science*, Vol. 32 n^o 1, pp. 2–47, 2006.

[209] Farrell J.T., Stevens J.G. and Weissman W. "A Second Law Analysis of High Efficiency Low Emission Gasoline Engine Concepts". *SAE Techinical Paper 2006-01-0491*, 2006.

[210] Rakopoulos C.D. and Giakoumis E.G. "Speed and load effects on the availability balances and irreversibilities production in a multi-cylinder turbocharged diesel engine". *Applied Thermal Engineering*, Vol. 17 n^o 3, pp. 299–313, March 1997.

[211] Modi A.J. "Experimental Study of Energy Balance in Thermal Barrier Coated Diesel Engine". *SAE Techinical Paper 2012-01-0389*, 2012.

Chapter 3

Experimental and theoretical tools

Contents

3.1 Introduction

As will be described in Chapter 4, the methodology for the integral determination of the energy flows through the engine as well as their interactions, require both a dedicated experimental installation and accurate modelling of the internal engine processes and elements. These information sources have a close relationship, inasmuch as some experimental measurements are inputs of the models and are necessary for their calibration. Taking into account these comments, the two main purposes of experimental measurements are:

1. Determine some energy terms of the thermal balance as detailed in Chapter 4.2.1.
2. Provide information aimed at the development, adjustment and validation of the sub-models required to complete the thermal balance, considering internal energy interactions difficult to be measured as presented in Chapter 4.2.2.

Therefore, the first part of this chapter is focused on the complete description of the engines features (e.g. engine architecture, combustion characteristics, etc.) as well as the instrumentation of the facilities where the experimental work was carried out.

To perform the modelling work, a thermodynamic model developed in the previous works [1, 2] is used as the basis for the further thermal balance models development, as presented in Chapter 5. The thermodynamic model can be used considering two different points of view, which share the sub-models and thermodynamic hypothesis as shown in Figure 3.1. In the *diagnosis approach*, the main objective is to determine the RoHR starting from the instantaneous in-cylinder pressure (p) and some mean values which characterize the engine operation, such analysis is performed with an in-house developed tool called **CALMEC**. On the other hand, the *predictive approach* is intended to simulate p, requiring for this purpose the definition of the operating conditions as well as the combustion law, being this analysis performed with an in-house developed tool called **SiCiclo**.

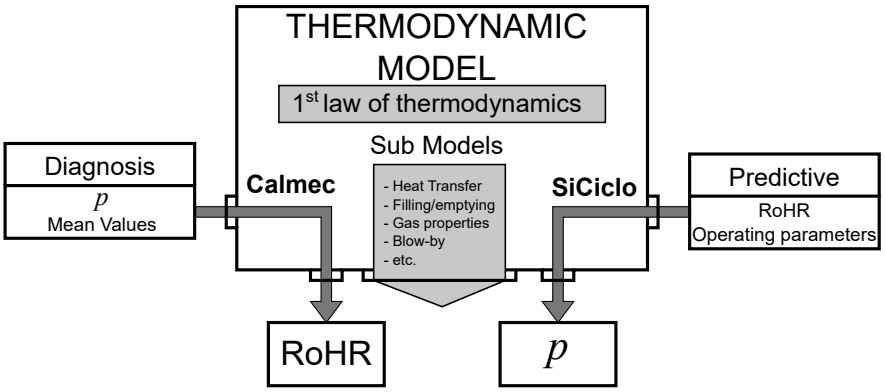

Figure 3.1. *Scheme of the thermodynamic model.*

In spite of the main outputs are either the RoHR or p, it is necessary to estimate several internal processes such as the HT, the intake/exhaust, etc. These results are crucial to determine the engine thermal interactions, thus being key parameters for the thermal balance. For this reason, in the second part of this chapter the thermodynamic model along with all the related sub-models are briefly but comprehensively described.

3.2 Experimental installations

Bearing in mind that one of the objectives of this work is to propose a general methodology to perform and analyse the thermal balance in automotive engines, it was decided to use different engine technologies. For that reason, two engines with different characteristics (hereinafter called **Engine A** and **Engine B**) have been selected:

- **Engine A** is a 4-stroke, compression ignition, multi-cylinder, High Speed Direct Injection (HSDI) Diesel engine. Most of the experimental work has been performed in this engine, since it is more representative of the current engine technologies used in automotive applications. Its main characteristics are presented in column "Engine A" of Table 3.1.

- **Engine B** is a 2-stroke, compression ignition, single cylinder engine. This research engine was selected to test the thermal balance methodology proposed in Chapter 4 for the evaluation of a new concept engine,

operating in PPC of gasoline. Its main characteristics are presented in column "Engine B" of Table 3.1.

	Engine A	**Engine B**
Cylinders	4 in-line	1
Bore	75 mm	76 mm
Stroke	88 mm	80.5 mm
Unitary displacement	390 cm^3	365 cm^3
Compression ratio	16:1	17:1
Air management	Turbocharged	Screw compressor
Maximum power	82 kW at 3600 rpm	22.5 kW at 3500 rpm
Maximum torque	270 Nm at 1750 rpm	72.5 Nm at 2000 rpm
Combustion mode	CDC	PPC
Injection	Common rail	Common rail
Valves per cylinder	2	4

Table 3.1. *Engines technical data.*

Following, a description of each experimental facility and their particularities is presented.

3.2.1 Multi-cylinder engine

To reproduce the repartition of the energy at each sub-system in realistic operating conditions, it is necessary the use of a multi-cylinder engine test bench. These installations have the drawback of more difficult control and measurement of the operating parameters and possible cylinder dispersion in comparison with a single-cylinder test bench [3]. However, its operation is closer to the real automotive application. Thus, a 4-cylinder engine, currently manufactured for automotive applications, was selected (**Engine A**) to perform most of the experimental work.

The complete test bench measuring equipment is summarized in Table 3.2. As obtaining the experimental information requires a highly instrumented test cell and several engine sub-systems modifications, its description is presented in two parts: the first deals with the engine gas lines, and the second with the cooling, lubrication and injection systems.

Variable	Equipment	Range	Accuracy
Speed	Dynamometer	6000 rpm	0.03% fs.
Torque	Dynamometer	±450 Nm	0.05% fs.
Cylinder pressure	AVL GH13P	0-250 bar	0.3% lin.
Amplifier	Kistler 5011B	± 10 V	-
Air flow	Sensiflow DN80	20 to 720 kg/h	2%
Fuel flow	AVL 733S Fuel meter	0-150 kg/h	0.2%
Blow-by flow	AVL blow-by Meter	1.5-75 l/min	1.5%
Temperature	K-type Thermocouples	-200-1250 °C	1.5 °C
	PT100 RTD	-200 to 850 °C	0.2°C
Mean pressure	Kistler Piezo-resistive Transmitters	0-10 bar	0.1-0.2% lin.
Gases analysis	Horiba mexa 7100 DEGR		1-4% fs.
Coolant flow	Krohne 4010 Optiflux	±12 m/s	0.5%
Oil cooler	Isoil MS500	0-1036 l/h	0.5% fs.
Fuel cooler	Yoko Admag AE208MG	0-10 m/s	0.5%
Turbo oil flow	Krohne Optimass 3050C	450 kg/h	0.5%

fs. means full scale.
lin. means linearity.

Table 3.2. Engine A *test bench instrumentation.*

3.2.1.1 Gas lines instrumentation

Figure 3.2 shows a scheme of the engine gas lines and their instrumentation. As shown, there are several pressure and temperature sensors located at different positions of the intake/exhaust gas lines. The objective is to have detailed information of the intake and exhaust gases thermodynamic conditions that depend on different sub-processes such as turbocharging, air/EGR mixing, air cooling, etc.

The gases mean temperatures are measured by means of K-type thermocouples or PT100 Resistance Temperature Detectors (RTD) depending on the accuracy required, whilst the mean pressures are measured with piezo-resistive pressure transmitters. The measurement of the gas and fuel mass flows is necessary to control the combustion process, and they are important

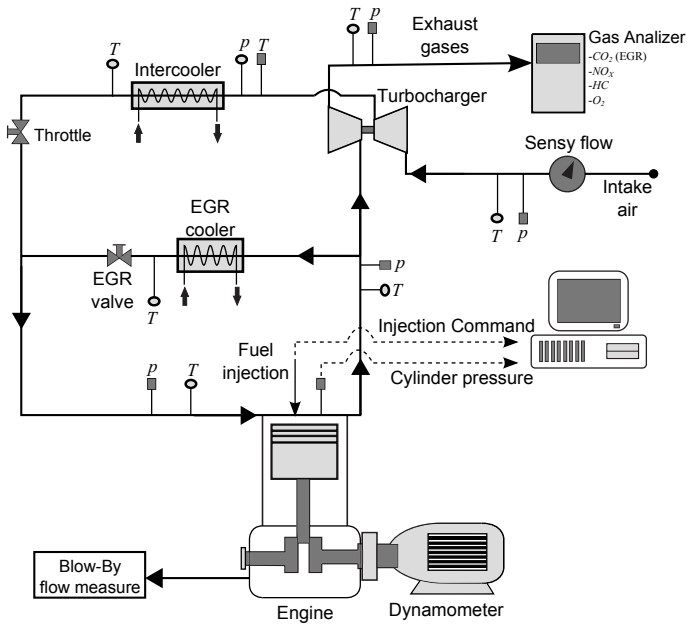

Figure 3.2. *Scheme of the gas lines instrumentation.*

to analyse the HT in the chamber; therefore, the injected fuel, the air flow and the blow-by leakage are measured with an AVL 733S Fuel meter, a DN80 sensiflow and an AVL blow-by Meter respectively. The exhaust emissions are analysed by means of an exhaust monitoring equipment (Horiba MEXA 7100 DEGR), which also allows measuring the CO_2 concentration at intake manifold to determine the EGR rate [4].

The most important experimental variable to be measured is the in-cylinder pressure, since it is the main input of the thermodynamic model. To measure the pressure trace, 4 AVL GH13P piezo-electric transducers were installed at the glow plug hole of each cylinder. The signal provided by the piezo-electric transducers with a resolution of 0.5° is conditioned by means of Kistler 5011B amplifiers, and the digital processing is performed following the method described in [5]. Considering the importance of accurate measuring the in-cylinder pressure, the acquisition chain is calibrated according to the traditional method proposed in [6]. The conditioned in-cylinder pressure signals are acquired by means of a Yokogawa DL708E Oscillographic recorder with 16 A/D converter module. Finally, the control of the Engine Control

Unit (ECU) and the acquisition of its variables were done by means of the INCA interface, which allows reading and modifying the engine cartography and setting the required operating conditions.

3.2.1.2 Liquid lines instrumentation

To attain a better control of the engine operating parameters and to perform the experimental measurements in the liquid lines, the original coolant and oil circuits were adapted and instrumented to measure the mass flows and temperatures necessary to determine the heat rejection to the coolant, block oil and turbocharger oil independently, as shown in Figure 3.3.

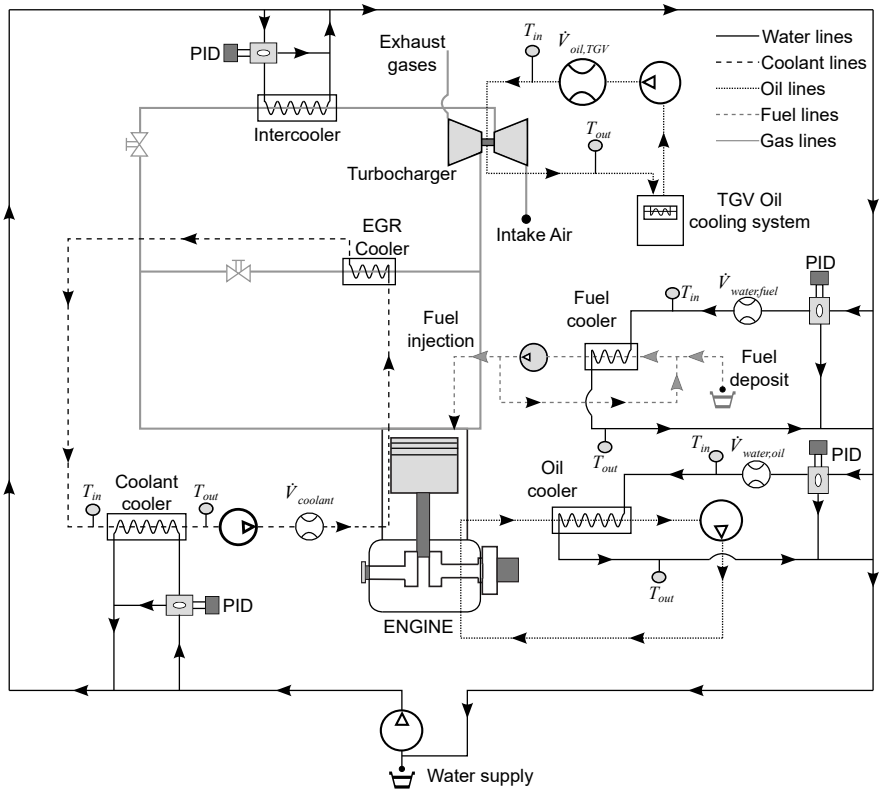

Figure 3.3. *Scheme of the cooling, lubricating and injection lines instrumentation.*

The temperatures along the liquid lines were measured with RTD because they are more accurate (±0.2°C) than K-type thermocouples (± 1.5°C).

This accuracy is key, as the temperature drop in the coolers is expected to be small in some cases (e.g. at low speed and load, the cooling water in the fuel return line has temperature variations about 1-2°C). For the same reason, to ensure the engine thermal stability, a good temperature control has to be attained, thus several Proportional-Integral-Derivative controllers (PID) and their corresponding valves were installed in the water supply lines before the coolant, oil, air and fuel coolers. Due to the small oil flow in the turbocharger, a special conditioning cart was used to ensure stable and safe temperature values.

The acquisition and control of the low-frequency signals (mass flows, mean pressures and temperatures[1]) was carried out with an in-house developed software called **SAMARUC**, which also allows visualizing the engine operating parameters and controlling the operating conditions, thus a precise monitoring and control of the interesting parameters can be done. The sensors signals were collected and processed in a PXI platform of National instruments, and in the specific case of the temperatures measured with the RTD, they were registered by means of a Datalogger 34972A LXI data acquisition system.

3.2.2 Single-cylinder engine

With the purpose of applying the methodology proposed in Chapter 4 in engines with very different characteristics, some part of the experimental work is performed in a single-cylinder engine, research version of a 2-stroke Diesel engine prototype [7]. The mean differences with **Engine A** (apart from the number of cylinders, valves and strokes) are the characteristic motion of the air in the chamber, as **Engine B** has *tumble* motion instead of *swirl* (key for the HT and thermal balance) and the feasibility of operating in PPC mode with gasoline. In the next sections, the engine architecture and the test bench are described.

3.2.2.1 Engine architecture and hardware

The cylinder head and combustion chamber geometries shown in Figure 3.4 are completely adapted to ensure a suitable in-cylinder flow pattern, in order to optimize the scavenging of burnt gases and reduce the short-circuit of fresh air going directly from intake to exhaust ports. The cylinder head

[1]Except RTD sensors.

geometry presents a staged roof for baffling the air flow between the intake and exhaust valves, forcing the air to follow the path of the cylinder wall towards the bottom of the cylinder, and hence enhancing the tumble motion. This geometry provides the best compromise between scavenging efficiency, acceptable permeability and convenient combustion chamber geometry [7].

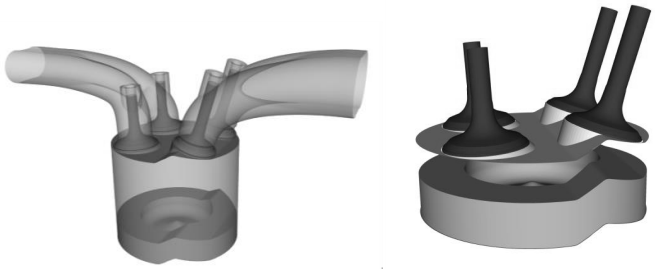

Figure 3.4. *Sketch of the cylinder head designed for the 2-stroke engine architecture (Patent Renault FR2931880).*

The engine is equipped with an hydraulic cam-driven variable valve timing system, allowing a flexibility of 30° on both intake and exhaust valve timings independently of the mechanical cam timing. The optimum camshaft configuration, presented in Table 3.3, was experimentally defined by testing different opening durations and maximum lifts in a medium load and medium speed operating point.

Type of scavenging	Poppet valves with scavenging loop
Intake camshaft profile	Duration: 80°/max. lift: 6 mm
Exhaust camshaft definition	Duration : 90°/max. lift: 8.5 mm

Table 3.3. Engine B *main technical data.*

Due to the characteristics of the engine, efforts had to be done in order to estimate the **short-circuit** and **residual masses**, which are specially high due to the characteristic intake/exhaust processes in 2-stroke engines. Thereby, the trapping ratio η_{tr}, which is an indicator of the engine capability to retain the fresh air during the intake process, is experimentally determined by means of a tracer gas as proposed in [8, 9]. The method consists on injecting a controlled quantity of CH_4 (tracer gas) at the intake flow, and then measuring its concentration at both the intake and exhaust manifolds. The trapped CH_4 at the IVC gets completely burned along the combustion process, since

the in-cylinder temperature after compression and during the combustion of the injected diesel is high enough to ensure the CH_4 autoignition. Taking into account that the in-cylinder and manifolds temperatures during the scavenging event are not high enough to force the CH_4 autoignition, the CH_4 flow from intake to exhaust ports during the scavenging process is not burned. From these observations, and taking into account that CH_4 is homogeneously mixed with the intake air, it can be stated that an accurate estimation of the short-circuited mass can be done by means of a mass balance, considering intake, exhaust and in-cylinder gases.

The **total trapped mass** in the cylinder is a key parameter to obtain the thermodynamic conditions at IVC [10], being very important for both, modelling and experimental determination of the HT [11]. The trapped mass is given by the addition of the trapped air/EGR mixture and the IGR at the IVC, being the IGR the fraction of residual gases retained from the previous combustion cycle over the total trapped mass in the cylinder. The IGR ratio and the total trapped mass are estimated using simplified thermodynamic calculations. This estimation is based on an enthalpy balance, where the enthalpy of the total trapped mass at the IVC equals to the enthalpy of the residual mass plus the enthalpy of the intake delivered trapped mass (fresh air plus external EGR), both estimated also at the IVC.

3.2.2.2 Single-cylinder engine test bench

Engine B was assembled into a fully instrumented test cell, whose scheme is shown in Figure 3.5 and its complete measuring equipment is summarized in Table 3.4.

The engine is fed with the compressed air provided by an external compressor, whose operation was set to simulate boost conditions. A throttle valve located at the exhaust line (after the exhaust settling chamber) is used to simulate the back-pressure that would be produced by the turbine. The experimental cell also includes a low pressure EGR system, designed to provide arbitrary levels of cooled EGR even at very high intake boost pressures. Water and oil cooling circuits are also independent of the engine, and their temperatures are strictly controlled and monitored during all the experimental tests. The fuel consumption of the engine is measured with a gravimetric dynamic fuel meter.

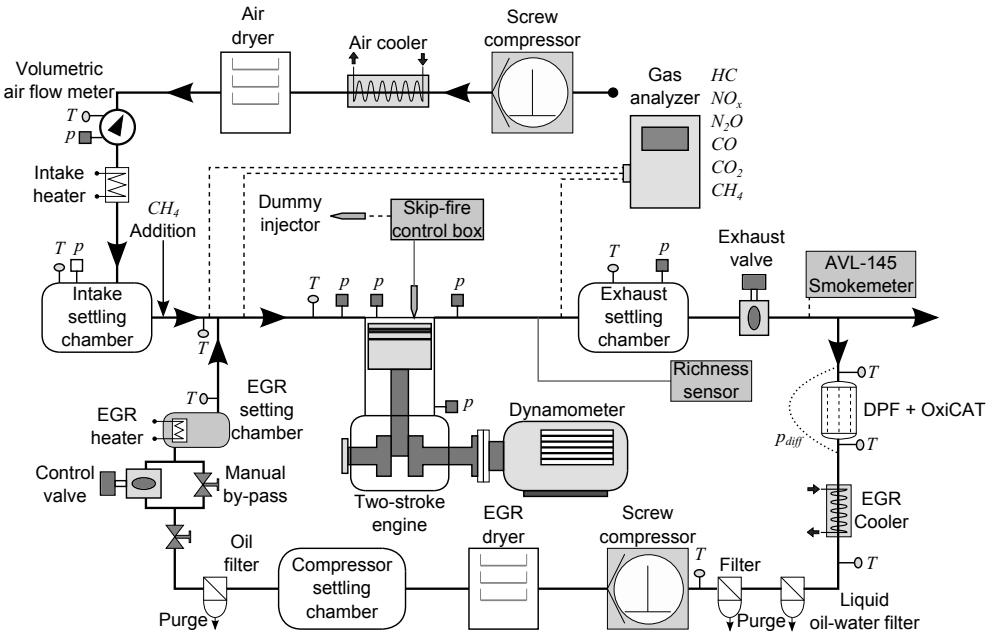

Figure 3.5. Engine B *test cell scheme.*

The most relevant mean variables of the test cell and engine, pollutant emissions, and high-frequency instantaneous signals are recorded using a dedicated data acquisition system. The high-frequency signals are acquired using an Yokogawa DL708E Oscillographic recorder synchronized with an optical angular encoder with a resolution of 0.2°. The in-cylinder pressure is measured by means of a Kistler 6061B piezoelectric sensor, while a Kistler 4007B piezo-resistive pressure sensor is placed at the cylinder liner near to the BDC, with the objective of pegging the differential pressure signal obtained from the piezoelectric sensor.

To adjust the thermodynamic model and some geometrical parameters, as will be explained in Chapter 5.3, it is necessary the measurement of motoring test. Due to the particularities of the 2-stroke engines [12], the thermodynamic state of the trapped mass[2] and the tumble air movement within the combustion chamber highly differ between firing and motoring conditions, leading to a poor performance of the tuning method in this engine. There-

[2]Due to high residuals in combustion operation, the temperature at IVC use to be much higher in 2-stroke than in 4-stroke engines.

Variable	Equipment	Range	Accuracy
Speed	Dynamometer	7000 rpm	0.006% fs.
Torque	Dynamometer	±450 Nm	0.1% fs.
Cylinder pressure	Kistler 6061B	0-250 bar	0.5% lin.
Cylinder pressure at BDC	Kistler 4007B	0-20 bar	<0.2% fs.
Amplifier	Kistler 5011A10	± 10 V	-
Air flow	Elster RVG65	0.6-100 m^3/h	1%
Fuel flow	AVL 733S	0-75 kg/h	0.12%
Blow-by flow	AVL blow-by Meter	1.5-75 l/min	1.5%
Temperature	K-type Thermocouples	-200-1250 °C	1.5 °C
Mean pressure	Kistler Piezo-resistive Transmitters	0-10 bar	0.1-0.2% lin.
Gases analysis	Horiba mexa 7100 DEGR	-	1-4% fs.
Smoke	Smoke meter	0-10 FSN	2%

fs. means full scale.
lin. means linearity.

Table 3.4. Engine B *test bench instrumentation.*

fore, to obtain suitable motoring cycles for the adjustment, the test bench was equipped with a special system to perform skip-fire measurements. It consists of skipping the injection of one cycle (every determined number of combustion cycles), thus obtaining a motoring cycle with the air management of a conventional combustion. This special device consists of a control box and a dummy injector, as shown in Figure 3.5. The electronic box deviates one injection command pulse to the dummy injector every determined number of pulses, thus skipping the fuel injection and combustion events during that specific cycle.

3.3 Thermodynamic model

This section is devoted to the comprehensive explanation of the base model used to estimate the thermodynamic processes within the combustion chamber, specially heat rejection, thus allowing the combustion analysis in **Engine A** and **Engine B** (with CALMEC), and the pressure simulation in **Engine B** (with SiCiclo). Although the main objective of the model is to accurately calculate the gas conditions in the chamber, it also includes specific sub-models to reproduce the intake/exhaust processes and the phenomena involved (HT in the chamber and ports, mass flows, etc.). This model was originally developed by Tinaut [13] and Armas [1], who stated the basic hypothesis and proposed the initial required sub-models. The model was further improved by Martín [2], who introduced several sub-model upgrades to achieve better accuracy on the RoHR and heat fluxes determination in CALMEC, and included all the sub-models in the predictive tool SiCiclo [14].

The next section is organized as follows: firstly, the main hypotheses in which the model is based are presented, followed by a brief description of the filling and emptying model and the mass and energy balances within the combustion chamber. Finally, the sub-models used to calculate the terms involved in the in-cylinder energy balance are detailed.

3.3.1 Basic hypotheses

To solve the first law of thermodynamics in the combustion chamber, some hypothesis and simplifications have to be accounted to determine the terms involved:

1. **The combustion chamber is considered an open system**. It is assumed in both, open cycle[3] (due to the flows through the intake/exhaust valves) and closed cycle[4] (due to injection and blow-by).

2. **Chamber pressure is uniform in the chamber**. This is usually assumed in combustion calculations because both fluid and flame velocities are much smaller than the speed of sound [15].

[3]Open cycle is defined as the engine operation when one of the valves is open, i.e. between EVO and IVC.

[4]Closed cycle is defined as the engine operation when the valves are closed, i.e. between IVC and EVO.

3. **Three species are considered in the chamber**: air, fuel vapour and stoichiometric combustion products. In a DI Diesel engine operating with CDC, the flame front is located at the stoichiometric fuel-air ratio region during the mixing-controlled burning phase, thus this hypothesis is suitable. In the case of PPC, this hypothesis is not completely accurate; however, take into account the particular characteristics of the mixture process requires complex mixing-combustion models, which are out of the scope of this work

4. **Perfect gas behaviour is assumed**. As reported by Lapuerta et al. [16], the error by considering perfect gas inside the chamber is negligible, thus this assumption is suitable for the application presented in this work.

5. **Specific heats depend on temperature and gas composition**. The value of the specific heat is highly dependent on temperature and the species properties. Taking into account that at high load the gas temperature can range between 80°C at IVO up to 1800°C at TDC, and that the fuel injection and combustion change the charge composition, this hypothesis is useful to improve accuracy and is consistent with the the hypotheses 3 and 4.

6. **Internal energy is calculated assuming mean uniform temperature within the chamber**. This is the most uncertain hypothesis assumed, taking into account that the calculation of the gas internal energy depends on the temperature. This can be especially important for the burned products at the beginning of the combustion; however, the error diminishes as the combustion advances because the dilution and the heat transfer tend to make the temperature uniform.

7. **Convective heat transfer to the chamber walls is assumed**. As stated in Chapter 2.4.1, the cooling losses in conventional RICEs (mostly due to HT to the chamber walls) can range between $25\%\dot{m}_f H_v$ and $40\%\dot{m}_f H_v$ in CDC, and between $15\%\dot{m}_f H_v$ and $30\%\dot{m}_f H_v$ in CGC; therefore, HT is a key topic in this work. Radiation is not considered explicitly due to its low relative weight.

8. **Deformation of the engine mechanism is assumed**. The engine mechanism (i.e. piston, connecting rod and crankshaft) undergoes mechanical deformations due to high pressure and the inertial loads.

These basic hypotheses, along with the sub-models described in Section 3.3.5, allow calculating all the terms of the in-cylinder energy balance, in order to obtain the gas state during open and closed cycle and the RoHR or in-cylinder pressure, as described in the next sections.

3.3.2 Filling and emptying model

The engine filling and emptying model is a simple model of the complete engine, which describes the physical processes taking place during the intake-exhaust strokes (between EVO and IVC). The model has two main objectives:

1. Obtaining the gas thermodynamic conditions during the open cycle at different engine parts, in particular chamber and ports. This is necessary to calculate the total heat rejection of the engine (key to perform the thermal balance, see Chapter 4.2.2) and affects wall temperatures.

2. Defining the residual and short-circuit masses. As commented, these masses affect the IVC conditions, thus affecting the subsequent evolution during closed cycle (very important to calculate chamber HT). They also affect the RoHR obtained with CALMEC (key parameter for combustion analysis) and the in-cylinder pressure obtained with SiCiclo.

In Figure 3.6, a scheme of the model for a multi-cylinder engine with z cylinders is presented. The model consists of a series of volumes (representing the intake and exhaust lines along with the cylinder) connected by means of some restrictions; therefore, one volume in the admission and two in the exhaust are considered, taking into account that the exhausts process is more important regarding the trapped mass estimation, and that the short-circuit is usually small in 4-stroke engines [2].

The restriction $R_{int,0}$ represents the intercooler[5], the intake volume (V_{int}) represents the intake ports and the intake manifold, the restrictions $R_{int,1}$ to $R_{int,z}$ between V_{int} and the cylinders (Cyl 1 to Cyl z) represent the intake valves of each i-cylinder (with variable section depending on the instantaneous valve lifting). The cylinders are communicated with the first exhaust volume ($V_{exh,1}$) through the restrictions $R_{exh,1}$ to $R_{exh,z}$, which represent the exhaust valves of each i-cylinder (with variable section as assumed

[5]If no intercooler is used, it represents the pressure losses at the intake manifold.

for intake valves). $V_{exh,1}$ represents the exhaust ports and the exhaust manifold, meanwhile the second exhaust volume $V_{exh,2}$ represents the rest of the exhaust system that has not been explicitly accounted (turbine, catalyst, DPF filter, muffler etc.). The restriction $R_{exh,12}$ represents the turbine effect in a simplified manner, and $R_{exh,0}$ the pressure losses in the exhaust line after the turbine[6]. The key elements for the calculation at exhaust are $V_{exh,1}$ and $R_{exh,12}$; however, $V_{exh,2}$ and $R_{exh,0}$ have to be included to limit reaching sonic conditions at $R_{exh,12}$.

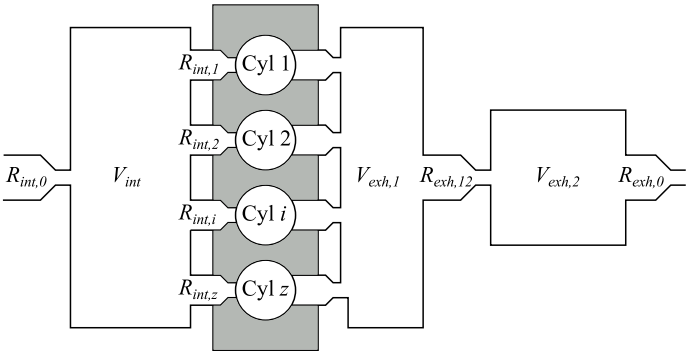

Figure 3.6. *Scheme of the filling and emptying model.*

In Table 3.5, the elements that conform the simplified engine system are presented, where $A_{v,int}$ and $A_{v,exh}$ are the intake and exhaust valve sections, $c_{d,int}(lift)$ and $c_{d,exh}(lift)$ are their corresponding discharge coefficients, where $(lift)$ indicates that they are function of the valve lifting. The characteristic sizes have been selected to maintain the simplicity as well as the physical meaning of the model.

The basic hypotheses of the model are:

1. Perfect mixture regarding temperature and composition is assumed.
2. After $R_{exh,0}$, atmospheric conditions are assumed for multi-cylinder engines, and the conditions in the exhaust settling chamber are assumed for single-cylinder engines.
3. The gas in the cylinders and volumes has no speed, it stops when entering in a volume, and it is initially stopped before leaving.

[6]Note that $R_{exh,0}$ does not represent any specific element of the exhaust line.

Element	**Volume**	**Section**
$R_{int,0}$	-	$A_{v,int}$
$R_{int,1}$ to $R_{int,z}$	-	$A_{v,int} \cdot c_{d,int}(lift)$
$R_{exh,1}$ to $R_{exh,z}$	-	$A_{v,exh} \cdot c_{d,exh}(lift)$
$R_{exh,12}$	-	To be adjusted
$R_{exh,0}$	-	To be adjusted
V_{int}	V_d	-
Cyl 1 to Cyl z	V_d	-
V_{int}	$V_d \cdot z/2$	-
V_{int}	$V_d \cdot z$	-

Table 3.5. *Geometry of the filling and emptying model elements.*

4. It is assumed that the flow-back entering the cylinders (from intake and exhaust) has no time to cool down, thus small gas packages are accumulated in the intake and exhaust ports, conserving their temperature and composition. When flow-back occurs, the last one went out from the cylinder is the first one re-entering.

5. No heat transfer in the volume's walls is considered, and heat transfer to the cylinder walls is calculated by means of the Woschni model [17, 18], as later discussed.

6. The flow through each restriction is calculated by means of the isentropic nozzle equation, assuming quasi-steady conditions [10]. If sonic conditions are reached in any restriction, critical pressure is assumed downstream of the corresponding nozzle.

7. During the valve overlap, if the in-cylinder pressure is lower than the V_{int} pressure and higher than the $V_{exh,1}$, shot-circuit from intake to exhaust will occur. Similarly, if the in-cylinder pressure is higher than the V_{int} pressure but lower than the $V_{exh,1}$, shot-circuit from exhaust to intake will take place. In both cases, the mass flow is estimated by considering the equivalent effective area of serial intake and exhaust sections [1].

By calculating the instantaneous flux at each restriction and then solving the first law for open systems, along with the ideal gas law, the instantaneous mass flow, temperature and pressure of each element are obtained.

The calculation starts at EVO and solves the complete thermodynamic cycle, considering at each instant all the volumes but only the cylinders with open valves. An iterative process is required to achieve the convergence in thermodynamic conditions. Effective areas of $R_{exh,1}$ and $R_{exh,0}$ are corrected at each iteration to have the same mean simulated pressure in $V_{exh,1}$ as that experimentally measured.

In Figure 3.7, an example of the model performance at two different speed levels is presented. As can be seen, the prediction of the exhaust pressure shows a good behaviour, fitting well the experimental pressure trace at both speed levels.

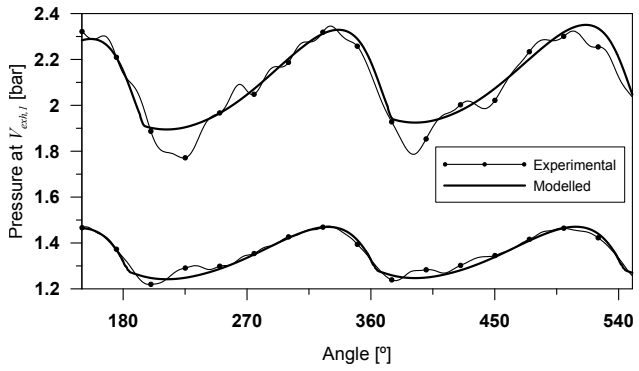

Figure 3.7. *Experimental and modelled pressures at $V_{exh,1}$. Up high speed level, bottom low speed level.*

By using instantaneous simulated pressure as boundary condition for the cylinder calculation, accurate estimation of residuals (m_{res}) and short-circuit (m_{sc}) masses are obtained. These model outputs are important to obtain the in-cylinder conditions at IVC, and hence initializing the calculation of the closed cycle.

3.3.3 Combustion chamber mass balance

The trapped mass at IVC (m_{IVC}) results from the addition of the induced fresh air mass (m_a), the EGR mass (m_{EGR}), and the residual gas of the previous cycle (m_{res}), minus the short-circuit mass (m_{sc}) during valve overlap, as presented in Equation (3.1):

$$m_{\text{IVC}} = m_a + m_{res} + m_{EGR} - m_{sc} \tag{3.1}$$

The incoming m_a and m_{EGR} are obtained from experimental measurements whilst m_{res} and m_{sc} are estimated with the filling and emptying model described in Section 3.3.2. From IVC on, the instantaneous evolution of the mass within the cylinder is affected by the blow-by losses and the fuel injection. Thus, the instantaneous mass can be obtained at each crank angle (α) as:

$$m_c(\alpha) = m_{\text{IVC}} - \int_{\text{IVC}}^{\alpha} \mathrm{d}m_{bb} + \int_{SoI}^{\alpha} \mathrm{d}m_{f,ev} \tag{3.2}$$

where $m_{f,ev}$ is the evaporated mass of fuel.

Taking into account the masses involved, the instantaneous mass fraction (Y) of the three species considered can be obtained; therefore, at any intermediate instant i between IVC and EVO, the instantaneous mass fraction of burned products can be written as a function of the Heat Release Fraction (HRF):

$$Y_b = \frac{\left(m_f + \frac{m_f}{F_s}\right)\ \text{HRF} + (m_{EGR} + m_{res})\ Y_{b,\text{EVO}} - m_{sc}\, Y_{b,\text{IVC}} - \int\limits_{\text{IVC}}^{i} Y_b\ \mathrm{d}m_{bb}}{m_{\text{IVC}} + \int\limits_{\text{IVC}}^{i} \mathrm{d}m_{f,ev} - \int\limits_{\text{IVC}}^{i} \mathrm{d}m_{bb}} \tag{3.3}$$

where F_s is the stoichiometric fuel/air ratio, and $Y_{b,\text{EVO}}$ and $Y_{b,\text{IVC}}$ are calculated as [2]:

$$Y_{b,\text{EVO}} = \frac{1 + \frac{1}{F_s}}{1 + \frac{1}{F} - \left(\frac{m_{sc} + m_{bb}/2}{m_f}\right) \frac{1}{1 + \frac{m_{EGR} + m_{res}}{m_a}}} \tag{3.4}$$

$$Y_{b,\text{IVC}} = \frac{Y_{b,\text{EVO}}}{1 + \frac{m_a}{m_{EGR} + m_{res}}} \tag{3.5}$$

being F the fuel/air ratio.

The unburned gaseous fuel mass fraction at any intermediate instant can also be obtained as a function of the instantaneous HRF:

$$Y_f = \frac{\int_{\text{IVC}}^{i} \mathrm{d}m_{f,ev} - m_f \text{ HRF}}{m_{\text{IVC}} + \int_{\text{IVC}}^{i} \mathrm{d}m_{f,ev} - \int_{\text{IVC}}^{i} \mathrm{d}m_{bb}} \tag{3.6}$$

And hence the instantaneous air mass fraction is calculated as:

$$Y_a = 1 - Y_b - Y_f \tag{3.7}$$

The fuel mass injected per cycle, m_f, is obtained from experimental measurements (along with m_a and m_{EGR}), the instantaneous blow-by leakage is calculated by means of the model described in Section 3.3.8, whereas the injection and evaporation processes are modelled as presented in Section 3.3.7.

3.3.4 Combustion chamber energy balance during closed cycle

Once the conditions at IVC and the heat rejection during open cycle are calculated with the filling and emptying model described in the previous section, the main concern of the thermodynamic model is the accurate calculation of in-cylinder conditions during closed cycle to obtain two main results: on the one hand, the RoHR (or simulated pressure in the predictive case), which is the main result of the combustion analysis and is used for the thermal balance tuning and validation (see Chapters 6.2.1 and 6.3.1). On the other hand, the HT during the closed cycle (necessary also for the RoHR calculation), which is the most important variable in the thermal balance methodology described in Chapter 4.2.2.

As stated in the hypotheses of Section 3.3.1, to solve the first law of thermodynamics, the combustion chamber is considered as an open system even during closed cycle, due to fuel injection and the blow-by leakage (hypothesis 1). Besides, the pressure and temperature are uniform within the combustion chamber (hypothesis 2); therefore, no spatial resolution of the thermodynamic properties is considered. Equation (3.8) shows the most general expression of the first law:

$$\begin{aligned} \mathrm{d}U_c &= -\mathrm{d}Q + \mathrm{d}W + h_{f,inj}\ \mathrm{d}m_{f,inj} - h_c\ \mathrm{d}m_{bb} \\ &= -\mathrm{d}Q - p\ \mathrm{d}V + h_{f,inj}\ \mathrm{d}m_{f,inj} - h_c\ \mathrm{d}m_{bb} \end{aligned} \tag{3.8}$$

where U_c is the internal energy of the charge, Q is the heat transfer to the walls, W is the work, $h_{f,inj}$ is the specific enthalpy of the fuel at the injection conditions, $m_{f,inj}$ is the injected fuel mass, h_c is the specific enthalpy of the charge and m_{bb} is the blow-by mass.

The model considers only one zone in the chamber, and hence a single gas phase. For this reason, the injected fuel is taken into account in the mass and energy balances just when it gets evaporated. A rigorous description of the process would involve the detailed evolution of the liquid fuel parcels from the injection conditions up to the vapour mass at mean chamber temperature. This would require the consideration of at least two zones (liquid and gaseous phases), and would result in higher model complexity. Therefore, a simple atomization and evaporation model is used to delay the fuel parcel evaporated with respect to the injection point, resulting in a slight improvement on the accuracy [2].

Considering the previous comments, the injected mass $m_{f,inj}$ in Equation (3.8) can be replaced by the evaporated mass $m_{f,ev}$, thus Equation (3.8) may be written as:

$$\mathrm{d}U_c = -\mathrm{d}Q - p\ \mathrm{d}V + h_{f,inj}\ \mathrm{d}m_{f,ev} - h_c\ \mathrm{d}m_{bb} \tag{3.9}$$

Furthermore, taking into account the three considered species (air, fuel vapour and stoichiometric combustion products), the left-hand side of Equation (3.9) can be expressed as:

$$\begin{aligned} \mathrm{d}U_c &= \mathrm{d}(m_c\ u_c) = \mathrm{d}(m_a\ u_a + m_{f,g}\ u_{f,g} + m_b\ u_b) \\ &= m_a\ \mathrm{d}u_a + m_{f,g}\ \mathrm{d}u_{f,g} + m_b\ \mathrm{d}u_b + \\ &\quad + u_a\ \mathrm{d}m_a + u_{f,g}\ \mathrm{d}m_{f,g} + u_b\ \mathrm{d}m_b \end{aligned} \tag{3.10}$$

where the subscripts c, a, b and f, g refer to chamber, air, stoichiometric burned products and gaseous fuel respectively. The determination of the internal energy of the three considered species (u_a, u_b, $u_{f,g}$) can be done through correlations such as those proposed by Lapuerta [19].

The terms with $\mathrm{d}u_a$, $\mathrm{d}u_{f,g}$ and $\mathrm{d}u_b$ in Equation (3.10) correspond to the variation of the internal sensible energy due to the change of chamber temperature:

$$\begin{aligned} & m_a \ \mathrm{d}u_a + m_{f,g} \ \mathrm{d}u_{f,g} + m_b \ \mathrm{d}u_b = \\ & = m_a \ c_{v,a} \ \mathrm{d}T \ + \ m_{f,g} \ c_{v,f} \ \mathrm{d}T \ + \ m_b \ c_{v,b} \ \mathrm{d}T = \\ & = m_c \left(Y_a \ c_{v,a} \ + \ Y_f \ c_{v,f} \ + \ Y_b \ c_{v,b}\right) \ \mathrm{d}T = m_c \ c_{v,c} \ \mathrm{d}T \end{aligned} \tag{3.11}$$

In Equation (3.10), the terms with $\mathrm{d}m_a$, $\mathrm{d}m_{f,g}$ and $\mathrm{d}m_b$ represent the variation of the charge internal energy due to the composition change associated with combustion, fuel injection and blow-by losses respectively:

$$\begin{aligned} \mathrm{d}m_a &= -\mathrm{d}m_{a,b} - Y_a \ \mathrm{d}m_{bb} \\ \mathrm{d}m_{f,g} &= \mathrm{d}m_{f,ev} - \mathrm{d}m_{f,b} - Y_{f,g} \ \mathrm{d}m_{bb} \\ \mathrm{d}m_b &= \mathrm{d}m_{a,b} + \mathrm{d}m_{f,b} - Y_b \ \mathrm{d}m_{bb} \end{aligned} \tag{3.12}$$

where $\mathrm{d}m_{a,b}$ and $\mathrm{d}m_{f,b}$ are the masses of air and fuel burned at stoichiometric conditions:

$$F_s = \frac{\mathrm{d}m_{f,b}}{\mathrm{d}m_{a,b}} \tag{3.13}$$

It is desirable to express the mass variations in terms of the stoichiometric burned mass, which is achieved by replacing Equation (3.13) in the last term of Equation (3.12):

$$\begin{aligned} \mathrm{d}m_b &= \mathrm{d}m_{a,b} + F_s \ \mathrm{d}m_{a,b} - Y_b \ \mathrm{d}m_{bb} \\ &= (F_s + 1) \ \mathrm{d}m_{a,b} - Y_b \ \mathrm{d}m_{bb} \end{aligned} \tag{3.14}$$

and solving Equation (3.14) for $\mathrm{d}m_{a,b}$:

$$\mathrm{d}m_{a,b} = \frac{1}{F_s + 1}(\mathrm{d}m_b + Y_b \ \mathrm{d}m_{bb}) \tag{3.15}$$

Then, replacing Equation (3.13) into (3.15), $\mathrm{d}m_{f,b}$ is expressed as:

$$\mathrm{d}m_{f,b} = \frac{F_s}{F_s + 1}(\mathrm{d}m_b + Y_b \ \mathrm{d}m_{bb}) \tag{3.16}$$

By combining Equations (3.12), (3.15), and (3.16), $\mathrm{d}m_a$ and $\mathrm{d}m_{f,g}$ can be expressed in terms of the stoichiometric burned mass as follows:

$$\mathrm{d}m_a = -\frac{1}{F_s+1}\ \mathrm{d}m_b - \left(\frac{Y_b}{F_s+1} + Y_a\right)\ \mathrm{d}m_{bb} \tag{3.17}$$

$$\mathrm{d}m_{f,g} = \mathrm{d}m_{f,ev} - \frac{F_s}{F_s+1}\ \mathrm{d}m_b - \left(\frac{F_s\ Y_b}{F_s+1} + Y_{f,g}\right)\ \mathrm{d}m_{bb} \tag{3.18}$$

Now, replacing Equations (3.17) and (3.18) in (3.10), and combining with Equation (3.11), the following expression for $\mathrm{d}U_c$ is obtained:

$$\begin{aligned}
\mathrm{d}U_c = \ & m_c\ c_{v,c}\ \mathrm{d}T + u_a\ \left[\frac{-1}{F_s+1}\ \mathrm{d}m_b - \left(\frac{Y_b}{F_s+1} + Y_a\right)\ \mathrm{d}m_{bb}\right] + \\
& + u_{f,g}\ \left[\mathrm{d}m_{f,ev} - \frac{F_s}{F_s+1}\ \mathrm{d}m_b - \left(\frac{F_s\ Y_b}{F_s+1} + Y_{f,g}\right)\ \mathrm{d}m_{bb}\right] + \\
& + u_b\ \mathrm{d}m_b \\
\\
= \ & m_c\ c_{v,c}\ \mathrm{d}T + u_a\ \left[-\frac{1}{F_s+1}\ (\mathrm{d}m_b + Y_b\ \mathrm{d}m_{bb}) - Y_a\ \mathrm{d}m_{bb}\right] + \\
& + u_{f,g}\ \left[\mathrm{d}m_{f,ev} - \frac{F_s}{F_s+1}\ (\mathrm{d}m_b + Y_b\ \mathrm{d}m_{bb}) - Y_{f,g}\ \mathrm{d}m_{bb}\right] + \\
& + u_b\ [(\mathrm{d}m_b + Y_b\ \mathrm{d}m_{bb}) - Y_b\ \mathrm{d}m_{bb}] \\
\\
= \ & m_c\ c_{v,c}\ \mathrm{d}T + \left[u_b - \frac{u_a + u_{f,g}\ F_s}{F_s+1}\right]\ (\mathrm{d}m_b + Y_b\ \mathrm{d}m_{bb}) - \\
& - u_a\ Y_a\ \mathrm{d}m_{bb} - u_{f,g}\ Y_{f,g}\ \mathrm{d}m_{bb} - u_b\ Y_b\ \mathrm{d}m_{bb} + u_{f,g}\ \mathrm{d}m_{f,ev}
\end{aligned}$$

thus finally obtaining:

$$\begin{aligned}
\mathrm{d}U_c = \ & m_c\ c_{v,c}\ \mathrm{d}T + \left[u_b - \frac{u_a + u_{f,g}\ F_s}{F_s+1}\right]\ (\mathrm{d}m_b + Y_b\ \mathrm{d}m_{bb}) - \\
& - u_c\ \mathrm{d}m_{bb} + u_{f,g}\ \mathrm{d}m_{f,ev}
\end{aligned} \tag{3.19}$$

By replacing Equation (3.19) in (3.9) and rearranging, the following expression is obtained:

$$\begin{aligned}
&\left[u_b - \frac{u_a + u_{f,g}\ F_s}{F_s + 1}\right]\ (\mathrm{d}m_b + Y_b\ \mathrm{d}m_{bb}) = \\
&= -m_c\ c_{v,c}\ \mathrm{d}T - \mathrm{d}Q - p\ \mathrm{d}V + (h_{f,inj} - u_{f,g})\ \ \mathrm{d}m_{f,ev} - (h_c - u_c)\,\mathrm{d}m_{bb} \\
&= -m_c\ c_{v,c}\ \mathrm{d}T - \mathrm{d}Q - p\ \mathrm{d}V + (h_{f,inj} - u_{f,g})\ \ \mathrm{d}m_{f,ev} - R\ T\ \mathrm{d}m_{bb} \qquad (3.20)
\end{aligned}$$

where the first term is the heat released due to the fuel combustion −dHR. The negative sign before dHR is used for consistency with the sign criterion used for the heat transfer to the walls: positive means that heat is lost by the charge and negative that heat is supplied to the charge. In this sense, dHR is positive and should be interpreted as the heat released to the gas as a result of combustion. If the negative sign was not included, dHR would be the reaction energy (which would be negative since the internal energy of the combustion products is lower than that of the reactants). With this criterion, Equation (3.20) can be written as:

$$\mathrm{dHR} = m_c\ c_{v,c}\ \mathrm{d}T + \mathrm{d}Q + p\ \mathrm{d}V - (h_{f,inj} - u_{f,g})\ \ \mathrm{d}m_{f,ev} + R\ T\ \mathrm{d}m_{bb} \quad (3.21)$$

In Equation (3.21) all the involved phenomena can be easily identified: in the left-hand side dHR is the heat released by combustion in a calculation step[7], whereas the terms in the right-hand side are, from left to right, the variation of the sensible internal energy of the gas, the heat transfer to the walls, the work done by the gas, the energy required for fuel injection, evaporation and heating (details of its determination can be found in [2]), and finally, the flow work associated with the blow-by leakage.

To complete the description of the energy balance, it must be remarked that even though all terms in Equation (3.21) depend on different variables, these variables depend only on pressure and temperature. Therefore, this equation has two unknown variables, being necessary an additional one. According to the ideal gas behaviour hypothesis, the equation of state is used to close the system of equations:

$$p\ V = m\ R\ T \qquad (3.22)$$

[7]The RoHR can be obtained directly by dividing dHR by the angle step, RoHR = dHR/dα.

Equation (3.21) and (3.22) can be explicitly solved to obtain dHR if p is available (CALMEC), or can be iteratively solved to compute p and T if dHR is known (SiCiclo) depending on whether the diagnosis or predictive path is taken (see Figure 3.1). The system of equations is solved for each calculation step from IVC to EVO, thus obtaining the main results (dHR or p) along with other key results used in this work (e.g. detailed heat flux to the combustion chamber walls and instantaneous mass and composition).

Once the core of the thermodynamic model has been thoroughly explained, the calculation of the terms in Equation (3.21) can be done by considering the mass balance presented in the previous section.

3.3.5 Sub-models description

The determination of some terms of the first law (Equation (3.21)) requires the use of the following specific models:

1. **Heat transfer models**. A properly HT determination is key if accurate predictions of engine heat rejection are required. Moreover, an accurate in-cylinder HT model is necessary to obtain the RoHR, and in the case of the thermodynamic predictive models, it is necessary to accurately determine indicated parameters and thermodynamic state of the charge [14, 20].

2. **Injection rate model**. Considering the injected fuel mass is important for both the mass and the energy balances. Payri et al. [14] found that the errors in mass and composition lead to poor temperature and gas properties estimation. These errors, along with the effect of the fuel energy term in Equation (3.21), lead to energy balance uncertainties that can reach values about 7% in the case of rich fuel/air equivalence ratio, therefore the fuel mass injection must be considered.

3. **Blow-by model**. In normal operating conditions, the blow-by mass flow is not important and it is not usually measured. However, in small DI Diesel engines at low engine speeds, blow-by mass rates about 4% of the trapped mass can be usually observed. Moreover, during cold start it is common to have more than 20% [21, 22]. On the other hand, the experimental blow-by mass flow measurement is a good indicator of the piston rings and lubricant integrity, and it is useful for piston rings

friction modelling [23]. For these reasons, considering the instantaneous blow-by leakage in the mass and energy balances is recommendable.

4. **Mechanical deformation model**. As stated in Section 3.3.1 (hypothesis 8), it is assumed that the chamber volume is affected by deformations due to pressure and inertia. Deformations of the engine mechanism are not usually accounted in simple thermodynamic models [14]; however, they should be considered to improve the volume calculation, specially for Diesel engines where pressure can reach more than 200 bar at the TDC. Estimations show that unaccounted deformations can lead to errors in the volume calculation higher than 2% at this high pressure conditions. Thus, the simple deformation model developed by Armas [1] and improved by Martín [2] is used.

In the next sections, a description of each model is presented, following the order presented in the previous list.

3.3.6 Heat transfer models

To account for the HT from gases to the combustion chamber walls, two models have been used. The first is based on the well-known Woschni proposal [17, 18], in which the HT from the gases to the combustion chamber walls is determined from the engine geometry, thermodynamic properties of the gas (p and T) and some operating conditions. This model allows calculating the HT to the different chamber walls (i.e. piston, liner and cylinder head) but not the subsequent repartition to coolant and oil. Besides, a proper HT determination by means of the Woschni model requires an accurate wall temperature estimation. Therefore, to estimate the wall temperatures and the detailed HT repartition to the coolant and oil, a lumped conductance model is used.

3.3.6.1 Reference in-cylinder heat transfer model

The HT to the combustion chamber walls in motoring or skip-fire tests (or during the compression stroke and after the end of combustion) is essentially governed by convection. Though gas radiation to the walls also occurs, its weight is negligible at these conditions [24]. The radiation gains relevance during the combustion process, since the formation of soot particles at high

temperature increases the flame radiation. There is no general agreement with respect to the fraction of the radiative HT, Morel and Keribar [25] obtained values ranging from 4% to 20%, whereas Heywood [26] states that this fraction can be higher than 20%. An accurate radiative model requires the calculation of the soot formed in the spray [27]; therefore, it is usual to consider that a tuned convective model can account for convection and radiation together. This approach is followed in this work, thus a experimentally adjusted combustion term will include both of them, similarly as Woschni proposal [17, 18].

The chamber HT is determined by means of the Newton's law of cooling (Equation (3.23)), where the index i refers to the chamber wall element considered (i.e. piston, liner or cylinder head), h is the heat transfer coefficient, $A_{w,i}$ is the area of each i element and T and $T_{w,i}$ are the gas temperature and the spatially averaged wall temperature. T is estimated from the in-cylinder pressure, the ideal gas law and the instantaneous mass, while $T_{w,i}$ is calculated with the lumped conductance model described in Section 3.3.6.2.

$$Q = h \sum A_{w,i} \ (T - T_{w,i}) \tag{3.23}$$

One of the most accepted expressions for the h determination is the Woschni correlation [17, 18]. Woschni developed his model based on a dimensional analysis, where the relation between the Nusselt, Reynolds and Prandtl numbers (N_u, R_e and P_r respectively) is defined as:

$$N_u = a \ R_e^b \ P_r^c \tag{3.24}$$

being a, b and c constant values. Expressing N_u and R_e in terms of the engine geometry and gas properties, Equation (3.25) is obtained:

$$h = C \ D^{b-1} \ p^b \ T^{0.75-1.62b} \ v_g^b \tag{3.25}$$

where $C = 0.012$ and $b = 0.8$ are the constant values assumed, D is the engine bore and v_g the gas velocity determined as:

$$v_g = C_{w1} \ c_m + C_{w2} \ c_u + C_2 \ \frac{V_d \ T_{\text{IVC}}}{V_{\text{IVC}} \ p_{\text{IVC}}} (p - p_0) \tag{3.26}$$

being C_{w1}, C_{w2} and C_2 constants, c_m the mean piston speed, c_u the tangential speed generated by the swirl vortex, V_d the displaced volume, T_{IVC}, V_{IVC}, p_{IVC}

the temperature, volume and pressure at IVC, p the instantaneous in-cylinder pressure and p_0 the motoring pressure obtained by assuming a polytropic evolution[8].

In the original Woschni equation, c_u is constant. However, the reference model used in this work takes into account the instantaneous variation of c_u due to the swirl acceleration. The vortex is assumed to be symmetrical between compression and expansion (i.e. between TDC), which is not strictly true since some energy is dissipated by friction between the vortex and the walls. However, it has been checked that the behaviour of the swirl is sufficiently well described by this assumption [28]. Thus, c_u is modelled by means of the trigonometric function $x(\alpha)$ that reproduces the vortex acceleration during the upward/downward piston movement as:

$$c_u(\alpha) = x(\alpha)\ c_{u,max} \tag{3.27}$$

where $x(\alpha)$ is defined as:

$$x(\alpha) = r_{\text{MSN}} + \frac{1}{\left[\cosh\left(\frac{\alpha}{100}\right)\right]^{40} + \frac{r_{\text{MSN}}}{1-r_{\text{MSN}}}} \tag{3.28}$$

being r_{MSN} the ratio between the Mean Swirl Number (MSN) at the IVC (experimentally obtained) and at the TDC (SN_{TDC}):

$$r_{\text{MSN}} = \frac{\text{MSN}}{SN_{\text{TDC}}} = \left(\frac{D_{bowl}}{D}\right)^2 \frac{1}{K_{\text{MSN}}} \tag{3.29}$$

and $c_{u,max}$ the maximum tangential speed:

$$c_{u,max} = K_{\text{MSN}}\ \text{MSN}\ \left(\frac{D}{D_{bowl}}\right)^2\ \omega_{en}\ \frac{D_{bowl}}{2} \tag{3.30}$$

which is expressed in terms of the bowl diameter (D_{bowl}), the engine angular speed (ω_{en}), the MSN and the fraction of angular moment which is not dissipated by friction during compression (K_{MSN}), this last being empirically obtained as [2]:

$$K_{\text{MSN}} = e^{-0.200979\ \text{MSN}^{0.4312}} \tag{3.31}$$

[8]Note that in motoring conditions $p \equiv p_0$.

3.3.6.2 Lumped conductance model

The calculation of the walls temperature and the HT repartition to the coolant and oil is performed by means of a conductance model developed in previous works [23, 29, 30]. The node definition was performed by dividing the engine complex geometries into smaller parts, whence the nodes characteristics were calculated: contact areas and distances between nodes centres. These, along with the thermal properties of the material, allow calculating the thermal resistor network. The size of each node ensures that Biot number of each element is lower than 0.1, thus each of them can be considered isotherm [31]. The following discretization, with a total amount of 105 metallic nodes was used:

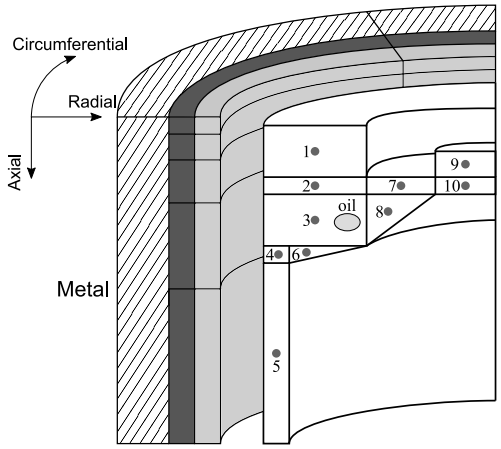

Figure 3.8. *Piston and liner simplified geometry.*

- The liner is divided into 5 axial, 2 radial, and 6 circumferential levels as depicted in Figure 3.8, so that the cylinder liner was represented by 60 nodes .
- The piston is divided into 10 nodes as shown in Figure 3.8 (axisymmetric behaviour was assumed). Nodes 1, 7 and 9 are in contact with in-cylinder gases, node 3 includes the piston rings (a conductive/convective conductance between piston and liner) and the oil gallery. The size of each node was set taking into account the real geometry of the piston.
- The cylinder head is divided into 35 nodes (see Figure 3.9): 14 nodes in contact with in-cylinder gases, including the 4 valve heads and the

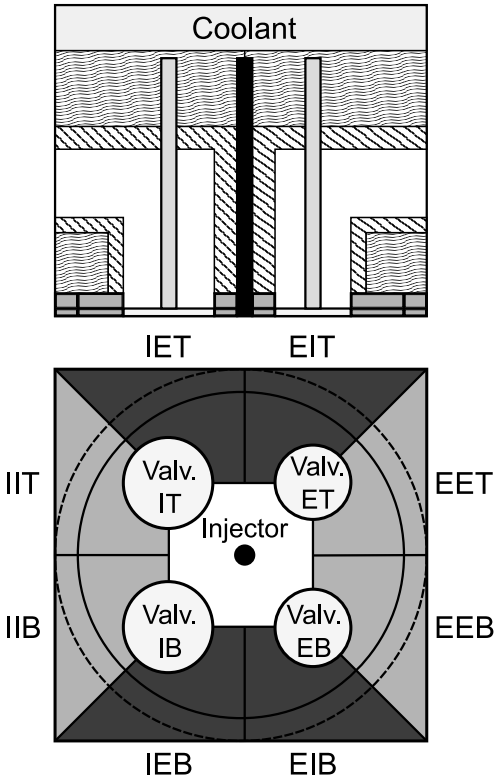

Figure 3.9. *Cylinder head, valves and ports simplified geometry.*

injector tip, 10 nodes just above the previous ones, 2 for the ports, 2 at the valves stems, 1 for the rest of the injector and 2 for the rest of the cylinder head material. In the bottom part of Figure 3.9, the nodes are identified taking into account their positions at intake (I), exhaust (E), top (T) or bottom (B).

The boundary conditions are represented by 6 convective nodes: in-cylinder gases, gas at the intake and exhaust ports, coolant at liner, coolant at the cylinder head, and lubricating oil. They are characterized by their average temperatures and film coefficients [29]. Once the thermal model is defined, a stationary energy balance is performed at each node, considering the corresponding conductive and convective HT flows. Equation (3.32) represents the energy balance in the node i, being j the adjacent metallic node, f a fluid node (gas or liquid) and K the conductance. The term at the left of Equation

(3.32) stands for the conductive HT between adjacent metallic nodes, whilst the term in the middle represents the convective HT with the fluids.

$$\sum_i K_{ij}(T_j - T_i) + \sum_f K_{fi}(T_f - T_i) = 0 \tag{3.32}$$

By applying Equation (3.32) to each node and arranging the set of equations into a matrix, the Equation (3.33) is obtained.

$$\begin{bmatrix} I_{conv} & 0 & 0 & 0 & 0 \\ 0 & I_{g-lin} & 0 & 0 & 0 \\ K_{conv-lin} & K_{g-lin} & K_{lin-lin} & K_{lin-pis} & 0 \\ K_{conv-pis} & 0 & K_{pis-lin} & K_{pis-pis} & 0 \\ K_{conv-ch} & 0 & 0 & 0 & K_{ch-ch} \end{bmatrix} \cdot \begin{bmatrix} T_{conv} \\ T_{g-lin} \\ T_{lin} \\ T_{pis} \\ T_{ch} \end{bmatrix} = \begin{bmatrix} T^*_{conv} \\ T^*_{g-lin} \\ 0 \\ 0 \\ 0 \end{bmatrix} \tag{3.33}$$

where I_{conv} and I_{g-lin} are identity sub-matrices corresponding to the boundary conditions in convective nodes (this part of the matrix is added for convenience, to have an invertible square matrix). $K_{conv-lin}$, $K_{conv-pis}$ and $K_{conv-ch}$ represent the convective conductances sub-matrix at liner, piston and cylinder head respectively. K_{g-lin} represents the convective conductance sub-matrix accounting for the HT between in-cylinder gas and liner nodes (with variable heat exchange area due to the piston movement). $K_{lin-lin}$, $K_{pis-pis}$ and K_{ch-ch} are the conductive sub-matrices between metallic adjacent nodes of liner, piston and cylinder head. $K_{pis-lin}$ and $K_{lin-pis}$ are the conductance sub-matrices between piston and liner nodes (in contact due to the rings).

T^*_{conv} is the boundary conditions temperature vector (T_{oil}, T_{cool}, mean gas temperature in the chamber, etc.), which is known through direct measurement or calculation, T^*_{g-lin} is a vector including the apparent gas temperatures seen by liner nodes (it is calculated taking into account that they are in contact with chamber gases only during part of the cycle). T_{lin}, T_{pis} and T_{ch} are the temperature vectors to be determined, corresponding to liner, piston and cylinder head nodes respectively.

Most of the required information to complete the analysis is obtained from the convective models described and from the nodes geometry and thermal properties. However, there is an important uncertainty of the HT coefficient of liquid convective nodes, i.e. coolant and oil in contact with liner, cylinder head, piston and ring-liner contact. By using metal temperature measurements, these convective HT coefficients were adjusted to minimize the differences between experimental and modelled results [23].

3.3.7 Injection rate model

The injection rate is a key input in predictive combustion models such as that proposed by Arrègle et al. [32, 33]. In the case of diagnosis models (as CALMEC), as the pressure contains the main combustion information, the injection rate shape is not a critical information; however, taking into account that fuel injection affects the mass balance, gas composition and energy balance, considering instantaneous fuel injection is recommendable to get accurate results.

The injection rate cannot be directly measured in a running engine but can be experimentally obtained by means of an injection rate meter. However, it is not always available, and hence some alternative information sources have to be used. Depending on the injector and the test bench, different signals can be used to get information of the injection rate in a running engine, i.e. the injection setting provided by the ECU, the injection command, and in some cases the needle lift signal.

Taking into account that the needle lift measurement requires a special electro-magnetic systems in solenoid injectors[9], it is not a suitable solution in most cases. Regarding the other two information sources (injection command or ECU injection setting), both of them provide accurate information about the Start of Energizing (SoE), which can be used to estimate the SoI through determination of the time delay between the electric command and the effective injection process. Thus, when no experimental injection rate is available, injection settings and fuel mass injected at each injection event are used by CALMEC to simulate the injection rate.

In Figure 3.10 the delay between the SoE and SoI (τ_{SoI}) as well as the Energizing Time (ET) are presented. It is assumed that τ_{SoI} depend on the injector type and the rail pressure (p_{rail}). Following these assumptions, Martín

[9] It cannot be measured in piezoelectric injectors.

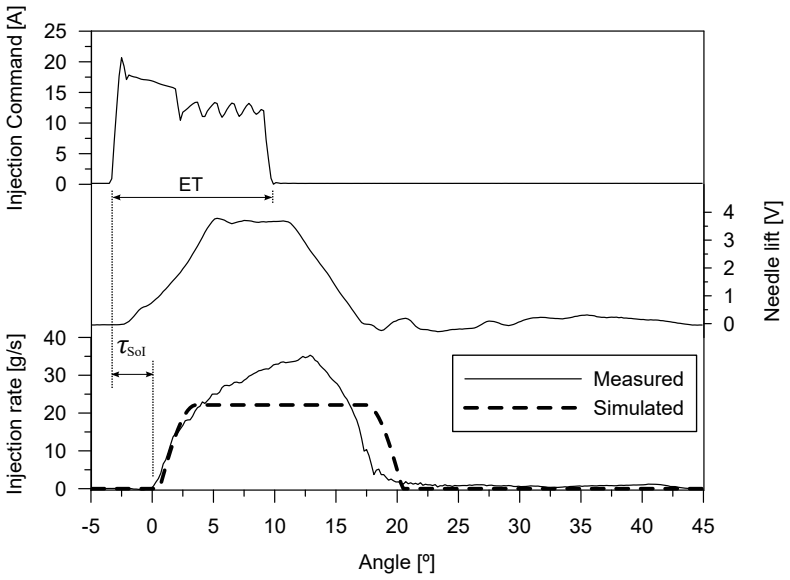

Figure 3.10. *Simulation of the injection rate.*

propose the Equation (3.34) for its determination in solenoid and piezoelectric injectors respectively.

$$\tau_{\mathrm{SoI}} = \begin{cases} 0.383 - 5.450 \times 10^{-5}\ p_{rail} & \text{if solenoid injector} \\ 0.228 + 3.162 \times 10^{-5}\ p_{rail} & \text{if piezoelectric injector} \end{cases} \tag{3.34}$$

with p_{rail} in [bar] and τ_{SoI} in $[\mu s]$.

Once τ_{SoI} is determined, the injection rate shape is assumed to be as presented in Figure 3.11, where the parameters A, B and C are determined as:

$$A = A_0 + A_1\ p_{rail} \tag{3.35}$$

$$B = B_1\ \sqrt{p_{rail} - 80} \tag{3.36}$$

$$C = C_0 + C_1\ p_{rail} \tag{3.37}$$

These values should be adjusted for the specific injection system used. However, as the information of the injection rate is not usually available,

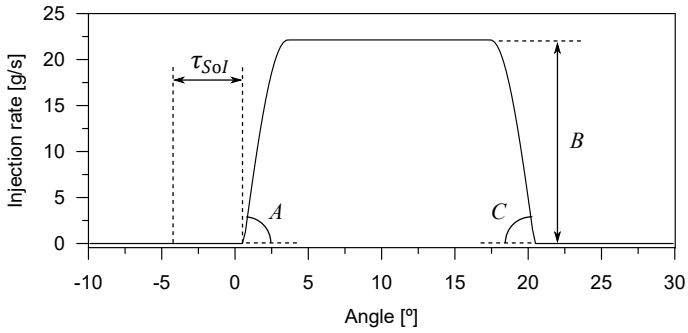

Figure 3.11. *Injection rate model shape.*

Equations (3.35) to (3.37) were adjusted for a reference engine (**Engine A**), and A, B and C can be scaled as a function of the engine size. In Table 3.6, the adjusted parameters for the reference engine are shown.

A_0	A_1	B_1	C_0	C_1
4523.3	55.161	0.61	-4523.3	-55.161

Table 3.6. *Injection rate reference values.*

To scale these parameters for a different engine, Equation (3.38) can be used:

$$k_i^{inj} = k_i^{ref}(1.26 \times 10^{-5} N_h \; D_{nozz}) \tag{3.38}$$

where k_i^{inj} is the parameter to be scaled, k_i^{ref} is the parameter reference value (see Table 3.6), N_h is the number of holes of the injector, D_{nozz} is the nozzle diameter and 1.26×10^{-5} is a constant value calculated with the reference injection system.

In Figure 3.10, the comparison between the experimental and simulated injection rate is presented. As observed, the modelled injection rate follows the main trend of the injection in spite of the complex experimental rate shape.

As stated, the thermodynamic model used in this thesis is a one zone model in which only a gaseous phase is considered; therefore, the vaporization time of the fuel (τ_{vap}) has to be accounted to preserve the model coherence.

In this work, the proposal of Martín [2], based on the spray characterization works of García [34] and López [35], is employed:

$$\tau_{vap} = 0.178 \times 10^{12} \ \frac{D_{nozz}}{u_0} \ \rho_{f,0}^{0.5} \ \rho_{a,\infty}^{-0.35} \ T_{a,\infty}^{-3.28} \tag{3.39}$$

being u_0 and $\rho_{f,0}$ the injection speed and density at the injector nozzle output and $\rho_{a,\infty}$ and T_a the air density and temperature far from the nozzle respectively (i.e. ambient conditions in the chamber). More details of the evaporation model can be found in the cited works.

3.3.8 Reference blow-by model

The accurate determination of the instantaneous in-cylinder mass requires taking into account the blow-by mass. Experimentally, the mean flow rate is measured; however, it does not provides information of the instantaneous gas leakage from the combustion chamber, necessary for the mass balance in the chamber. Therefore, a simple model to estimate the instantaneous mass flow of blow-by based on the equation of the adiabatic nozzle [36] is provided:

$$\dot{m}_{bb}(\alpha) = c_{bb} \ A_{bb} \ p \ \sqrt{\frac{x}{R \ T}} \tag{3.40}$$

where

$$x = \frac{2\gamma}{(\gamma - 1)} \left[\left(\frac{p_{crank}}{p} \right)^{\frac{2}{\gamma}} - \left(\frac{p_{crank}}{p} \right)^{\frac{\gamma+1}{\gamma}} \right] \tag{3.41}$$

being $\dot{m}_{bb}(\alpha)$ the instantaneous blow-by flow at the α crank angle position, A_{bb} a reference section proposed by Hohenberg [37] ($3.5 \cdot 10^{-6} D$), p_{crank} the crankcase pressure and c_{bb} the discharge coefficient of the nozzle, which is adjusted with the experimental blow-by measurement so that the cumulative blow-by matches with the actual flow.

When the pressure ratio satisfies sonic conditions, the nozzle flow is calculated considering the critical pressure (p_{crit}) instead of the crankcase pressure.

3.3.9 Mechanical deformations model

The cylinder volume is affected by chamber deformations due to gases pressure and inertia [38]. These effects are lower in comparison with compression ratio uncertainty [39], and hence diagnosis models do not usually include specific sub-models for their estimation. However, the volume variation due to these deformations leads to errors in the *imep* and the gas temperature estimation [40]; therefore, to get accurate in-cylinder conditions and RoHR calculation, it is interesting to take them into account [2].

The instantaneous chamber volume is calculated in CALMEC as the addition of the combustion chamber volume (V_{cc}), the instantaneous displaced volume ($V_{d,inst}$) and the deformation due to pressure (ΔV_p) and inertial forces (ΔV_i), as shown in Equation (3.42).

$$V = V_{cc} + V_{d,inst} + \Delta V_p + \Delta V_i \tag{3.42}$$

where

$$V_{cc} = \frac{V_d}{\mathrm{CR} - 1} \tag{3.43}$$

being V_d the total displaced volume and CR the compression ratio.

ΔV_p and ΔV_i are obtained by means of a simple deformation model [1, 2] in which the engine mechanism is assumed to be a bar with a certain Young's modulus (E) under tensile-compressive pressure (F_p) and inertial (F_i) loads, as presented in Figure 3.12.

The instantaneous displaced volume ($V_{d,inst}$) is calculated taking into account the engine geometry, including the piston eccentricity. Assuming an elastic deformation of the bar, the deformation terms in Equation (3.42) can be expressed as follows:

$$\Delta V_p = k_{def} \; \frac{\pi D^2}{4} \; \frac{p}{E_{steel}} \; \left(\frac{D}{D_{pin}}\right)^2 \; L_0 \tag{3.44}$$

$$\Delta V_i = k_{def} \; \frac{m_{rec} \; a}{E_{steel}} \; \left(\frac{D}{D_{pin}}\right)^2 \; L_0 \tag{3.45}$$

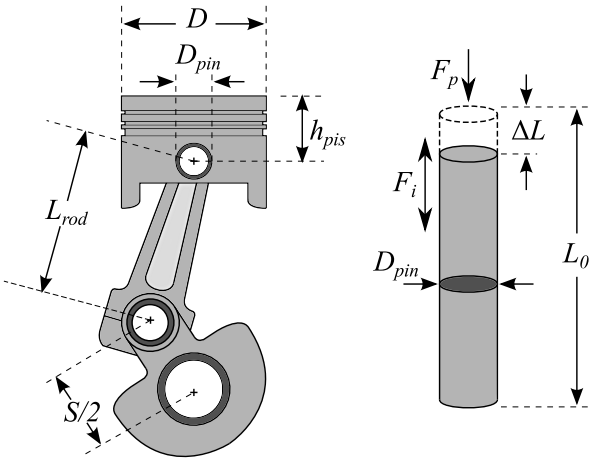

Figure 3.12. *Simplified engine mechanism.*

where $E_{steel} = 2.1 \cdot 10^{11}\ N/m^2$ is the Young's modulus of the steel, $k_{def} = E_{steel}/E$ is the deformation coefficient (that must be adjusted as described in Chapter 5.3), whose typical values range between 1 and 3 [14], D_{pin} is the piston pin diameter, m_{rec} is the mass with reciprocating motion, a is the instantaneous piston acceleration and L_0 is a characteristic length defined as:

$$L_0 = h_{pis} + L_{rod} + \frac{S}{2} \tag{3.46}$$

being h_{pis} the distance from the piston pin axis to the top surface of the piston, L_{rod} the connecting rod length and S the stroke.

In an automotive engine, the volume variation due to deformations ranges between 1.5% and 5% of the volume at TDC, depending on the operating conditions. Figure 3.13 shows some modelled results: at low speed and low load the deformations are mainly due to the in-cylinder pressure, being the inertial effect negligible; however, the inertial effect becomes higher at higher speed. The detailed analysis of the deformations effect on the RoHR calculation are presented in Chapter 5.3.1.1.

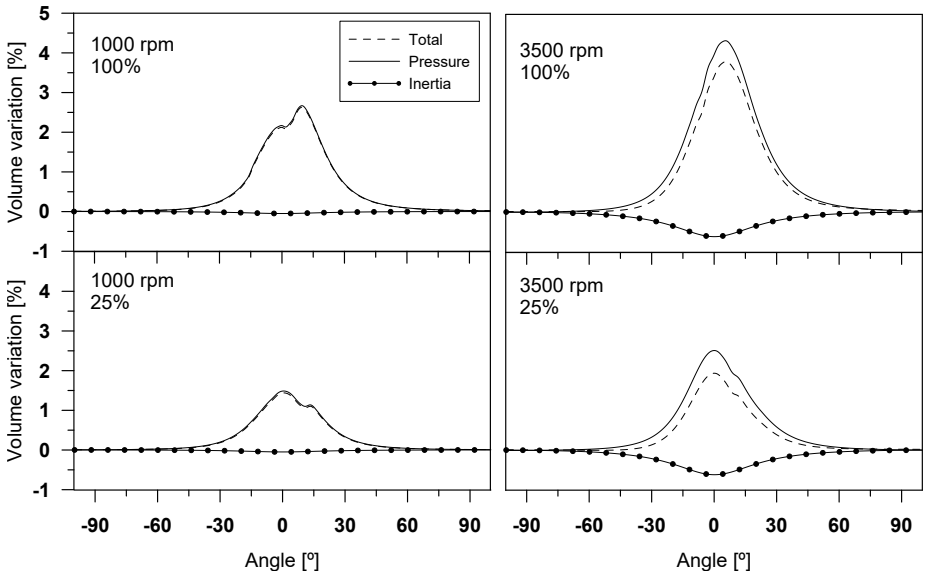

Figure 3.13. *Variation of the instantaneous volume due to deformations.*

Bibliography

[1] Armas O. *Diagnóstico experimental del proceso de combustión en motores Diesel de inyección directa*. Servicio de Publicaciones UPV, ISBN 84-7721-772-X, Valencia, 1999.

[2] Martín J. *Diagnóstico de la combustión en motores de Diesel de inyección directa*. Reverté, ISBN 978-84-291-4717-9, Barcelona, 2012.

[3] Torregrosa A.J., Olmeda P., Martín J. and Degraeuwe B. "Experiments on the influence of inlet charge and coolant temperature on performance and emissions of a DI Diesel engine". *Experimental Thermal and Fluid Science*, Vol. 30 n^o 7, pp. 633–641, 2006.

[4] Bermúdez V., Lujan J.M., Pla B. and Linares W.G. "Effects of low pressure exhaust gas recirculation on regulated and unregulated gaseous emissions during NEDC in a light-duty diesel engine". *Energy*, Vol. 36 n^o 9, pp. 5655–5665, 2011.

[5] Payri F., Luján J.M., Martín J. and Abbad A. "Digital signal processing of in-cylinder pressure for combustion diagnosis of internal combustion engines". *Mechanical Systems and Signal Processing*, Vol. 24 n^o 6, pp. 1767–1784, 2010.

[6] Tichý J. and Gautschi G. *Piezoelektrische Meßtechnik*. Springer, ISBN 978-3-642-52202-4, Berlin, 1980.

[7] Tribotte P., Ravet F., Dugue V., Obernesser P., Quechon N., Benajes J., Novella R. and De Lima D. "Two Strokes Diesel Engine - Promising Solution to Reduce CO2 Emissions". *Procedia - Social and Behavioral Sciences*, Vol. 48, pp. 2295–2314, January 2012.

[8] Olsen D., Hutcherson G., Willson B. and Mitchell C. "Development of the tracer gas method for large bore natural gas engines: part 1 - method validation". *J. Eng. Gas Turbines Power*, Vol. 124 n^o 3, pp. 678–685, 2002.

[9] Olsen D., Hutcherson G., Willson B. and Mitchell C. "Development of the tracer gas method for large bore natural gas engines: part 2 - measurement of scavenging parameters". *J. Eng. Gas Turbines Power*, Vol. 124 n^o 3, pp. 686–694, 2002.

[10] Payri F., Galindo J., Martín J. and Arnau F.J. "A Simple Model for Predicting the Trapped Mass in a DI Diesel Engine". *SAE Techinical Paper 2007-01-0494*, 2007.

[11] Armas O., Rodríguez J., Payri F., Martín J. and Agudelo J.R. "Effect of the trapped mass and its composition on the heat transfer in the compression cycle of a reciprocating engine". *Applied Thermal Engineering*, Vol. 25 n^o 17-18, pp. 2842–2853, December 2005.

[12] Heywood J.B. and Sher E. *The Two-Stroke Cycle Engine: It's Development, Operation and Design*. Taylor and Francis, ISBN 978-1560328315, Pennsylvania, 1th edition, 1999.

[13] Tinaut F. *Contribución al estudio del proceso de combustión en motores de encendido por compresión de inyección directa*. Ph.D. Thesis, Universidad Politécnica de Valencia, 1986.

[14] Payri F., Olmeda P., Martín J. and García A. "A complete 0D thermodynamic predictive model for direct injection diesel engines". *Applied Energy*, Vol. 88 n^o 12, pp. 4632–4641, December 2011.

[15] Williams F. *Combustion Theory*. The Benjamin/Cummings Publishing Co, ISBN 978-0201407778, 1985.

[16] Lapuerta M., Ballesteros R. and Agudelo J. "Effect of the gas state equation on the thermodynamic diagnostic of diesel combustion". *Applied Thermal Engineering*, Vol. 26 n^o 14-15, pp. 1492–1499, October 2006.

[17] Woschni G. "A Universally Applicable Equation for the Instantaneous Heat Transfer Coefficient in the Internal Combustion Engine". *SAE Technical Paper 670931*, 1967.

[18] Woschni G. "Die Berechnung der Wandverluste und der thermischen Belastung der Bauteile von Dieselmotoren.". *MTZ*, Vol. 31 n^o 12, pp. 491–499, 1970.

[19] Lapuerta M., Armas O. and Hernandez J.J. "Diagnosis of DI Diesel combustion from in-cylinder pressure signal by estimation of mean thermodynamic properties of the gas". *Applied Thermal Engineering*, Vol. c, pp. 513–529, 1999.

[20] Rakopoulos C.D., Kosmadakis G.M. and Pariotis E.G. "Critical evaluation of current heat transfer models used in CFD in-cylinder engine simulations and establishment of a comprehensive wall-function formulation". *Applied Energy*, Vol. 87 n^o 5, pp. 1612–1630, May 2010.

[21] Payri F., Broatch A., Serrano J.R., Rodríguez L.F. and Esmorís A. "Study of the Potential of Intake Air Heating in Automotive DI Diesel Engines". *SAE Techinical Paper 2006-01-1233*, 2006.

[22] Rakopoulos C.D., Kosmadakis G.M., Dimaratos A.M. and Pariotis E.G. "Investigating the effect of crevice flow on internal combustion engines using a new simple crevice model implemented in a CFD code". *Applied Energy*, Vol. 88 n^o 1, pp. 111–126, 2011.

[23] Payri F., Olmeda P., Martín J. and Carreño R. "A New Tool to Perform Global Energy Balances in DI Diesel Engines". *SAE Int. J. Engines*, Vol. 7 n^o 1, pp. 43–59, 2014.

[24] Annand W.J.D. "Heat transfer in the cylinders of reciprocating internal combustion engines". *Proc. Inst. Mech. Engrs.*, Vol. 177, pp. 973–990, 1963.

[25] Morel T. and Keribar R. "Heat radiation in DI Diesel engines". *SAE Technical Paper 860445*, 1986.

[26] Heywood J.B. *Internal Combustion Engines Fundamentals*. McGraw-Hill, ISBN 978-0-07-028637-5, New York, 1988.

[27] López J.J., García-Oliver J.M., Martín J., Chemisky J.P. and Bouet A. "A Soot Radiation Model for Diesel Sprays". *SAE Techinical Paper 2012-01-1069*, 2012.

[28] Payri F., Margot X., Gil A. and Martín J. "Computational Study of Heat Transfer to the Walls of a DI Diesel Engine". *SAE Technical paper 2005-01-0210*, April 2005.

[29] Torregrosa A.J., Olmeda P., Degraeuwe B. and Reyes M. "A concise wall temperature model for DI Diesel engines". *Applied Thermal Engineering*, Vol. 26 n^o 11-12, pp. 1320–1327, August 2006.

[30] Torregrosa A.J., Broatch A., Olmeda P. and Martín J. "A contribution to film coefficient estimation in piston cooling galleries". *Experimental Thermal and Fluid Science*, Vol. 34 n^o 2, pp. 142–151, February 2010.

[31] Degraeuwe B. *Contribution to the thermal management of DI Diesel engines*. Ph.D. Thesis, Universidad Politécnica de Valencia, 2007.

[32] Arrègle J., López J.J., García J.M. and Fenollosa C. "Development of a zero-dimensional Diesel combustion model Part 2: Analysis of the transient initial and final diffusion combustion phases". *Applied Thermal Engineering*, Vol. 23 n^o 11, pp. 1319–1331, August 2003.

[33] Arrègle J., López J.J., García J.M. and Fenollosa C. "Development of a zero-dimensional Diesel combustion model. Part 1: Analysis of the quasi-steady diffusion combustion phase". *Applied Thermal Engineering*, Vol. 23 n^o 11, pp. 1301–1317, August 2003.

[34] García J.M. *Aportaciones al estudio del proceso de combustión turbulenta de chorros en motores Diesel de inyección directa*. Reverté, ISBN 978-84-291-4709-4, Barcelona, 2005.

[35] López J.J. *Estudio teórico-experimental del chorro Diesel no evaporativo y de su interacción con el movimiento del aire*. Reverté, ISBN 978-84-291-4703-2, Barcelona, 2003.

[36] Aghdam E.A. and Kabir M.M. "Validation of a blowby model using experimental results in motoring condition with the change of compression ratio and engine speed". *Experimental Thermal and Fluid Science*, Vol. 34 n^o 2, pp. 197–209, February 2010.

[37] Hohenberg G. "Definition und Eigenschaften des thermodynamischen Verlustwinkels von Kolbenmaschinen". *Automobil-Industrie*, Vol. 4, pp. 15–21, 1976.

[38] Aronsson U., Solaka H., Chartier C., Andersson O. and Johansson B. "Impact of Mechanical Deformation Due to Pressure, Mass, and Thermal Forces on the In-Cylinder Volume Trace in Optical Engines of Bowditch Design". *SAE Technical Paper 2011-26-0082*, 2011.

[39] Benajes J., Olmeda P., Martín J. and Carreño R. "A new methodology for uncertainties characterization in combustion diagnosis and thermodynamic modelling". *Applied Thermal Engineering*, Vol. 71, pp. 389–399, 2014.

[40] Payri F., Molina S., Martín J. and Armas O. "Influence of measurement errors and estimated parameters on combustion diagnosis". *Applied Thermal Engineering*, Vol. 26 n^o 2-3, pp. 226–236, February 2006.

Chapter 4

Methodology to analyse the Global Energy Balance (GEB)

Contents

4.1 Introduction

As discussed in Chapter 2, the awareness towards the protection of the environment and the preservation of energetic resources, has motivated the development of more clean and efficient RICEs. To comply with the emissions normative, the use of aftertreatment systems has become a common solution, thus giving room to in-cylinder process optimization aimed at the engine efficiency enhancement. In this sense, the development of new engine technologies requires a comprehensive understanding of the engine thermal processes. Thus, performing and analysing the thermal balance are essential steps in the global engine optimization.

As shown in Chapter 2, several possibilities to perform the engine thermal balance can be found in the literature. The methodologies found have in common two main aspects:

- *The simplified definition of the thermal balance*, since most definitions only accounts for the main terms (brake efficiency, heat rejection and exhaust losses).
- *The information sources to determine the energy terms are either, experimental or modelled.* Thus, there is a lack of methodologies that combine experimental and modelling analysis of the thermal balance.

In order to understand the complex thermodynamic processes occurring during the engine operation, the use of experimental and/or simulated information sources allows different approaches to analyse the engine energy usage. Therefore, one of the objectives of this work is to **propose a general methodology** that allows facing the thermal balance from the widest possible point of view, thus considering all the essential energy terms and engine sub-systems. Progressively, the larger energy terms are split into smaller ones, so that going deeper in the understanding of the input fuel energy degradation

from the chemical energy released during combustion, until the obtaining of useful work at the engine axis. For this purpose, the combination of experimental and theoretical tools is a key task.

As a result of this experimental and modelling work, a large number of energy terms conforming a comprehensive database is obtained, being necessary to develop a smart and consistent schema to handle all the energy terms. The proposed methodology is named in this work **Global Energy Balance** (GEB), and it is described in detail in this chapter. According to it, the energy terms are grouped in two different but comparable definitions of the GEB as detailed in the next sections:

- **External Global Energy Balance (EGEB)**: in this definition, the engine is considered as a black box exchanging energy with the surroundings. This system takes into account the flows going in and out of the engine, which are mostly experimentally determined.
- **Internal Global Energy Balance (IGEB)**: it includes the engine internal interactions and sub-processes. It allows composing a detailed distribution of the energy split, whose energy terms cannot be easily measured; thus, they are obtained mostly by means of modelling approaches.

Although two different points of view are defined, it is important to bear in mind that they are closely related, since the energy terms considered in the EGEB somehow *lead to* or *are due to* different terms of the IGEB. Thus, it is necessary to clearly identify the relationships between several internal/internal and internal/external terms.

As will be explained in Chapter 5, this approximation is useful for two purposes, on the one hand, the assessment of the GEB reliability through the comparison of equivalent experimental and modelled terms (e.g. HT to coolant and oil), and on the other hand, the development and adjustment of several sub-models.

This chapter starts describing how to obtain each energy term involved in the GEB, followed by the definition of some equivalent terms between the internal and external systems, and to close the chapter, an experimental uncertainty analysis is carried out in order to clarify the limitation of the experimental approach, thus assessing the methodology strengths and weaknesses.

4.2 Global energy balance system definition

The engine sub-systems can vary depending on the engine type and the specific application. In Figure 4.1, a general scheme of a turbocharged automotive engine is presented. Although this work is mainly focused on CI engines, the scheme with small modifications can be also applied to other engines. In conventional automotive engines, the lubrication, EGR and air cooling systems are connected with the main cooling circuit, thus the heat rejection from oil, EGR and air is evacuated to the coolant[1]. However, the lubrication systems (engine and turbocharger) are considered independently in this work[2], as shown in Figure 4.1.

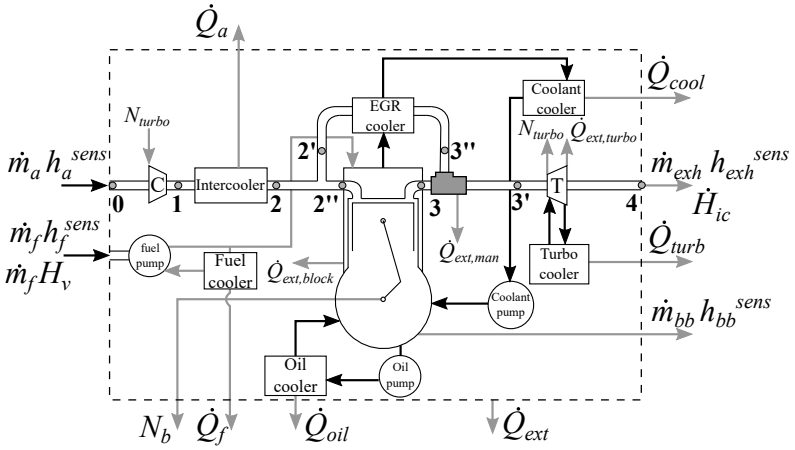

Figure 4.1. *Engine and sub-systems scheme.*

As shown, the energy flows entering the engine[3] are the sensible enthalpy of air ($\dot{m}_a h_a^{sens}$) and fuel ($\dot{m}_f h_f^{sens}$), and the chemical energy of the fuel heating value ($\dot{m}_f H_v$). The outlet energy flows are the brake power (N_b), the heat flow to the coolant ($\dot{Q}_{cool}$), the sensible energy of the exhaust gases ($\dot{m}_{exh} h_{exh}^{sens}$), the heat flow rejected to the oil exchanger ($\dot{Q}_{oil}$), the HT to the turbo oil ($\dot{Q}_{turbo}$), the heat flow in the intercooler ($\dot{Q}_a$), the small term corresponding to the heating of the returning fuel ($\dot{Q}_f$), the convective and radiative HT to the ambient from the engine surface ($\dot{Q}_{ext,block}$), the exhaust manifold ($\dot{Q}_{ext,man}$) and turbocharger case ($\dot{Q}_{ext,turbo}$), the enthalpy flow due to blow-by losses

[1] Except in air-air intercoolers.
[2] This was justified in Chapter 3.2.
[3] A more general energy balance approach is included in Appendix 4.A.

($\dot{m}_{bb}h_{bb}^{sens}$), and finally, the energy losses due to incomplete combustion ($\dot{H}_{ic}$). Usually experimental test benches have an external electrical supply; however, its power consumption use to be negligible and hence it is not included in this GEB definition.

Taking into account all the energy transformations that take place in a RICE, the paths followed by the different energy terms are presented in the Figure 4.2. During the engine operation, the input energy undergoes several transformations until becoming mechanical work and heat rejection to the surroundings.

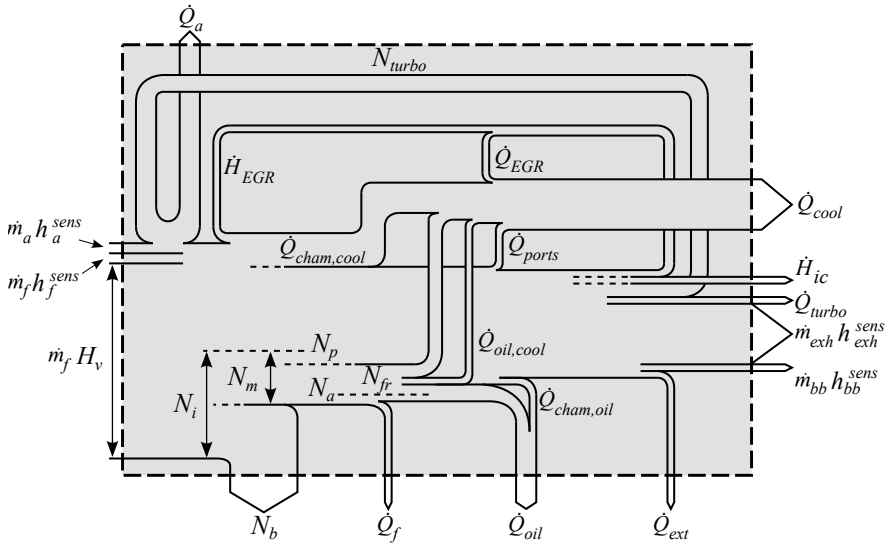

Figure 4.2. *Energy interactions occurring in an engine.*

Starting from the fuel energy, part of it becomes mechanical power released to the piston throughout the high pressure cycle (gross indicated work), other part is rejected to the chamber walls as heat transfer, and the rest becomes enthalpy of the gases at the chamber outlet:

- The gross indicated work (N_i) is degraded by the pumping work (N_p), the auxiliary systems activation energy (N_a) and the friction (N_{fr}), becoming finally in the brake power (N_b).
- The HT to the chamber walls can be split, depending on the final destination, into HT from chamber to the coolant ($\dot{Q}_{cham,cool}$) and oil

($\dot{Q}_{cham,oil}$). Heat rejection to the coolant also includes HT to ports walls ($\dot{Q}_{ports}$) and EGR cooling ($\dot{Q}_{\mathrm{EGR}}$), whilst friction and auxiliary losses are somehow dissipated as heat to both, coolant and oil. At the same time, the different operating temperatures of the coolant and oil gives place to HT between them ($\dot{Q}_{oil,cool}$).

- Regarding the enthalpy of the exhaust gases, part of the available energy at the valves outlet becomes HT (to ports, oil, coolant and ambient) and part is recirculated as EGR enthalpy ($\dot{H}_{\mathrm{EGR}}$), while the rest is available energy at the turbine intake. In turbocharged engines, part of the exhaust energy is recovered as turbocharging work (N_{turbo}) on the intake air, increasing the air induction each cycle, and hence the power output. The part of the exhaust enthalpy that does not become an enthalpy increase of the intake flow in the compressor is lost as HT to the ambient, either from the turbo casing ($\dot{Q}_{ext,turbo}$) or as exhaust enthalpy rejected to the ambient.

As shown in Figure 4.2, the engine systems will be delimited by a dashed line, which defines the external and internal GEB described in the next paragraphs. Thus, the following sections deal with the external and internal GEB points of view and how the involved energy terms are calculated and linked. For the sake of generality, the following description is based on the experimental installation of the **Engine A**, which is presented in Chapter 3.2.1, since it represents a conventional automotive engine, which include most of the current engine technologies in the market. It is important to take into account that the methodology described in this work can be extended to any other engine, paying special attention to the engine sub-systems driven by the engine and any other significant thermal interaction.

4.2.1 External global energy balance

In this analysis, the engine is assumed to be a black-box that exchanges energy with the surrounding through the brake power, heat flows and incoming and outgoing enthalpy fluxes as presented in Figure 4.3.

From a thermodynamic point of view, the energy terms presented in Figure 4.3 are coherent, but for the sake of comprehension, it is interesting to rearrange some of them to perform the detailed analysis of the energy repar-

tition. In this sense, the first law in the case of the EGEB can be expressed as:

$$\dot{m}_f H_v = N_b + \dot{Q}_{cool} + \dot{Q}_{oil} + \dot{H}_{g,ex} + \dot{Q}_a + \dot{Q}_{turbo} + \\ + \dot{Q}_f + \dot{H}_{ic} + \dot{H}_{bb} + \dot{Q}_{ext} + \dot{Q}_{unbal,ex} \quad (4.1)$$

where $\dot{H}_{g,ex}$ and $\dot{H}_{bb}$ are the net flows of sensible enthalpy of exhaust and blow-by, and $\dot{Q}_{unbal,ex}$ is the unbalance term due to experimental and modelling uncertainties.

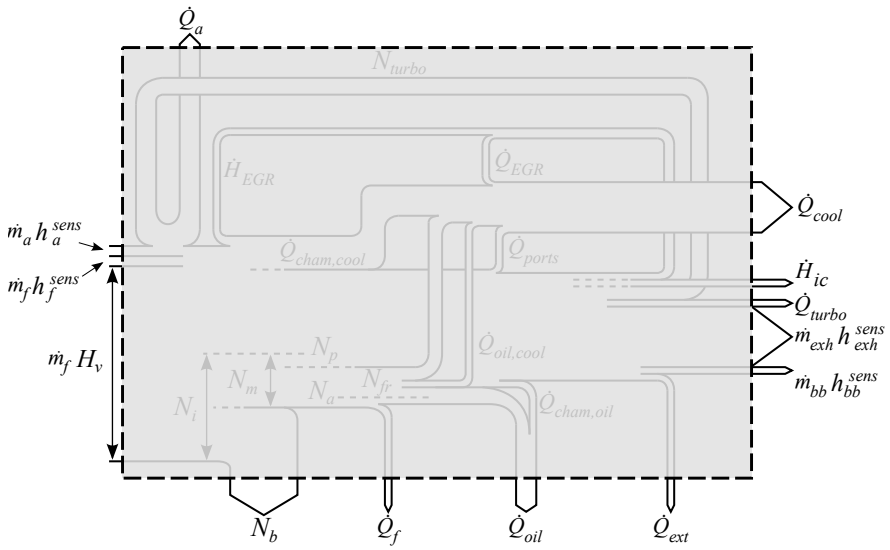

Figure 4.3. *External global energy balance system.*

In this particular approach, most of these terms are experimentally obtained. Following, a list of the calculation processes of each term is presented:

- $\dot{m}_f H_v$: it is the chemical power of the fuel, determined by measuring the fuel mass flow $\dot{m}_f$ and its heating value[4].
- $\dot{H}_{g,ex}$: as shown in Equation (4.2), it is the net flow of sensible enthalpy determined by means of a balance between the incoming and outgoing

[4]The heating values of Diesel and gasoline used in this work are 42.92 MJ/kg and 43.95 MJ/kg respectively.

enthalpy flows between compressor inlet (point 0) and turbine outlet (point 4) in Figure 4.1.

$$\dot{H}_{g,ex} = \dot{m}_{exh} h_{exh}^{sens} - \dot{m}_a^{exh} h_a^{sens} - \dot{m}_f^{exh} h_f^{sens} \tag{4.2}$$

where $\dot{m}_a^{exh}$ and $\dot{m}_f^{exh}$ are the intake air and injected fuel flow rates that finally leave the engine by the exhaust, $\dot{m}_{exh}$ is the exhaust mass flow rate, and h_a^{sens}, h_f^{sens} and h_{exh}^{sens} are the specific sensible enthalpies of air, fuel and exhaust gases, determined from the corresponding specific heats ($c_{p,a}$, $c_{p,f}$ and $c_{p,exh}$) as shown in Equation (4.3) to Equation (4.5).

$$h_a^{sens} = \int_{T_0}^{T_a} c_{p,a}\ dT \tag{4.3}$$

$$h_f^{sens} = \int_{T_0}^{T_f} c_{p,f}\ dT \tag{4.4}$$

$$h_{exh}^{sens} = \int_{T_0}^{T_{exh}} c_{p,exh}\ dT \tag{4.5}$$

where the reference temperature T_0 is 25°C, and T_a, T_f and T_{exh} are the air, fuel and exhaust gases temperatures at which the enthalpy is computed. Finally, the exhaust mass flow is calculated as:

$$\dot{m}_{exh} = \dot{m}_a + \dot{m}_f - \dot{m}_{bb} \tag{4.6}$$

being $\dot{m}_{bb}$ the blow-by flow rate.

A more detailed description of the determination of the net flow of sensible enthalpy at exhaust can be found in Appendix 4.A.

- N_b: it is the brake power that is determined by measuring the engine speed (n) and torque (M) in the dynamometer:

$$N_b = 2\pi\ n\ M \tag{4.7}$$

- $\dot{Q}_{cool}$: it is the total HT to the coolant that can be estimated from the specific heat of the coolant ($c_{p,cool}$), the coolant flow rate ($\dot{m}_{cool}$)

and the coolant flow temperature at exchanger inlet ($T_{cool,in}$) and outlet ($T_{cool,out}$), as presented in Equation (4.8):

$$\dot{Q}_{cool} = \dot{m}_{cool}\ c_{p,cool}\ (T_{cool,out} - T_{cool,in}) \tag{4.8}$$

- $\dot{Q}_{oil}$: it is the heat rejection to the oil in the engine block (excluding $\dot{Q}_{turbo}$, which is considered independently) that is determined with Equation (4.9), by measuring the water flow rate that refrigerates the oil exchanger ($\dot{m}_{w,oil}$), and the temperatures at the heat exchanger inlet ($T_{w,oil,in}$) and outlet ($T_{w,oil,out}$):

$$\dot{Q}_{oil} \cong \dot{Q}_{w,oil} = \dot{m}_{w,oil}\ c_{p,w,oil}\ (T_{w,oil,out} - T_{w,oil,in}) \tag{4.9}$$

  where $\dot{Q}_{w,oil}$ is the HT evacuated by the oil exchanger cooling water, and $c_{p,w,oil}$ is the specific heat of the water.

- $\dot{Q}_{turbo}$: it is the HT rejected from the turbocharger to the oil[5], which is obtained by using an independent conditioning system as explained in Chapter 3.2.1.2, in which the turbo oil flow rate ($\dot{m}_{oil,t}$) and the temperatures at the turbo inlet ($T_{oil,t,in}$) and outlet ($T_{oil,t,out}$) are measured:

$$\dot{Q}_{turbo} = \dot{m}_{oil,t}\ c_{p,oil,t}\ (T_{oil,t,out} - T_{oil,t,in}) \tag{4.10}$$

  were $c_{p,oil,t}$ is the specific heat of the oil in the turbocharger.

- $\dot{Q}_a$: it is the heat rejection in the intercooler. Intercoolers can be cooled either by coolant or air; in the case of the **Engine A**, the original exchanger was an air-air cooler one, but the installation was modified to include a water-air cooler system to have higher cooling capacity; therefore, $\dot{Q}_a$ can be determined by measuring the flow and temperature drop of either the coolant fluid or the air. In this case, it was determined directly from the air mass flow and its temperature variation:

$$\dot{Q}_a = \dot{m}_a\ c_{p,a}\ (T_{a,out} - T_{a,in}) \tag{4.11}$$

  where $T_{a,in}$ and $T_{a,out}$ are the temperatures at inlet and outlet of the intercooler, and $c_{p,a}$ is the specific heat of the air.

[5] In the case of water-cooled turbochargers, $\dot{Q}_{turbo}$ should include oil and coolant heat rejection.

- $\dot{Q}_f$: it is the heat loss due to the heating of the returning fuel, which is due to the fuel compression in the injection pump, and the fluid friction in the fuel pump and the injection system walls. This term is more relevant in Diesel engines, where the fuel is compressed up to 2000 bar and about 30-40% is returned to the fuel deposit. At these conditions, the returned fuel can be heated about 40-50°C in conventional Diesel injection systems[6].

  To evacuate this thermal power, the original circuit was modified to control the returning fuel temperature by means of a shell and tube heat exchanger, which allowed cooling the fuel returning line to maintain the same temperature as at the high pressure pump inlet. Then, the HT is estimated as presented in Equation (4.12) by measuring the water flow through the exchanger ($\dot{m}_{w,f}$), and the temperature at inlet ($T_{w,f,in}$) and outlet ($T_{w,f,out}$):

$$\dot{Q}_f = \dot{Q}_{w,f} = \dot{m}_{w,f}\ c_{p,w,f}\ (T_{w,f,out} - T_{w,f,in}) \tag{4.12}$$

  where $c_{p,w,f}$ is the specific heat of the water.

- $\dot{Q}_{ext}$: it is the HT to the ambient due to convection and radiation from the engine block ($\dot{Q}_{ext,block}$), manifolds ($\dot{Q}_{ext,man}$) and turbocharger case ($\dot{Q}_{ext,turbo}$)[7]. These terms are usually determined by encapsulating the engine, as done by Smith *et al.* [1], who report maximum HT values about 10-15%$\dot{m}_f H_v$ in the case of the engine body and 5-7%$\dot{m}_f H_v$ in the case of the turbocharger, both reached at low engine speed and load, where the engine and turbine power are also low [2] and the weight of the losses to the ambient is maximum [3].

  The necessity of a special experimental installation to measure $\dot{Q}_{ext}$, along with the fact that it is only important at determined operating conditions, led to the decision of not measuring it but to perform a simple estimation by assuming the following hypotheses:

  - The engine is assumed to be a box.
  - The temperature of the box external walls is the same as the coolant.
  - Natural convection between flat surfaces of the box and the ambient was assumed to estimate the convective heat transfer.

[6] These estimations were made for the injection system of **Engine A**.

[7] Note that they are not explicitly shown in Figure 4.2 because they are part of $\dot{Q}_{ext}$.

  - The box emissivity to estimate the radiative heat transfer was assumed to be 0.6.

- $\dot{H}_{bb}$: it is the net flow of blow-by sensible enthalpy, determined by measuring the blow-by flow mass ($\dot{m}_{bb}$) and assuming a blow-by mean temperature similar to the oil temperature in the crank case, in order to determine its specific enthalpy (h_{bb}^{sens}). A detailed description of the net flow of blow-by sensible enthalpy determination can be found in Appendix 4.A, where the final expression obtained is:

$$\dot{H}_{bb} = \dot{m}_{bb} h_{bb}^{exh} - \dot{m}_{a}^{bb} h_{a}^{sens} - \dot{m}_{f}^{bb} h_{f}^{sens} \tag{4.13}$$

  being $\dot{m}_{a}^{bb}$ and $\dot{m}_{f}^{bb}$ the intake air and injected fuel finally lost with the blow-by.

- $\dot{H}_{ic}$: it is the energy loss due to incomplete combustion, which is determined by considering the HC, CO and soot emissions measured at exhaust as:

$$\dot{H}_{ic} = (Y_{HC}\ H_{v,HC} + Y_{CO}\ H_{v,CO} + Y_{C}\ H_{v,C})\ \dot{m}_{exh} \tag{4.14}$$

  where Y_{HC}, Y_{CO} and Y_{C} are the mass fractions of the HC, CO and soot, and $H_{v,HC}$, $H_{v,CO}$ and $H_{v,C}$ are their heating values respectively[8].

  The mass of unburned fuel is a mixture of the sub-products formed during the combustion process; therefore, an equivalent incomplete combustion mass ($\dot{m}_{f,ic}$) can be estimated taking into account that:

$$\dot{H}_{ic} = \dot{m}_{f,ic}\ H_{v} \tag{4.15}$$

  then, by replacing and solving in Equation (4.14), $\dot{m}_{f,ic}$ is obtained as:

$$\dot{m}_{f,ic} = \frac{(Y_{HC}\ H_{v,HC} + Y_{CO}\ H_{v,CO} + Y_{C}\ H_{v,C})\ \dot{m}_{exh}}{H_{v}} \tag{4.16}$$

- $\dot{Q}_{unbal,ex}$: It is the experimental unbalance, resulting from unavoidable systematic and random experimental uncertainties. It is determined

[8] $H_{v,HC}$ has a value of 42.9 MJ/kg, $H_{v,CO}$ of 10.1 MJ/kg and $H_{v,C}$ of 32.8 MJ/kg respectively.

by calculating the difference between the rest of the terms involved in the energy balance and the total chemical fuel energy, as presented in Equation (4.17):

$$\dot{Q}_{unbal,ex} = \dot{m}_f H_v - N_b - \dot{Q}_{cool} - \dot{Q}_{oil} - \dot{Q}_a - \dot{H}_{g,ex} - \\ - \dot{Q}_{turbo} - \dot{Q}_{ext} - \dot{Q}_f - \dot{H}_{ic} - \dot{H}_{bb} \quad (4.17)$$

Although the described terms allow completing the GEB, an additional term composed of some of them will be used in the analysis. This consist on the miscellanea term ($\dot{Q}_{misc}$), defined in Equation (4.18), which includes some quantities difficult to be measured ($\dot{Q}_{ext}$), some terms with small relative weight ($\dot{Q}_{turbo}$, $\dot{Q}_f$, $\dot{H}_{bb}$ and $\dot{H}_{ic}$), and finally the experimental unbalance ($\dot{Q}_{unbal,ex}$).

$$\dot{Q}_{misc} = \dot{Q}_{ext} + \dot{Q}_{turbo} + \dot{Q}_f + \dot{H}_{ic} + \dot{H}_{bb} + \dot{Q}_{unbal,ex} \quad (4.18)$$

In the analysis presented in Chapter 6.2.2.5, it is shown that the terms composing $\dot{Q}_{misc}$ have a minor impact, where the most relevant is $\dot{Q}_{ext}$, being about the 90% of $\dot{Q}_{misc}$. Thus, in CDC, this parameter can be understood as an indicator of the HT to the ambient[9].

4.2.2 Internal global energy balance

The internal analysis of the energy balance includes all the terms inside the box delimited by the dashed line of Figures 4.1 and 4.4. Contrary to the external analysis, the IGEB is mainly based on modelling estimations and only few experimental variables are required, being the most important the in-cylinder pressure. Some of the models used to estimate the energy terms were presented in Chapter 3.3, and the improvements necessary to enhance the estimations, as well as new models, will be presented in Chapter 5.

Taking into account the internal interactions observed in Figures 4.1 and 4.4, the first law can be expressed as:

$$\dot{m}_f H_v = N_b + (N_{fr} + N_a) + \dot{Q}_{cham} + \dot{Q}_{ports} + \dot{Q}_{\mathrm{EGR}} + \\ + \dot{H}_{g,ex} + \dot{Q}_a + \dot{Q}_{turbo} + \dot{Q}_{ext,turbo} + \dot{Q}_{ext,man} + \\ + \dot{H}_{bb} + \dot{H}_{ic} + \dot{Q}_{unbal,in} \quad (4.19)$$

[9] This is not strictly true in alternative combustion modes, e.g. in RCCI operation, where the unburned fuel is an important loss and has to be carefully analysed.

where $\dot{Q}_{unbal,in}$ is the unbalance term due to experimental and modelling uncertainties and $\dot{Q}_{cham}$ is the HT to the chamber. Note that $\dot{Q}_{ext,turbo}$ and $\dot{Q}_{ext,man}$ are not explicitly shown in Figure 4.4 because they are part of $\dot{Q}_{ext}$, as explained in the previous section.

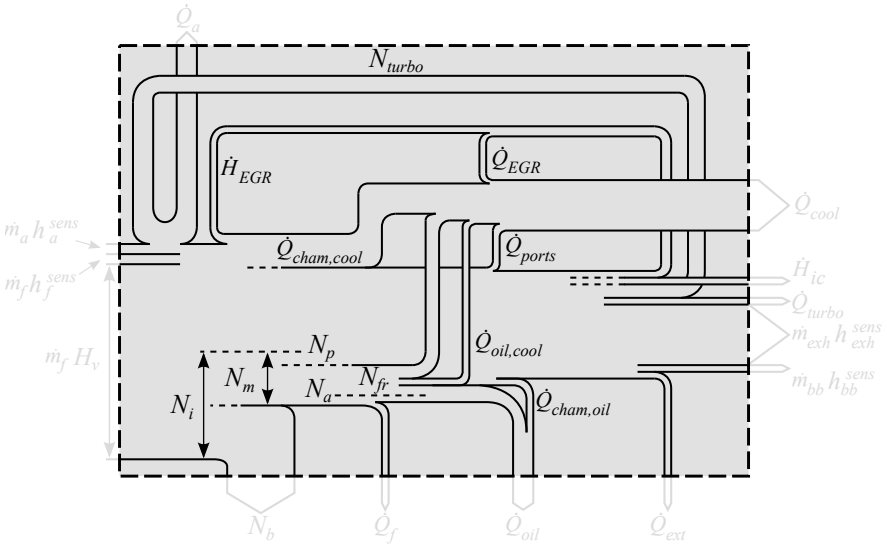

Figure 4.4. *Internal global energy balance system.*

Equation (4.19) is consistent with the scheme presented in Figure 4.2; however, it is interesting to rearrange Equation (4.19). Thus, an internal net flow of sensible enthalpy ($\dot{H}_{g,in}$) is calculated between the intake manifold, before air and EGR mixing, and exhaust manifold, after EGR extraction[10]. The detailed analysis of the net flow of sensible enthalpy from the internal and external points of views is described in Appendix 4.B, where it is obtained that:

$$\dot{H}_{g,in} = \dot{H}_{g,ex} + \dot{Q}_a + \dot{Q}_{turbo} + \dot{Q}_{ext,turbo} \tag{4.20}$$

[10]That is, between points 2 and 3' of Figure 4.1.

thus, by replacing in Equation (4.19) and considering that $\dot{Q}_{ext,man}$ has a negligible weight[11], the following definition of the IGEB is obtained:

$$\dot{m}_f H_v = N_b \; + \; (N_{fr} + N_a) \; + \; \dot{Q}_{cham} \; + \; \dot{Q}_{ports} \; + \; \dot{H}_{g,in} \; + \\ + \; \dot{Q}_{\mathrm{EGR}} \; + \dot{H}_{bb} \; + \; \dot{H}_{ic} \; + \; \dot{Q}_{unbal,in} \tag{4.21}$$

Note that some terms are not explicitly included in Equation (4.21):

- The turbo work (N_{turbo}) is used to increase the air flow enthalpy, and hence, it is not an energy flow leaving the system.
- The EGR enthalpy is recirculated from exhaust to intake, thus, it does not affect the net enthalpy balance. That means that the total EGR enthalpy deducted at exhaust is equal to the EGR enthalpy added at intake ($\dot{H}_{\mathrm{EGR}}$) plus the heat transfer rejected from the EGR cooler to the coolant ($\dot{Q}_{\mathrm{EGR}}$).
- The HT from oil to coolant ($\dot{Q}_{oil,cool}$) is an internal thermal flow, which is included in $\dot{Q}_{cham}$ and N_{fr}. A more detailed discussion of this term and why it is not included in Equation (4.21) is presented in Section 4.3.

The description and the determination process of all the terms included in the IGEB (focused on the in-cylinder processes), and their relation with EGEB terms are following explained:

- N_i and N_p: they are the indicated and pumping power respectively. Despite these terms are not explicitly considered in the IGEB, their determination and analysis is important for the understanding of some terms such as the brake power or the heat rejection.

  These terms are calculated from the $p - V$ diagram as presented in Equations (4.22) to (4.25). Thus, the gross indicated work is obtained through integration during compression and expansion strokes (between

[11] This assumption is reasonable considering that $\dot{Q}_{ext,man}$ depends on exhaust temperature and is a small part of $\dot{Q}_{ext}$, which in turn is a small part of the fuel energy and is only relevant at low load, where the exhaust temperature is low.

their corresponding BDCs), and the pumping work is obtained analogously during the intake and exhaust strokes.

$$W_i = \int_{-180}^{180} p \, dV \tag{4.22}$$

$$N_i = \frac{n \, W_i}{n_r} \tag{4.23}$$

$$W_p = \int_{180}^{-180} p \, dV \tag{4.24}$$

$$N_p = \frac{n \, W_p}{n_r} \tag{4.25}$$

where n is the engine speed and n_r is the number of crank revolutions per power stroke[12].

In Figure 4.5, a typical $p - V$ diagram is shown, where following the conventional criteria [4], the gross indicated work (delivered by the gases thanks to the combustion process) is positive while pumping work (work used for the expulsion of burned gases and induction of fresh air) is negative.

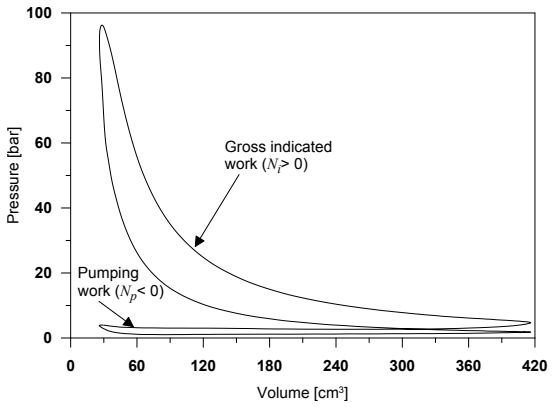

Figure 4.5. *$p - V$ diagramm.*

[12] $n_r = 1$ for 2-stroke engines and $n_r = 2$ for 4-stroke engines.

- N_{fr} and N_a: they are the friction and auxiliary losses, which are obtained together by subtracting N_b from $N_i + N_p$ as:

$$N_{fr} + N_a = N_i + N_p - N_b \tag{4.26}$$

These terms can be also split as follows:

$$N_{fr} = N_{fr,pis} \ + \ N_{fr,bear} \ + \ N_{fr,valv} \tag{4.27}$$

$$N_a = N_{cool} \ + \ N_{oil} \ + \ N_f \tag{4.28}$$

where $N_{fr,pis}$, $N_{fr,bear}$ and $N_{fr,valv}$ are the friction losses in the piston (rings and skirt), bearings and valve train, and N_{cool}, N_{oil} and N_f are the activation energy of the coolant, oil and fuel pumps respectively.

This detailed repartition of $N_{fr}+N_a$ is necessary to determine equivalent terms between EGEB and IGEB, considering that $N_{fr,pis}$ heats the liner that is cooled by the coolant, thus $N_{fr,pis}$ is mainly dissipated into $\dot{Q}_{cool}$, whilst $N_{fr,bear}$ and $N_{fr,valv}$ heat the lubricating oil, thus becoming part of $\dot{Q}_{oil}$. In the case of the auxiliary, their energy consumption is used to increase the enthalpy of each fluid, which is finally dissipated in their respective cooler. A dedicated model to determine this repartition is comprehensively described in Chapter 5.4.

- $\dot{Q}_{cham}$ and $\dot{Q}_{ports}$: they are the total HT to the chamber walls and HT to the engine ports respectively. As can be seen in Figure 4.4, $\dot{Q}_{cham}$ is split into two terms: the HT from chamber to coolant ($\dot{Q}_{cham,cool}$) and oil ($\dot{Q}_{cham,oil}$). They are determined by means of the heat transfer model presented in Chapter 3.3.6.2 (in-cylinder HT for **Engine A**) and the proposals in Chapter 5.2 for $\dot{Q}_{ports}$ and in-cylinder HT for **Engine B**. Taking into account the detailed HT to the liner ($\dot{Q}_{lin}$), cylinder head ($\dot{Q}_{ch}$) and piston ($\dot{Q}_{pis}$), and assuming that they are dissipated to coolant and oil, the following expressions can be written:

$$\dot{Q}_{cham,cool} = \dot{Q}_{lin} + \dot{Q}_{ch} \tag{4.29}$$

$$\dot{Q}_{cham,oil} = \dot{Q}_{pis} \tag{4.30}$$

- $\dot{H}_{g,in}$: it is the net flow of sensible enthalpy of the exhaust gases, determined through an enthalpy balance between points 2 and 3' in Figure

4.1, that is, between the intercooler outlet and the turbine inlet. Thus, $\dot{H}_{g,in}$ is calculated by means of Equation (4.2) but considering the temperature at the stated points.

- $\dot{Q}_{\text{EGR}}$: it is the heat lost in the EGR cooler, determined from the EGR mass flow ($\dot{m}_{\text{EGR}}$) and the temperature drop of the recirculated gas as it passes through the cooler. The enthalpy difference can be calculated as presented in Equation (4.31), where $c_{p,\text{EGR}}$ is the specific heat of the burned gases.

$$\dot{Q}_{\text{EGR}} = \dot{m}_{\text{EGR}}\ c_{p,\text{EGR}}\ (T_{\text{EGR},out} - T_{\text{EGR},in}) \tag{4.31}$$

being $T_{\text{EGR},in}$ and $T_{\text{EGR},out}$ the temperature at EGR cooler inlet and outlet and $\dot{m}_{\text{EGR}}$ obtained from the EGR rate (τ_{EGR}) as follows:

$$\dot{m}_{\text{EGR}} = \dot{m}_a \left(\frac{\tau_{\text{EGR}}}{1 - \tau_{\text{EGR}}} \right) \tag{4.32}$$

where τ_{EGR} is determined based on the CO_2 compositions measured at intake, exhaust and atmospheric conditions as:

$$\tau_{\text{EGR}} = \frac{Y_{CO_2}^{intake} - Y_{CO_2}^{atm}}{Y_{CO_2}^{exhaust} - Y_{CO_2}^{atm}} = \frac{\dot{m}_{\text{EGR}}}{\dot{m}_a + \dot{m}_{\text{EGR}}} \tag{4.33}$$

Note that $\dot{Q}_{\text{EGR}}$ was determined by means of an enthalpy balance between EGR cooler inlet and outlet ports; however, the EGR circuit passes through the engine block and exchanges heat with the coolant. Besides, in the EGR cooler the heat is finally rejected to the coolant and becomes part of $\dot{Q}_{cool}$.

- $\dot{Q}_{unbal,in}$: it is the internal unbalance term. Since most of the terms involved in the internal GEB are determined with models, this term accounts for the energy necessary to close the energy balance, as presented in Equation (4.34), thus providing quantitative information of the general modelling performance.

$$\begin{aligned} \dot{Q}_{unbal,in} = \dot{m}_f H_v\ -\ N_b\ -\ (N_{fr} + N_a)\ -\ \dot{Q}_{cham}\ -\ \dot{Q}_{ports}\ - \\ -\ \dot{H}_{g,in}\ -\ \dot{Q}_{\text{EGR}}\ -\ \dot{H}_{ic}\ -\ \dot{H}_{bb} \end{aligned} \tag{4.34}$$

4.3 Equivalence between heat rejection terms in the internal and external analysis

The transformation of the energy during the engine operation is a complex process, considering the relationship between the energy terms described. Moreover, the energy balance definition can also differ depending on the energy terms considered, the features of the experimental installation and the models used. In this work, the GEB has been defined by two different paths: one that considers the engine as a black box, whose terms are mainly experimentally determined, and the other that takes into consideration the internal energy transformations, whose terms are mainly modelled. Due to the different nature of these two points of view, it is necessary to define comparable HT terms between them. Such terms helps to improve the HT analysis because they will be used for the sub-models development, fitting and validation.

A description of some comparable and key terms is presented in this section.

4.3.1 Total heat transfer

As will be shown in Chapters 6.2.1 and 6.3.1, the comparison between internal and external heat flows is important for some sub-models calibration, in order to get reliable results from each engine. The first parameter to consider is the total heat transfer ($\dot{Q}_{tot}$), which includes all the heat rejected from the gases circulating through the engine block, including chamber and ports. In order to adjust the sub-models, the experimental ($\dot{Q}_{tot,exp}$) and modelled ($\dot{Q}_{tot,mod}$) values of $\dot{Q}_{tot}$ has to be defined.

In the case of $\dot{Q}_{tot,mod}$, it corresponds to the addition of the HT to the chamber and ports as presented in Equation (4.35):

$$\dot{Q}_{tot,mod} = \dot{Q}_{cham,cool} + \dot{Q}_{ports} + \dot{Q}_{cham,oil} \tag{4.35}$$

However; some considerations have to be done to obtain $\dot{Q}_{tot,exp}$, in order to maintain the equivalence with the modelled term:

- The EGR is cooled with the engine coolant; therefore, its corresponding heat rejection has to be deducted from the measured $\dot{Q}_{cool}$. The experimental $\dot{Q}_{\mathrm{EGR}}$ is subtracted to have the total heat rejected to the coolant due to the HT in the block, excluding external heat rejection.

- The HT from gases to the chamber and ports is not completely rejected to $\dot{Q}_{cool}$ and $\dot{Q}_{oil}$ since some energy is lost to the ambient, thus $\dot{Q}_{ext,block}$ has to be also included in $\dot{Q}_{tot,exp}$.
- The terms $\dot{Q}_{ext,turbo}$ and $\dot{Q}_{ext,man}$ have not been included in $\dot{Q}_{tot,exp}$ to keep the coherence with the terms included in $\dot{Q}_{tot,mod}$, which do not consider the HT after the ports.
- The $N_a + N_{fr}$ term is mainly dissipated in $\dot{Q}_{cool}$ and $\dot{Q}_{oil}$; thus, these terms should be subtracted from $\dot{Q}_{tot,exp}$. It is important to underline that N_f (included in N_a) is not dissipated in the coolant nor the oil, thus it must not be subtracted from $\dot{Q}_{tot,exp}$.

Taking these comments into consideration, Equation (4.36) is obtained:

$$\dot{Q}_{tot,exp} = (\dot{Q}_{cool} - \dot{Q}_{\mathrm{EGR}}) + \dot{Q}_{oil} + \dot{Q}_{ext,block} - (N_a + N_{fr}) + N_f \tag{4.36}$$

All the energy terms presented in Equation (4.35) and (4.36) are known except $\dot{Q}_{ext,block}$, which can be determined by means of subtraction between the total energy ($\dot{m}_f H_v$) and the addition of all the GEB terms of Equation (4.1), as presented in Equation (4.37):

$$\begin{aligned}\dot{Q}_{ext} &= \dot{Q}_{ext,block} + \dot{Q}_{ext,turbo} + \dot{Q}_{ext,man} \\ &= \dot{m}_f H_v \; - \; \dot{Q}_a \; - \; \dot{Q}_{cool} \; - \; \dot{Q}_{oil} \; - \; \dot{Q}_{turbo} - N_b \; - \\ &\quad - \; \dot{Q}_f \; - \; \dot{H}_{g,ex} \; - \; \dot{H}_{bb} \; - \; \dot{H}_{ic} \; - \; \dot{Q}_{unbal,ex}\end{aligned} \tag{4.37}$$

As described in Appendix 4.B, the net flow of sensible enthalpy can be calculated at the ports conditions, thus obtaining the following expression:

$$\dot{H}_{g,ex} = \dot{H}_{g,ports} - \dot{Q}_a - \dot{Q}_{\mathrm{EGR}} - \dot{Q}_{turbo} - \dot{Q}_{ext,turbo} - \dot{Q}_{ext,man} \tag{4.38}$$

and combining Equations (4.37) and (4.38), $\dot{Q}_{ext,block}$ can be expressed as:

$$\begin{aligned}\dot{Q}_{ext,block} = \dot{m}_f H_v \; - \; \dot{Q}_{cool} \; - \; \dot{Q}_{oil} \; - N_b \; + \dot{Q}_{\mathrm{EGR}} - \; \dot{Q}_f \; - \\ - \; \dot{H}_{g,ports} \; - \; \dot{H}_{bb} \; - \; \dot{H}_{ic} \; - \; \dot{Q}_{unbal,ex}\end{aligned} \tag{4.39}$$

It is reasonable to assume that $\dot{Q}_f \approx N_f$ considering that, on the one hand, an important part (about 40%) of the pumped fuel is returned and cooled, and on the other hand, the small weight of this term (lower than $1\%\dot{m}_f H_v$ in all the cases [3]) makes its uncertainty negligible. Taking into account this comment and replacing $\dot{Q}_{ext,block}$ of Equation (4.39) in Equation (4.36), the following expression for $\dot{Q}_{tot,exp}$ is obtained:

$$\begin{aligned}\dot{Q}_{tot,exp} = \dot{m}_f H_v \; - \; N_b \; - \; \dot{H}_{g,ports} \; - \; (N_a + N_{fr}) - \\ - \; \dot{H}_{bb} \; - \; \dot{H}_{ic} \; - \; \dot{Q}_{unbal,ex}\end{aligned} \tag{4.40}$$

This last expression is more convenient than Equation (4.36), since all the terms involved are experimentally acquired, and the most important of them (i.e. $\dot{m}_f H_v$, N_b and $\dot{H}_{g,ports}$) have lower experimental uncertainty than $\dot{Q}_{cool}$ and $\dot{Q}_{oil}$, as will be discussed in Sections 4.4.4 and 4.4.5. Once both, $\dot{Q}_{tot,mod}$ and $\dot{Q}_{tot,exp}$ are defined, it is interesting to do some comments:

- All the terms conforming $\dot{Q}_{tot,mod}$ in Equation (4.35) are part of the IGEB and are obtained through modelling.
- All the terms conforming $\dot{Q}_{tot,exp}$ in Equation (4.40) are part of the EGEB and are experimentally obtained.
- Strictly speaking, $\dot{H}_{ic}$ and $\dot{H}_{bb}$ are part of both, IGEB and EGEB. However, they are experimentally obtained.
- $\dot{Q}_{tot,mod}$ and $\dot{Q}_{tot,exp}$ are equivalent. Hence, considering that the experimental equipment have been properly calibrated, and all the terms carefully measured, the good agreement between these terms is an indicator of the good HT models performance.

4.3.2 Heat transfer to coolant

The total HT presented in previous section is an interesting parameter to assess the global consistency of the HT models based on some experimental measurements. However, to characterize the thermal behaviour of an engine, it is also interesting to compare the specific repartition of the HT to coolant and oil. In the previous section, it was commented that the friction and auxiliary terms are mostly dissipated in the coolant and oil, but it was not detailed the specific repartition between them. As for the total HT, the coolant HT can be

obtained from modelled or experimental sources, but some hypotheses have to be assumed:

- All the HT to the ports is assumed to be dissipated into the coolant ($\dot{Q}_{ports}$).
- It is assumed that the piston friction ($N_{fr,pis}$) is dissipated into the coolant. This can be justified considering that most of the piston assembly friction takes place in the rings, thus heating both, the liner and the rings. Moreover, the liner temperature is much cooler than that of the piston nodes in contact with the rings (90-150°C vs 110-250°C), thus having a higher temperature drop and hence higher conductive HT.
- The work of the coolant pump (N_{cool}) increases the coolant enthalpy and is dissipated as friction in the fluid, thus slightly increasing its temperature. As a consequence, it is rejected in the coolant cooler.
- There is some HT between the oil and coolant ($\dot{Q}_{oil,cool}$) as they circulate through the engine block and cylinder head, thus leading to some convective HT between them and the gallery walls. This heat is transferred by conduction through the walls between coolant or oil circuits. Thus, it can be stated that the engine works as a heat exchanger between them. For convenience, it is assumed that this term is positive when it goes from oil to coolant, since in most of the cases the oil temperature is higher than the coolant temperature.
- Part of the HT from chamber to coolant goes through the engine body to the engine surface, and there is finally lost to the ambient by convection.

Considering these comments, the modelled HT to the coolant ($\dot{Q}_{cool,mod}$) is defined as presented in Equation (4.41):

$$\dot{Q}_{cool,mod} = \dot{Q}_{cham,cool} + \dot{Q}_{ports} + N_{fr,pis} + N_{cool} + \dot{Q}_{oil,cool} - \dot{Q}_{ext,block} \quad (4.41)$$

In the experimental case, the HT to the coolant is directly measured in the coolant cooler. As explained earlier, the EGR is cooled with the engine coolant; thus, to maintain the equivalence between terms, $\dot{Q}_{\mathrm{EGR}}$ is subtracted from $\dot{Q}_{cool}$ as follows:

$$\dot{Q}_{cool,exp} = \dot{Q}_{cool} - \dot{Q}_{\mathrm{EGR}} \tag{4.42}$$

If experimental uncertainties are controlled, and the models work properly, $\dot{Q}_{cool,exp}$ and $\dot{Q}_{cool,mod}$ must show good agreement.

4.3.3 Heat transfer to oil

Similarly as for the HT to the coolant, some hypotheses have to be made to determine the modelled HT to the oil:

- The friction of the bearings ($N_{fr,bear}$) and camshaft (N_{valv}) is finally dissipated into the oil.
- The work of the oil pump (N_{oil}) increases the oil enthalpy and is dissipated as friction in the fluid, thus slightly increasing its temperature. As a consequence, it is rejected in the oil cooler.
- The energy lost by HT from oil to coolant ($\dot{Q}_{oil,cool}$) has to be considered with negative sign, as it produces a reduction of the oil circuit energy.

Considering these hypotheses, the modelled HT to the oil ($\dot{Q}_{oil,mod}$) is defined as presented in Equation (4.43):

$$\dot{Q}_{oil,mod} = \dot{Q}_{cham,oil} + N_{fr,bear} + N_{fr,valv} + N_{oil} - \dot{Q}_{oil,cool} \tag{4.43}$$

In the experimental case, the HT to the oil ($\dot{Q}_{oil,exp}$) is directly measured in the oil heat exchanger and no further assumptions are necessary:

$$\dot{Q}_{oil,exp} \equiv \dot{Q}_{oil} \tag{4.44}$$

As for the coolant, $\dot{Q}_{oil,exp}$ and $\dot{Q}_{oil,mod}$ have to range within similar values when the experimental uncertainties are controlled and a proper modelling work is done.

4.4 Experimental uncertainty analysis

To perform a proper analysis of the GEB, it is important to know the reliability of the determination of the experimental energy terms. The experimental measurements provide valuable information, on the one hand, to analyse the thermal processes taking place during the engine operation, and on the other hand, to improve and validate the models performance. Therefore, the uncertainty analysis has to be carefully carried out to take advantage of the GEB potential to obtain accurate results and to assess the limitations. This section deals only with the experimental uncertainty, as the analysis of the modelled terms reliability is further discussed in the Chapters 6.2.1 and 6.3.1, where the sub-models calibration and validation for each engine are comprehensively explained.

The experimental uncertainty study is conducted in the complete **Engine A** map[13] (i.e. load ranging between 25% and 100% of maximum torque, and speed between 1000 rpm and 4000 rpm), thus considering all the operating conditions of a reference commercial multi-cylinder engine. The results obtained from this study are representative of the main trends in other similar experimental installations; however, the relative weights of each uncertainty can vary depending on the engine technology tested and the accuracy of the sensors used. As an example, the weight of the HT use to be lower in LTC modes[14] in comparison with CDC, but the unburned fuel becomes relevant [5], thus the relative uncertainty of the HT estimation will be lower in fuel energy terms, in spite of using sensors with the same accuracy. Therefore, the results presented in this section provide guidelines of the uncertainties that can be expected when performing GEBs in CDC with up to date instrumentation, and provide an insight of what can occur when testing alternative hardware configurations or combustion modes.

The determination of the experimental uncertainty of each energy term is performed through the *propagation of uncertainty*, which states that for a variable y that depends on several variables x_1, x_2,..., x_n, its uncertainty ($\pm\varepsilon_y$) depends as well on each i variable uncertainty (ε_{x_i}) as follows [6]:

[13] The minimum load considered is 25%, this limit can affect the maximum uncertainty in some cases, as it tends to increase when the load decreases, as will be shown.

[14] Note that LTC is the abbreviation defined for *low temperature combustion*.

$$\varepsilon_y = \sqrt{\sum_i^n \left(\frac{\partial y}{\partial x_i} \, \varepsilon_{x_i} \right)^2} \tag{4.45}$$

Despite several terms are obtained by experimental means, for the sake of clarity some of them have been excluded from the following analysis, i.e. the HT to the turbocharger oil, the HT to from the fuel in the return line, the unburned energy losses and the blow-by losses. This was decided taking into account that their relative weight is lower than $1\%\dot{m}_f H_v$ [3], and hence their uncertainty becomes negligible for the analysis of the GEB. The energy terms presented in this section are then listed in Table 4.1.

Energy term	**Variable from which is calculated**	**Equation**
$\dot{m}_f H_v$	$\dot{m}_f, H_v$	-
N_i	$p(\alpha)$	(4.22)
N_p	$p(\alpha)$	(4.22)
N_b	M_e, n	(4.7)
$N_a + N_{fr}$	N_i, N_p, N_b	(4.26)
$\dot{Q}_{cool}$	$\dot{m}_{cool}, T_{cool}$	(4.8)
$\dot{Q}_{oil}$	$\dot{m}_{w,oil}, T_{w,oil}$	(4.9)
$\dot{H}_g$	$\dot{m}_a, \dot{m}_f, T_{int}, T_{exh}$	(4.2)
$\dot{Q}_{\text{EGR}}$	$Y_{CO_2}, \dot{m}_a, T_{\text{EGR}}$	(4.31)
$\dot{Q}_a$	$\dot{m}_a, T_a$	(4.11)

Table 4.1. *Experimental energy terms and their calculation procedure.*

The experimental uncertainty in terms of accuracy and precision[15] depends directly on the experimental equipment used to measure the variables required to determine each energy term. The expected uncertainty of the experimental equipment used to determine the values listed in Table 4.1 is presented in Table 4.2.

It is worth to highlight that the relative uncertainties of the fuel mass flow and the heating value are 0.2% and 0.3% respectively. Therefore, by applying Equation (4.45), a constant error of 0.4% is obtained. Since this

[15] Accuracy refers to the closeness of a measured value to a real value, meanwhile precision refers to the closeness of two or more measurements to each other.

Variable	Equipment	Accuracy
$\dot{m}_f$	AVL 733S Fuel meter	0.2%
H_v	Bomb calorimeter	0.3%*
$p(\alpha)$	AVL GH13P	$\pm 0.2^{\circ\ddagger}$
n	Tachometer	0.03% fs.
M	Dynamometer	0.05% fs.
$\dot{m}_a$	Sensiflow DN80	2%
T_a, T_f, T_{EGR}, T_{exh}	K-type Thermocouples	1.5 °C
T_{cool}, T_{oil}	PT100 RTD	0.2°C
Y_{CO_2}	Horiba mexa 7100 DEGR	4%
$v_{cool}{}^{\dagger}$	Krohne 4010 Optiflux	$\begin{cases} 0.02 \text{ m/s} & \text{if } v_{cool} < 0.4 \text{ m/s} \\ 0.5\% & \text{if } v_{cool} \geq 0.4 \text{ m/s} \end{cases}$
$v_{oil}{}^{\dagger}$	Isoil MS500	0.025 m/s

fs. means full scale.
*The difference between successive results would exceed the repeatability value only in one case in twenty, according to [7]
‡The uncertainty is assumed to be due to TDC position
†The flow meter provides flow speed, which is used to determine the mass flow

Table 4.2. Engine A *measurement equipment uncertainty.*

value is constant and affects all the energy terms in the same extent, no further analysis of this uncertainty is discussed.

The results are presented taking into account the relative uncertainty of each term with respect to the energy term value (%), and their weight in terms of the total input fuel energy ($\%\dot{m}_f H_v$). This allows analysing both, the specific accuracy of each term determination and their weight in the GEB. In all the cases, the uncertainty is shown in positive terms, but it must be assumed an uncertainty range of $\pm\varepsilon$, being ε the uncertainty in the figures.

4.4.1 Indicated and pumping power

The indicated power is calculated by integration of the indicated cycle, thus the only uncertainties that affect the indicated power estimation are the sensor calibration, the TDC determination and the experimental noise[16]. To

[16]The pressure pegging does not affect the indicated parameters.

avoid calibration uncertainties, the acquisition chain was regularly calibrated according to the traditional method proposed in [8], having an uncertainty in the calibration constant lower than 0.15%. To reduce the random effect of the noise, three measurements of each operating point were obtained, each of them consisting of 25 consecutive cycles processed and averaged as presented in [9]. Thus, the only significant parameter affecting the indicated power calculation was the TDC position ($\Delta\alpha_{\mathrm{TDC}}$).

To accurately determine $\Delta\alpha_{\mathrm{TDC}}$, the adjustment methodology described in Chapter 5.3 was used. The uncertainty of the $\Delta\alpha_{\mathrm{TDC}}$ determination is not expected to be higher than 0.1°; however, a slightly higher uncertainty value of 0.2° was considered. In Figure 4.6, the effect of the stated variation on the indicated power is shown.

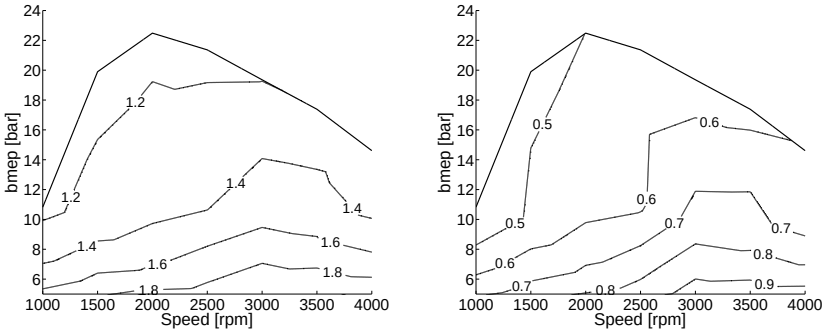

Figure 4.6. *Uncertainty of N_i. Left: relative to the energy term (%); right: relative to the fuel energy (%$\dot{m}_f H_v$).*

The uncertainty due to the TDC position on the indicated power estimation (ε_{N_i}) ranges between 1 and 2%. Since the indicated power ranges between 38-46%$\dot{m}_f H_v$, its uncertainty ranges between 0.5 and 1%$\dot{m}_f H_v$. The maximum uncertainty is observed at low load and diminishes as the load increases.

Despite the weight of the pumping power uncertainty is low, its value (ε_{N_p}) is presented because it has a slightly impact on the friction and auxiliary uncertainty determination, as will be discussed later. As can be seen in Figure 4.7, it can reach values up to 1%. However, these values result in a weight lower than 0.01%$\dot{m}_f H_v$, thus being negligible.

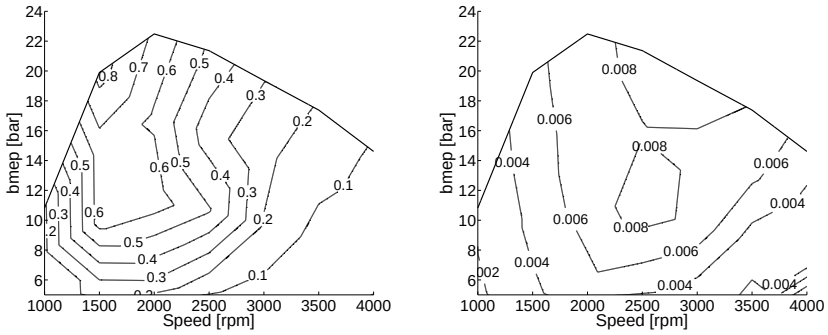

Figure 4.7. *Uncertainty of N_p. Left: relative to the energy term (%); right: relative to the fuel energy (%$\dot{m}_f H_v$).*

4.4.2 Brake power

By applying the *propagation of uncertainty* to Equation (4.7), the following expression to determine the uncertainty of the brake power estimation is obtained:

$$\varepsilon_{N_b} = 2\pi \sqrt{(\varepsilon_n \ M)^2 + (n \ \varepsilon_M)^2} \tag{4.46}$$

where n and M are the engine speed and torque, and ε_n and ε_M are their respective uncertainties (see Table 4.2).

In Figure 4.8, the uncertainty of the brake power is presented. It is possible to see how its values are always lower than 0.4% in the complete engine map. Only a third of this uncertainty is reflected in terms of fuel energy, thus reaching values lower than 0.15%$\dot{m}_f H_v$. The uncertainty is slightly higher at low load. In a lower extent, these trends are also followed when speed changes.

4.4.3 Auxiliary and friction power

Since experimental $N_a + N_{fr}$ is obtained from the indicated cycle and the brake power (see Equation (4.26)), its uncertainty can be expressed as:

$$\varepsilon_{(N_a+N_{fr})} = \sqrt{\varepsilon_{N_i}^2 + \varepsilon_{N_p}^2 + \varepsilon_{N_b}^2} \tag{4.47}$$

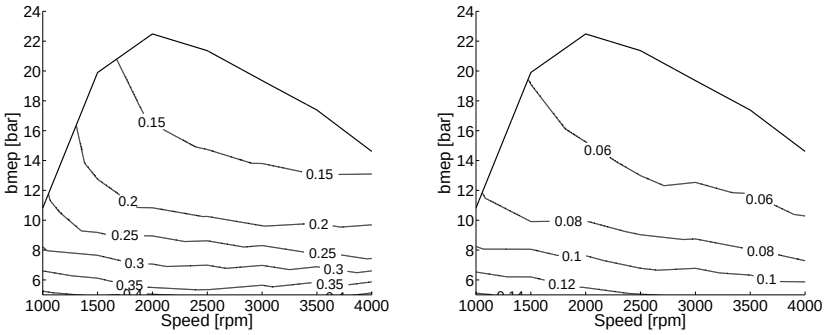

Figure 4.8. *Uncertainty of N_b. Left: relative to the energy term (%); right: relative to the fuel energy ($\%\dot{m}_f H_v$).*

In Figure 4.9, the values of $\varepsilon_{(N_a+N_{fr})}$ in the complete engine map are shown. As expected, the uncertainty of $N_a + N_{fr}$ is higher than that of the indicated and brake power. It reaches its maximum of about 13% at low speed, while no clear trend with the load is observed. In spite of this high value, the relative low weight of N_a+N_{fr} in the GEB [3] leads to a low impact in terms of the input fuel energy, where its maximum uncertainty is lower than $1\%\dot{m}_f H_v$.

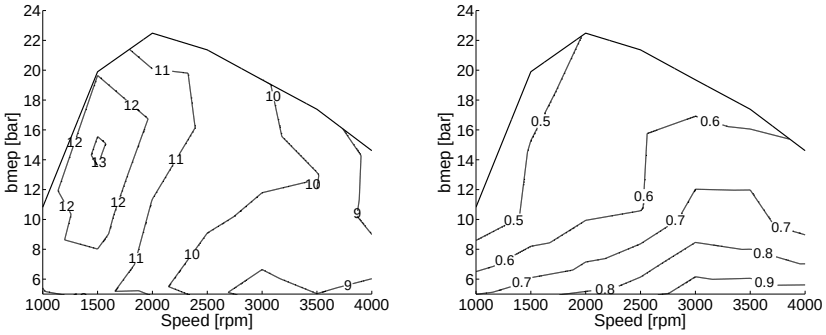

Figure 4.9. *Uncertainty of $N_{fr} + N_a$. Left: relative to the energy term (%); right: relative to the fuel energy ($\%\dot{m}_f H_v$).*

4.4.4 Heat transfer to coolant

The uncertainty of the HT to the coolant is determined by means of Equation (4.48), which is obtained by applying the *propagation of uncertainty* to Equation (4.8).

$$\varepsilon_{\dot{Q}_{cool}} = c_{p,cool}\sqrt{(\varepsilon_{\dot{m}_{cool}}\ \Delta T_{cool})^2 + (2\ \dot{m}_{cool}\ \varepsilon_{T_{cool}})^2} \tag{4.48}$$

where ΔT_{cool} is the temperature drop through the coolant cooler, $\varepsilon_{\dot{m}_{cool}}$ is the coolant flow rate uncertainty and $\varepsilon_{T_{cool}}$ is the coolant temperature uncertainty.

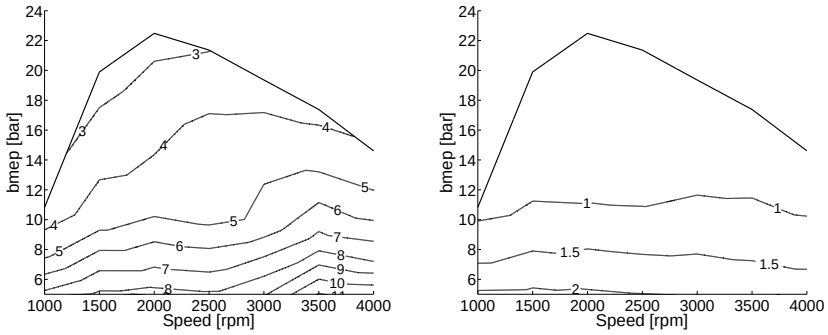

Figure 4.10. *Uncertainty of $\dot{Q}_{cool}$. Left: relative to the energy term (%); right: relative to the fuel energy (%$\dot{m}_f H_v$).*

As shown in Figure 4.10, the uncertainty of the coolant HT ranges between 3 and 12%, being mostly dependent on the load. The maximum uncertainty is observed at low load, which is explained by the low temperature variation (due to the smaller heat rejected). At high load, the HT to the coolant increases (in absolute terms), thus the relative effect of the uncertainty decreases. This relatively high weight at low load represent about 2%$\dot{m}_f H_v$, thus becoming one of the most uncertain parameters to be experimentally determined. For this reason, the total HT defined in Section 4.3.1 uses different experimental data, thus avoiding $\dot{Q}_{cool}$ uncertainty.

4.4.5 Heat transfer to oil

Similarly as for the coolant, the uncertainty in the calculation of the HT to the oil is obtained by applying Equation (4.45) to Equation (4.9):

$$\varepsilon_{\dot{Q}_{oil}} = c_{p,w,oil}\sqrt{(\varepsilon_{\dot{m}_{w,oil}}\ \Delta T_{w,oil})^2 + (2\ \dot{m}_{oil}\ \varepsilon_{T_{w,oil}})^2} \tag{4.49}$$

where $\varepsilon_{\dot{m}_{w,oil}}$ is the uncertainty in the measurement of the cooling water of the oil cooler, and $\varepsilon_{T_{w,oil}}$ is the uncertainty of the water temperature at inlet and outlet of the oil cooler.

In this case, no oil cooling was needed at low speed and load, since the maximum oil temperature setting was 90°C and it was not reached at those conditions. In Figure 4.11, the uncertainty of the HT to the oil is presented.

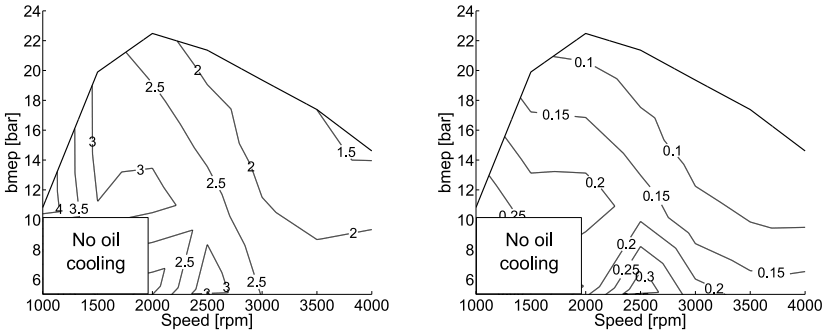

Figure 4.11. *Uncertainty of $\dot{Q}_{oil}$. Left: relative to the energy term (%); right: relative to the fuel energy (%$\dot{m}_f H_v$).*

As can be seen, the uncertainty ranges between 1.5 and 3%, being lower than that of the coolant. In terms of the input fuel energy, the HT to the oil has a low effect, ranging between 0.1 and 0.2%$\dot{m}_f H_v$. Even thought the oil is required for both, lubrication and cooling purposes, its mass flow is significantly lower than the coolant mass flow, thus its uncertainty in terms of fuel energy is about an order of magnitude lower than that of the coolant.

4.4.6 Net sensible enthalpy

To determine the uncertainty of the net sensible enthalpy, some comments have to be done:

– The uncertainty of $\dot{H}_{g,ex}$ is analysed, taking into account that the uncertainty of $\dot{H}_{g,in}$ has a similar behaviour but with a slightly lower weight.

This is explained by considering that $\dot{H}_{g,in}$ is calculated for a higher temperature (at the turbine intake), being its relative uncertainty lower.

– For the sake of clarity, the blow-by flow was neglected from this analysis, taking into account that it is a very small portion of $\dot{m}_a + \dot{m}_f$.

Taking into account these comments, the *propagation of uncertainty* is applied in Equation (4.2), thus obtaining the following expression:

$$\varepsilon_{\dot{H}_{g,ex}} = \sqrt{\varepsilon^2_{(\dot{m}_{exh} h^{sens}_{exh})} + \varepsilon^2_{(\dot{m}_a h_a)} + \varepsilon^2_{(\dot{m}_f h_f)}} \tag{4.50}$$

To solve Equation (4.50), the uncertainties of $\dot{m}_{exh}$ and the sensible enthalpy have to be determined. Therefore, the following considerations have to be made:

– Accounting for the definition of $\dot{m}_{exh}$ presented in Equation (4.6), and neglecting the blow-by as commented, $\varepsilon_{\dot{m}_{exh}}$ can be expressed in terms of the air and fuel mass uncertainties as follows:

$$\varepsilon^2_{\dot{m}_{exh}} = \varepsilon^2_{\dot{m}_a} + \varepsilon^2_{\dot{m}_f} \tag{4.51}$$

where $\varepsilon_{\dot{m}_a}$ and $\varepsilon_{\dot{m}_f}$ are the air and fuel flow rates uncertainties.

– As the sensible enthalpy depends on the temperature at which it is computed, its uncertainty is estimated as the difference between the sensible enthalpy at the measured temperature and at the maximum temperature variation expected (± 1.5°C, see Table 4.2) as follows:

$$\varepsilon_{h^{sens}_i} = |h^{sens}_i(T_i) - h^{sens}_i(T_i \pm 1.5)| \tag{4.52}$$

where i represents the air, fuel or exhaust.

Therefore, by applying the *propagation of uncertainty* to each term on the right hand side of Equation (4.50), the following expressions are obtained:

$$\varepsilon^2_{(\dot{m}_{exh} h^{sens}_{exh})} = h^{sens\ 2}_{exh}\ (\varepsilon^2_{\dot{m}_a} + \varepsilon^2_{\dot{m}_f}) + (\dot{m}_a + \dot{m}_f)^2\ \varepsilon^2_{h^{sens}_{exh}} \tag{4.53}$$

$$\varepsilon^2_{(\dot{m}_a h^{sens}_a)} = (\varepsilon_{\dot{m}_a}\ h^{sens}_a)^2 + (\dot{m}_a\ \varepsilon_{h^{sens}_a})^2 \tag{4.54}$$

$$\varepsilon^2_{(\dot{m}_f h^{sens}_f)} = (\varepsilon_{\dot{m}_f}\ h^{sens}_f)^2 + (\dot{m}_f\ \varepsilon_{h^{sens}_f})^2 \tag{4.55}$$

Finally, $\varepsilon_{\dot{H}_{g,ex}}$ is obtained by replacing Equations (4.53), (4.54) and (4.55) in Equation (4.50).

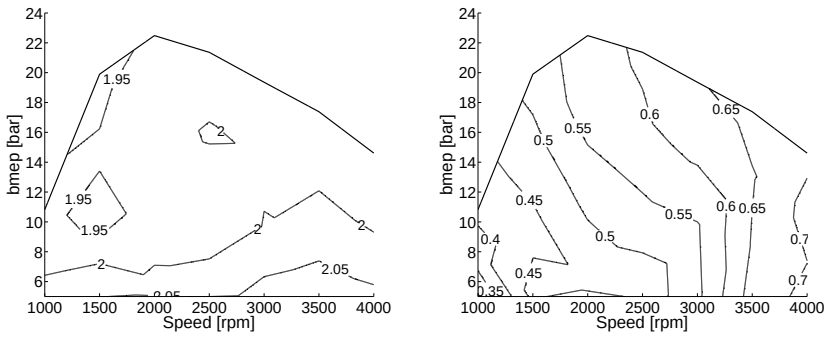

Figure 4.12. *Uncertainty of $\dot{H}_{g,ex}$. Left: relative to the energy term (%); right: relative to the fuel energy (%$\dot{m}_f H_v$).*

As can be seen in Figure 4.12, the uncertainty of $\dot{H}_{g,ex}$ is almost constant, having a value about 2% in the engine map; however, its weight in terms of the fuel energy ranges between 0.4 and 0.7%$\dot{m}_f H_v$, being increasingly higher with the speed but almost independent of the load. This is explained by the increase of the $\dot{H}_{g,ex}$ weight with the speed rather than the load, as will be described in Chapter 6.2.2.4.

4.4.7 Heat transfer from air

Starting from Equation (4.11) and (4.45), the expression to calculate the uncertainty in HT removed from the air in the intercooler is obtained.

$$\varepsilon_{\dot{Q}_a} = c_{p,a}\sqrt{(\varepsilon_{\dot{m}_a}\ \Delta T_a)^2 + (2\ \dot{m}_a\ \varepsilon_{T_a})^2} \tag{4.56}$$

where $\varepsilon_{\dot{m}_a}$ and ε_{T_a} are the air flow rate and air temperature uncertainties.

In Figure 4.13 the uncertainty of $\dot{Q}_a$ is presented. As can be seen, the uncertainty lies between 3 and 8% of $\dot{Q}_a$, being maximum at low speed and load. However, the relative weight in terms of fuel energy is much lower, having values between 0.1 and 0.2%$\dot{m}_f H_v$, slightly increasing when the speed gets higher. This is explained, as in the case of $\dot{H}_{g,ex}$, by the higher dependency of $\dot{Q}_a$ with the speed rather than the load, as will be described in Chapter 6.2.2.4.

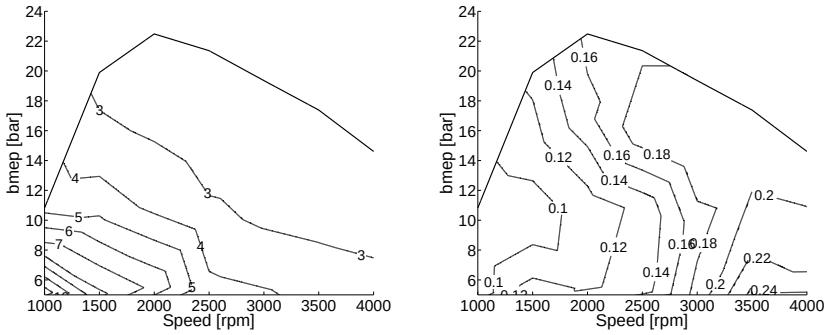

Figure 4.13. *Uncertainty of $\dot{Q}_a$. Left: relative to the energy term (%); right: relative to the fuel energy (%$\dot{m}_f H_v$).*

4.4.8 Heat transfer from EGR

This uncertainty is analysed only in the map region where EGR strategy is used, i.e. between low and mid speed and load. As for the other terms, by applying the *propagation of uncertainty* on the Equation (4.31), the $\dot{Q}_{\mathrm{EGR}}$ uncertainty can be expressed as:

$$\varepsilon_{\dot{Q}_{\mathrm{EGR}}} = c_{p,\mathrm{EGR}} \sqrt{(\varepsilon_{\dot{m}_{\mathrm{EGR}}}\ \Delta T_{\mathrm{EGR}})^2 + (2\ \dot{m}_{\mathrm{EGR}}\ \varepsilon_{T_{\mathrm{EGR}}})^2} \tag{4.57}$$

where the uncertainty in $\dot{m}_{\mathrm{EGR}}$ estimation is obtained by applying Equation (4.45) to Equation (4.32):

$$\frac{\varepsilon_{\dot{m}_{\mathrm{EGR}}}}{\dot{m}_{\mathrm{EGR}}} = \sqrt{\left(\frac{\varepsilon_{\dot{m}_a}}{\dot{m}_a}\right)^2 + \left(\frac{\varepsilon_{\tau_{\mathrm{EGR}}}}{\tau_{\mathrm{EGR}} - \tau_{\mathrm{EGR}}^2}\right)^2} \tag{4.58}$$

where $\varepsilon_{\tau_{\mathrm{EGR}}}$ is the EGR rate uncertainty. For its determination, a simplification in Equation (4.33), consisting on neglecting the atmospheric CO_2, is performed. Then, by applying Equation (4.45), the following expression can be obtained:

$$\varepsilon_{\mathrm{EGR}} = \sqrt{2}\ \frac{\varepsilon_{Y_{CO_2}}}{Y_{CO_2}} \tag{4.59}$$

where $\varepsilon_{Y_{CO_2}}/Y_{CO_2}$ is the relative uncertainty on the CO_2 determination presented in Table 4.2.

In Figure 4.14, the uncertainty of the HT rejected to the EGR cooler is presented. The maximum uncertainty is about 1.4%, which is observed at low load. This uncertainty becomes lower at higher load, having a minimum value about 0.2%. In terms of fuel energy, it is observed a very low effect of the uncertainty, having values lower than $0.1\%\dot{m}_f H_v$. This is easily explained by the low weight of $\dot{Q}_{\mathrm{EGR}}$ in the GEB as explained in Chapter 6.2.2.4.

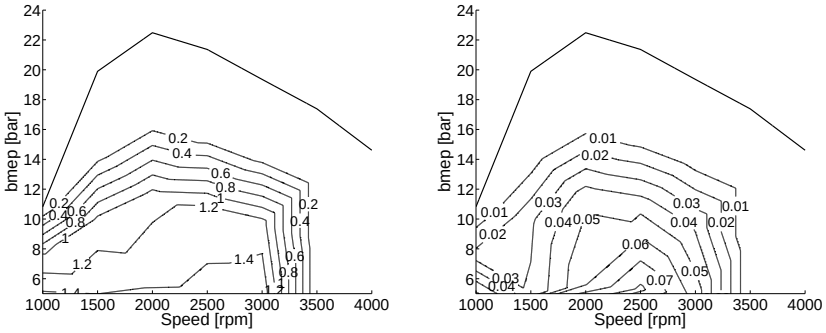

Figure 4.14. *Uncertainty of $\dot{Q}_{\mathrm{EGR}}$. Left: relative to the energy term (%); right: relative to the fuel energy ($\%\dot{m}_f H_v$).*

4.5 Conclusions

In this chapter, a comprehensive methodology to perform and analyse the GEB has been proposed. As discussed, the GEB can be performed from 2 different points of view:

- In the EGEB, the engine is considered as a black box exchanging energy with the surroundings. The energy terms are mostly experimentally determined.
- In the IGEB, a detailed description of the energy split due to engine internal interactions and sub-processes is presented. Despite some energy terms of the IGEB can be experimentally determined, most of them cannot be easily measured, thus they are modelled.

Along with the GEB definitions, a detailed description of the determination process of each energy term and the relationship between internal and external terms have been presented.

In order to provide some parameters for the sub-models calibration and the thermal validation, three equivalent terms have been defined:

- Total heat transfer. These terms include all the HT from chamber and ports. Consistent definitions of these terms are obtained for both internal and external points of view. $\dot{Q}_{tot,mod}$ is directly obtained as the addition of the modelled HT from chamber and ports; however, $\dot{Q}_{tot,exp}$ requires careful analysis of the energy terms involved in the EGEB. A convenient expression based on experimental terms with low uncertainty is finally proposed.
- Heat transfer to coolant. These terms are obtained by considered all the energy flows going in and out of the coolant. Therefore, $\dot{Q}_{cool,mod}$ is the addition of the energy contributions from chamber, ports, friction and auxiliary, and HT between oil an coolant, bearing in mind that part of this addition is lost to the ambient. $\dot{Q}_{cool,exp}$ is the subtraction between the heat rejection in the coolant and EGR coolers, as this last is cooled with the engine coolant and has to be subtracted to maintain the equivalence between terms.

– Heat transfer to oil. These terms are obtained similarly as for the coolant. $\dot{Q}_{oil,mod}$ is the addition of the energy contributions from chamber, friction and auxiliary, and considering the HT between oil and coolant. Meanwhile, $\dot{Q}_{oil,exp}$ is directly the heat rejection measured in the oil cooler.

These terms will be conveniently used to calibrate the sub-models and validate the results, depending on the information available, as will be described in Chapters 6.2.1 and 6.3.1.

To determine the reliability of the experimental work, an uncertainty analysis of the most relevant terms was performed. In this regard, the following conclusions can be highlighted:

– The parameter with the highest uncertainty is the $N_a + N_{fr}$, reaching values up to 12%; however, its impact in terms of fuel energy is always lower than $1\%\dot{m}_f H_v$.

– Despite the relative high uncertainty of N_i and N_p (1.8 and 0.8%) due to variations of the TDC position, these terms have low uncertainty in terms of fuel energy, being always lower than $0.9\%\dot{m}_f H_v$ and $0.01\%\dot{m}_f H_v$ respectively.

– The parameter with the highest uncertainty in terms of fuel energy is $\dot{Q}_{cool}$, having values between 1 and $2\%\dot{m}_f H_v$ and reaching its maximum at low speed and load. This uncertainty confirms the necessity of defining a heat transfer term ($\dot{Q}_{tot,exp}$) based on more accurately determined terms, as done in Section 4.3.1.

– N_b and $\dot{H}_{g,ex}$, which are very important terms of the GEB, have low uncertainty levels (0.06-0.12$\%\dot{m}_f H_v$ and 0.4-0.7$\%\dot{m}_f H_v$ respectively).

– The rest of the terms analysed have very low uncertainty in terms of the fuel energy, being always lower than $0.5\%\dot{m}_f H_v$ regardless their own uncertainty. As an example, the maximum uncertainty of $\dot{Q}_a$ is about 8%, but its weight in terms of fuel energy is lower than $0.2\%\dot{m}_f H_v$.

As a final conclusion of the chapter, it is evident the important modelling work required to perform the IGEB, thus several sub-models must de proposed. For this reason, the next chapter deals with the complete description of all the new sub-models developed in this work.

4.A Appendix: development of the energy balance equation

Figure 4.15 shows a more general scheme of the energy balance in a control volume than that presented in Figure 4.1. The energy terms related with the enthalpy fluxes were considered separately from the engine effective power and the heat losses. Besides, in order to facilitate the analysis of the unburned fuel, the equivalent unburned fuel mass ($\dot{m}_{f,nb}$) defined in Equation (4.15) has been considered, assuming that it goes out the system at the exhaust ($\dot{m}^{exh}_{f,nb}$) and the blow-by flow ($\dot{m}^{bb}_{f,nb}$) with the same chemical composition as injected. This is not rigorous, since the unburned fuel has the form of sub-products (i.e. HC, CO and soot); however, taking into account that the combustion chemical process is not a key topic in this work, the assumptions made are considered accurate enough for the energy analysis presented.

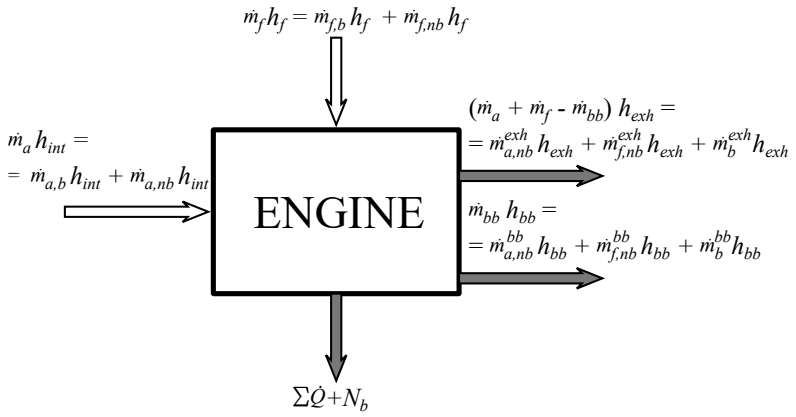

Figure 4.15. *General engine energy balance scheme.*

The mass flows observed in Figure 4.15 are:

- $\dot{m}_f$: the fuel mass flow can be expressed as the addition of two terms, the burned ($\dot{m}_{f,b}$) and unburned ($\dot{m}_{f,nb}$) fuel mass flow[17]. Depending on

[17] In CDC, $\dot{m}_{f,b} \approx \dot{m}_f$ and $\dot{m}_{f,nb} \approx 0$.

whether these masses go out by the exhaust or as blow-by losses, they can be expressed as:

$$\dot{m}_{f,b} = \dot{m}_{f,b}^{exh} + \dot{m}_{f,b}^{bb} \tag{4.60}$$

$$\dot{m}_{f,nb} = \dot{m}_{f,nb}^{exh} + \dot{m}_{f,nb}^{bb} \tag{4.61}$$

- $\dot{m}_{f,nb}^{exh}$ and $\dot{m}_{f,nb}^{bb}$: they are the unburned masses going out by the exhaust and as blow-by respectively. As explained in Section 4.2.1, $\dot{m}_{f,nb}^{exh}$ can be estimated through the HC, CO and soot emissions. $\dot{m}_{f,nb}^{bb}$ is calculated by means of the blow-by model developed in Appendix 5.B, assuming homogeneous mixture in the chamber (thus homogeneous blow-by composition).

- $\dot{m}_{f,b}^{exh}$ and $\dot{m}_{f,b}^{bb}$: they are the burned masses going out by the exhaust and as blow-by respectively. They are calculated as:

$$\dot{m}_{f,b}^{bb} = \frac{\dot{m}_{b}^{bb}}{1 + \frac{1}{F_s}} \tag{4.62}$$

$$\dot{m}_{f,b}^{exh} = \dot{m}_f - (\dot{m}_{f,b}^{bb} + \dot{m}_{f,nb}^{bb}) - \dot{m}_{f,nb}^{exh} \tag{4.63}$$

  being $\dot{m}_{b}^{bb}$ the burned gas going out as blow-by and F_s the stoichiometric fuel/air ratio.

- $\dot{m}_a$: it is the air flow at intake. It can be expressed as the addition of the air used in the combustion ($\dot{m}_{a,b}$) and the excess of air ($\dot{m}_{a,nb}$). $\dot{m}_{a,b}$ is the stoichiometric burned air, which is determined as:

$$\dot{m}_{a,b} = \frac{\dot{m}_{f,b}}{F_s} \tag{4.64}$$

  and hence, the excess of air is calculated as the difference between the stoichiometric burned air and the total intake air:

$$\dot{m}_{a,nb} = \dot{m}_a - \dot{m}_{a,b} \tag{4.65}$$

  Similarly as for the fuel, these masses can be decomposed depending on whether they go out the engine by the exhaust or as blow-by:

$$\dot{m}_{a,b} = \dot{m}_{a,b}^{exh} + \dot{m}_{a,b}^{bb} \tag{4.66}$$

$$\dot{m}_{a,nb} = \dot{m}_{a,nb}^{exh} + \dot{m}_{a,nb}^{bb} \tag{4.67}$$

- $\dot{m}_{a,nb}^{exh}$ and $\dot{m}_{a,nb}^{bb}$: they are the excess of air going out by the exhaust and as blow-by[18]. $\dot{m}_{a,nb}^{bb}$ is obtained from the blow-by model (see Appendix 5.B) assuming homogeneous blow-by composition, $\dot{m}_{a,nb}^{exh}$ can be obtained through an air mass balance as:

$$\dot{m}_{a,nb}^{exh} = \dot{m}_a - \dot{m}_{a,b} - \dot{m}_{a,nb}^{bb} \tag{4.68}$$

- $\dot{m}_{a,b}^{exh}$ and $\dot{m}_{a,b}^{bb}$: they are the air masses which participate in the stoichiometric combustion, which lead to the burned gases. They are calculated as:

$$\dot{m}_{a,b}^{exh} = \frac{\dot{m}_{f,b}^{exh}}{F_s} \tag{4.69}$$

$$\dot{m}_{a,b}^{bb} = \frac{\dot{m}_{f,b}^{bb}}{F_s} \tag{4.70}$$

- $\dot{m}_b^{exh}$ and $\dot{m}_b^{bb}$: they are the burned gases resulting from combustion, which are actually going out the chamber by the exhaust or as blow-by. They can be obtained as:

$$\dot{m}_b^{exh} = \dot{m}_{f,b}^{exh} + \dot{m}_{a,b}^{exh} \tag{4.71}$$

$$\dot{m}_b^{bb} = \dot{m}_{f,b}^{bb} + \dot{m}_{a,b}^{bb} \tag{4.72}$$

The analysis of the enthalpies observed in Figure 4.15 leads to obtaining the energy released during the combustion process, the net sensible enthalpy of the gases and the net sensible enthalpy of blow-by. To perform the analysis, it was assumed that the enthalpies depend only on the species considered as well as the temperature. Following, a description of the enthalpies involved is presented:

- h_f: it is the liquid fuel enthalpy, calculated at the fuel pump inlet conditions as:

$$\begin{aligned} h_f(T_f) &= h_f^0(T_0) + \int_{T_0}^{T_f} c_{p,f}(T)\mathrm{d}T \\ &= h_f^0(T_0) + h_f^{sens}(T_f) \end{aligned} \tag{4.73}$$

[18]These masses do not participate in the combustion and are only heated between intake and exhaust or blow-by respectively.

where h_f^0 is the fuel enthalpy of formation at standard conditions ($T_0 = 25°C$, 1 atm) and $h_f^{sens}(T_f)$ is the fuel sensible enthalpy increase at the fuel pump inlet conditions (T_f).

- h_{int}: it is the intake gas enthalpy (pure air), calculated at the compressor inlet conditions as:

$$\begin{aligned} h_{int}(T_{int}) &= h_{int}^0(T_0) + \int_{T_0}^{T_{int}} c_{p,int}(T)\mathrm{d}T \\ &= h_{int}^0(T_0) + h_{int}^{sens}(T_{int}) \end{aligned} \tag{4.74}$$

where h_{int}^0 is the intake gas enthalpy of formation at standard conditions and $h_{int}^{sens}(T_{int})$ is the intake gas sensible enthalpy increase at compressor inlet conditions (T_{int}).

- h_{exh}: it is the burned gas enthalpy, calculated at the turbine exhaust conditions (T_{exh}) as:

$$h_{exh}(T_{exh}) = Y_{a,nb}^{exh} h_a(T_{exh}) + Y_{f,nb}^{exh} h_f(T_{exh}) + Y_b^{exh} h_b(T_{exh}) \tag{4.75}$$

where $Y_{a,nb}^{exh}$, $Y_{f,nb}^{exh}$ and Y_b^{exh} are the mass fractions of the excess of air, unburned fuel, and stoichiometric burned gases in the exhaust gases respectively.

- h_{bb}: it is the blow-by enthalpy calculated assuming that its temperature is equal to that of the coolant ($T_{bb} = T_{cool}$):

$$h_{bb}(T_{bb}) = Y_{a,nb}^{bb} h_a(T_{bb}) + Y_{f,nb}^{bb} h_f(T_{bb}) + Y_b^{bb} h_b(T_{bb}) \tag{4.76}$$

where $Y_{a,nb}^{bb}$, $Y_{f,nb}^{bb}$ and Y_b^{bb} are the mass fractions of the excess of air, unburned fuel, and stoichiometric burned gases in the blow-by respectively.

Taking into account Equations (4.75) and (4.76), the exhaust and blow-by enthalpy flows can be written as:

$$\begin{aligned} &(\dot{m}_a + \dot{m}_f - \dot{m}_{bb})\ h_{exh}(T_{exh}) = \\ &= (\dot{m}_a + \dot{m}_f - \dot{m}_{bb})\ \left[Y_{a,nb}^{exh} h_a(T_{exh}) + Y_{f,nb}^{exh} h_f(T_{exh}) + Y_b^{exh} h_b(T_{exh})\right] \\ &= \dot{m}_{a,nb}^{exh} h_a(T_{exh}) + \dot{m}_{f,nb}^{exh} h_f(T_{exh}) + \dot{m}_b^{exh} h_b(T_{exh}) \end{aligned} \tag{4.77}$$

$$\begin{aligned}
&\dot{m}_{bb}\ h_{bb}(T_{bb}) = \\
&= \dot{m}_{bb}\ \left[Y^{bb}_{a,nb}h_a(T_{bb}) + Y^{bb}_{f,nb}h_f(T_b) + Y^{bb}_{b}h_b(T_b)\right] \\
&= \dot{m}^{bb}_{a,nb}h_a(T_{bb}) + \dot{m}^{bb}_{f,nb}h_f(T_{bb}) + \dot{m}^{bb}_{b}h_b(T_{bb})
\end{aligned} \tag{4.78}$$

Considering the energy terms presented in Figure 4.15, the general energy balance is expressed as:

$$\begin{aligned}
\sum \dot{m}h &= \dot{m}_a h_{int} + \dot{m}_f h_f - (\dot{m}_a + \dot{m}_f - \dot{m}_{bb})h_{exh} - \dot{m}_{bb}h_{bb} = \\
&= N_b + \sum \dot{Q}
\end{aligned} \tag{4.79}$$

Taking into account the decomposition presented in Equations (4.77) and (4.78), and by replacing in Equation (4.79), the following expression is obtained:

$$\begin{aligned}
\sum \dot{m}h = &(\dot{m}^{exh}_{a,nb} + \dot{m}^{bb}_{a,nb})h_a(T_{int}) + (\dot{m}^{exh}_{a,b} + \dot{m}^{bb}_{a,b})h_a(T_{int}) + \\
&+ (\dot{m}^{exh}_{f,nb} + \dot{m}^{bb}_{f,nb})h_f(T_f) + (\dot{m}^{exh}_{f,b} + \dot{m}^{bb}_{f,b})h_f(T_f) - \\
&- \dot{m}^{exh}_{a,nb}h_a(T_{exh}) - \dot{m}^{exh}_{f,nb}h_f(T_{exh}) - \dot{m}^{exh}_{b}h_b(T_{exh}) - \\
&- \dot{m}^{bb}_{a,nb}h_a(T_{bb}) - \dot{m}^{bb}_{f,nb}h_f(T_{bb}) - \dot{m}^{bb}_{b}h_b(T_{bb}) = \\
= &N_b + \sum \dot{Q}
\end{aligned} \tag{4.80}$$

From the analysis of Equation 4.80, some terms can be identified. On the one hand, the variation of the sensible enthalpy of the species that do not participate in the combustion:

$$\begin{aligned}
&(\dot{m}^{exh}_{a,nb} + \dot{m}^{bb}_{a,nb})h_a(T_{int}) + (\dot{m}^{exh}_{f,nb} + \dot{m}^{bb}_{f,nb})h_f(T_f) - \\
&- \dot{m}^{exh}_{a,nb}h_a(T_{exh}) - \dot{m}^{exh}_{f,nb}h_f(T_{exh}) - \dot{m}^{bb}_{a,nb}h_a(T_{bb}) - \dot{m}^{bb}_{f,nb}h_f(T_{bb}) = \\
= &- \dot{m}^{exh}_{a,nb}\left[h_a(T_{exh}) - h_a(T_{int})\right] - \dot{m}^{exh}_{f,nb}\left[h_f(T_{exh}) - h_f(T_f)\right] - \\
&- \dot{m}^{bb}_{a,nb}\left[h_a(T_{bb}) - h_a(T_{int})\right] - \dot{m}^{bb}_{f,nb}\left[h_f(T_{bb}) - h_f(T_f)\right] = \\
= &- \dot{m}^{exh}_{a,nb}\left[h^{sens}_a(T_{exh}) - h^{sens}_a(T_{int})\right] - \dot{m}^{exh}_{f,nb}\left[h^{sens}_f(T_{exh}) - h^{sens}_f(T_f)\right] - \\
&- \dot{m}^{bb}_{a,nb}\left[h^{sens}_a(T_{bb}) - h^{sens}_a(T_{int})\right] - \dot{m}^{bb}_{f,nb}\left[h^{sens}_f(T_{bb}) - h^{sens}_f(T_f)\right] = \\
= &- \dot{H}^{exh}_{nb} - \dot{H}^{bb}_{nb}
\end{aligned} \tag{4.81}$$

being $\dot{H}_{nb}^{exh}$ and $\dot{H}_{nb}^{bb}$ the sensible enthalpy flows going out by the exhaust and blow-by.

On the other hand, the remaining terms correspond to the species that participate in the stoichiometric combustion:

$$\begin{aligned}
&(\dot{m}_{a,b}^{exh} + \dot{m}_{a,b}^{bb})h_a(T_{int}) + (\dot{m}_{f,b}^{exh} + \dot{m}_{f,b}^{bb})h_f(T_f) - \\
&- \dot{m}_b^{exh}h_b(T_{exh}) - \dot{m}_b^{bb}h_b(T_{bb}) = \\
= &(\dot{m}_{a,b}^{exh} + \dot{m}_{a,b}^{bb})h_a^0(T_0) + (\dot{m}_{a,b}^{exh} + \dot{m}_{a,b}^{bb})h_a^{sens}(T_{int}) + \\
&+ (\dot{m}_{f,b}^{exh} + \dot{m}_{f,b}^{bb})h_f^0(T_0) + (\dot{m}_{f,b}^{exh} + \dot{m}_{f,b}^{bb})h_f^{sens}(T_f) - \\
&- \dot{m}_b^{exh}h_b^0(T_0) - \dot{m}_b^{exh}h_b^{sens}(T_{exh}) - \dot{m}_b^{bb}h_b^0(T_0) - \dot{m}_b^{bb}h_b^{sens}(T_{bb})
\end{aligned} \tag{4.82}$$

where $h_b^0(T_0)$, $h_b^{sens}(T_{exh})$ and $h_b^{sens}(T_{bb})$ are the burned gas enthalpy of formation and the sensible enthalpy increase of the burned products from the standard conditions to T_{exh} and T_{bb} respectively.

In Equation (4.82), two terms can be identified:

- The energy released during combustion:

$$\begin{aligned}
&(\dot{m}_{a,b}^{exh} + \dot{m}_{a,b}^{bb})h_a^0(T_0) + (\dot{m}_{f,b}^{exh} + \dot{m}_{f,b}^{bb})h_f^0(T_0) - \dot{m}_b^{exh}h_b^0(T_0) - m_b^{bb}h_b^0(T_0) = \\
&= \dot{m}_{a,b}h_a^0(T_0) + \dot{m}_{f,b}h_f^0(T_0) - \dot{m}_b h_b^0(T_0) = \\
&= \dot{m}_{f,b}\left[\frac{h_a^0(T_0)}{F_s} + h_f^0(T_0) - \frac{F_s+1}{F_s}h_b^0(T_0)\right] = \dot{m}_{f,b}H_v
\end{aligned} \tag{4.83}$$

- The variation of the sensible enthalpy of the species that are taking part on the stoichiometric combustion:

$$\begin{aligned}
&(\dot{m}_{a,b}^{exh} + \dot{m}_{a,b}^{bb})h_a^{sens}(T_{int}) + (\dot{m}_{f,b}^{exh} + \dot{m}_{f,b}^{bb})h_f^{sens}(T_f) - \\
&- \dot{m}_b^{exh}h_b^{sens}(T_{exh}) - \dot{m}_b^{bb}h_b^{sens}(T_{bb}) = \\
= &- \dot{m}_{f,b}^{exh}\left[\frac{F_s+1}{F_s}h_b^{sens}(T_{exh}) - \frac{h_a^{sens}(T_{int})}{F_s} - h_f^{sens}(T_f)\right] - \\
&- \dot{m}_{f,b}^{bb}\left[\frac{F_s+1}{F_s}h_b^{sens}(T_{bb}) - \frac{h_a^{sens}(T_{int})}{F_s} - h_f^{sens}(T_f)\right] = \\
= &- \dot{H}_b^{exh} - \dot{H}_b^{bb}
\end{aligned} \tag{4.84}$$

where $\dot{H}_b^{exh}$ and $\dot{H}_b^{bb}$ are the sensible enthalpy flows of the stoichiometric burned gases going out by the exhaust and blow-by.

Taking into account Equations (4.81) and (4.84), it is possible to obtain the net sensible enthalpy flow of the engine ($\dot{H}_g$) as:

$$\begin{aligned}\dot{H}_g &= (\dot{H}_{nb}^{exh} + \dot{H}_b^{exh}) + (\dot{H}_{nb}^{bb} + \dot{H}_b^{bb}) = \\ &= (\dot{m}_a + \dot{m}_f - \dot{m}_{bb})h_{exh}^{sens}(T_{exh}) + \dot{m}_{bb}h_{bb}^{sens}(T_{bb}) - \\ &\quad - \dot{m}_a h_a^{sens}(T_{int}) - \dot{m}_f h_f^{sens}(T_f)\end{aligned} \tag{4.85}$$

Taking into account that some part of the intake air and the injected fuel goes out by the exhaust or as blow-by, the last term of Equation (4.85) can be written as:

$$\begin{aligned}&\dot{m}_a h_a^{sens}(T_{int}) + \dot{m}_f h_f^{sens}(T_f) = \\ &= (\dot{m}_a^{exh} + \dot{m}_a^{bb})h_a^{sens}(T_{int}) + (\dot{m}_f^{exh} + \dot{m}_f^{bb})h_f^{sens}(T_{int}) = \\ &= \dot{m}_a^{exh}h_a^{sens}(T_{int}) + \dot{m}_f^{exh}h_f^{sens}(T_f) + \dot{m}_a^{bb}h_a^{sens}(T_{int}) + \dot{m}_f^{bb}h_f^{sens}(T_f)\end{aligned} \tag{4.86}$$

and by replacing in Equation (4.85), two terms can be identified:

- The **net sensible enthalpy flow at exhaust** ($\dot{H}_g^{exh}$):

$$\begin{aligned}\dot{H}_g^{exh} &= \dot{H}_{nb}^{exh} + \dot{H}_b^{exh} = \\ &= (\dot{m}_a + \dot{m}_f - \dot{m}_{bb})h_{exh}^{sens}(T_{exh}) - \dot{m}_a^{exh}h_a^{sens}(T_{int}) - \dot{m}_f^{exh}h_f^{sens}(T_f)\end{aligned} \tag{4.87}$$

- The **net sensible enthalpy flow of blow-by** ($\dot{H}_g^{bb}$):

$$\begin{aligned}\dot{H}_g^{bb} &= \dot{H}_{nb}^{bb} + \dot{H}_b^{bb} = \\ &= \dot{m}_{bb}h_{bb}^{exh}(T_{bb}) - \dot{m}_a^{bb}h_a^{sens}(T_{int}) - \dot{m}_f^{bb}h_f^{sens}(T_f)\end{aligned} \tag{4.88}$$

Taking into account Equations (4.81), (4.83), (4.84) and (4.85), the Equation (4.80) can be rewritten as:

$$\begin{aligned}\sum \dot{m}h &= \dot{m}_{f,b}H_v - \left(\dot{H}_{nb}^{exh} + \dot{H}_b^{exh} + \dot{H}_{nb}^{bb} + \dot{H}_b^{bb}\right) = \\ &= \dot{m}_{f,b}H_v - \dot{H}_g = \\ &= N_b + \sum \dot{Q}\end{aligned} \tag{4.89}$$

being

$$\dot{H}_g = \dot{H}_g^{exh} + \dot{H}_g^{bb} \tag{4.90}$$

where the sensible enthalpies of the exhaust gases and blow-by are obtained as:

$$h_{exh}(T_{exh}) = Y_{a,nb}^{exh} h_a^{sens}(T_{exh}) + Y_{f,nb}^{exh} h_f^{sens}(T_{exh}) + Y_b^{exh} h_b^{sens}(T_{exh}) \tag{4.91}$$

$$h_{bb}(T_{bb}) = Y_{a,nb}^{bb} h_a^{sens}(T_{bb}) + Y_{f,nb}^{bb} h_f^{sens}(T_{bb}) + Y_b^{bb} h_b^{sens}(T_{bb}) \tag{4.92}$$

Equation (4.89) shows how the addition of the enthalpy flows at the intake and exhaust can be expressed as the difference between the energy released ($\dot{m}_{f,b} H_v$) and the exhaust ($\dot{H}_g^{exh}$) and blow-by ($\dot{H}_g^{bb}$) sensible enthalpies.

In Equation (4.89), the total input fuel energy ($\dot{m}_f H_v$) can be considered instead of $\dot{m}_{f,b} H_v$, taking into account the incomplete combustion enthalpy ($\dot{H}_{ic}$) as:

$$\dot{H}_{ic} = \dot{m}_f H_v - \dot{m}_{f,b} H_v \tag{4.93}$$

thus:

$$\begin{aligned} \sum \dot{m} h &= \dot{m}_{f,b} H_v - \dot{H}_g = \\ &= \dot{m}_f H_v - \dot{H}_g - \dot{H}_{ic} = \\ &= N_b + \sum \dot{Q} \end{aligned} \tag{4.94}$$

where $\dot{H}_{ic}$ can be expressed in terms of incomplete combustion enthalpies at exhaust ($\dot{H}_{ic}^{exh}$) and blow-by ($\dot{H}_{ic}^{bb}$)[19] as:

$$\dot{H}_{ic} = \dot{m}_{f,ic} H_v = (\dot{m}_{f,nb}^{exh} + \dot{m}_{f,nb}^{bb}) H_v = \dot{H}_{ic}^{exh} + \dot{H}_{ic}^{bb} \tag{4.95}$$

Equation (4.94) indicates that the addition of the enthalpy flows equals the total input fuel energy minus the net sensible exhaust and blow-by enthalpies, and the enthalpy flow due to incomplete combustion. Taking into account Equation (4.90), Equation (4.94) can be rearranged as:

[19] $\dot{H}_{nb}^{bb}$ can be neglected except in particular operating conditions in which blow-by mass is important such as cold-start.

$$\dot{m}_f H_v = N_b + \sum \dot{Q} + \dot{H}_g^{exh} + \dot{H}_g^{bb} + \dot{H}_{ic} \tag{4.96}$$

This expression of the energy balance in the engine is assumed for convenience, being equivalent to Equation (4.1) and coherent with Figures 4.1, 4.2 and 4.3.

Note that in the rest of this work, particularly from Equation (4.1), the net sensible exhaust enthalpy (equivalent to $\dot{H}_g^{exh}$) is called $\dot{H}_{g,ex}$. Similarly, the net sensible enthalpy of blow-by (that is $\dot{H}_g^{bb}$) is called $\dot{H}_{bb}$. These variables are renamed to simplify the nomenclature and use only subscripts.

4.B Sensible enthalpy flows

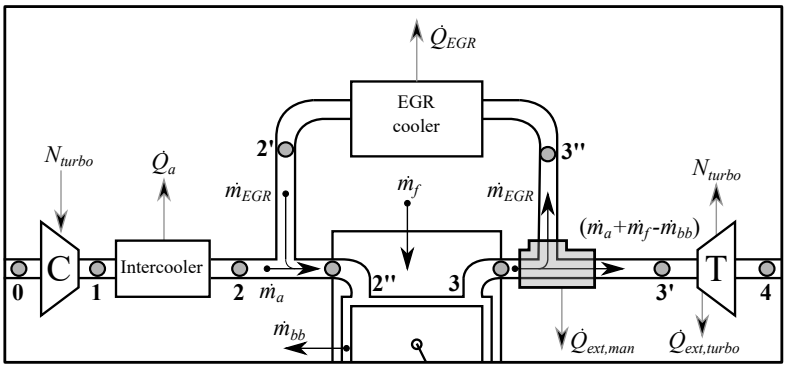

Figure 4.16. *Detail of the gas lines near the combustion chamber.*

As explained in Section 4.2.1, $\dot{H}_{g,ex}$ is defined as the enthalpy variation between points 0 and 4 of Figure 4.16. As can be seen, $\dot{H}_{g,ex}$ can be divided into three paths: the first corresponds to the enthalpy variation from ambient to intercooler outlet ($\dot{H}_{2,0}$), the second from intercooler outlet to turbine inlet, which is defined as internal net sensible flow of sensible enthalpy ($\dot{H}_{3',2} = \dot{H}_{g,in}$), and the third from turbine inlet to exhaust outlet ($\dot{H}_{4,3'}$):

$$\dot{H}_{g,ex} = \dot{H}_{2,0} + \dot{H}_{g,in} + \dot{H}_{4,3'} \tag{4.97}$$

where $\dot{H}_{2,0}$ can be written in terms of the energy variations in the intake line:

$$\begin{aligned} \dot{H}_{2,0} &= \dot{m}_a \ (h_2 - h_0) \\ &= N_{turbo} - \dot{Q}_a \end{aligned} \tag{4.98}$$

and similarly, $\dot{H}_{4,3'}$ is expressed in terms of the enthalpy variations in the exhaust:

$$\begin{aligned} \dot{H}_{4,3'} &= (\dot{m}_a + \dot{m}_f - \dot{m}_{bb}) \ h_4 - (\dot{m}_a + \dot{m}_f - \dot{m}_{bb}) \ h_{3'} \\ &= (\dot{m}_a + \dot{m}_f - \dot{m}_{bb}) \ (h_4 - h_{3'}) \\ &= -N_{turbo} - \dot{Q}_{ext,turbo} - \dot{Q}_{turbo} \end{aligned} \tag{4.99}$$

To determine $\dot{H}_{g,in}$, it is necessary to analyse the intake and exhaust manifolds (points 2 to 3' of Figure 4.16). Therefore, $\dot{H}_{g,in}$ can be calculated as:

$$\begin{aligned}\dot{H}_{g,in} &= \dot{H}_{3',2} \\ &= (\dot{m}_a + \dot{m}_f - \dot{m}_{bb})\ h_{3'} - \dot{m}_a\ h_2 - \dot{m}_f\ h_f\end{aligned} \tag{4.100}$$

Through the analysis of the mixture process in the intake manifold, the following expression can be written:

$$\begin{aligned}\dot{m}_a\ h_2 + \dot{m}_{\text{EGR}}\ h_{2'} &= (\dot{m}_a + \dot{m}_{\text{EGR}})\ h_{2''} \\ \dot{m}_a\ h_2 &= (\dot{m}_a + \dot{m}_{\text{EGR}})\ h_{2''} - \dot{m}_{\text{EGR}}\ h_{2'}\end{aligned} \tag{4.101}$$

and in the case of the exhaust manifold:

$$\begin{aligned}(\dot{m}_a + \dot{m}_f + \dot{m}_{\text{EGR}} - \dot{m}_{bb})\ h_3 &= (\dot{m}_a + \dot{m}_f - \dot{m}_{bb})\ h_{3'} + \\ &\quad + \dot{m}_{\text{EGR}}\ h_{3''} + \dot{Q}_{ext,man} \\ (\dot{m}_a + \dot{m}_f - \dot{m}_{bb})\ h_{3'} &= (\dot{m}_a + \dot{m}_f + \dot{m}_{\text{EGR}} - \dot{m}_{bb})\ h_3 - \\ &\quad - \dot{m}_{\text{EGR}}\ h_{3''} - \dot{Q}_{ext,man}\end{aligned} \tag{4.102}$$

By replacing Equations (4.101) and (4.102) in (4.100), the following expression is obtained:

$$\begin{aligned}\dot{H}_{g,in} = (\dot{m}_a + \dot{m}_f + \dot{m}_{\text{EGR}} - \dot{m}_{bb})\ h_3 - \dot{m}_{\text{EGR}}\ h_{3''} - \dot{Q}_{ext,man} - \\ - (\dot{m}_a + \dot{m}_{\text{EGR}})\ h_{2''} + \dot{m}_{\text{EGR}}\ h_{2'} - \dot{m}_f\ h_f\end{aligned} \tag{4.103}$$

where two terms can be identified:

- The heat rejection in the EGR cooler:

$$-\dot{Q}_{\text{EGR}} = \dot{m}_{\text{EGR}}(h_{2'} - h_{3''})$$

- The net flow of sensible enthalpy at ports ($\dot{H}_{g,ports}$) between points 2" and 3:

$$\dot{H}_{g,ports} = (\dot{m}_a + \dot{m}_f + \dot{m}_{\text{EGR}} - \dot{m}_{bb})\ h_3 - (\dot{m}_a + \dot{m}_{\text{EGR}})\ h_{2''} - \dot{m}_f\ h_f$$

Taking these terms into consideration, Equation (4.103) is finally expressed as:

$$\dot{H}_{g,in} = \dot{H}_{g,ports} - \dot{Q}_{\mathrm{EGR}} - \dot{Q}_{ext,man} \tag{4.104}$$

Replacing Equations (4.98), (4.99) and (4.104) in Equation (4.97), the relationship between $\dot{H}_{g,ex}$ and $\dot{H}_{g,ports}$ can be correlated as a function of the GEB terms as shown in Equation (4.105). This relationship is interesting to define the total heat transfer as presented in Section 4.3.1.

$$\dot{H}_{g,ex} = \dot{H}_{g,ports} - \dot{Q}_a - \dot{Q}_{\mathrm{EGR}} - \dot{Q}_{turbo} - \dot{Q}_{ext,turbo} - \dot{Q}_{ext,man} \tag{4.105}$$

Finally, the relationship between $\dot{H}_{g,ex}$ and $\dot{H}_{g,in}$ can be obtained by combining Equations (4.104) and (4.105) as:

$$\dot{H}_{g,ex} = \dot{H}_{g,in} - \dot{Q}_a - \dot{Q}_{turbo} - \dot{Q}_{ext,turbo} \tag{4.106}$$

Bibliography

[1] Smith L.A., Preston W.H., Dowd G., Taylor O. and Wilkinson K.M. "Application of a First Law Heat Balance Method to a Turbocharged Automotive Diesel Engine". *SAE Technical Paper 2009-01-2744*, 2009.

[2] Payri F., Olmeda P., Arnau F.J., Dombrovsky A. and Smith L. "External heat losses in small turbochargers: Model and experiments". *Energy*, Vol. 71, pp. 534–546, July 2014.

[3] Payri F., Olmeda P., Martín J. and Carreño R. "Experimental analysis of the global energy balance in a DI diesel engine". *Applied Thermal Engineering*, Vol. 89, pp. 545–557, October 2015.

[4] Heywood J.B. *Internal Combustion Engines Fundamentals*. McGraw-Hill, ISBN 978-0-07-028637-5, New York, 1988.

[5] Kokjohn S.L., Hanson R.M., Splitter D.A. and Reitz R.D. "Fuel reactivity controlled compression ignition (RCCI): a pathway to controlled high-efficiency clean combustion". *International Journal of Engine Research*, Vol. 12 n^o 3, pp. 209–226, 2011.

[6] Taylor J.R. *An Introduction to Error Analysis: The Study of Uncertainties in Physical Measurements*. University Science Books, ISBN 978-0-935702-75-0, Colorado, 2nd edition, 1997.

[7] ASTM. "Standard Test Method for Heat of Combustion of Liquid Hydrocarbon Fuels by Bomb Calorimeter". *ASTM Standards D240*, 2002.

[8] Tichý J. and Gautschi G. *Piezoelektrische Meßtechnik*. Springer, ISBN 978-3-642-52202-4, Berlin, 1980.

[9] Payri F., Luján J.M., Martín J. and Abbad A. "Digital signal processing of in-cylinder pressure for combustion diagnosis of internal combustion engines". *Mechanical Systems and Signal Processing*, Vol. 24 n^o 6, pp. 1767–1784, 2010.

Chapter 5

Sub-models development and improvement

Contents

5.1 Introduction

As commented in Chapter 4, some sub-models are required to perform the IGEB. Therefore, this chapter is addressed, on the one hand, to upgrade the reference sub-models, and on the other hand, to the development of new ones. A brief description of the models presented in this chapter is then provided:

- Due to the different features between the engines used in this work, it is necessary to account with suitable correlations to calculate the heat transfer to chamber for each one. As **Engine A** is a conventional TDI engine, the reference HT model presented in Chapter 3.3.6.1 is accurate enough; however, **Engine B** is a research engine, design to generate high *tumble* motion within the chamber. For this reason, a HT model that accounts for this motion is developed based on CFD studies and skip-fire tests.
- As will be discussed, the HT in the exhaust port during the open cycle is relevant for the GEB, for this reason, a dedicated model to determine the HT to ports, paying special attention to the HT to exhaust ports during the open cycle, is developed.
- As mentioned in Chapter 4.3, there is some HT between coolant and oil. The experimental determination is complex since it occurs between the coolant and oil circuits and the walls. For this reason, a simplified model to determine this term is presented.
- As the determination of the in-cylinder processes are affected for some uncertainties regarding the engine-installation, i.e. the compression ratio, the heat transfer, the TDC position, the engine mechanism deformation and the pegging pressure, a methodology to adjust them together based on multiple linear regression is proposed.
- The determination of HT to coolant and oil requires detailed friction and auxiliary losses estimation. For this reason, several models are proposed to determine these terms in different types of engines.

Along with the description of each sub-model, some results regarding their calibration are provided. The specific methodologies followed for their calibration in the engines used in this work are included in Chapter 6.

5.2 Heat transfer model improvement

5.2.1 Heat transfer model for engines with tumble motion

In this section, the comprehensive description of a semi-empirical HT model, which takes into account the tumble motion pattern in the combustion chamber is presented. The model was developed following three main stages as shown in Figure 5.1. Following, a description of each step is presented:

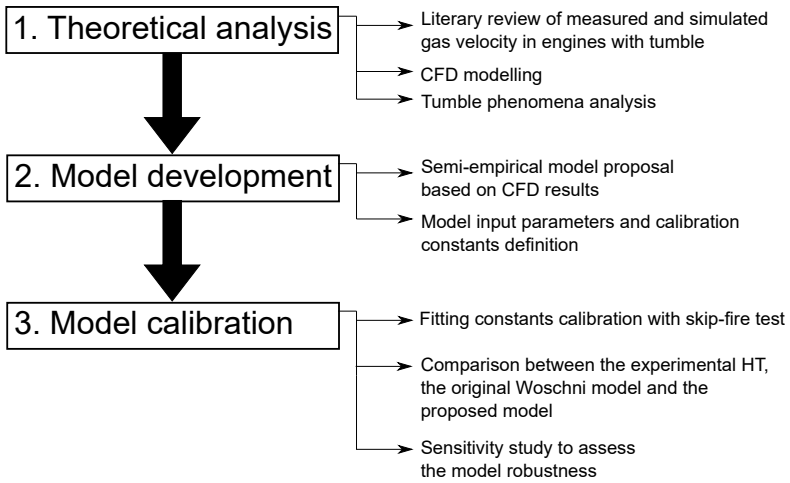

Figure 5.1. *Heat transfer model development methodology.*

1. **Theoretical analysis:** a well-grounding model requires a first deep understanding of the phenomena involved, and thus a comprehensive literature review regarding the tumble generation and dissipation processes, and the influence of the geometrical and operating parameters was carried out. In order to analyse the instantaneous gas evolution in the specific engine under investigation, CFD simulations of the complete skip-fire cycle were used. The results are discussed in detail with the aim of identifying the operating parameters that must be taken into account by the model.

2. **Model development:** starting from the CFD results, a semi-empirical model able to reproduce the gas velocity dissipation was developed. The model must be suitable for combustion diagnosis, and hence it considers

the main mechanisms involved in the tumble generation (geometry and operating conditions), but is still simple and keeps low computational cost in terms of power and time. The input parameters required consist mainly of those mean values generally acquired in a test bench.

3. **Model calibration:** this stage was carried out based on skip-fire measurements, which consist of skipping the injection of one cycle, thus obtaining a motoring measurement with the air management of a conventional combustion. The calibration focuses on the determination of the fitting constant values, with the objective of reducing the difference between the experimental and modelled HT. The skip-fire tests are used instead of motoring measurements to reproduce a realistic intake process in **Engine B**, being this specially important to ensure the scavenging process in two-stroke engines [1, 2], and also to get the same thermodynamic properties (pressure, temperature and gas composition) in the chamber during the compression stroke, and similar wall temperature in comparison with those of a conventional combustion, being this critical for the HT process.

   Once the model is calibrated, it is compared with the model for swirl motion included in CALMEC, which was described in Chapter 3.3.6.1. The objective is to asses the effect of the tumble gas velocity evolution on the HT. Finally, a sensitivity study is carried out with the objective of evaluating the model robustness against the effects of possible experimental and calibration uncertainties, being this information important when the model is transferred to different engines.

5.2.1.1 Tumble formation, evolution and dissipation

The determination of the specific generation and dissipation timing as well as the mechanisms that enhance or reduce the vortex formation requires dedicated experimental techniques [3, 4] or CFD simulations [5, 6]. Moreover, the tumble characteristics depend on the engine geometry and the operating conditions; however, there is a general agreement regarding the main process. The vortex formation starts few crank angle degrees after the IVO, when the air enters the chamber at high speed. Due to the combustion chamber geometry, the air is forced to sweep the wall and tries to form a small vortex; however, at this stage the piston is in the proximities of the TDC and the small size of the combustion chamber is not enough to allow the vortex formation. In

the early intake process (scavenging process in two-stroke engines), both intake and exhaust valves are simultaneously opened, thus some air is short-circuited as shown in Figure 5.2a, which also goes in detriment of the tumble generation. Figure 5.2b shows how during the intake stroke a small vortex is generated and continuously accelerated thanks to the angular moment added by the incoming air. This process lasts until the IVC, as shown in Figure 5.2c. The completely developed vortex is then accelerated along the compression stroke as a result of the angular momentum conservation (since the vortex radius decreases). At some stage of the compression stroke, the tumble is completely dissipated by the effect of friction with the wall and the increasingly smaller vortex radius, which forces the formation of turbulent microstructures as depicted in Figure 5.2d.

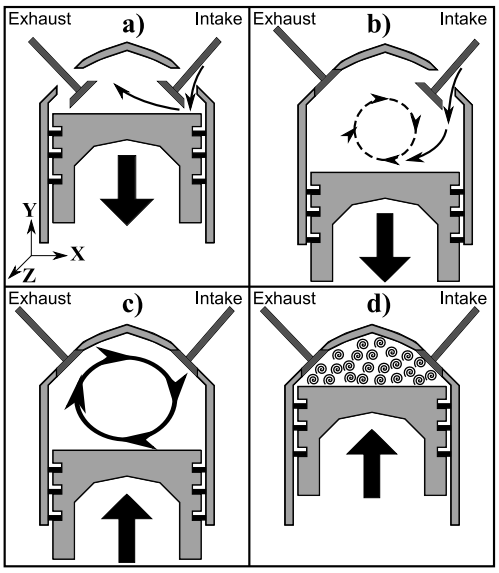

Figure 5.2. *Tumble evolution scheme.*

Regardless the specific application, the gas movement inside the chamber has a major importance in the HT coefficient calculation since the high rotational speed increases the HT before the TDC. Once the tumble dissipates, the resulting high turbulence still contributes in a smaller extent to the HT, extending the gas velocity influence several degrees after the TDC. It is interesting to highlight that, contrary to the tumble, the swirl is considered to be accelerated in the compression stroke, and decelerated similarly in the expansion stroke, resulting in a symmetrical effect on the HT. Thus, the swirl

model included in CALMEC is not suitable to accurately determine the effect of the gas velocity on the HT, when engines with tumble motion are evaluated. Therefore, a model that considers the instantaneous evolution of the spatially averaged gas velocity is necessary, taking into account the previous discussed characteristics. This objective is achieved in this work based on simplifications of the more complex 3D phenomena described in the next section.

5.2.1.2 CFD analysis

The computational model was built in the CONVERGE CFD platform. Full coupled open and closed cycle computations using the full intake/exhaust and cylinder geometries were carried out since the combustion chamber is non-symmetric. The computational domain at the intake valve closing angle (IVC) is shown in the left plot from Figure 5.3. The CFD code uses a structured Cartesian grid with base cell size of 3 mm. Three additional grid refinements linked to flow velocity and temperature were performed by means of an adaptive mesh refinement as well as a fixed three level refinement within the spray region.

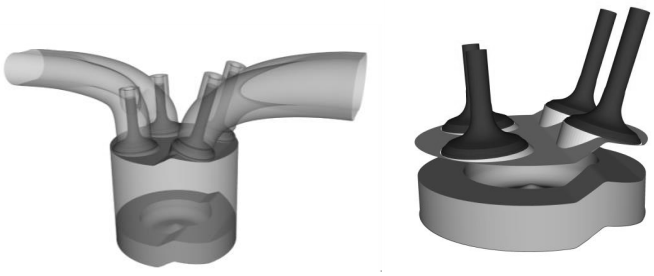

Figure 5.3. *Sketch of the cylinder head designed for the 2-stroke engine architecture (Patent Renault FR2931880).*

The injection rate profile was generated from the experimental database available after the injector characterization (mass flow rate and spray momentum flux) performed in dedicated test rigs. The diesel injection is simulated by the standard droplet discrete model. Diesel fuel physical properties are defined using Diesel 2 as surrogate. Spray atomization and break-up are simulated by means of the KH-RT model. Turbulent flow is modelled by means of the RNG $k-\varepsilon$ model with wall-functions to account for wall heat transfer. The combustion chamber wall temperatures are calculated by means of the

lumped conductance model described in Chapter 3.3.6.2. The size of each node was set to ensure that Biot number of each element is lower than 0.1. To set the boundary conditions for CFD calculation, the combustion chamber is divided in three parts (liner, fire deck and piston) and the mean wall temperature of each part is calculated by weighting the nodes temperature with the area in contact with the gas. Concerning combustion modelling, a direct integration of detailed chemistry approach was used by means of the CONVERGE code and the SAGE solver. Finally, the chemical properties of Diesel fuel are defined using n-heptane as surrogate.

The set-up and validation of the CFD model was performed at the reference case (see Figure 5.4) operating in CDC. The quality of the model was evaluated by comparing its combustion and emissions results with those obtained experimentally in the engine as presented in Table 5.1. Figure 5.4 shows the comparison between the CFD and experimental cylinder pressure and RoHR profiles. The CFD model performance is considered enough to be used for evaluating the gas flow motion within the chamber and the HT from the gas to the combustion chamber walls.

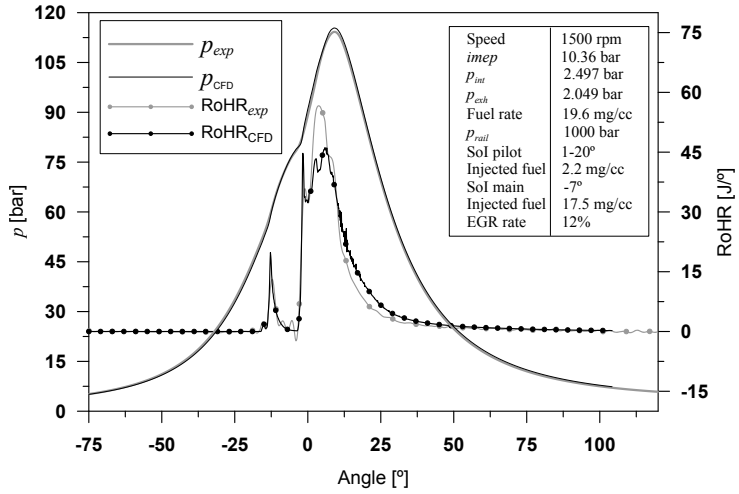

Figure 5.4. *CFD Validation.*

The main flow pattern in the cylinder in terms of the gas speed is shown in Figure 5.5. The patterns presented correspond to the same diametrical view but different instants during the intake stroke, starting close to the BDC until

	CFD	**Experiment**
CO	2,2017 mg/s	3,7500 mg/s
soot	0,0565 mg/s	0,0670 mg/s
HC	0,0032 mg/s	0,3000 mg/s
NO_x	5,4780 mg/s	5,9000 mg/s

Table 5.1. *CFD emissions validation.*

reaching the IVC. In the view plane, the intake and exhaust ports are aligned, thus allowing the best outline of the intake process. Figure 5.5a confirms how at the beginning of the intake process the air flows into the chamber at high speed. A clear vortex is still not defined but a small rotary structure is observed close to the intake port. After some crank angle degrees (Figure 5.5b), a main rotary structure is evident close to the upper centre of the cylinder, being slightly higher when the exhaust port is closed (Figure 5.5c). In Figure 5.5d, when the IVC is reached, the vortex is completely formed and the speed vectors are slightly lower than in the previous time step, this is explained by the end of the intake process and the energy loss due to friction between the gas and the cylinder walls.

The average tumble ratio (TR) is presented in Figure 5.6, where the X-Y plane (defined in Figure 5.2a) is sketched. Results obtained confirm how the TR in the Z-Y plane and the swirl ratio (SR) in the X-Z plane are negligible. Figure 5.6 shows that the tumble formation begins in the piston upward stroke about -175° ATDC, reaching its maximum around -130° ATDC (before the IVC). It means that the tumble dissipation starts in the compression stroke, which is in accordance with that found in the literature [3]. As observed in Figure 5.6, the tumble is dissipated close to TDC.

To understand the TR effect, the model to estimate the HT coefficient presented in Chapter 3.3.6.1 is rewritten in Equation (5.1):

$$h = C\ D^{b-1}\ p^{b}\ T^{0.75-1.62b}\ v_g^{b} \tag{5.1}$$

where the gas velocity (v_g) is determined as:

$$v_g = C_{w1}\ c_m + C_{w2}\ c_u + C_2\ \frac{V_d\ T_{\mathrm{IVC}}}{V_{\mathrm{IVC}}\ p_{\mathrm{IVC}}}(p - p_0) \tag{5.2}$$

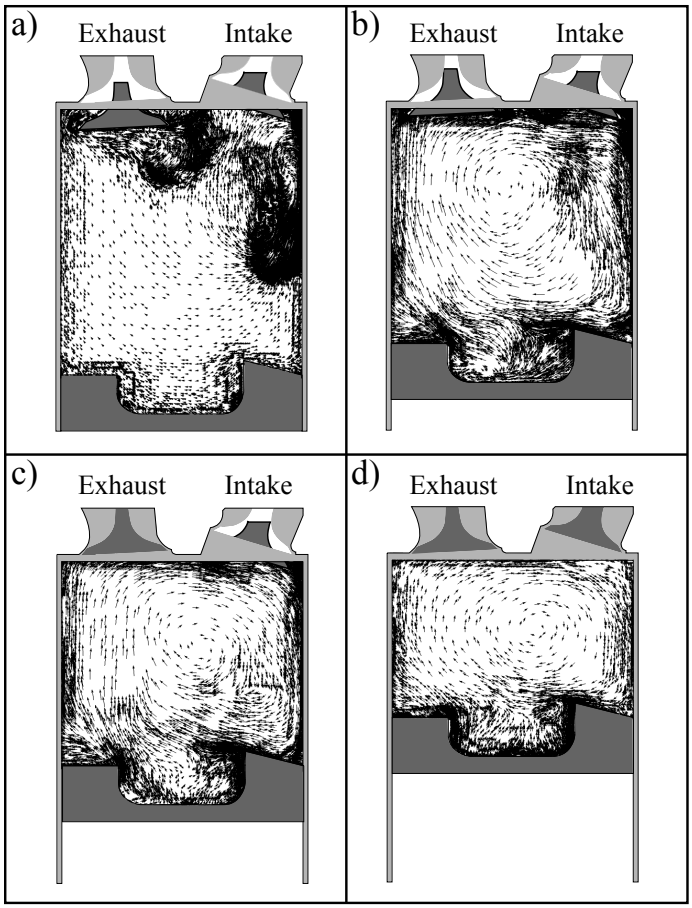

Figure 5.5. *CFD in-cylinder gas speed evolution. a)-174 °ATDC, b)-132 °ATDC, c)-116 °ATDC, d)-93 °ATDC (IVC).*

Note that higher TR boosts the HT from the gases to the walls by increasing the value of the gas velocity in Equation (5.1). In Figure 5.7, the HT obtained with CFD simulations ($\dot{Q}_{\mathrm{CFD}}$) is presented, along with a HT calculated accounting only for the piston speed term ($\dot{Q}_{c_m}$), but neither swirl nor tumble. $\dot{Q}_{c_m}$ is calculated by adjusting the constant C_{w1} of Equation (5.2) in order to fit $\dot{Q}_{c_m}$ to $\dot{Q}_{\mathrm{CFD}}$ during the expansion stroke (keeping $c_u = 0$). This step was performed to assess the effect of the vortex (swirl or tumble) on the HT, by determining the spatially averaged gas velocity. The CFD spatially averaged gas velocity (v_{CFD}) presented in Figure 5.7 is the velocity generated by

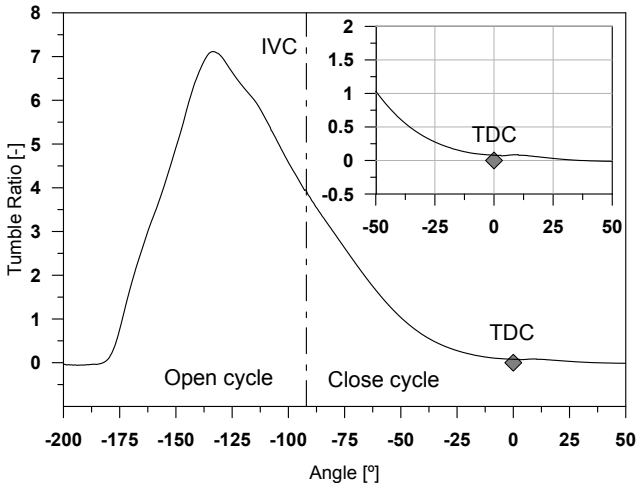

Figure 5.6. *Tumble ratio evolution in a perpendicular plane of the cylinder axis.*

the tumble vortex. It is calculated from a HT coefficient h' obtained from the difference between $\dot{Q}_{\mathrm{CFD}}$ and $\dot{Q}_{c_m}$ as presented in Equation (5.3), then v_{CFD} is obtained by combining Equations (5.3) and (5.1) as presented in Equation (5.4). It is interesting to notice how the v_{CFD} presented in Figure 5.7 becomes zero near to 30° ATDC, although the tumble has been completely dissipated. This can be explained by the turbulence generated as result of the tumble destruction, which has an important effect in the HT coefficient since it occurs in the proximities of the TDC, where the in-cylinder pressure and the temperature difference between gas and walls are the highest.

$$h' = \frac{\dot{Q}_{\mathrm{CFD}} - \dot{Q}_{c_m}}{A\ \Delta T} \tag{5.3}$$

$$v_{\mathrm{CFD}} = \sqrt[0.8]{\frac{h'}{C\ D^{-0.2}\ p^{0.8}\ T^{-0.55}}} \tag{5.4}$$

The results obtained from the CFD model regarding the description of the shape of v_{CFD}, allow the development of a HT model that accounts for the instantaneous tumble velocity characteristics. The HT model proposed in this work is detailed described in the following section.

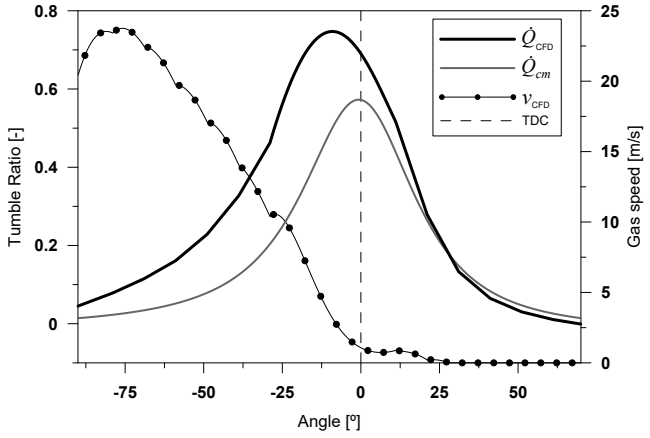

Figure 5.7. *CFD HT and tumble gas velocity.*

5.2.1.3 Model adaptation

The last term in Equation (5.1) corresponds to the gas velocity v_g, it is replaced by a gas velocity $v_{g,t}$, which is assumed to be dependent on the mean piston speed c_m, the gas velocity due to tumble c_t and a velocity term due to combustion as follows:

$$v_{g,t} = C_{t1}\ c_m + C_{t2}\ c_t + C_2\ \frac{V_d\ T_{\mathrm{IVC}}}{V_{\mathrm{IVC}}\ p_{\mathrm{IVC}}}\ (p - p_0) \tag{5.5}$$

where C_{t1}, C_{t2} and C_2 are proportionality constants.

As can be observed, first and last terms of Equation (5.5) are the same as in the reference model for swirl (Equation (3.26)); however, the second term was replaced to specially account for the tumble. Thus, c_t is assumed to be:

$$c_t = \bar{v}_m\ f_w \tag{5.6}$$

where $\bar{v}_m$ is a characteristic gas mean velocity during the intake process and f_w is a dissipation function for the tumble gas velocity.

Starting from the results obtained for the gas velocity in the CFD simulations, it was found that an exponential Wiebe-like function (Equation (5.7)) suitably follows the trend observed for the tumble gas velocity.

$$f_w(\alpha) = exp^{a(\frac{\alpha-\alpha_0}{\alpha_f-\alpha_0})^m} \tag{5.7}$$

where f_w is a S-shape function, with values between 0 and 1, m is a fitting constant used to adjust the shape, α is the crank angle, α_0 and α_f are angles related to the begin and the end of the gas velocity dissipation process, and $a = -6.907$ is a constant value adjusted to ensure a $v_{g,t}$ dissipation of 99.9% at $\alpha = \alpha_f$.

The mean gas velocity during the intake process $\bar{v}_m$ can be determined by means of the mean tumble ratio of the engine (MTR), which is defined as:

$$\text{MTR} = \frac{60\ \omega_t}{2\pi\ n} \tag{5.8}$$

where ω_t is the vortex angular speed in rad/s and n is the engine speed in rev/min. Assuming a vortex radius equals to the cylinder radius ($D/2$), $\bar{v}_m$ can be determined as:

$$\bar{v}_m = \frac{\pi\ n\ \text{MTR}\ D}{60} \tag{5.9}$$

To determine the mean tumble ratio of the engine, a prior calibration of the air flow during the intake is required, either by measuring in a flow test rig or by means of CFD modelling. As this information is not always available an alternative process to determine $\bar{v}_m$ is proposed. Considering the parameters that can affect the vortex formation, the mean gas velocity during the intake process $\bar{v}_m$ was defined as:

$$\bar{v}_m = \frac{360\ \eta_{tr}\ \dot{m}_a}{A_{eff}\ \bar{\rho}_a\ \Delta\alpha_{\text{IVO}-\text{IVC}}} \tag{5.10}$$

Equation (5.10) takes into account the air mass going into the cylinder ($\dot{m}_a$), the intake process duration ($\Delta\alpha_{\text{IVO}-\text{IVC}}$), the mean air density during the intake process ($\bar{\rho}_a$), the trapping efficiency[1] (η_{tr}) and the effective intake valve area (A_{eff}). $\bar{\rho}_a$ was calculated considering a mean gas in-cylinder temperature $\bar{T}_{cyl,int}$, estimated assuming an isentropic process between the intake and the in-cylinder mean pressures as follows:

[1]The experimental determination of the trapping efficiency was presented in Chapter 3.2.2.1.

$$\bar{T}_{cyl,int} = \bar{T}_{int} \left(\frac{\bar{p}_{cyl,int}}{\bar{p}_{int}} \right)^{\frac{\gamma-1}{\gamma}} \tag{5.11}$$

being $\bar{T}_{int}$ and $\bar{p}_{int}$ the mean temperature and pressure at the intake settling chamber, $\bar{p}_{cyl,int}$ the mean in-cylinder pressure during the intake process and γ the adiabatic gas constant. Finally, the instantaneous gas velocity $v_{g,t}$ is defined in Equation (5.12), which was determined by combining Equations (5.5), (5.6), (5.7) and (5.10).

$$v_{g,t}(\alpha) = C_{t1}\ c_m + C_{t2}\ \bar{v}_m\ exp^{-6.907(\frac{\alpha-\alpha_0}{\alpha_f-\alpha_0})^m} + C_2 \frac{V_d T_{IVC}}{V_{IVC} p_{IVC}} (p - p_0) \tag{5.12}$$

5.2.1.4 Model calibration

The model calibration was carried out on the basis of reducing the difference between the experimental HT calculated from polytropic exponent ($\dot{Q}_n$) and the modelled one, following the methodology explained in Section 5.3 and using skip-fire test, thus, the last term of Equation (5.12) that accounts for the combustion effect on HT was not included ($C_2 = 0$). Therefore, the calibration consisted on the determination of the function shape parameters (i.e. α_0, α_1 and m) and the proportionality constants (i.e. C_{t1} and C_{t2} in Equation 5.12). Since the increase of variables to be adjusted could result in undesired behaviour and non-convergence [7], a constant ratio $r_t = C_{t1}/C_{t2}$ was defined to assure the model stability and generality.

As mentioned, the model calibration was made on a set of skip-fire tests, whose main operating conditions are presented in Table 5.2. This experimental work consist on a sweep of engine speed and Δp, this last defined as $p_{int} - p_{exh}$ in **Engine B**.

The final adjusted values obtained from the calibration in **Engine B** are presented in Table 5.3.

The comparison between CFD and model gas velocities is presented in Figure 5.8 along with the resulting heat transfer of an operating point at 1500 rpm and Δp of 400 mbar. As can be seen, the velocities are in good agreement, being remarkable how the model follows the trend observed in the CFD simulation. However, there are some differences between the gas velocity obtained from the CFD and the model, mainly due to the adjustment criterion

Speed [rpm]	Δp* [mbar]	**Air mass flow rate** [g/s]	η_{tr} [%]
1200	300	7.4	69
1200	400	10.1	72
1200	500	12.2	84
1500	300	9.6	78
1500	400	11.0	79
1500	500	13.4	79
1800	300	8.7	80
1800	400	11.4	84
1800	500	14.7	85

*Δp is defined as $p_{int} - p_{exh}$ in **Engine B**.

Table 5.2. *Skip-fire test measured.*

Parameter	**Value**
m	6
a	-6.907
α_0	-34.15° ATDC
α_f	14.9° ATDC
C_{t1}	1.05
C_{t2}	0.53
r_t	2

Table 5.3. *Model adjusted parameters.*

that is based on the reduction of the HT difference instead of that of the gas velocity itself. This criterion is reasonable because the final objective is to accurately calculate the HT; therefore the HT adjustment observed in Figure 5.8 is better than that obtained for the gas velocity.

To allow a fair comparison between the experimental HT ($\dot{Q}_n$), the HT obtained with the proposed model ($\dot{Q}_t$) and the reference Woschni model ($\dot{Q}_w$), this last one was also calibrated for the engine tested through the adjustment of the constants C_{w1} and C_{w2} of Equation (3.26). In Figure 5.9, the HT obtained with each model in a speed sweep with a fixed Δp of 400 mbar are

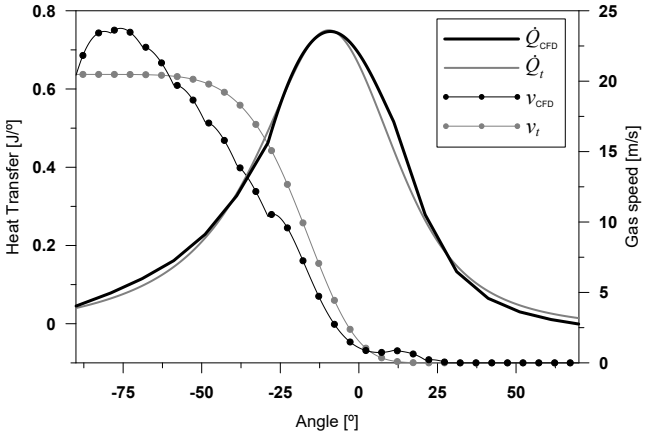

Figure 5.8. *Gas velocity and HT comparison between CFD and model results at 1500 rpm and 400 mbar.*

shown. It is evident that $\dot{Q}_t$ fits better with $\dot{Q}_n$ than $\dot{Q}_w$; therefore, some qualitative and quantitative remarks can be underlined:

- Low discrepancy is observed between the instantaneous evolution of $\dot{Q}_n$ and $\dot{Q}_t$, which indicates that in the studied cases, $v_{g,t}$ accounts well for the spatially averaged gas velocity. The good agreement between the maximum $\dot{Q}_n$ and $\dot{Q}_t$ observed in Figure 5.9 indicates that $\bar{v}_m$ can retain the information regarding the operating condition variations. Moreover, the C_{t2} value close to 1 (see Table 5.3) indicates that $\bar{v}_m$ is also representative of the maximum gas velocity in the combustion chamber.

- In motoring tests, the swirl-model used in Equation (3.26) assumes that the vortex is accelerated in the compression stroke, and since no friction between gas and walls is considered, the vortex is symmetrically decelerated in the expansion stroke. Therefore, $\dot{Q}_w$ is almost symmetric with respect to the TDC, having its maximum value few degrees before TDC. The slight asymmetry of $\dot{Q}_w$ is caused by the effect of the higher pressure and temperature before the TDC in the HT estimation (see Equation (3.25)). In the case of $\dot{Q}_t$, the maximum value is reached about -12° ATDC, which is more reasonable considering the mechanism of the tumble dissipation explained in Section 5.2.1.1.

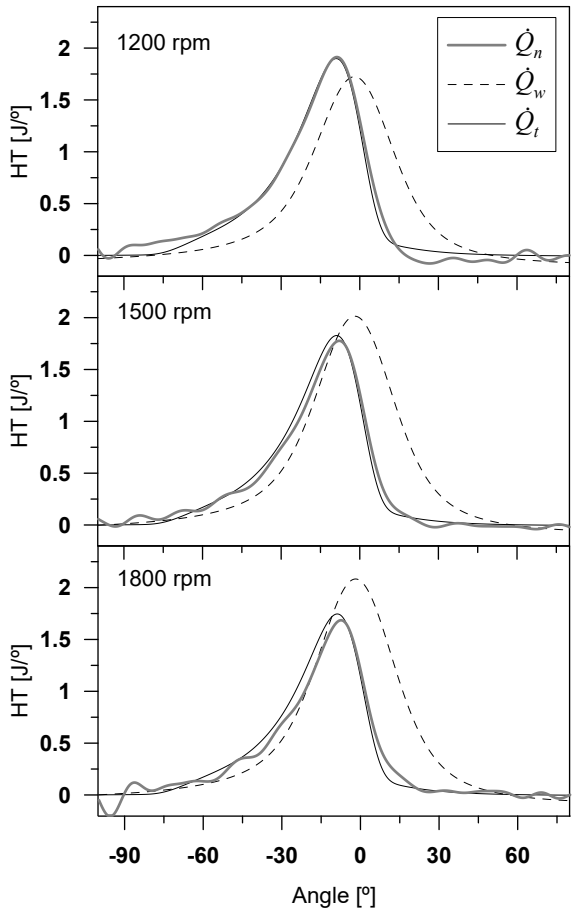

Figure 5.9. *Heat transfer comparison (speed sweep and $\Delta p = 400$ mbar).*

- The RMSE of the complete experimental matrix is included in Table 5.4. It is observed how the uncertainty of $\dot{Q}_t$ is remarkably lower than that of $\dot{Q}_w$ in all the cases, showing an average improvement of about 70%. This corroborates the better performance of the proposed model in all the operating range. In the particular case of 1800 rpm and Δp of 500 mbar, the uncertainty reduction of $\dot{Q}_t$ is lower than in the rest of the operating points (being about 40%), this is probably due to the

higher experimental uncertainty at this operating condition, since this point shows the highest noise-to-signal ratio.

Speed [rpm]	Δp [mbar]	Q_w **RMSE** [J/°]	Q_t **RMSE** [J/°]	**Improvement** [%]
1200	300	0.30	0.09	70
1200	400	0.33	0.08	77
1200	500	0.38	0.10	74
1500	300	0.31	0.08	75
1500	400	0.30	0.07	76
1500	500	0.31	0.12	61
1800	300	0.28	0.05	82
1800	400	0.28	0.08	72
1800	500	0.31	0.18	41

Table 5.4. *RMSE of the HT computation by using the Woschni model and the proposed model.*

5.2.1.5 Sensitivity analysis

In order to determine the robustness of the proposed model due to uncertainties of the parameters involved in Equation (5.5), a sensitivity study of the most relevant variables is performed. This study is interesting if the model is applied in different engines, since obtaining the input variables required is not always possible. In this sense, knowing the key parameters allows performing properly assumptions and simplifications to obtain reliable results.

Equation (5.5) indicates that the parameters affecting the gas velocity in motoring conditions are the calibration constants (C_{t1} and C_{t2}), the characteristic gas velocity ($\bar{v}_m$) and the exponential function (f_w). By observing Equation (5.10), it can be concluded that the product $\eta_{tr}\dot{m}_a$ is the only uncertainty affecting $\bar{v}_m$, considering that A_{eff} and $\Delta\alpha_{\mathrm{IVO-IVC}}$ are defined by the engine geometry, meanwhile $\dot{m}_a$ is subject of experimental uncertainty and η_{tr} is not usually measured. Regarding f_w, Equation (5.7) shows that the constant a is mathematically settled, therefore only the exponent m and the angles α_0 and α_f can vary. It is important to remark that these three parameters cannot be simultaneously adjusted, since a different exponent would lead to different α_0 and α_f; therefore, in this study the exponent m was kept constant and

only the angles were varied. A sensitivity study was carried out to determine the variation of $\eta_{tr}\dot{m}_a$, α_0 and α_f that produces a given uncertainty in the HT computation. Each parameter is swept to produce maximum variations of $\pm 20\%$ in the accumulated HT, with steps of $\pm 5\%$.

The results presented in Figure 5.10 indicate that the term $\eta_{tr}\dot{m}_a$ has a linear effect, and a variation of 1.4% in $\eta_{tr}\dot{m}_a$ results in a variation of 1% in Q_t. α_f shows also a linear trend, and a variation of 0.5° produces an uncertainty of 1% in Q_t, so the model is very sensitive to this parameter and it should be carefully calibrated. Finally α_0 has a different behaviour depending on its value: advancing α_0 about 1.5° results in a reduction of Q_t about 1% (being this trend linear); however, delaying α_0 leads to a non-linear tend, thus a variation of 14° leads to the maximum Q_t uncertainty of 5%, whilst a higher delay of α_0 yields to lower Q_t uncertainty. This behaviour is explained by the instantaneous evolution of $\dot{Q}_t$ which is discussed later.

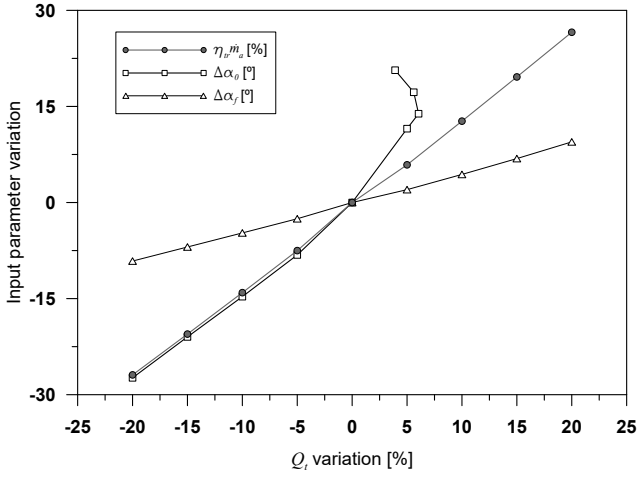

Figure 5.10. *Sensitivity analysis.*

To analyse the instantaneous effect of each parameter on $\dot{Q}_t$, a reference well-adjusted test at 1200 rpm and Δp 400 mbar is compared with the HT resulting by considering the uncertainties analysed in the previous paragraph. The results shown in Figure 5.11 correspond to variations of $\pm 10\%$ on Q_t except in the case of delaying α_0, where the maximum uncertainty in Q_t is 5%. $\dot{Q}_w$ is also presented in Figure 5.11 with the objective of highlighting

how, in spite of the parameters variation, the qualitative fit of the proposed model is always better than the reference Woschni model. Some remarkable effects on the instantaneous HT profile are:

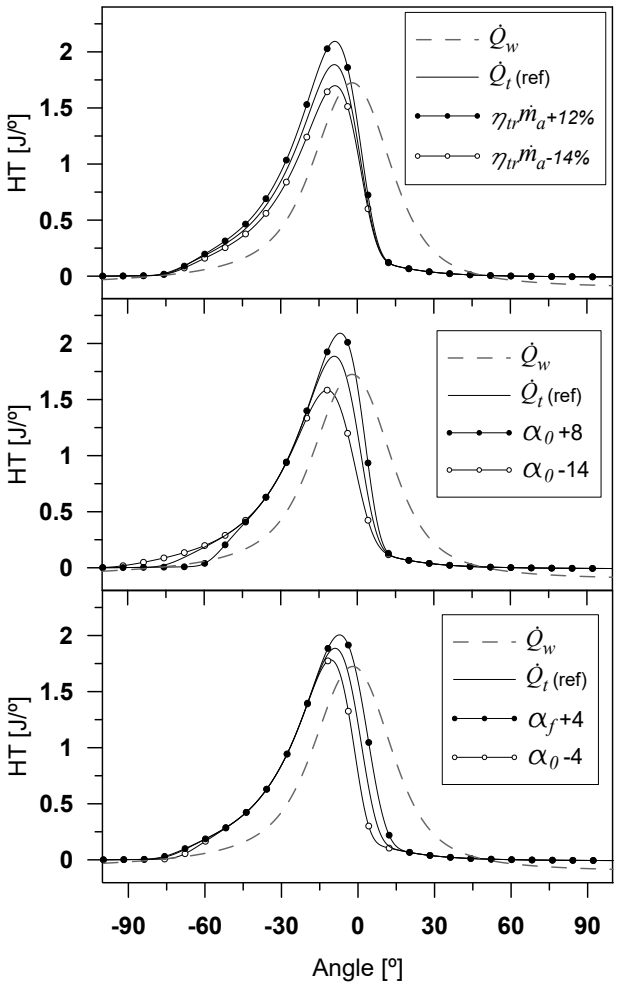

Figure 5.11. *HT sensitivity at 1200 rpm and* $\Delta p = 400$ *mbar.*

- Positive or negative variations of $\eta_{tr}\dot{m}_a$ affect directly the maximum HT reached, being the instantaneous difference more evident between -30° ATDC and 20° ATDC.

- Advancing α_0 has a moderate effect on the HT shape, while its effect on the maximum HT is higher. It is interesting to notice how advancing α_0 results in slightly more HT in the early compression stroke. It is explained because the model considers a slightly higher tumble during this phase; however, at the beginning of compression, the pressure and temperature of the chamber are low, thus the global effect on the HT is small. Since the tumble dissipation starts earlier, a lower HT is observed in the proximities of the TDC, which is not compensated by the small increase at the beginning of the compression stroke so the accumulated HT decreases.

- Delaying α_0 has a major effect on the HT shape, reducing significantly the HT at the beginning of the compression stroke and increasing the HT close to the TDC. This HT increment close to the TDC is compensated by the reduction at the beginning of compression, thus the HT change is limited (about 5%) as can be seen in the Figure 5.10. In spite of this moderate uncertainty, the main issue of delaying α_0 is the deformation of the $\dot{Q}_t$, which results in higher HT peaks but abnormally low HT in the compression stroke.

- The effect of α_f can be observed between the maximum HT peak and the end of the tumble dissipation as can be seen in Figure 5.11. Delaying α_f results in a longer dissipation process, and hence higher HT. Consequently, advancing α_f has the contrary trend. The shape of $\dot{Q}_t$ is moderately affected by the variation of this parameter, but due to the cumulative effect on the mean HT, an accurate determination of α_f is important.

From this analysis, it can be concluded that the model is reliable enough to be generally applied for engines with tumble, and it is robust against uncertainties of the parameters in reasonable ranges, performing better in both the instantaneous evolution and the mean HT determination than the reference HT model, which considers swirl.

5.2.1.6 Combustion analysis

As described, the model development and calibration have been performed using motoring cycles, obtained through the skip-fire method. However, the model was designed for being applied to combustion cycles, where

proper combustion diagnosis and energy thermal characterization require accurate HT estimation. To assess the performance of the proposed model in combustion, it is compared with the reference model in firing conditions. Figure 5.12, shows the HT and HR obtained with the reference and proposed models. As combustion phenomena has not been considered in previous analysis, a final model adjustment is required to account for the effect of the combustion evolution in the gas speed estimation. With this purpose, the combustion constant C_2 in Equations (3.26) and (5.12) was adjusted for both models, in order to reach a maximum cumulative HR equal to the chemical energy of the fuel (minor losses due to unburned products were neglected). From the analysis of the HT and HR profiles, the following conclusions can be highlighted:

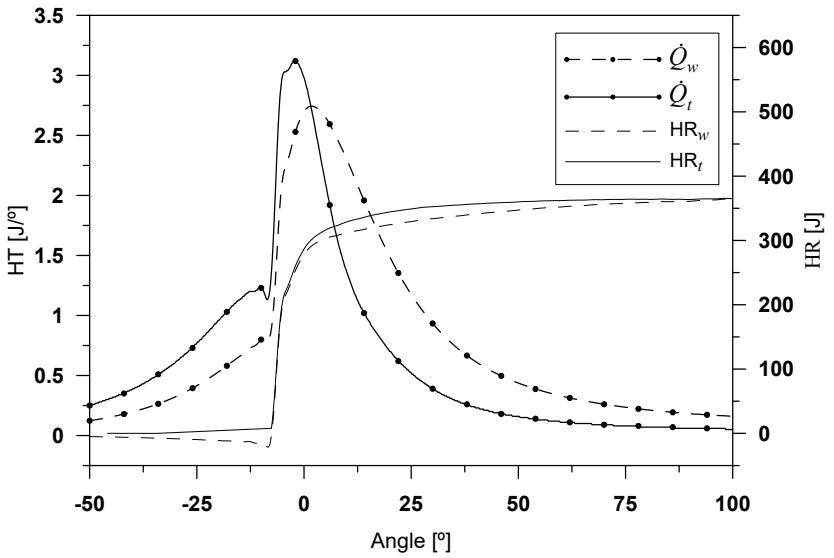

Figure 5.12. *HT and HR in a combustion test at 1500 rpm and 3.6 bar of imep.*

- The HR calculated with the reference HT model $\dot{Q}_w$ (HR_w) shows a negative slope during the compression stroke leading to negative values, whilst the HR calculated with the proposed HT model $\dot{Q}_t$ (HR_t) follows a flat shape until the start of combustion (about -10° ATDC). As HR stands for the chemical energy release during the combustion process,

negative values have no physical meaning. The better performance of HR_t is attained by considering the tumble effect on the HT during compression, leading to high $\dot{Q}_t$ as explained in section 5.2.1.4 and clearly seen in Figure 5.12.

- During the fast combustion process (from -10° ATDC to TDC) there is no clear difference between HR_w and HR_t; however, in the final combustion stage taking place during the expansion stroke, HR_w has a higher slope than HR_t. In CDC is common that only a small amount of residual fuel remains unburned after the fast combustion stage since the injection event enhances the fuel/air mixing, thus the proposed model behaves better because it shows a flatter shape after 20-25° ATDC. This trend can be explained taking into account that the tumble vortex is completely dissipated around TDC, and hence the combustion term has the main role in the HT along the expansion. However, the velocity terms of the reference model in Equation (3.26) lead to a symmetric evolution of the HT with respect to the TDC (see Figure 5.9), having a relevant weight after TDC and clearly overestimating the HT, and hence the HR, during late combustion.

This example confirms the importance of accurately accounting for the tumble motion in the HT estimation and how the proposed model definitely improves the HR calculation. Both, HT and HR, will be conveniently used in the methodology described in Section 5.3 for the convective HT model adjustment in the chamber of **Engine B**. Thus, starting from an accurate and validated model is mandatory.

5.2.2 Heat transfer to the ports

As presented in Chapter 4.2.2, the IGEB requires the determination of the HT to the ports ($\dot{Q}_{ports}$). This term can be about 30% of the total HT losses and can reach values about $10\%\dot{m}_f H_v$ [8]; therefore, having a reliable estimation of $\dot{Q}_{ports}$ is crucial for a proper GEB modelling. The specific energy distribution to each element of the intake/exhaust ports is achieved thanks to the lumped model described in Chapter 3.3.6.2; however, the main input of this model is the HT from exhaust gases to the port walls that will be determined through a physical convective model. CALMEC and SiCiclo include a simple model based on conventional convective correlations [9] that does not

consider the instantaneous exhaust temperature variation, thus, the model has to be improved to achieve higher sensitivity with this temperature. Thereby, the proposal presented in this section takes into consideration the thermal differences between intake/exhaust ports as well as in the open/closed cycles.

The HT from gases to the walls is mainly due to convection, thus the Newton's law of cooling can be used through prior determination of the heat transfer coefficient, which can be obtained from a convective HT relationship between Nusselt (N_u), Reynolds (R_e) and Prandtl (Pr) numbers as follows:

$$N_u = a\ R_e^{m1}\ P_r^{m2} \tag{5.13}$$

where a, m_1 and m_2 are constant values and the N_u, R_e and P_r are defined as:

$$N_u = \frac{h\ d_v}{k} \tag{5.14}$$

$$R_e = \frac{d_v\ v\ \rho}{\mu} \tag{5.15}$$

$$P_r = \frac{c_p\ \mu}{k} \tag{5.16}$$

being d_v the valve diameter and h, k, v, ρ and μ the heat transfer coefficient, thermal conductivity, speed, density and viscosity of the gas respectively, which characterize its fluid and thermal properties. Note that the terms involved in Equations (5.14) to (5.16) correspond to known geometrical and thermodynamic parameters except h, and hence Equation (5.13) can be solved for its determination.

In the case of k and μ, the empirical correlations proposed by Dolz [9] can be used to their determination:

$$k = -8.34 \times 10^{-9}\ T^2 + 7.05 \times 10^{-5}\ T + 6.51 \times 10^{-3} \tag{5.17}$$

$$\mu = 1.16 \times 10^{-6}\ \frac{T^{1.5}}{T + 110.4} \tag{5.18}$$

where T is the temperature at which they are calculated.

To solve Equation (5.13), it is important to pay special attention to the differences in the thermo-fluid-dynamic processes between ports. To help in

this explanation, the CFD results of the spatially-averaged gas temperature evolution at intake (T_{ip}) and exhaust (T_{ep}) ports of **Engine B** are presented in Figure 5.13. Complementary, the temporal-averaged temperature at intake ($\bar{T}_{ip}$) and exhaust ($\bar{T}_{ep}$) are presented in Table 5.5 along with the deviation at different cycle stages. The following observations can be made:

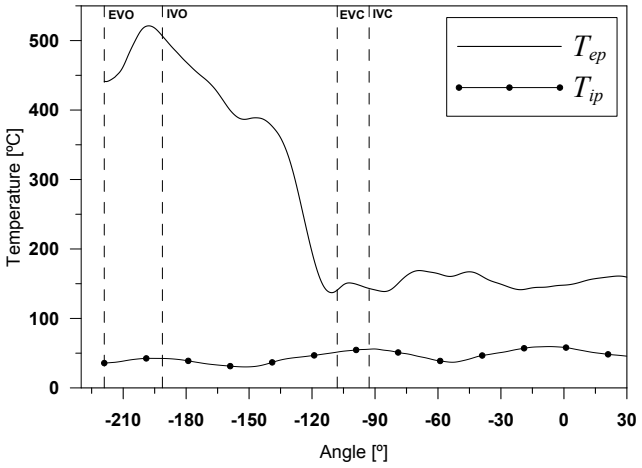

Figure 5.13. *Cylinder, intake and exhaust instantaneous temperatures along the open cycle. CFD simulation on Engine B.*

Cycle	$T_{ip} = \bar{T}_{ip} \pm \Delta T$ [°C]	$T_{ep} = \bar{T}_{ep} \pm \Delta T$ [°C]
Complete	47 ± 8	226 ± 127
Open	41 ± 8	392 ± 109
Closed	50 ± 6	152 ± 8

Table 5.5. *Mean temperatures and standard deviation at ports.*

– T_{ip} has an almost constant value, having a deviation about ±8°C during the complete cycle as confirmed in Table 5.5. Therefore, $\bar{T}_{ip}$ is a good estimation of this temperature during the complete cycle.

– T_{ep} shows a high variation during the cycle that is strongly related with the exhaust process.

– $\bar{T}_{ep}$ has a value of 226°C and a deviation of 127°C during the complete cycle. As can be seen, the variation of the temperature is about 60%. However, when the closed and open cycles are analysed separately, it is evident that T_{ep} is almost constant during the closed cycle (152°C and a deviation of 8°C). On the other hand, the open cycle has higher T_{ep} and deviation values (392°C and 109°C respectively).

Taking into account these comments, $\dot{Q}_{ports}$ can be split as:

$$\dot{Q}_{ports} = \dot{Q}_{ip} + \dot{Q}_{ep,cc} + \dot{Q}_{ep,oc} \tag{5.19}$$

where $\dot{Q}_{ip}$ is the HT to the intake ports, $\dot{Q}_{ep,cc}$ is the HT to the exhausts ports during closed cycle and $\dot{Q}_{ep,oc}$ is the HT to the exhausts ports during open cycle.

In the following sections, specific models to determine the terms of Equation (5.19) are presented.

5.2.2.1 Heat transfer to the intake ports

The low thermal variation on the intake ports makes easier the determination of its HT. Bearing in mind the discussion presented in the previous section, it can be assumed a flow at constant temperature through the intake ports during the complete cycle. As $\bar{T}_{ip}$ is close to the mean temperature at intake manifold (T_{int}), this last is used to determine the gas properties.

Following the proposal of Depcik and Assanis [10] for Equation (5.13), it is assumed that:

$$\bar{N_u} = 0.0694 \ \bar{R_e}^{0.75} \tag{5.20}$$

where the Nusselt ($\bar{N_u}$) and Reynolds ($\bar{R_e}$) numbers are cycle-averaged calculated by means of Equations (5.14) and (5.15) at the T_{int} conditions.

$$\bar{N_u} = \frac{\bar{h}_{int} \ d_{v,int}}{\bar{k}_{int}} \tag{5.21}$$

$$\bar{R_e} = \frac{d_{v,int} \ \bar{v}_{int} \ \bar{\rho}_{int}}{\bar{\mu}_{int}} \tag{5.22}$$

being $d_{v,int}$ the intake valve diameter, and $\bar{h}_{int}$, $\bar{k}_{int}$, $\bar{v}_{int}$, $\bar{\rho}_{int}$ and $\bar{\mu}_{int}$ the cycle-averaged heat transfer coefficient, thermal conductivity, speed, density and viscosity of the gas respectively.

The mean gas speed through the intake port can be determined from the flow through the port and the port section ($A_{v,int}$) as:

$$\begin{aligned} \bar{v}_{int} &= \frac{\dot{m}_a + \dot{m}_{_{EGR}}}{z\ N_{v,int}\ A_{v,int}\ \bar{\rho}_{int}} \\ &= \frac{4\ (\dot{m}_a + \dot{m}_{_{EGR}})}{z\ N_{v,int}\ \pi\ d_{v,int}^2\ \bar{\rho}_{int}} \end{aligned} \tag{5.23}$$

where $\dot{m}_a$ and $\dot{m}_{_{EGR}}$ are the intake air and EGR flow rates, z is the number of cylinders and $N_{v,int}$ is the number of intake valves per cylinder.

Combining Equations (5.20) to (5.23), the expression to determine $\bar{h}_{int}$ is finally obtained:

$$\bar{h}_{int} = 0.0694\ \bar{k}_{int}\ d_{v,int}^{-1.75} \left[\frac{4\ (\dot{m}_a + \dot{m}_{_{EGR}})}{\pi\ z\ N_{v,int}\ \bar{\mu}_{int}} \right]^{0.75} \tag{5.24}$$

Finally, the HT to the intake ports ($\dot{Q}_{ip}$) is determined as:

$$\dot{Q}_{ip} = z\ N_{v,int}\ \bar{h}_{int}\ A_{w,ip}\ (T_{int} - T_{w,ip}) \tag{5.25}$$

where $A_{w,ip}$ is the intake port area in contact with the gas and $T_{w,ip}$ is the port wall temperature, determined by means of the lumped model presented in Chapter 3.3.6.2.

5.2.2.2 Heat transfer to the exhaust ports during closed cycle

There are two thermodynamic properties that differentiate the HT process during open and closed cycle, thus the following comments have to be done:

1. The gas temperate during the closed cycle has lower values and lower variability than during open cycle, as shown in Figure 5.13.

2. The gas speed during closed cycle is lower than during open cycle. The gas movement when the valve is closed is a result of the vortex formed during the open cycle as consequence of the high speed flow of burned gases [9].

Taking into account comment 1, the gas temperature in the exhaust port during closed cycle ($T_{ep,cc}$) can be assumed to be constant. Therefore, the mean experimental temperature at exhaust (T_{exh}) is used for the determination of the gas properties.

Similarly as for the intake ports, the heat transfer coefficient in the closed cycle ($\bar{h}_{exh,cc}$) is estimated by solving Equation (5.13), where the proposal of Caton [11] is used:

$$\bar{N_u} = 0.022 \ \bar{R_e}^{0.8} \tag{5.26}$$

Equation (5.26) is a correlation for steady flow, which can be solved by assuming a mean speed during the complete cycle as described in [9], being this assumption in accordance with comment 2. Therefore, the gas speed at exhaust during closed cycle is estimated as:

$$\begin{aligned} \bar{v}_{exh} &= \frac{\dot{m}_a + \dot{m}_f + \dot{m}_{EGR}}{z \ N_{v,exh} \ A_{v,exh} \ \bar{\rho}_{exh}} \\ &= \frac{4 \ (\dot{m}_a + \dot{m}_f + \dot{m}_{EGR})}{z \ N_{v,exh} \ \pi \ d_{v,exh}^2 \ \bar{\rho}_{exh}} \end{aligned} \tag{5.27}$$

where $d_{v,exh}$ is the exhaust valve diameter, $N_{v,exh}$ is the number of exhaust valves per cylinder and $\bar{\mu}_{exh,cc}$ is the viscosity at exhaust during closed cycle.

Taking into account Equations (5.26) and (5.27), and following the same procedure presented for the intake ports, $\bar{h}_{exh,cc}$ is finally obtained as:

$$\bar{h}_{exh,cc} = 0.022 \ \bar{k}_{exh,cc} \ d_{v,exh}^{-1.8} \left[\frac{4 \ (\dot{m}_a + \dot{m}_{EGR} + \dot{m}_f)}{\pi \ z \ N_{v,exh} \ \bar{\mu}_{exh,cc}} \right]^{0.8} \tag{5.28}$$

where $\bar{k}_{exh,cc}$ is the thermal conductivity at exhaust during closed cycle.

The HT to the exhaust ports during the closed cycle ($\dot{Q}_{ep,cc}$) is then determined as:

$$\dot{Q}_{ep,cc} = z\ N_{v,exh}\ h_{exh,cc}\ A_{w,ep}\ (T_{exh} - T_{w,ep}) \tag{5.29}$$

where $A_{w,ep}$ is the exhaust port area in contact with the gas and $T_{w,ep}$ is the port wall temperature, determined by means of the lumped model.

5.2.2.3 Heat transfer to the exhaust ports during open cycle

The high temperature variation and high velocity of the exhaust gas during the open cycle make the HT determination at exhaust ports a challenging task. As can be seen in Figure 5.13, the temperature drop between EVO and EVC is about 400°C ± 109°C, thus it does not seem reasonable to use a temporal-averaged temperature during this phase. In addition, the variation of the velocity at the exhausts ports makes more reasonable to assume instantaneous conditions [9].

To consider instantaneous temperature and heat transfer coefficient, the HT in the exhaust port during the open cycle is estimated based on the Sieder and Tate proposal [12] as follows:

$$N_u(\alpha) = C\ R_e^{0.6}(\alpha)\ P_r(\alpha)\ \left(\frac{\mu_{exh,oc}(\alpha)}{\mu_p}\right)^{0.14} \tag{5.30}$$

where C is a fitting constant, whose value has to be adjusted as explained in Chapter 6.2.1.2, and μ_p and $\mu_{exh,oc}(\alpha)$ are the gas viscosities calculated at the port wall and exhaust gas temperatures ($T_{w,ep}$ and $T_{ep,oc}(\alpha)$). The relation $(\mu_{exh,oc}(\alpha)/\mu_p)^{0.14}$ accounts for the instantaneous viscosity gradient of the gases at each crank angle due to the gas and wall temperature difference.

The HT coefficient during the open cycle ($h_{exh,oc}(\alpha)$) can be determined by combining Equations (5.14) and (5.30) as:

$$h_{exh,oc}(\alpha) = C\ R_e^{0.6}(\alpha)\ P_r(\alpha)\ \left(\frac{\mu_{exh,oc}(\alpha)}{\mu_p}\right)^{0.14}\ \frac{k_{exh,oc}(\alpha)}{d_{v,exh}} \tag{5.31}$$

where $k_{exh,oc}(\alpha)$ is the instantaneous gas thermal conductivity at $T_{exh,oc}(\alpha)$ and $R_e(\alpha)$ is determined as follows:

$$\begin{aligned} R_e(\alpha) &= \frac{d_{exh}\ \rho_{exh,oc}(\alpha)\ v_{exh,oc}(\alpha)}{\mu_{exh,oc}(\alpha)} \\ &= \frac{4\ \dot{m}_{exh}(\alpha)}{\pi\ d_{v,exh}\ N_{v,exh}\ \mu_{exh,oc}(\alpha)} \end{aligned} \tag{5.32}$$

where the instantaneous gas velocity ($v_{exh,ca}(\alpha)$) is calculated from the instantaneous mass flow at exhaust ($\dot{m}_{exh}(\alpha)$), which is obtained through the filling and emptying model described in Chapter 3.3.2.

Similarly, $P_r(\alpha)$ is determined as:

$$P_r(\alpha) = \frac{c_{p,exh}(\alpha)\ \mu_{exh,oc}(\alpha)}{k_{exh,oc}(\alpha)} \tag{5.33}$$

being $c_{p,exh}(\alpha)$ the instantaneous heating value at exhaust during the open cycle.

At this point, is evident that the determination of the instantaneous $T_{ep,oc}$ is crucial to estimate the gas properties as well as the HT during the open cycle ($\dot{Q}_{ep,oc}$). This temperature can be measured or modelled; however, some comments have to be done:

- The experimental determination of $T_{eo,oc}(\alpha)$ requires the use of fast thermocouples. Their complex installation makes their use difficult from a practical point of view, and hence they are not used in common test benches.
- $T_{ep,oc}(\alpha)$ can be accurately obtained by means of CFD models; however, the time consumption of these simulations is not allowed for the application presented in this work.

Taking into account these comments, a 0D quasi-steady model is proposed, since these types of models provide enough accuracy with shorter calculation time, thus being more suitable for the application of this work.

In Figure 5.14, a scheme of the exhaust ports configuration is presented. The gas temperature at the port inlet (T) is obtained from instantaneous

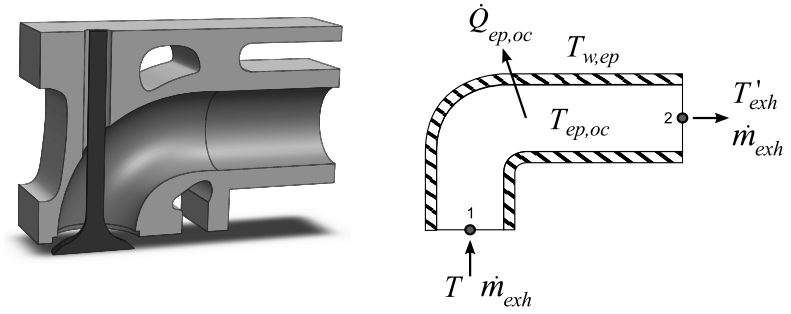

Figure 5.14. *Exhaust port boundary conditions scheme.*

in-cylinder temperature by assuming an isenthalpic process at invariant stagnation enthalpy. $\dot{Q}_{ep,oc}$ can be determined as the HT between the gas and port wall (Equation (5.34)) as well as the enthalpy difference between points 1 and 2 (Equation (5.35)):

$$\dot{Q}_{ep,oc}(\alpha) = z\ N_{v,exh}\ h_{exh,oc}(\alpha)\ A_{w,ep}\,(T_{ep,oc}(\alpha) - T_{w,ep}) \tag{5.34}$$

$$= \dot{m}_{exh}(\alpha)\ c_{p,exh}(\alpha)\ \left(T'_{exh}(\alpha) - T(\alpha)\right) \tag{5.35}$$

where $T'_{exh}(\alpha)$ is the gas temperature at the exhaust port outlet and $T_{ep,oc}(\alpha)$ is instantaneously determined as:

$$T_{ep,oc}(\alpha) = \frac{T(\alpha) + T'_{exh}(\alpha)}{2} \tag{5.36}$$

Note that the value of $T'_{exh}(\alpha)$ is unknown, thereby, Equations (5.34) and (5.35) are solve through an iterative process, assuming in a first step that $T'_{exh}(\text{EVO}) = T_{exh}$. The result of this iterative process is the spatially averaged temperature in the exhaust port ($T_{ep,oc}(\alpha)$) and the instantaneous HT to the exhaust port ($\dot{Q}_{ep,oc}(\alpha)$), both during open cycle.

To assess the exhaust model performance, a comparison of the HT estimated at each port for some operating conditions is summarized in Table 5.6 for **Engine A**. It is possible to see that the HT to the exhaust ports in the open cycle accounts for more than 90% of the total HT to the ports. Therefore, the efforts made to improve $\dot{Q}_{ep,oc}$ results in a global enhancement of $\dot{Q}_{ports}$, which is key for the GEB as described in Chapter 6.2.1.

Speed/Load [rpm]/[%]	**Intake** [kW]	**Exhaust closed cycle** [kW]	**Exhaust open cycle** [kW]
1000/25	-0,008	0,017	0,252
1000/100	-0,027	0,074	1,009
2000/50	-0,037	0,175	1,746
4000/25	-0,088	0,124	1,098
4000/100	-0,160	0,374	2,969

Table 5.6. *HT to the ports comparison between the intake and exhaust ports of* ***Engine A****.*

5.2.3 Heat transfer from oil to coolant

As commented in Chapter 4.3.2, there is some HT between the oil and coolant ($\dot{Q}_{oil,cool}$) as both circulates through the engine. The coolant and oil reject heat to the gallery walls due to convection. This heat is transferred by conduction through the walls between coolant or oil circuits, depending on the temperature difference between them. Usually, the oil temperature is higher than that of the coolant, thus, $\dot{Q}_{oil,cool}$ is assumed to be positive when it goes from oil to coolant.

This HT process can be identified by comparing the experimental and modelled HT to oil defined in Chapter 4.3.3. As shown in Figure 5.15, $\dot{Q}_{oil,mod}$ is higher than $\dot{Q}_{oil,exp}$ at mid and high load operating points. This can be explained by the high oil temperature at these conditions as shown in Figure 5.16. It can be observed how the oil temperature increases between 85°C and 125°C when increasing the speed and load, whilst the coolant temperature remains almost constant (about 85°C); therefore, the difference between oil and coolant temperature ($T_{oil} - T_{cool}$) increases up to 45°C.

To account for $\dot{Q}_{oil,mod}$, a simple model which considers the thermal resistances of the oil, the engine walls and the coolant is developed. The model is based on the scheme shown in Figure 5.17; as can be seen, $\dot{Q}_{oil,cool}$ can be determined as:

$$\dot{Q}_{oil,cool} = \frac{T_{oil} - T_{cool}}{R_{oil} + R_{cond} + R_{cool}} \tag{5.37}$$

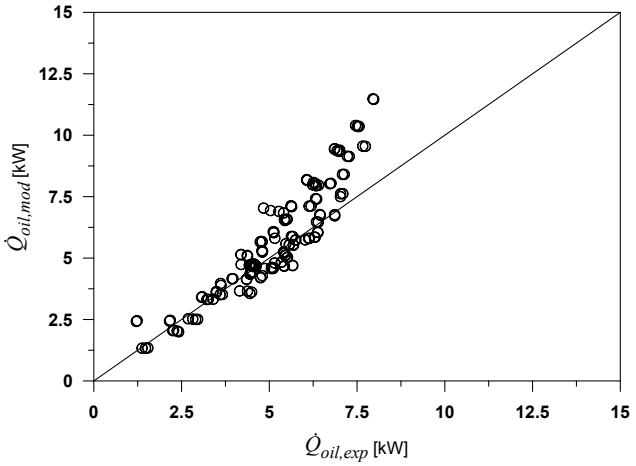

Figure 5.15. *Comparison between experimental and modelled HT to oil.*

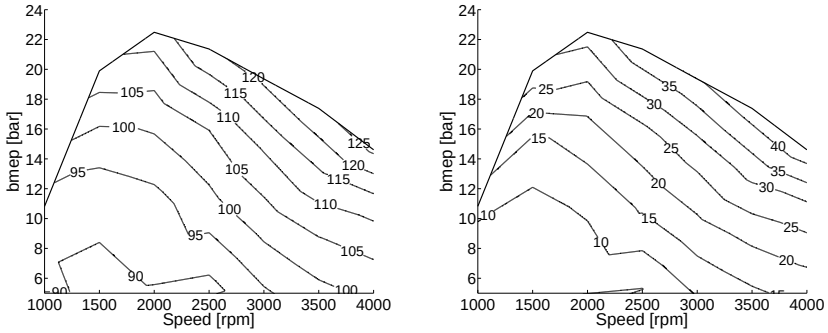

Figure 5.16. *Left: oil temperature; right: Difference between oil and coolant temperatures.*

being R_{oil}, R_{cond} and R_{cool} the thermal resistances between the oil and the wall, due to conduction through the wall, and between the wall and coolant respectively:

$$R_{oil} = \frac{1}{\bar{h}_{oil}\ A} \tag{5.38}$$

$$R_{cond} = \frac{e}{k_{wall}\ A} \tag{5.39}$$

$$R_{cool} = \frac{1}{\bar{h}_{cool}\ A} \tag{5.40}$$

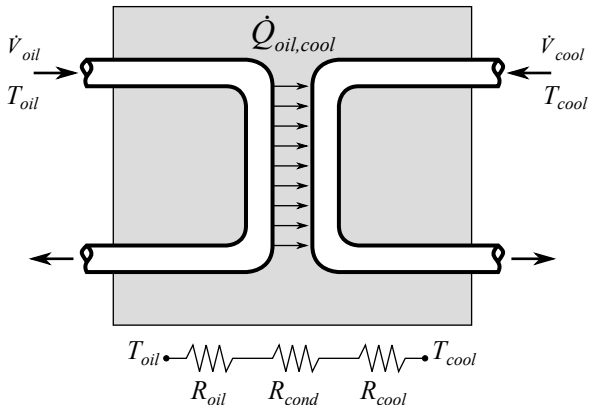

Figure 5.17. *Heat transfer between oil and coolant within the engine.*

where A is the heat transfer area, e is the wall thickness, k_{wall} is the thermal conductivity of the engine (block and cylinder head), and $\bar{h}_{oil}$ and $\bar{h}_{cool}$ are the oil and coolant mean heat transfer coefficients.

Due to the complex design of the engine cooling and lubricating systems, the geometrical information necessary to solve the Equation (5.37) cannot be obtained from a specific engine part; moreover, the thermal conditions are changing along these systems and the assumption of some hypotheses is necessary:

- $\bar{h}_{oil}$ and $\bar{h}_{cool}$ were assumed to be proportional to the engine speed as $\bar{h}_{oil} = k'_1\ n$ and $\bar{h}_{cool} = k''_1\ n$.
- A characteristic thickness proportional to the cylinder bore as $e = k'_2\ D$ is assumed.
- The equivalent HT area is assumed to be proportional to the piston area as $A = k'_3\ D^2$.

Taking into account these hypotheses, and replacing Equations (5.38), (5.39) and (5.40) in (5.37), the following expression is obtained:

$$\dot{Q}_{oil,cool} = \frac{T_{oil} - T_{cool}}{\frac{1}{k'_1\ n\ k'_3\ D^2} + \frac{k'_2\ D}{k'_3\ D^2\ k_{wall}} + \frac{1}{k''_1\ n\ k'_3\ D^2}} \tag{5.41}$$

As the specific information to determine all the constant in Equation (5.41) is not available, constants k_1' and k_1'' have to be considered altogether. Taking this comment into account and grouping all the constants values, $\dot{Q}_{oil,cool}$ can be finally calculated as:

$$\dot{Q}_{oil,cool} = \frac{D^2(T_{oil} - T_{cool})}{\frac{2}{k_1\ n} + \frac{D}{k_2\ k_{wall}}} \tag{5.42}$$

where $2/k_1 n$ is an equivalent convection resistance and $D/k_2 k_{wall}$ is an equivalent conduction resistance, and the constants k_1 and k_2 are the calibration constants whose value were adjusted as described in Chapter 6.2.1.4.

5.3 Uncertainties adjustment

To perform a precise evaluation of the IGEB terms presented in Chapter 4.2.2, it is necessary to reduce the uncertainty on the determination of some parameters that affect the in-cylinder calculations. A brief description of the effect of these uncertainties on the IGEB terms, along with proposals found in the literature for their determination are following presented:

- **Pressure pegging:** a proper pressure pegging is necessary to accurately determine the gas temperature, thus, it is important for the $\dot{Q}_{cham}$ and $\dot{Q}_{ports}$ estimation.

  Different methods for its determination [13, 14] can be grouped in two categories: experimental methods based on the measurement of a reference pressure [14] and thermodynamic methods such as the simulation of the gas polytropic evolution[2].

- **Compression ratio:** the Compression Ratio (CR) is the main geometrical uncertainty, it affects the instantaneous volume calculation and hence the gas temperature, which impacts the $\dot{Q}_{cham}$ and $\dot{Q}_{ports}$ determination [16].

  Klein [17] evaluated four methods for the CR determination by comparing the real compression process with polytropic evolutions. Striker [18] proposed a methodology in which available sensors of production engines, a high gain observer and a volumetric efficiency model were combined. Lapuerta [19] used characteristic geometrical points to adjust CR with a symmetry criterion.

- **Engine deformations:** It has a similar but lower effect on gas temperature than the CR [16], thus having a small influence on $\dot{Q}_{cham}$ and $\dot{Q}_{ports}$. The deformation also affects the calculation of N_i due to its effect on the volume derivative, as a consequence, it also affects the $N_{fr} + N_a$ calculation.

  In some works, a simple model to determine the clearance variations taking into account the pressure and the inertial effects is used [16, 20]. Aronsson [21] used a similar model in an optical engine, and measured

[2]During compression stroke in combustion tests or in the compression and expansion stroke in motoring test [15].

the variation of the piston position by means of an optical window in the liner.

- **Heat transfer model fitting:** this is the main uncertainty of the HT model, thus affecting directly $\dot{Q}_{cham}$ determination. A proper calibration of the HT model is key to perform an accurate IGEB.

  Nowadays, each author carries out a tuning process for a specific engine, based on experimental measurements or thermodynamic assumptions [22, 23], in order to adapt the models to one specific engine.

- **TDC position:** this parameter has an important influence on the $p-V$ digram, thus affecting the N_i determination, specially at low load operating conditions. Besides, this parameter slightly affects the gas temperature estimation, having a small effect on $\dot{Q}_{cham}$ and $\dot{Q}_{ports}$.

  The TDC position can be obtained by means of experimental techniques [24] or thermodynamic methods. The last ones allow determining the angular interval ($\Delta\alpha_{\text{TDC}}$) between the TDC and the trigger, based on the effect of $\Delta\alpha_{\text{TDC}}$ on some variables such as heat release [25], simulated pressure [17] or entropy [26]. In this work, the TDC is determined following the Hohenberg's proposal [27].

The stated uncertainties have different influence on the results but, in general, they are all relevant for the calculation of the thermodynamic conditions in the chamber [28], and hence for the accurate prediction of the affected energy terms. Although different approaches for the determination of one uncertainty have been commented, there are very few works dealing with the adjustment of several of them at the same time while taking into account their cross effect. Therefore, the estimation of one parameter can be affected by the incorrect value of other uncertainties that are simultaneously adjusted. Moreover, a combination of parameters can provide a low residual, according to one criterion, but being worse according to another one. For example, the effect of an incorrect pressure pegging and CR is similar in terms of simulated peak pressure, but they are quite different in terms of heat release [16]. Thus, a methodology to simultaneously determine all the uncertainties (taking into account their specific effects) and considering more than one criterion is recommendable to ensure accuracy.

In this section, a global methodology to adjust the stated uncertainties at the same time is described. The proposal is based on the thermodynamic

analysis in motoring conditions as described in [28], thus the effect of the uncertainties in the compression and expansion strokes can be assessed using the RoHR obtained in motoring conditions[3], and the experimental and simulated pressure comparison. Although the methodology has been developed using specific sub-models, it is flexible enough to be used with different models and different engines. It is worth to clarify that regarding the HT calibration, after the adjustment of the model in motoring conditions, additional calibration in combustion will be done, as presented in Chapters 6.2.1 and 6.3.1.

The method presented is based on motoring tests; however, its suitability in combustion tests is included in Appendix 5.A. To illustrate the method, the results shown in the next section correspond only to **Engine A**, but they are representative of those obtained in both **Engine A** and **Engine B**.

5.3.1 Engine characterization

To determine the optimal set of engine-installation parameters, an adjustment methodology, henceforth called *Engine characterization*, is shown in Figure 5.18. It can be split in three main phases:

1. Firstly, the adjustment of engine characteristics (CR, deformation and heat transfer models) is performed.
2. After the adjustment of the heat transfer, $\Delta\alpha_{\text{TDC}}$ is calculated using the Hohenberg's proposal [27].
3. Finally, the pressure pegging (which is different for each test) is carried out.

The processes during the first and third steps are similar, and can be summarised as follows:

- Starting from a reference set of values, a sensitivity study to determine the effect of each uncertainty during the closed cycle is carried out (see Section 5.3.1.1). The effect is analysed in terms of the uncertainty on RoHR and in the simulated in-cylinder pressure. In the first case, a value different from zero is due to incorrect uncertainties values, in the second

[3] As there is no energy release in motoring conditions, the RoHR should be zero. Non-zero values are due to uncertainties in the stated parameters.

case, the simulated pressure is compared with the experimental one. The result of this step is the instantaneous evolution of the characteristic effects of each uncertainty in a set of motoring tests.

- Using the information provided by the previous step, a minimization of the difference between the real and simulated pressure and RoHR residuals is performed. For that, a Multiple Linear Regression (MLR) [29] is carried out (Section 5.3.1.2), thus obtaining a new set of values for the uncertainties.

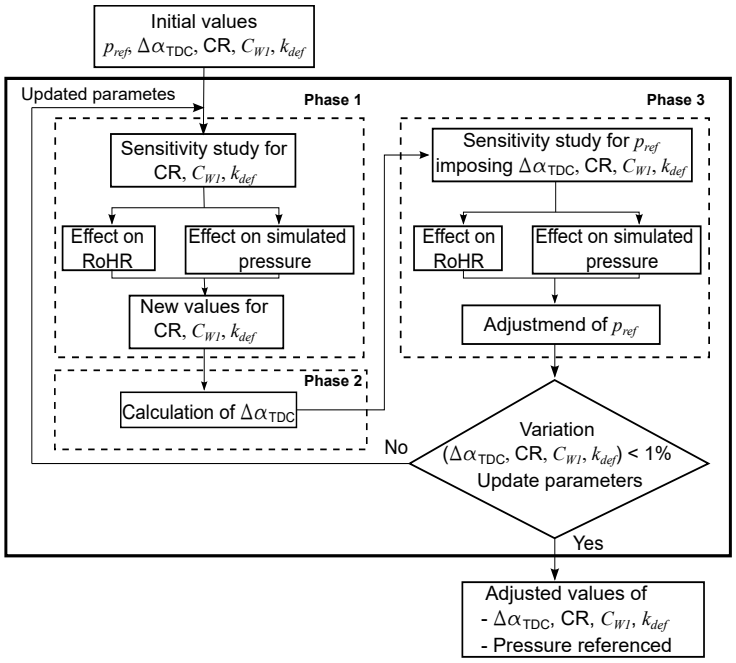

Figure 5.18. *Engine characterization.*

As the effect of each parameter on RoHR residuals and pressure evolution can be slightly different for different values of the other parameters, an iterative process is performed until the variation of all of them, in comparison with the previous iteration, becomes negligible.

The parameters resulting from the *Engine characterization* are ready to be used for combustion analysis and GEB[4].

5.3.1.1 Sensitivity study

By solving the first law of thermodynamics as presented in the Chapter 3.3.4, the following expression for RoHR is obtained:

$$\begin{aligned}\text{RoHR} &= \frac{\mathrm{d}HR}{\mathrm{d}\alpha} \\ &= m\ c_v\ \frac{\mathrm{d}T}{\mathrm{d}\alpha} + \frac{\mathrm{d}Q}{\mathrm{d}\alpha} + p\frac{\mathrm{d}V}{\mathrm{d}\alpha} - (h_{f,inj} - u_{f,g})\ \frac{\mathrm{d}m_{f,ev}}{\mathrm{d}\alpha} + R\ T\ \frac{\mathrm{d}m_{bb}}{\mathrm{d}\alpha}\end{aligned} \tag{5.43}$$

In motoring conditions, the real RoHR is zero; however, it can have a non-zero value (ε^{RoHR}) due to experimental and modelling uncertainties. At these conditions, Equation (5.43) becomes:

$$\varepsilon^{\text{RoHR}} = m\ c_v\ \frac{\mathrm{d}T}{\mathrm{d}\alpha} + \frac{\mathrm{d}Q}{\mathrm{d}\alpha} + p\frac{\mathrm{d}V}{\mathrm{d}\alpha} + R\ T\ \frac{\mathrm{d}m_{bb}}{\mathrm{d}\alpha} \tag{5.44}$$

Although some experimental uncertainties and signal noise can affect $\varepsilon^{\text{RoHR}}$, it is assumed that the averaging of the 25 measured cycles and the filtering process reduce the signal noise sufficiently [14]. It is also assumed that all the relevant uncertainties have been considered, and any additional effect on $\varepsilon^{\text{RoHR}}$ is due to random experimental uncertainties.

On the other hand, from a predictive point of view, the simulated motoring pressure can be calculated by solving Equation (5.44) for p, assuming that $\varepsilon^{RoHR} = 0$, which means an ideal motoring test, thus obtaining:

$$p_{sim} = -\frac{m\ c_v\ \mathrm{d}T + dQ + R\ T\ \mathrm{d}m_{bb}}{\mathrm{d}V} \tag{5.45}$$

As T and $\mathrm{d}T$ depends on p_{sim}, Equation (5.45) is solved using an iterative process. The simulated pressure deviation is straightforward obtained through differentiation of experimental and simulated pressures:

[4]The referenced in-cylinder pressure in the motoring tests are also obtained. Although they will not be used any more, it is important to highlight that the correct pressure level is necessary to properly adjust the other uncertainties.

$$\varepsilon^p = p_{sim} - p \tag{5.46}$$

The identification of the characteristic effect of each parameter is key to ensure their independence for the MLR method. For this reason, a sensitivity study on ε^{RoHR} and ε^p due to variations of the stated parameters is performed. The variation range is summarized in Table 5.7, these values are reasonable variations on the determination of these parameters, as justified by Martín [15], and are considered appropriate for the application described in this section.

Parameter	**Variation**
CR	± 0,75
k_{def}	± 1
C_{w1}	± 2
$\Delta\alpha_{\mathrm{TDC}}$	± 0,5°
p_{ref}	± 100 mbar

Table 5.7. *Parameters variation.*

Figure 5.19 shows the effect of the engine parameters variation presented in Table 5.7 on $\varepsilon^{\mathrm{RoHR}}$ (left) and ε^p (right), whilst Figure 5.20 shows the effect of pressure pegging for 1 motoring test. The main conclusions are:

- CR: its increment leads to a lower combustion chamber volume. Although CR does not affect $\mathrm{d}V$, it modifies T through the application of the ideal gas law, thus affecting the specific heat and the HT term in Equation (5.44). The main effect of CR on $\varepsilon^{\mathrm{RoHR}}$ (Figure 5.19 (a)) is due to the variation of $\mathrm{d}T$ in the internal energy term, that can be expressed as $\mathrm{d}T = -\frac{(n-1)p\mathrm{d}V + T\mathrm{d}(mR)}{mR}$, being $n = -\frac{\mathrm{d}p/p}{\mathrm{d}V/V}$ the politropic exponent. The CR affects n, producing the asymmetric behaviour of $\varepsilon^{\mathrm{RoHR}}$. Its effect is higher in the proximities of TDC, where the variation of the chamber volume has a higher relative effect. On the other hand, a higher CR leads to a higher simulated pressure, and hence a positive ε^p as shown in Figure 5.19 (e).

- k_{def}: it also affects the volume calculation, and hence the temperature and the politropic exponent; however, its effect is qualitatively and quantitatively different from CR. Whilst the CR change produces a deviation in the volume that remains constant during all the cycle, deformations

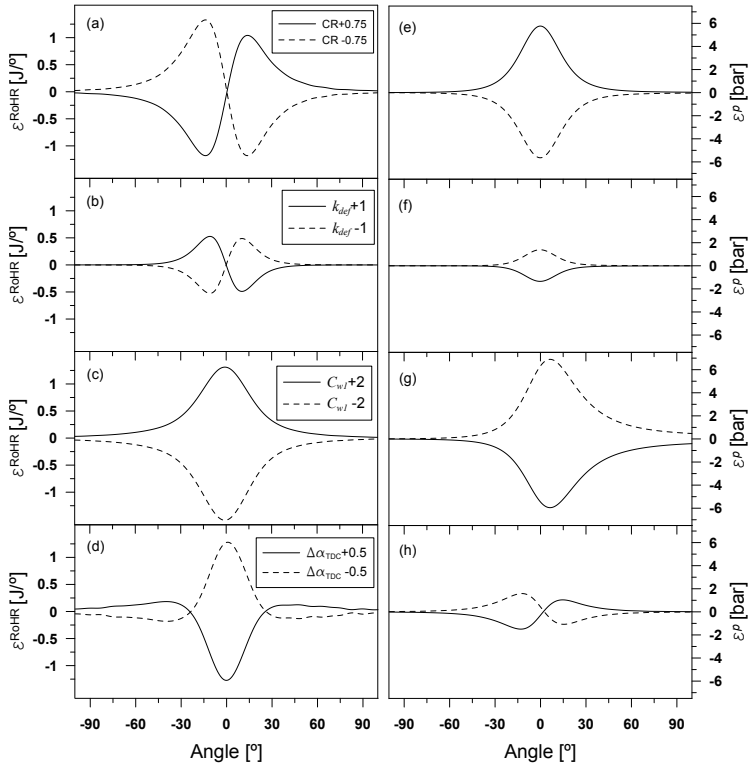

Figure 5.19. *Effects of CR, k_{def}, C_{w1} and $\Delta\alpha_{\mathrm{TDC}}$ on $\varepsilon^{\mathrm{RoHR}}$ (left) and ε^{p} (right).*

depend on pressure and acceleration, thus their effect vary during compression and expansion, being more important near TDC (see Figure 5.19 (b) and (f)), where the pressure reaches its maximum value. On the other hand, the higher the load, the higher the effect of the deformations; therefore, $\varepsilon^{\mathrm{RoHR}}$ and ε^{p} will change slightly at different operation points. In comparison with CR, deformations have a lower maximum effect for the considered variations.

- C_{w1}: the higher this constant is, the higher the HT becomes. In Equation (5.44) it is possible to see that the heat transfer uncertainty is directly transferred to $\varepsilon^{\mathrm{RoHR}}$, as can be seen in Figure 5.19 (c). Contrary to CR and k_{def}, the uncertainty of C_{w1} has an almost symmetric effect on $\varepsilon^{\mathrm{RoHR}}$, being more important as the pressure and temperature

increase. The effect on ε^p shows the opposite trend, because a less adiabatic evolution of the gas leads to a lower simulated pressure, as shown in Figure 5.19 (g). The effect on pressure is not completely symmetric due to the fact that heat rejection during the compression stroke is not compensated in the expansion stroke.

- $\Delta\alpha_{\text{TDC}}$: the thermodynamic gap between the peak pressure and TDC depends on the HT; therefore, it is not included as an independent variable in the phase 1 of the adjustment but it is later obtained with the Hohenberg proposal [27]. However, for the sake of completeness, it is interesting to analyse separately its effect on $\varepsilon^{\text{RoHR}}$ and ε^p. $\Delta\alpha_{\text{TDC}}$ variation leads to different p and dp for a determined α, leading to inaccuracies in the work, T and dT, and hence, in the variations of heat transfer and the internal energy. The combination of these effects produces the $\varepsilon^{\text{RoHR}}$ shown in Figure 5.19 (d). As p in Equation (5.46) is slightly affected by the variation of $\Delta\alpha_{\text{TDC}}$, the effect observed in Figure 5.19 (h) is explained by the small change in the IVC pressure, and mostly by the change of experimental p for each crank angle.

As stated in Section 5.3.1, the motoring pressure has to be referenced. For this reason, a sensitivity study, similar to that carried out for the other uncertainties, is performed for the pressure pegging (p_{ref}).

The variations on p_{ref} have two main effects; on the one hand, it leads to temperature and specific heat variations, on the other hand, it results in uncertainties in the politropic exponent, and hence in the work estimation. The pressure pegging affects the whole compression and expansion strokes, being its effect on $\varepsilon^{\text{RoHR}}$ higher far from TDC (see Figure 5.20 left), because the relative effect is smaller when the cylinder pressure increases. In contrast, the effect on ε^p is more important near the TDC (see Figure 5.20 right), because a small variation of the pressure level at IVC is amplified during the compression stroke.

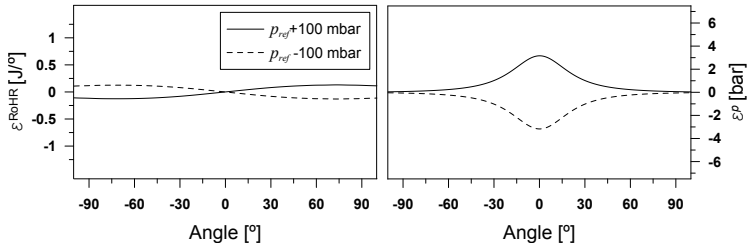

Figure 5.20. *Effect of pegging pressure on $\varepsilon^{\mathrm{RoHR}}$ (left) and ε^{p} (right).*

5.3.1.2 Uncertainties determination based on multiple linear regression

Starting from the characteristic effects determined in the previous section, and assuming the hypothesis of linearity [15], the total deviation of the RoHR ($\varepsilon_{un}^{\mathrm{RoHR}}$) and simulated pressure (ε_{un}^{p}) due to the uncertainties can be expressed as:

$$\varepsilon_{un}^{\mathrm{RoHR}}(\alpha) \simeq c_1\varepsilon_{\mathrm{CR}}^{\mathrm{RoHR}}(\alpha) + c_2\varepsilon_{C_{w1}}^{\mathrm{RoHR}}(\alpha) + c_3\varepsilon_{k_{def}}^{\mathrm{RoHR}}(\alpha) + c_4\varepsilon_{p_{ref}}^{\mathrm{RoHR}}(\alpha) \quad (5.47)$$

$$\varepsilon_{un}^{p}(\alpha) \simeq c_1\varepsilon_{\mathrm{CR}}^{p}(\alpha) + c_2\varepsilon_{C_{w1}}^{p}(\alpha) + c_3\varepsilon_{k_{def}}^{p}(\alpha) + c_4\varepsilon_{p_{ref}}^{p}(\alpha) \quad (5.48)$$

where α is the crank angle, $\varepsilon_{\mathrm{CR}}$, $\varepsilon_{C_{w1}}$, $\varepsilon_{k_{def}}$ and $\varepsilon_{p_{ref}}$ are the effect of the uncertainties variation on RoHR and pressure residuals, and c_1 to c_4 are weighting constants. The mathematical expressions for $\varepsilon^{\mathrm{RoHR}}$ and ε^{p} are similar, thus Equation (5.47) and Equation (5.48) can be written in a general expression as:

$$\varepsilon_i(\alpha) = \sum_{j=1}^{m} c_j\varepsilon_{i,j}(\alpha) \quad (5.49)$$

where ε_i is the effect on RoHR or p produced by the $m = 4$ uncertainties considered at the operating point i. $\varepsilon_{i,j}$ is the specific effect of the uncertainty j in the operating point i, and c_j the corresponding weighting constant[5]. The equation system (Equation (5.49)) can be solved by knowing m equations;

[5]Note that the possibility of including additional uncertainties is implicitly considered, being $m > 4$ in that case.

however, as a pressure signal has $n >> m$ samples, it is an overdetermined system that must be solved in order to minimize $\varepsilon^{\mathrm{RoHR}}$ and ε^{p} during the closed cycle. This is done by means of MLR taking into account the considered parameters, whose optimal solution is found by means of the least square method. For a determined operation point i, the instantaneous uncertainty on the RoHR or simulated pressure ($\varepsilon_{exp,i}$) can be expressed as:

$$\varepsilon_{exp,i}(\alpha) = \varepsilon_i(\alpha) + \varepsilon_{res,i}(\alpha) \tag{5.50}$$

where $\varepsilon_{res,i}$ accounts for the effect of the terms not considered specifically with the stated uncertainties, such as some experimental uncertainties or signal noise. In order to diminish these residuals, a sweep of engine speed was considered in motoring conditions taking into account several cycles, so that the addition of the uncertainty on RoHR or simulated pressure in all tests at a defined crank angle will be:

$$\sum_{i=1}^{tests} \varepsilon_{exp,i}(\alpha) = \sum_{i=1}^{tests} \varepsilon_i(\alpha) + \sum_{i=1}^{tests} \varepsilon_{res,i}(\alpha) \tag{5.51}$$

Taking into account the differentiation between engine characteristics and pressure pegging described in Section 5.3.1, Equation (5.51) can be written as:

$$\sum_{i=1}^{tests} \varepsilon_{exp,i}(\alpha) = \sum_{i=1}^{tests} \sum_{j=1}^{m-1} c_j \varepsilon_{i,j}(\alpha) + \sum_{i=1}^{tests} c_i \; \varepsilon_{p_{ref,i}}(\alpha) + \sum_{i=1}^{tests} \varepsilon_{res,i}(\alpha) \tag{5.52}$$

On the one hand, the last term of Equation (5.52) corresponds to the neglected uncertainties and noise that have an aleatory effect; therefore, the addition of different operation points compensates it, being $\sum_{i=1}^{tests} \varepsilon_{res}(\alpha) \approx 0$. On the other hand, as described in Section 5.3.1, p_{ref} is adjusted for each operating point in a second phase after the engine characteristic adjustment; thereby, it can be assumed that after some iterations $\sum_{i=1}^{test} c_i \; \varepsilon_{p_{ref,i}} \approx 0$ in Equation (5.52), thus:

$$\sum_{i=1}^{tests} \varepsilon_{exp,i}(\alpha) = \sum_{i=1}^{tests} \sum_{j=1}^{m-1} c_j \varepsilon_{i,j}(\alpha) \tag{5.53}$$

If Equation (5.53) is written for each crank angle, the following matrix is obtained:

$$\begin{bmatrix} \sum_{i=1}^{tests} \varepsilon_{exp,i}(\alpha_1) \\ \sum_{i=1}^{tests} \varepsilon_{exp,i}(\alpha_2) \\ \vdots \\ \sum_{i=1}^{tests} \varepsilon_{exp,i}(\alpha_n) \end{bmatrix} = \begin{bmatrix} \sum_{i=1}^{tests} \varepsilon_{i,1}(\alpha_1) & \dots & \sum_{i=1}^{tests} \varepsilon_{i,m-1}(\alpha_1) \\ \sum_{i=1}^{tests} \varepsilon_{i,1}(\alpha_2) & \dots & \sum_{i=1}^{tests} \varepsilon_{i,m-1}(\alpha_2) \\ \vdots & & \vdots \\ \sum_{i=1}^{tests} \varepsilon_{i,1}(\alpha_n) & \dots & \sum_{i=1}^{tests} \varepsilon_{i,m-1}(\alpha_n) \end{bmatrix} \begin{bmatrix} c_1 \\ c_2 \\ \vdots \\ c_{m-1} \end{bmatrix} \tag{5.54}$$

The solution of this matrix results in a set of correction parameters $c_1, c_2, ...c_{m-1}$, that weight the effect of each specific uncertainty on the RoHR or simulated pressure. The iterative process is carried out by applying the following correction at each step:

$$P_{j,k} = P_{j,k-1} + c_{j,k}\ \Delta P_j \tag{5.55}$$

where $P_{j,k}$ is the estimation of the P_j parameter (CR, k_{def} and C_{w1}) in the k iteration, $c_{j,k}$ is the correction factor obtained by the MLR in the k iteration, and ΔP_j is the variation of each parameter in the sensitivity study as detailed in Table 5.7. The procedure can be performed only in one step; however, it was checked that it provides more accurate results when an iterative process is used, since the effect of each uncertainty on $\varepsilon^{\text{RoHR}}$ and ε^p can vary slightly depending on its value. It was found that after the third iteration, the variation of the parameters is lower than 1%, which was assumed to be an acceptable outcome.

Since both the effect of RoHR and simulated pressure are considered, the process is carried out to find the optimal values that minimize separately $\varepsilon^{\text{RoHR}}$ and ε^p. Finally the optimal values obtained for each of them are averaged.

5.3.2 Evaluation of the methodology performance

5.3.2.1 Motoring conditions

To evaluate the methodology performance, it was tested in a speed sweep of motoring tests performed on **Engine A**, changing the engine speed from 1000 rpm to 4000 rpm with steps of 500 rpm. To reduce the experimental uncertainty, three repetitions of each operating point were measured.

The initial values of the parameters to be adjusted are shown in the "Reference" column of Table 5.8. The initial TDC position was assumed to be at the peak pressure, the initial CR value is the one provided by the engine manufacturer, k_{def} is the average value obtained in several engines proposed by Martín [15], and C_{w1} is the value proposed by Woschni [30]. The pressure pegging was initially carried out assuming that the pressure at the BDC coincides with the pressure at the inlet manifold in each test. It was checked that the final values provided by the proposed method do not depend on the initial values, thus demonstrating that the calibration process is robust; however, they must lie in a determined range around the actual value, so that the hypothesis of linear and independent behaviour of each uncertainty is accomplished. If the initial values are far from the actual ones, the iterative method can provide results with no physical meaning or it cannot converge at all. In both cases the problem can be detected.

	Reference	**Adjusted**
CR	16:1	15,9:1
k_{def}	2,20	1,29
C_{w1}	2,28	1.74
$\Delta\alpha_{\mathrm{TDC}}$	369,0	369,9

Table 5.8. *Characterization results.*

The values of the parameters adjusted are presented in the "Adjusted" column of Table 5.8. The residuals obtained with the reference and the adjusted parameters are shown in Table 5.9, where the RMSE of $\varepsilon^{\mathrm{RoHR}}$ and the difference between the modelled and measured peak pressures are shown. Following, some observations regarding the model performance for each parameter are presented:

- The difference between the reference and the adjusted TDC position is 0.9°. This phase gap uses to be longer in smaller engines because they have higher HT, as reported by Hohenberg [27]. It is interesting to highlight the importance of the adjusted TDC position provided by the method. Indeed, assuming that TDC is located at the peak pressure in motoring tests would lead to an effect on *imep* that can only be admissible at full load in combustion operation. A deviation of 0.5° at mid load could lead to an effect on *imep* about 3% [16] and much higher at low load.

- The CR correction obtained with the method is -0.1. This variation leads, in the worst case, to a deviation in the simulated peak pressure of about 3 bar, which can increase in the case of combustion simulation, where the inlet pressure will be higher.
- Regarding k_{def}, the correction obtained is -0.9 with respect to the reference value. Although having a lower effect than CR, it can lead to variations in the volume at the TDC about 2% at full load, where the high pressure produces important deformations. The uncertainty in the volume would directly affect the in-cylinder temperature calculation, thus affecting the RoHR (in the combustion diagnosis) and the pressure evolution (in the case of thermodynamic simulation).
- Finally, the C_{w1} correction of -0.54 can produce a maximum variation of the HT peak in combustion about 14%, and leads to a deviation of 3 bar in the peak pressure in motoring conditions (higher in combustion). The effect of the HT changes on cumulative HR can reach 1-2%$\dot{m}_f H_v$ at low speed and load, where HT to the chamber walls is about one third of the fuel energy [31].

	RMSE of RoHR		**Error in p_{max}**	
Speed [rpm]	**Reference** [J/°]	**Final** [J/°]	**Reference** [%]	**Final** [%]
1000	0,09	0,11	5,5	1,1
1500	0,17	0,13	9,0	0,5
2000	0,10	0,07	8,9	0,8
2500	0,15	0,11	8,7	0,8
3000	0,10	0,06	8,7	0,8
3500	0,14	0,07	9,0	0,7
4000	0,21	0,17	8,7	0,5

Table 5.9. *Residuals of RoHR and simulated p_{max}.*

As shown in Table 5.9, the adjusted parameters provide a lower uncertainty in the two observed variables in almost all the operating conditions. Since the method optimizes the global results for the sake of the accuracy in most of the operating conditions, slightly worse results can be obtained in some specific tests. Thus, the RoHR at 1000 rpm shows a slightly higher residual than that obtained with the original values. It has been checked that it is

not a general trend at low engine speed in other engines. In fact, the method has been tested in smaller [32] and bigger [33] engines (omitted for the sake of brevity), and the residuals of RoHR and simulated pressure showed similar trends at low and high engine speed.

As seen in Table 5.9, the performance of the method is even better if the simulated pressure is considered: the difference between the simulated and experimental peak pressures diminishes from 9% to less than 1% after the adjustment.

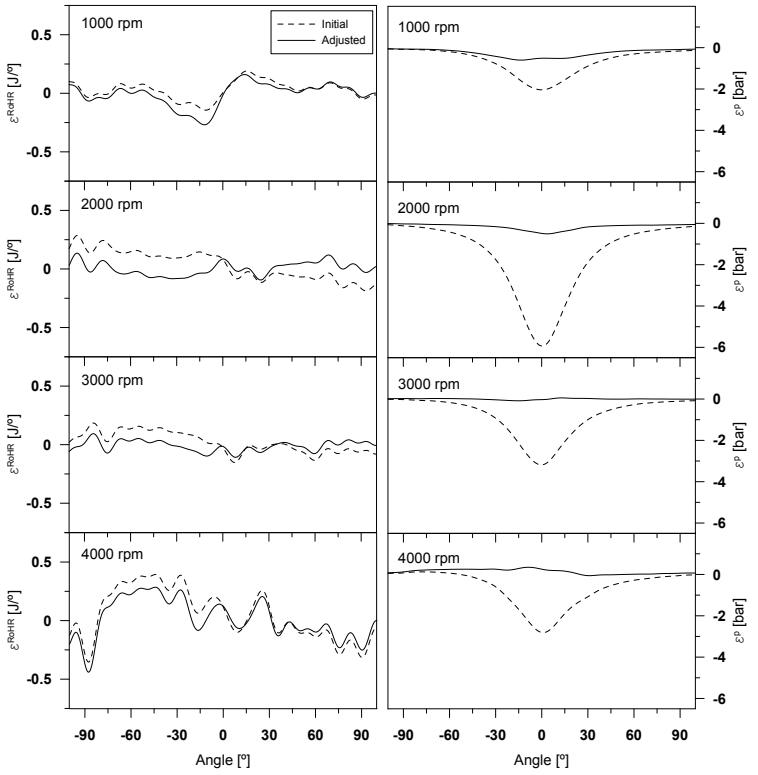

Figure 5.21. *ε^{RoHR} (left) and ε^{p} (right) in motoring tests.*

To evidence the adjustment effect on the instantaneous evolution of a compression cycle, Figure 5.21 shows $\varepsilon^{\mathrm{RoHR}}$ and ε^{p} in four motoring tests used for the adjustment. The mid-frequency oscillations of $\varepsilon^{\mathrm{RoHR}}$ due to signal noise have not been removed but have been centred around zero, since the low-

frequency deviation due to incorrect parameters has been effectively corrected. In the case of ε^p the effect on pressure is clearly reduced.

5.3.2.2 Evaluation of combustion results

Finally, combustion tests are used to evaluate the *Engine characterization* results, taking into account that the final objective of this methodology is to improve the combustion diagnosis to have reliable results to be used in GEB.

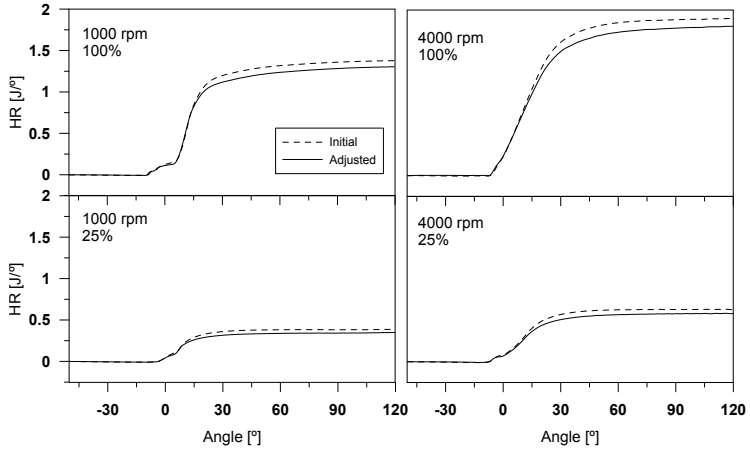

Figure 5.22. *Cumulative HR with the reference parameters and the adjusted ones.*

The cumulative HR obtained at four operating conditions is shown in Figure 5.22. It can be stated that the HR is overestimated with the reference parameters, mainly explained by the high C_{w1} and the incorrect TDC position.

For the sake of brevity, the analysis is completed only with two additional parameters. Thus, Figure 5.23 shows the difference of the indicated efficiency and peak temperatures in the complete engine map, calculated with the adjusted and reference parameters. On the one hand, it can be seen that the reference parameters (mainly due to TDC position) lead to overestimating the indicated efficiency more than 4% at low load, where the maximum deviation takes place. On the other hand, the variation of the peak temperature is a key parameter for both, the thermal behaviour of the engine and NO_x formation. As shown, the maximum variation reaches 57°C at high load, being the

relative effect more important at low speed. This variation can lead to heat transfer differences up to 9%. Moreover, even though out of the scope of this work, in case that the chamber conditions were used as boundary conditions for combustion models, these variations would have important effects on NO_x modelling.

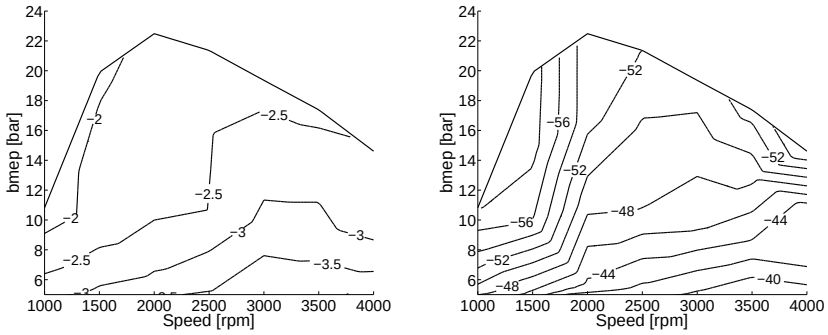

Figure 5.23. *Difference of indicated efficiency (left) and maximum temperature (right) after characterization.*

5.4 Mechanical losses model

As explained in Chapter 4.3, to determine the specific energy flow to the coolant and oil, it is necessary the detailed determination of the mechanical losses. Strictly speaking, the mechanical losses power (N_m) is defined as:

$$N_m = N_{fr} + N_a - N_p \tag{5.56}$$

As detailed in Chapter 4.2.2, N_p is directly determined from the indicated cycle[6], and the terms N_{fr} and N_a can be split as shown in Equations (4.27) and (4.28), recalled here for convenience:

$$N_{fr} = N_{fr,pis} + N_{fr,bear} + N_{fr,valv} \tag{5.57}$$

$$N_a = N_{cool} + N_{oil} + N_f \tag{5.58}$$

[6]The negative sign is used for coherence with the sign convention explained in Chapter 4.2.2. In naturally aspirated engines, N_p is negative, thus increasing N_m value, whilst in highly turbocharged engines N_p can be positive thus reducing the N_m.

As explained in Chapter 4.3, these terms lead to part of the coolant and oil heat rejection externally measured. Therefore, to separate its contribution from HT in the chamber and ports, it is necessary to determine them accurately. Taking into account that their experimental determination cannot be performed in conventional engine test benches, they were indirectly determined from available experimental information along with specific sub-models proposed in the next sections.

5.4.1 Lubrication fundamentals

To determine the friction between surfaces in contact, it is necessary to take into account the lubrication mechanism at which they operate. The lubricating regimes can be identified by means of the *Stribeck diagram*, presented in Figure 5.24. In this diagram, the friction coefficient (f) in a bearing is represented as function of the *Sommerfeld number*(S), also known as *duty parameter*, which is defined as:

$$S = \frac{\mu\ \omega}{\sigma} \tag{5.59}$$

where μ is the oil viscosity, ω is the rotational speed and σ is the load per unit area.

In Figure 5.24, S_0 is the duty parameter at which transition between boundary and mixed lubrication occurs, f_0 is the dry friction coefficient during boundary lubrication, S_{cr} is the critical duty parameter at which the transition between mixed and hydrodynamic lubrication occurs and f_{cr} is the friction coefficient when $S = S_{cr}$.

As can be seen in Figure 5.24, depending on the duty parameter, three defined lubricating zones are considered:

- **Boundary region**: in this region, the surfaces in contact are not completely separated by a lubricant film and there is a contact surface similar to that in dry contact. The friction losses at these conditions depend directly on the material rugosity and the dry contact between the surfaces, having higher friction levels than the other lubrication regimes.
- **Hydrodynamic region**: at hydrodynamic conditions, there is a lubricant film between the moving surfaces, and hence no direct contact

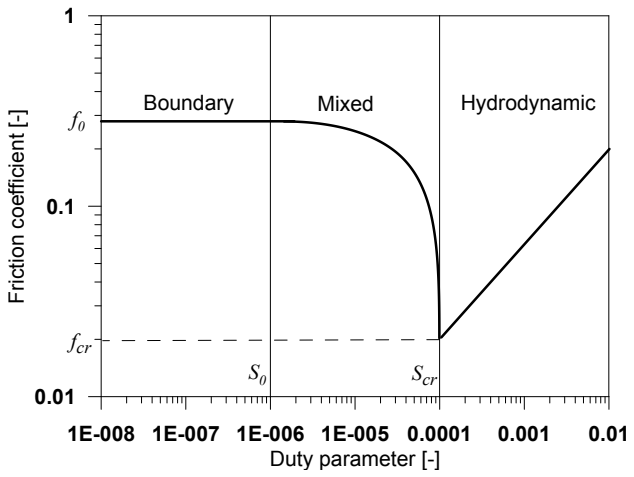

Figure 5.24. *Stribeck Diagram.*

between them take place. This kind of lubrication occurs at stable steady operation, where the movement of the pieces constantly drag oil towards the lubricant film, thus keeping it stable.

– **Mixed region**: in this lubricating regime, the asperities of the surfaces protrude through the oil film, thus some dry contact takes place between them. This occurs when the oil drag speed is low and its temperature is high, thus reducing both the viscosity and film thickness. At this regime, both boundary and hydrodynamic lubrication occurs.

– **Elastohydrodynamic region**: this region is not represented in the Figure 5.24; however, it is explained here because this regime is presented in some elements of the engine as will be explained later. The elastohydrodynamic lubrication occurs when the lubricant between surfaces in rolling contact is subject to sufficiently high load to elastically deform them during the hydrodynamic action. The oil viscosity increases importantly due to the high pressure, thus allowing keeping the film.

In RICEs, depending on the element analysed and the instantaneous operating condition, all the described lubricating regimes can take place. Figure 5.25 shows the main lubrication zones for the elements considered in this work.

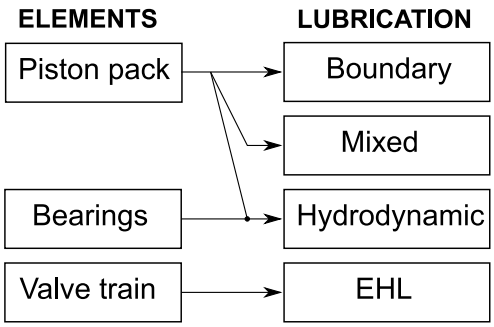

Figure 5.25. *Lubrication regimes for each element.*

5.4.2 Friction losses between piston pack and liner

The piston elements considered to be in contact with the liner are the compression, wiper and oil rings and the piston skirt. These elements are referred henceforth as *piston pack*. The friction in these elements is about 40-75% of N_{fr} [31]. The seal between the liner and the rings is not perfect, thus some gas leakage occurs. This leakage produce a pressure load on the rings back-face, which increase the contact force between them and the liner, and hence the friction. The piston-rings assembly depends on the engine design, thus several different configuration are used in current production engines; however, a rather common configuration of three rings (i.e. compression, wiper and oil rings) is considered for the model development.

To determine the friction of each element it is necessary to do some simplifications of the real operation:

- No movement of the ring in the groove is considered.
- At each crank angle (α), the oil film has a uniform thickness around the perimeter of the ring and it is treated as an incompressible fluid.
- After assembled, the rings and liner are assumed to be a rigid body, thus no twist, mechanical nor thermal deformations are allowed.
- The ring's face is always in contact with the lower face of its groove.

The simplifications assumed in this work are similar as those found in the literature review [34]. More complex models assume twist and relative

motion of the rings within the groove [35]. This kind of approaches require detailed geometrical information and must be performed by means of finite element analysis or dedicated experimental installations. For the application presented in this work, where the main input is the in-cylinder pressure, the results obtained with the assumptions made are considered to be accurate enough.

5.4.2.1 Piston pack load determination

In Figure 5.26, a scheme of the loads acting on the piston pack are presented (for the sake of clearness, piston-ring interactions were omitted).

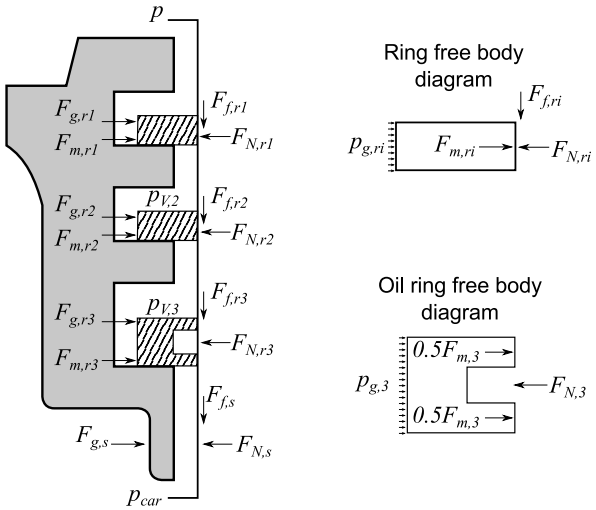

Figure 5.26. *Forces acting on the piston pack.*

The normal force ($F_{N,ri}$) exerted on each ring is due to the gas force ($F_{g,ri}$) applied onto the ring's back-face, and the ring's mounting force[7] ($F_{m,ri}$), thus:

$$F_{N,ri} = F_{g,ri} + F_{m,ri} \tag{5.60}$$

[7]This is the pre-load of the ring due to the elastic deformation when the ring is assembled between the piston and liner. This load should be as low as possible but high enough to ensure the proper combustion chamber sealing.

where ri refers to the ring i (i.e. $r1$ -compression ring-, $r2$ -wiper ring- or $r3$ -oil ring-).

$$\begin{aligned} F_{g,ri} &= p_{ri} \ \times A_{ri} \\ &= p_{ri} \ \pi \left(D - 2 \ x_{ri}\right) \ h_{ri} \end{aligned} \tag{5.61}$$

where A_{ri} is the ring area in contact with the gas and p_{ri} is the pressure in each groove/ring volume. As shown in Figure 5.26, p, p_{V2} and p_{V3} are the gas pressures applied in the compression, wiper and oil rings respectively, being the in-cylinder pressure (p) experimentally obtained, and p_{V2} and p_{V3} estimated by means of the blow-by model described in Appendix 5.B.

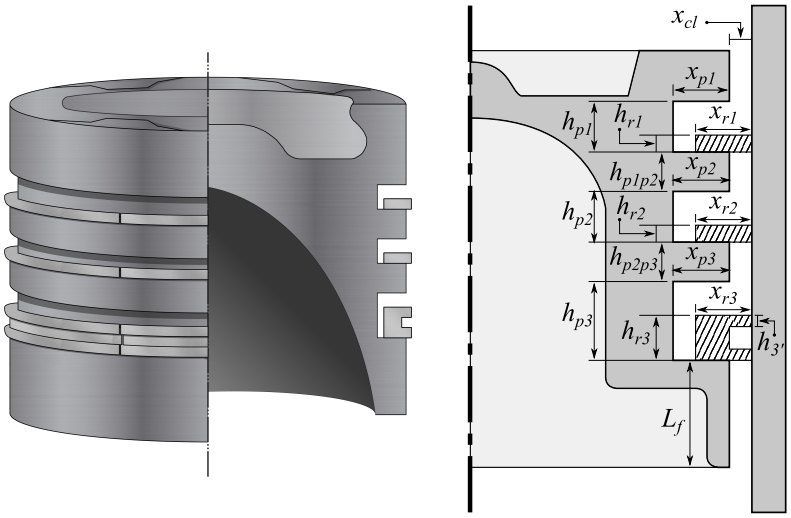

Figure 5.27. *Rings and grooves geometry.*

To determine the mounting force of each ring ($F_{m,ri}$) it is necessary to know the contact pressure of the assembled ring[8] ($p_{c,ri}$); however, the experimental determination of this pressure is difficult, and hence it is commonly

[8] A detailed description of the contact pressure determination can be found in Appendix 5.C.

calculated from the tangential ($F_{t,ri}$) or the diametral ($F_{d,ri}$) forces[9], according to Equations (5.62) and (5.63) respectively [36]:

$$F_{m,ri} = 2\ \pi\ F_{t,ri} \tag{5.62}$$

$$= 0.9\ \pi\ F_{d,ri} \tag{5.63}$$

where $A_{c,ri}$ is the contact area between the ring and the liner.

In the case of the piston skirt, it is assumed that the resulting normal force exerted over the piston (F_{N_B}) is applied in the skirt ($F_{N,s} = F_{N,_B}$). This force is determined from the engine mechanism dynamics as presented in the Appendix 5.D.

5.4.2.2 Friction between piston pack and liner

To determine the friction coefficient between piston pack and liner, the instantaneous lubrication regime characterized by the duty parameter has to be estimated. Since the piston has an alternative movement, some modifications have to be made in Equation (5.59), thus obtaining the instantaneous duty parameter for the rings (S_{ri}) as follows [37]:

$$S_{ri}(\alpha) = \frac{\pi\ D\ \mu\ v_{y,_B}(\alpha)}{F_{N,ri}(\alpha)} \tag{5.64}$$

where ω in Equation (5.59) was replaced by the instantaneous piston speed[10] ($v_{y,_B}$), and σ was calculated from the load in the ring ($F_{N,ri}$) and the contact length (πD), following the considerations made by Taraza and Henein [37].

According to Stanley et al. [34], there is a linear correlation between the $Ln(f_{ri}(\alpha))$ and $Ln(S_{ri}(\alpha))$ in the hydrodynamic region ($S_{ri} > S_{cr}$); thus, known the duty parameter, the friction coefficient (f_{ri}) at hydrodynamic conditions is instantaneously determined as:

$$Ln(f_{ri}(\alpha)) = m\ Ln(S_{ri}(\alpha)) + Ln(B) \tag{5.65}$$

[9] These values depend on the rings design and requirements. As a reference, the values of $F_{d,ri}$ provided by the manufacturer in the case of **Engine A** are 75, 40 and 90 N for the compression, wiper and oil rings respectively.

[10] Details of $v_{y,_B}$ calculation can be found in Appendix 5.D.

where m and $Ln(B)$ are the slope and y intercepts, whose values depends on the rings geometry. In this work, the mean value of those proposed in [34] were used, thus $m = 0.625$ and $Ln(B) = 1.962$.

In the case of operating in the mixed region ($S_0 < S_{ri} < S_{cr}$), $f_{ri}(\alpha)$ is determined following the proposal of Taraza and Henein [37]:

$$f_{ri}(\alpha) = f_0 \left(1 - \frac{|S_{ri}(\alpha)|}{S_{cr}}\right) + f_{cr} \left(\frac{|S_{ri}(\alpha)|}{S_{cr}}\right) \tag{5.66}$$

where $S_{cr} = 1 \times 10^{-4}$ is the critical duty parameter, $f_{cr} = 0.0225$ is the friction coefficient when $S_{ri} = S_{cr}$, and $f_0 = 0.14$ is the dry friction coefficient.

Note that if $S_{ri}(\alpha)$ tends to zero, $f_{ri}(\alpha)$ can be determined as:

$$\lim_{S_{ri}(\alpha)\to 0} \left[f_0 \left(1 - \frac{|S_{ri}(\alpha)|}{S_{cr}}\right) + f_{cr} \left(\frac{|S_{ri}(\alpha)|}{S_{cr}}\right)\right] = f_0 \tag{5.67}$$

which means that for small enough S_{ri} values, the lubrication is in the boundary regime.

Similarly as for the rings, the friction coefficient between the piston skirt and the liner ($f_s(\alpha)$) depends on the lubrication regime. As there is high contact surface, there is always an oil film between skirt and liner, therefore, hydrodynamic regime is assumed. The instantaneous duty parameter of the skirt ($S_s(\alpha)$) is determined as [34, 37]:

$$S_s(\alpha) = \frac{\mu \; v_{y,B}(\alpha)}{p_{c,s}(\alpha) \; L_s} \tag{5.68}$$

being L_s the skirt length and $p_{c,s}(\alpha)$ the contact pressure applied on the skirt, which is estimated from the normal force in the skirt ($F_{N,s}$) as:

$$p_{c,s}(\alpha) = \frac{F_{N,s}(\alpha)}{\pi \; D \; L_s} \tag{5.69}$$

The friction coefficient between skirt and liner is then determined as proposed in [37]:

$$f_s(\alpha) = k_s \; \sqrt{S_s(\alpha)} \tag{5.70}$$

where k_s is a constant, whose value is 2.5 according to Taraza and Henein [37].

Once the friction coefficient of each element of piston pack is determined, the friction force of each ring ($F_{fr,ri}$) and the skirt ($F_{fr,s}$) is calculated as:

$$F_{fr,ri}(\alpha) = f_{ri}(\alpha)\ F_{N,ri}(\alpha) \tag{5.71}$$

$$F_{fr,s}(\alpha) = f_{s}(\alpha)\ F_{N,s}(\alpha) \tag{5.72}$$

and the total power lost by friction in the piston pack during one cycle ($N_{fr,pis}$) is determined as:

$$N_{fr,pis} = \sum_{ri=1}^{3} \left[\oint F_{fr,ri}(\alpha)\ v_{y,_B}(\alpha)\ \mathrm{d}\alpha \right] + \oint F_{fr,s}(\alpha)\ v_{y,_B}(\alpha)\ \mathrm{d}\alpha \tag{5.73}$$

5.4.3 Bearings friction

The friction in the bearings ranges between 20 and 40% of N_{fr} [31]. The detailed determination of the losses due to friction and housing deformation of the bearings can be performed by means of finite element analysis [38, 39]. As has been justified before, this approximation is not suitable for the application presented in this work. Notwithstanding, by considering the bearing lubrication along with the kinematics and dynamics of the engine mechanism, a simplified and accurate friction model can be developed [37].

The model presented is based on the mobility method [40], in which the minimum oil film thickness (h_0) and the journal centre location and trajectory inside the bearing are calculated. In Figure 5.28, the geometry of a loaded bearing is presented, where e is the eccentricity between the journal and bearing centres, $v_{_O}$ is the journal centre speed, F_{bear} is the instantaneous load, φ the angle between F_{bear} and the centres line (attitude angle) and ψ is the angle between F_{bear} and $v_{_O}$.

Note that F_{bear} depends on the bearing location on the engine mechanism (i.e. connecting rod or crankshaft). Figure 5.29 presents the forces exerted on each bearing in a 4-cylinder engine. The load applied on a connecting rod bearing ($F_{A,i}$, where i is the cylinder analysed) can be directly obtained from the dynamic analysis of the engine mechanism. On the other hand, despite the force exerted by each cylinder in the crankshaft ($F_{O,i}$, where i is the cylinder analysed) can be also determined from the dynamic analysis

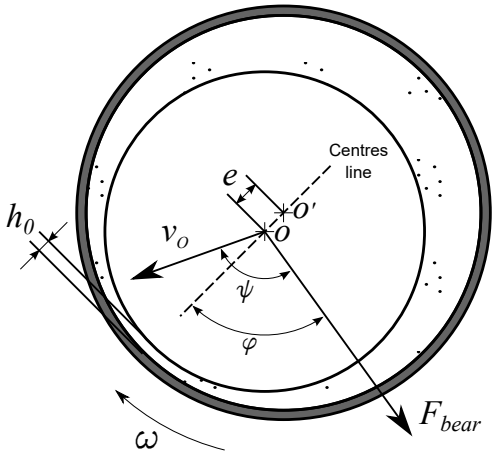

Figure 5.28. *Scheme of bearings geometry.*

of the engine mechanism, how this force is supported by each crankshaft bearing requires specific measurements or finite element analysis. According to the results shown in [41], it is accurate to assume that each of them supports half of the force of adjacent cylinders, as shown in Figure 5.29. The detailed calculation of $F_{A,i}$ and $F_{O,i}$ is provided in Appendix 5.D.

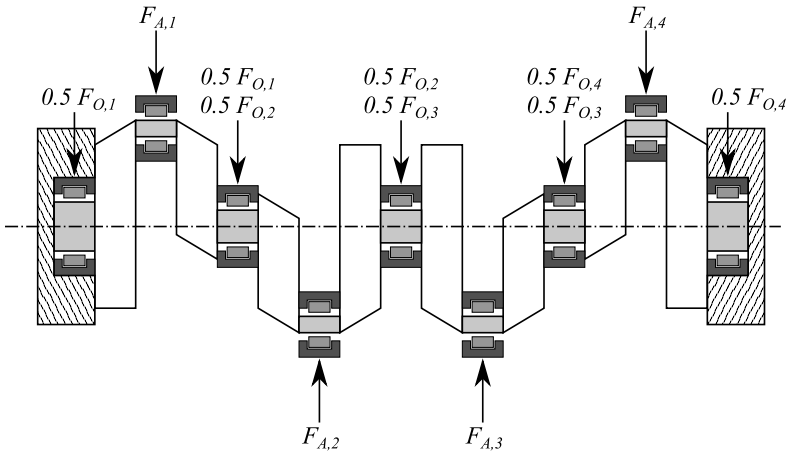

Figure 5.29. *Scheme of loads applied on the bearings in a 4-cylinder engine.*

According to [40], the friction force in the bearings ($F_{fr,bear}$) can be determined as:

$$F_{fr,bear} = \frac{\mu\ D_{bear}^2\ \omega\ L_{bear}\ J_1^{00}}{4\ c} + \frac{c\ \epsilon\ F_{bear}}{D_{bear}} sin\varphi + \frac{2\ v_{_O}\ F_{bear}}{D_{bear}\ \omega} sin\psi \quad (5.74)$$

where ω is the angular speed assumed to be the same for the journal and bearing, D_{bear} is the bearing diameter, L_{bear} is the bearing length, μ is the oil viscosity, c is the clearance between journal and bearing, $\epsilon = e/c$ is the eccentricity ratio, $v_{_O}$ is the speed of the bearing centre displacement and J_1^{00} is a parameter that characterize the film extent and film thickness change along the bearing, which is determined for a complete film extent as proposed by Taylor [40]:

$$J_1^{00} = \int_{\theta=0}^{\theta=2\pi} \frac{1}{1+\epsilon cos\theta}\ \mathrm{d}\theta = \frac{2\ \pi}{\sqrt{1-\epsilon^2}} \quad (5.75)$$

The terms of the friction force in Equation (5.74) correspond, from left to right, to the shear stress (known as *Couette constituent*), the pressure constituent and the translatory constituent, this last related with the movement of the journal centre [40]. The model presented in this work is a quasi-steady model; therefore, equilibrium values of F_{bear}, e and φ are reached at each crank angle, and hence, there is no translatory component ($v_{_O} = 0$) [37]. Taking this into account and replacing Equation (5.75) in (5.74), $F_{fr,bear}$ can be finally calculated as:

$$F_{fr,bear} = \frac{2\ \pi\ \mu\ D_{bear}^2\ \omega\ L_{bear}}{c\ \sqrt{1-\epsilon^2}} + \frac{c\ \epsilon\ F_{bear}}{D_{bear}} sin\varphi \quad (5.76)$$

For a constant loaded bearing, as considered in this model, the friction force correspond to the Ocvirk's short bearing theory [42]. According to this theory, ϵ can be determined as [37]:

$$\frac{2F_{bear}/L_{bear}}{\omega\mu D_{bear}} \left(\frac{2c}{D_{bear}}\right)^2 \left(\frac{D_{bear}}{L_{bear}}\right)^2 = \frac{\pi\epsilon}{(1-\epsilon^2)^2}\sqrt{0.62\epsilon^2+1} \quad (5.77)$$

and φ as:

$$\varphi = tan^{-1}\left[\frac{\pi\sqrt{1-\epsilon^2}}{4\epsilon}\right] \quad (5.78)$$

To solve the Equations (5.77) and (5.78), it is necessary to know specific bearing geometry. As this geometrical information is not usually available, in Table 5.10, typical geometrical values of engine bearings as function of engine bore are provided.

Parameter	**Connecting rod**	**Crankshaft**
D_{bear}	0.7 D	0,6 D
L_{bear}	0,28 D	0,24 D
e	0,0005 D	0,0004 D
c	0,0018 D	0,0015 D

Table 5.10. *Bearings geometrical parameters determination in function of cylinder bore.*

Once the friction components presented in Equation (5.76) are determined, the power lost by friction in the bearings during one cycle can be calculated as:

$$N_{fr,bear} = \sum_{i=1}^{NB} \left[\oint \frac{\omega \ D_{bear,i}}{2} F_{fr,bear,i}(\alpha) \ \mathrm{d}\alpha \right] \tag{5.79}$$

where i is the analysed bearing and NB is the total number of bearings considered.

5.4.4 Valve train friction

The friction losses in valve train mechanisms depend on their design but commonly ranges between 7 and 30% of N_{fr} [31]; in a conventional Diesel engine with tappet follower, the rocker arm bearing accounts for about 10% of the total friction in the valve train system, the cam bearing between 1 and 12%, the stem and valve guide about 2% and the cam/tappet contact between 85 and 90% [43]. As most of the friction occurs in the cam/tappet contact, in some designs the sliding contact is replaced by a rolling contact by using a roller instead of a tappet, thus reducing the friction about 50% [44].

The model presented in this work is focused on the tappet follower mechanism, which is the case of the **Engine A** and **Engine B**; however, to provide a model suitable for most widespread valve train systems, the kinematics and dynamics of both, tappet and rolling contacts, are presented in Appendix 5.E.

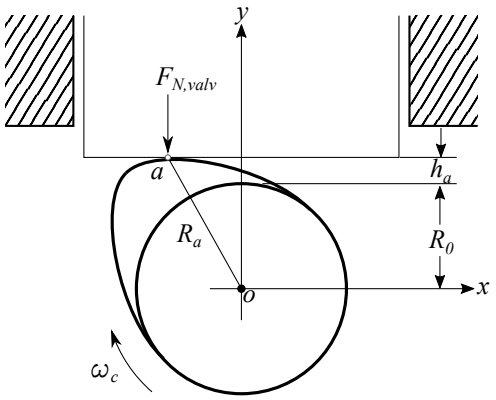

Figure 5.30. *Scheme of the contact between cam and tappet.*

The cam and follower contact surface is separated by a thin oil film, which is exposed to very high load. This causes an elastic deformation in the cam and the follower that is comparable with the oil film thickness. To estimate the oil film thickness, the elastohydrodynamic lubrication theory can be used [45]. Therefore, the non-dimensional film thickness (H) is estimated through the Dowson and Higginson proposal for line contact between two cylinders [46]:

$$H = \frac{h_0}{R_c} = 2.65\ U^{0.7}\ G^{0.54}\ W^{-0.13} \tag{5.80}$$

where h_0 is the minimum oil film thickness, key parameter to calculate the friction in the valve train, R_c is the equivalent radius of curvature (determined as described in Appendix 5.E.1) and U, G and W are dimensionless parameters defined as:

$$U = \frac{\mu\ v_e}{E_c\ R_c} \tag{5.81}$$

$$G = \alpha_c\ E_c \tag{5.82}$$

$$W = \frac{F_{N,valv}}{E_c\ R_c\ L_{cam}} \tag{5.83}$$

being v_e the entrainment velocity, $F_{N,valv}$ the force normal to the common tangent[11], α_c the pressure viscosity coefficient, L_{cam} the cam width and E_c the effective elastic modulus calculated as [47]:

$$\frac{1}{E_c} = 0.5 \left[\frac{1-\nu_{cam}^2}{E_{cam}} + \frac{1-\nu_{fol}^2}{E_{fol}} \right] \tag{5.84}$$

where E_{cam} and E_{fol} are the Young's modulus and ν_{cam} and ν_{fol} are the Poisson's ratios of the cam and follower respectively[12].

The friction in the cam/follower contact ($F_{fr,valv}$) has two components, the boundary friction ($F_{b,valv}$) due to the asperity contact, and the viscous friction component ($F_{v,valv}$) due to the shear of lubricant [47, 48]:

$$F_{fr,valv} = F_{b,valv} + F_{v,valv} \tag{5.85}$$

$F_{b,valv}$ is determined as proposed in [49][13]:

$$F_{b,valv} = \tau_0 \ A_a + k_m \ P_a \tag{5.86}$$

where τ_0 is the Eyring shear stress, A_a is the asperity area, k_m is the pressure coefficient of the boundary shear strength and P_a is the load carried by the asperities. The asperity area is calculated as [49]:

$$A_a = \pi^2 (\varrho \ \zeta \ \sigma)^2 A \ F_2 \tag{5.87}$$

and P_a can be determined as:

$$P_a = \frac{16\sqrt{2}}{15} \ \pi (\varrho \ \zeta \ \sigma)^2 \ \sqrt{\frac{\sigma}{\zeta}} \ E_c \ A \ F_{5/2} \tag{5.88}$$

being ϱ the asperity density, ζ the asperities radius of curvature, σ the composite surface roughness parameter and A the Hertzian contact area that can be

[11] Detailed determination of v_e and $F_{N,valv}$ is included in Appendix 5.E.

[12] As this information is not usually available, a reasonable assumption is to use the Young's modulus of the steel as the effective elastic modulus ($E_c = E_{steel}$).

[13] Although the engine used in this work have tappet contact, Equation (5.86) can also be applied to rolling contact.

calculated by modelling the cam/follower contact as in the case of two cylinders [48]. In Figure 5.31, the typical load distribution in the cam/follower contact is presented. Thus, the Hertzian area is:

$$A = 2\ b\ L_{cam} \tag{5.89}$$

being b the half Hertzian width calculated as [45]:

$$b = \sqrt{\frac{8\ F_{N,valv}\ R_c}{\pi\ E_c}} \tag{5.90}$$

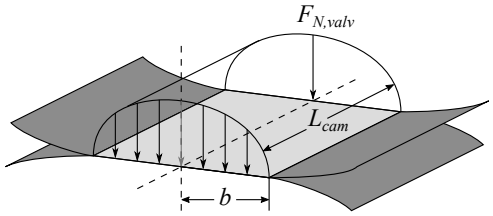

Figure 5.31. *Hertzian contact area.*

The statistical functions F_2 and $F_{5/2}$ (see Equations (5.87) and (5.88)) are defined as function of the separation parameter ($\lambda = \frac{h_0}{\sigma}$) as follows [47, 48]:

$$F_n(\lambda) = \frac{1}{\sqrt{2\ \pi}} \int_{\lambda}^{\infty} (s-\lambda)^n\ e^{-s^2/2} \mathrm{d}s \tag{5.91}$$

It is convenient to use simplified expressions to solve Equation (5.91); therefore, several empirical correlations are presented in Equations (5.92) and (5.93). This kind of simplification facilitates the application of the model, and similar expressions can be also found in related works [47].

$$F_2 = 1.47\ e^{-\lambda} + 0.0117\lambda^3 - 0.143\lambda^2 + 0.61\lambda - 0.93 \tag{5.92}$$

$$F_{5/2} = 2.26\ e^{-\lambda} + 0.03\lambda^3 - 0.31\lambda^2 + 1.172\lambda - 1.64 \tag{5.93}$$

The viscous friction component ($F_{v,valv}$) is determined as [48][14]:

[14]The model presented in this section was developed for a cam/tappet contact. A similar model to estimate $F_{fr,valv}$ in a cam/rolling contact can be found in Appendix 5.F.

$$F_{v,valv} = \tau \ (A - A_a) \tag{5.94}$$

where τ is the shear stress of the oil, which is calculated depending on whether the oil has a Newtonian or non-Newtonian behaviour. This can be determined by comparison of the Eyring shear stress with the actual shear stress. Therefore:

$$\tau = \frac{\mu_c \ v_s}{h_0} \quad ; \ \text{if} \ \ \tau \leq \tau_0 \tag{5.95}$$

$$\tau = \tau_0 + \kappa \ p_c \quad ; \ \text{if} \ \ \tau > \tau_0 \tag{5.96}$$

being v_s the sliding velocity determined as shown in Appendix 5.E.1, κ the rate of change of shear stress with pressure, p_c the pressure on the oil film contact and μ_c the oil viscosity at the contact point. p_c is determined as [50]:

$$p_c = \frac{F_{N,valv} - P_a}{A - A_a} \tag{5.97}$$

and μ_c as [51]:

$$\mu_c = \mu \ e^{(\alpha_c \ p_c)} \tag{5.98}$$

Note that several parameters regarding the lubricant and surface properties are required to determine the friction components. Table 5.11 summarises typical values of these parameters [47, 48, 52].

Taking into account the previous analysis, Equation (5.99) provides the final expression used to determine the total friction in the valve train $N_{fr,valv}$:

$$N_{fr,valv} = N_{IV} \left[\oint F^{int}_{fr,valv}(\alpha) \ v^{int}_c(\alpha) \ \mathrm{d}\alpha \right] + \\ + N_{EV} \left[\oint F^{exh}_{fr,valv}(\alpha) \ v^{exh}_c(\alpha) \ \mathrm{d}\alpha \right] \tag{5.99}$$

where the index *int* and *exh* refers to intake and exhaust, v_c is the contact speed determined as shown in Appendix 5.E.1 and N_{IV} and N_{EV} are the total number of intake and exhaust valves respectively.

Parameter	Value	Units
α_c	1.4×10^{-8} - 1.8×10^{-8}	m^2/N
σ	0.4	μm
(σ/ζ)	0.001	-
$(\varrho\ \zeta\ \sigma)$	0.055	-
τ_0	2-10	MPa
k_m	0.17	-
κ	0.08	
E_c	187 - 210	GPa

Table 5.11. *Typical values of the model parameters.*

5.4.5 Coolant pump power

To pump the coolant, centrifugal pumps with straight blades are used, thus the energy consumption (N_{cool}) can be determined as:

$$N_{cool} = \frac{\Delta p_{cool}\ \dot{V}_{cool}}{\eta_{cool}} \tag{5.100}$$

where $\dot{V}_{cool}$ is the coolant flow rate, η_{cool} is the pump efficiency and Δp_{cool} is the coolant pressure drop. As these parameters are not always available, they can be determined as follows:

$$\Delta p_{cool} = k_{1,cool}\ \dot{V}_{cool}^2 \tag{5.101}$$

being $k_{1,cool}$ a proportionality value experimentally adjusted.

Since the coolant pump is a centrifugal machine, the mass flow does not necessarily share a linear trend with the rotating speed. However, from the experimental results showed in Figure 5.32, it can be stated that this hypothesis is suitable. As can be seen, the pressure and flow rate intersection points fits linearly with the engine speed having a coefficient of determination (R^2) close to 1. Therefore, it is reasonable to assume that:

$$\dot{V}_{cool} = k_{2,cool}\ n \tag{5.102}$$

where $k_{2,cool}$ is the proportionality constant between coolant flow and engine speed.

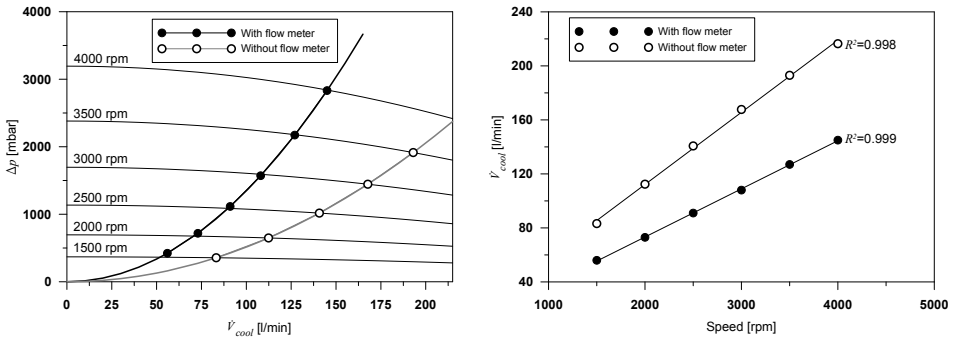

Figure 5.32. *Pressure drop at different coolant flow and engine speed in* ***Engine A****.*

By combining Equations (5.100), (5.101) and (5.102), the following expression for N_{cool} can be obtained:

$$N_{cool} = \frac{k_{1,cool}\ \dot{V}_{cool}^3}{\eta_{cool}} = \frac{k_{1,cool}\ k_{2,cool}^3\ n^3}{\eta_{cool}} \tag{5.103}$$

In the case of **Engine A**, the values of the adjustment constants are provided in Chapter 6.2.1. In the case of **Engine B**, the pumps are driven externally and are not taken into account in the IGEB.

5.4.6 Oil pump power

In RICEs, the oil is usually pumped by means of gear or lobe pumps. Therefore, the power consumption (N_{oil}) can be calculated as:

$$N_{oil} = \frac{\Delta p_{oil}\ \dot{V}_{oil}}{\eta_{oil}} \tag{5.104}$$

where η_{oil} is the pump efficiency, Δp_{oil} is the oil pressure drop and $\dot{V}_{oil}$ is the coolant flow rate. In the case that Δp_{oil} and $\dot{V}_{oil}$ are not available from measurements, they must be estimated. On the one hand, taking into account that the oil pump is a volumetric machine, the oil flow rate can be obtained as a function of the engine speed as:

$$\dot{V}_{oil} = k_{1,oil}\ n \tag{5.105}$$

where $k_{1,oil}$ is the proportionality between oil flow and engine speed.

On the other hand, since the pump has a relief valve, Δp_{oil} depends on $\dot{V}_{oil}$ until a certain engine speed ($n_{\Delta p,max}$) at which the maximum oil pressure ($\Delta p_{oil,max}$) is reached. For values lower than $\Delta p_{oil,max}$ ($n < n_{\Delta p,max}$), Δp_{oil} can be determined by considering a simplified model in which the pressure losses in a pipe is computed.

The friction factor in a pipe (f_{pipe}) can be obtained with the Darcy-Weisbach equation:

$$\begin{aligned}\Delta p_{oil} &= \frac{8\ f_{pipe}\ L_{pipe}}{\pi^2\ D_{pipe}^2\ g}\ \dot{V}_{oil}^2 \\ &= k'_{2,oil}\ f_{pipe}\ \dot{V}_{oil}^2\end{aligned} \tag{5.106}$$

being L_{pipe} the pipe length, D_{pipe} the pipe diameter, g the gravity and $k'_{2,oil} = 8L_{pipe}/\pi^2 D_{pipe}^2\ g$ a constant value. To determine f_{pipe}, the empirical formula of Moody can be used [53]:

$$f_{pipe} = 0.001375 \left\{ 1 + \left[200\ \sigma_r\ + \frac{\pi\ D_{pipe}\ \mu_{oil} \times 10^6}{4\ \dot{V}\ \rho_{oil}} \right]^{1/3} \right\} \tag{5.107}$$

where σ_r is the pipe rugosity, μ_{oil} is the oil viscosity and ρ_{oil} is the oil density.

In practice, it is not easy to choose representative values for σ_r and D_{pipe} to solve Equation (5.107), thus, a simpler proposal based on this expression is presented:

$$f_{pipe} = \left(\frac{k'_{3,oil}\ \mu_{oil}}{\dot{V}_{oil}} \right)^{k_{3,oil}} \tag{5.108}$$

Replacing Equation (5.108) into (5.106), and bearing in mind that $\dot{V}_{oil} = k_{1,oil}\ n$, the following expression for Δp_{oil} is obtained:

$$\begin{aligned}\Delta p_{oil} &= k'_{2,oil} \left(\frac{k'_{3,oil}\ \mu_{oil}}{\dot{V}_{oil}} \right)^{k_{3,oil}}\ \dot{V}_{oil}^2 \\ &= \left(\frac{k_{2,oil}\ \mu_{oil}}{k_{1,oil}\ n} \right)^{k_{3,oil}}\ (k_{1,oil}\ n)^2\end{aligned} \tag{5.109}$$

Note that, if the oil pressure is measured at some point along the oil line, it can be used either directly in Equation (5.104) or to calibrate the constants $k_{2,oil}$ and $k_{3,oil}$ of Equation (5.109). Regardless of whether this information is available, the set of equations presented in this section allows modelling the oil pump power consumption. Therefore, from Equation (5.104) and taking into account Equations (5.105) and (5.109), the oil pump power can be determined as:

$$N_{oil} = \frac{k_{1,oil}\ n\ \Delta p_{oil,max}}{\eta_{oil}}\ ;\ \text{if} \quad \Delta p_{oil} = \Delta p_{oil,max} \tag{5.110}$$

$$N_{oil} = \frac{(k_{1,oil}\ n)^3}{\eta_{oil}} \left(\frac{k_{2,oil}\ \mu_{oil}}{k_{1,oil}\ n} \right)^{k_{3,oil}}\ ;\ \text{if} \quad \Delta p_{oil} < \Delta p_{oil,max} \tag{5.111}$$

Similar as for the coolant pump, the values of the adjustment constants for **Engine A** are provided in Chapter 6.2.1.

5.4.7 Fuel pump power

In conventional piston pumps, the total amount of fuel compressed by the pistons (part of which is injected and part returns to the low pressure circuit) depends on the pump rotating speed and pump size, thus the volumetric flow ($\dot{V}_f$) is proportional to the engine speed. Thereby, the fuel pump power depends on the engine speed and the pressure drop (Δp_f), which can be assumed to be equal to the rail pressure (p_{rail}), taking into account that p_{rail} is much higher than the feeding pressure[15]. Taking into account these comments, Equations (5.112) and (5.113) are proposed:

$$N_f = \frac{\dot{V}_f\ \Delta p_f}{\eta_f} \tag{5.112}$$

$$= \frac{k'_{1,f}\ n\ p_{rail}}{\eta_f} \tag{5.113}$$

where k'_f is the proportionality constant between $\dot{V}_f$ and n, and η_f is the pump efficiency.

It is important to consider that, some new fuel pumps include both, a pressure control valve and a volume control valve, whose behaviour differs

[15] p_{rail} ranges between 200 and 2000 bar meanwhile the feeding pressure goes up to 5 bar.

from conventional piston pumps. As can be seen in Figure 5.33 (a), the fuel pump power consumption (N_f) in this kind of pumps depends on p_{rail}, n and the injected fuel mass as well. To determine the power consumption, a characterization campaign was carried out through a modification of **Engine A** test bench, consisting on dismounting the injectors from the combustion chambers and performing motoring tests at different speed, p_{rail} and injected fuel mass (injecting in a vessel). The rest of friction losses were kept constant by controlling the oil temperature, thus the mechanical losses variations can be only attributed to injection setting changes.

Firstly, a motoring test without fuel pump activation ($p_{rail} = 0$) is measured to determine the reference power consumption ($N_{f,0}$). Then, p_{rail} and the injected fuel mass were swept. The power required to drive the fuel pump is then calculated as the difference between the current power consumption and the reference power as presented in Equation (5.114):

$$N_f = 2\pi\ n\ M_e - N_{f,0} = \frac{\Delta p_f\ \dot{V}_f}{\eta_f} \tag{5.114}$$

where M_e is the brake torque.

In Figure 5.33 (b), the variation of M_e due to the injection of a high (m_f+) or a low (m_f-) fuel amount is presented. This dependency with m_f is explained by the strategy of the ECU, which manages the volume control valve and regulates the amount of fuel compressed in the high pressure pump to reduce the power waste.

Due to the difficulty to determine $\dot{V}_{fuel}$ in this kind of pumps, an empirical correlation was adjusted based on the experimental results obtained from **Engine A**:

$$\dot{V}_f = k_{1,f}\ \dot{m}_f^{k_{2,f}} \tag{5.115}$$

where $k_{1,f}$ and $k_{2,f}$ are calibration constants and $\dot{m}_f$ is the total fuel mass injected.

Finally, by replacing Equation (5.115) in (5.112), the power consumption can be estimated as:

$$N_f = \frac{k_{1,f}\ \dot{m}_f^{k_{2,f}}\ p_{rail}}{\eta_f} \tag{5.116}$$

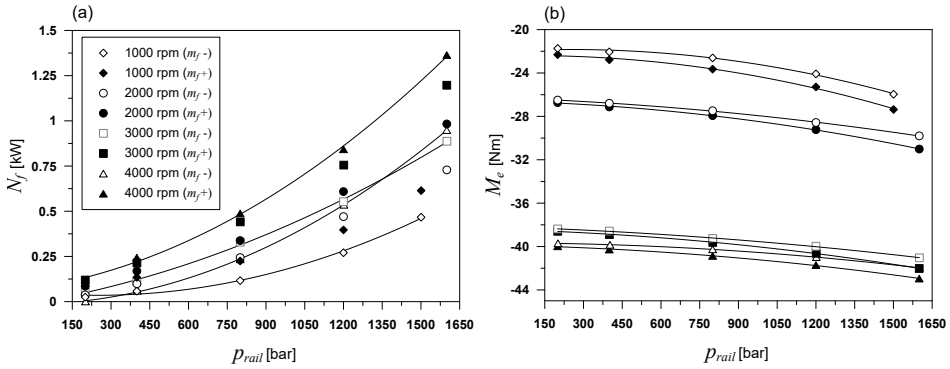

Figure 5.33. *Fuel pump power (left) and brake torque (right) at two levels of injected fuel mass.*

In Figure 5.34, the comparison between the experimental and modelled fuel pump power is presented. It is possible to see how the model behaves well in all operating conditions measured, considering a wide engine speed, p_{rail} and fuel mass range.

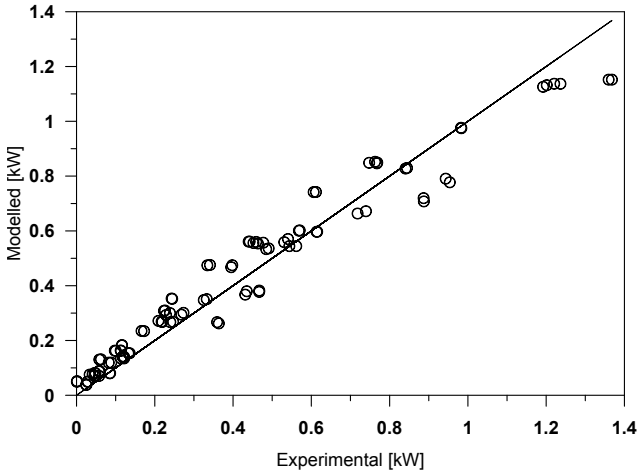

Figure 5.34. *Experimental and modelled fuel pump power consumption.*

5.5 Summary

As commented in Chapter 4.2.2, performing the IGEB requires the modelling of some thermo-fluid-dynamics processes that are difficult to be measured. The reference analysis tools (CALMEC and SiCiclo, described in Chapter 3.3) include some of these sub-models, but they need to be upgraded through addition of specific ones. This allows dealing with the IGEB in both, **Engine A** and **Engine B**. Moreover, some of the existing HT sub-models must be enhanced to achieve accurate predictions of in-cylinder and ports HT, key for the IGEB analysis.

In short, the proposals for new and improved sub-models and HT calibration are the following:

- **HT model for engines with tumble motion:** the development of a HT model that accounts for the tumble motion was required to determine the HT to the chambers walls of **Engine B**. CFD results were used to the theoretical analysis and the empirical model development, whilst skip-fire test were used to calibrate the model. Through a sensitivity study in skip-fire test and an analysis of the model performance in combustion conditions, the model robustness has been demonstrated, showing a clearly better suitability for engines with tumble motion in comparison with the reference Woschni-like model.

- **HT to ports:** several sub-models to determine the HT to intake and exhaust ports have been described. In the case of intake ports during the whole cycle and exhaust ports during closed cycle, convective equations that considers mean values of temperature and mass flow have been used. The use of mean values was justified by the low weight of the HT during these stages and the small variation of temperature and gas velocity. Nevertheless, as the HT to the exhaust port during open cycle has higher impact on the GEB (more than 90% of the total HT to ports), a 0D quasi-steady model for its determination was developed. In this convective model, the instantaneous gas temperature and heat transfer coefficient were considered.

- **Heat transfer from oil to coolant:** HT between oil and coolant takes place through the engine block and cylinder head, thus, a simple lumped model which considers the thermal resistances of the oil, coolant and engine material has been proposed.

- **Uncertainties adjustment:** to attain accurate HT to engine walls, the determination of some uncertain parameters (i.e. CR, k_{def}, $\Delta\alpha_{\text{TDC}}$ and C_{w1}) is required. An *Engine characterization* methodology based on the sensitivity study of each parameter on the RoHR and the simulated pressure has been described, where a set of optimal values was determined thanks to a MLR method.

- **Mechanical losses model:** the HT to oil and coolant determination requires detailed friction and auxiliary power modelling in order to separate their effect on $\dot{Q}_{cool}$ and $\dot{Q}_{oil}$, which are experimentally measured. Thereby, some specific semi-empirical sub-models to calculate the friction between piston pack and liner, bearings and valve train have been proposed, considering the kinematic, dynamic and tribological processes of each element. Similarly, simple sub-models to determine the coolant, oil and fuel pumps power have been developed, taking into account simplified geometrical information to estimate the mass flow and pressure drop of each pump. For these friction and auxiliary models, calibration constants can be adjusted based on experimental information.

Once all the models required were developed, the next step is to provide a calibration methodology. Therefore, the next chapter is addressed at the description of a general sub-models adjustment methodology, along with some applications of the GEB in **Engine A** and **Engine B**.

5.A Appendix: adjustment methodology performance with late SoI tests

The adjustment methodology was tested in a set of delayed injection tests performed on **Engine A**. The main potential advantage of using combustion tests instead of motoring tests is the similar thermal and thermodynamic conditions (gas and wall temperatures, pressure and gas composition) with respect to the nominal combustion tests. The main drawback is the smaller crank angle slot in which the thermodynamic analysis can be applied: about half the duration than in motoring conditions, because it can be applied only between IVC and SoI. The operating conditions tested are summarized in Table 5.12. To reduce the experimental uncertainties, three repetitions of each operating point were measured.

Speed [rpm]	**Load** [%]	**SoI** [°ATDC]
1000	50	1,7
2000	50	2,9
3000	50	4,9
4000	50	0,8

Table 5.12. *Set of delayed SoI points used to test the adjustment methodology.*

The result of the test are presented in Figure 5.35, where the behaviour of RoHR and pressure deviations during the compression are in agreement with those described for the motoring test, having an important reduction in both $\varepsilon^{\mathrm{RoHR}}$ and ε^{p}. However, despite the good performance in the reduction of the instantaneous deviation, the values of CR, C_{w1} and k_{def} obtained (see "Delayed SoI 1" column in Table 5.13), are not in agreement with those obtained in motoring conditions. This difference can be explained through the observation of the sensitivity effects shown in Figure 5.19: when compared the effect of each uncertainty, they have a similar trend up to -30° ATDC and is in the range ±30° where the characteristic behaviour of each parameter is more evident. As only some part of this region is available for the analysis, the method cannot differentiate correctly their effects, thus providing results that adjust reasonably the compression stroke but that are not coherent.

From these results, it can be stated that if the information of the complete closed cycle (or at least most of it) is not available, the assumption of

	Reference	Motoring	Delayed SoI 1	Delayed SoI 2
CR	16:1	15,9:1	15,4:1	15,9:1
k_{def}	2,20	1,29	1,25	1,29
C_{w1}	2,28	1.74	0,65	2,04
$\Delta\alpha_{\mathrm{TDC}}$	369,0	369,9	369,6	369.9

Table 5.13. *Results of Engine characterization.*

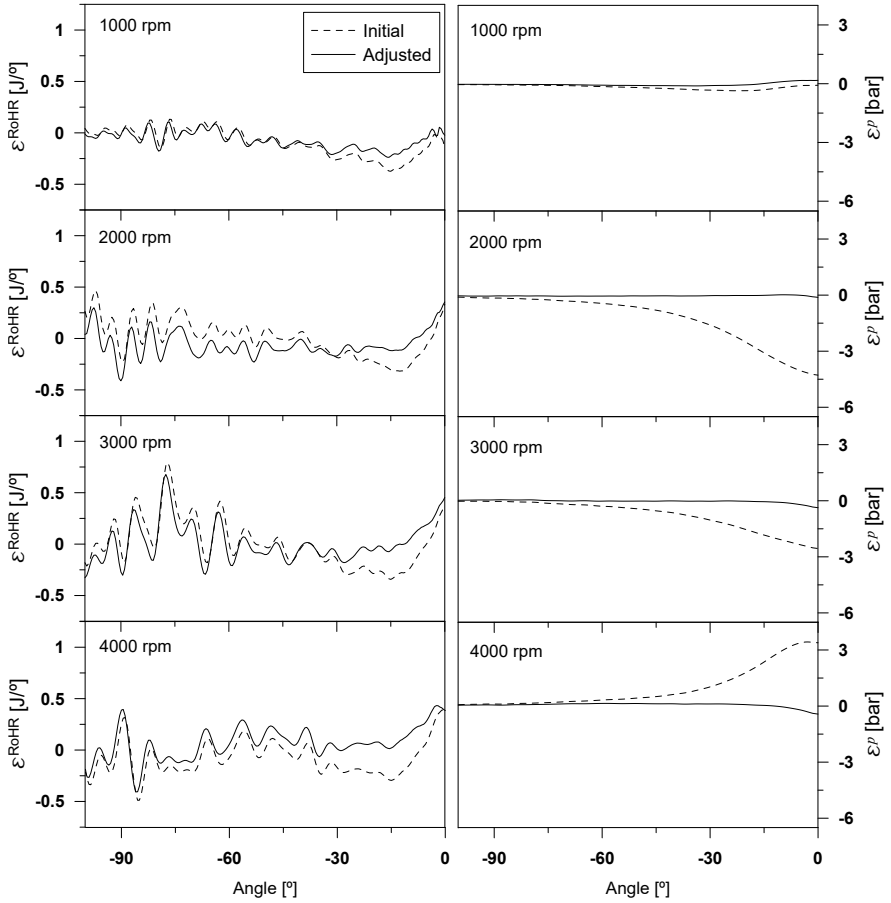

Figure 5.35. *ε^{RoHR} (left) and ε^{p} (right) for the delayed SoI study.*

independent effects is not fulfilled and the method does not perform properly. Thus, using late SoI is not suitable to adjust all the uncertainties at the same time. Taking into account this limitation, the method was tested for determining only the CR. This can be a convenient solution taking into account that C_{w1} and k_{def} are parameters that remain constant during the engine life and do not change for different cylinders. Thus, if they were obtained previously using a set of motoring tests, the TDC position can be obtained knowing the heat transfer, and the CR can be determined with the proposed method as shown in "Delayed SoI 2" column in Table 5.13, which can be useful if the chamber geometry is modified.

5.B Appendix: blow-by model

The accurate determination of instantaneous blow-by[16] presents several challenges regarding the rings assembly dynamics, the rings deformation, the gas thermal and fluid dynamic when the flow passes through the crevices, etc.

In this section, a model which consider instantaneous flow through each ring gap is described. Firstly, some simplifications and hypotheses have to be made regarding the piston-rings assembly and blow-by phenomena:

- No rings relative motion nor deformation is taken into account. The rings are assumed to be rigid bodies always in contact with the bottom face of the groove. Accordingly, the volumes between rings and grooves, and between adjacent rings are constant.
- It is assumed that all the gas leakage occurs only through the rings gaps, which are modelled as nozzles. This is consistent with the previous hypothesis, since the bottom ring face is always in contact with the groove and hence no gas leakage through them can occur.
- The flow through the gap is modelled as an isentropic nozzle. Due to the fast flow through the gap, no time for HT is assumed, and hence the process is considered adiabatic [54, 55].
- Volumes between rings are assumed to be isothermal systems and the gas temperature is assumed to be the mean temperature between the piston and liner walls ($T_{V_i} = (T_{pis} + T_{cyl})/2$). This is explained by the high HT rate due to the high area/volume ratio. This assumption is supported by the work of Furuhama and Tada [54], who experimentally determined the gas an the wall temperatures, observing very similar values between them.

In Figure 5.36, the simplified scheme of the piston pack geometry is presented. The model is composed by 4 volumes and 3 nozzle: the 1^{th} volume corresponds to the combustion chamber and the crevice between the chamber

[16] The blow-by accounts for the gas flow from the combustion chamber to the crankcase; however, during the intake stroke the in-cylinder pressure could reach values below those in the volumes between the piston and the liner, thus the gas flows from those volumes to combustion chamber, such phenomenon is known as blow-back. For the sake of simplicity, in the description presented the models is always referred as blow-by.

and the compression ring, the 2nd volume is the clearance between the compression and wiper rings, the 3rd volume is the clearance between the wiper and the oil rings and the 4th volume is the clearance between the oil ring, the piston skirt and the crank case. As explained, each gap between rings is represented by a nozzle.

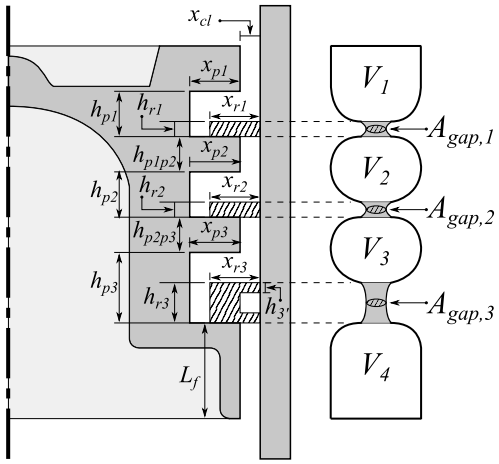

Figure 5.36. *Piston/rings assembly geometry.*

As stated, the gas in the volumes is assumed to be isothermal, thus the continuity equation for each volume can be expressed as:

$$\frac{\mathrm{d}p_i}{\mathrm{d}t} = \frac{R\ T_i}{V_i}\left(\dot{m}_{i,in} - \dot{m}_{i,out}\right) \tag{5.117}$$

where for each i volume, R is the gas constant, T_i is the gas temperature, V_i is the volume and $\dot{m}_{i,in}$ and $\dot{m}_{i,out}$ are the instantaneous mass flow rates entering and exiting the volume respectively.

The mass flow through the ring gap is calculated by means of the isentropic nozzle model:

$$\dot{m}_{i,j}(\alpha) = c_{bb}\ A_{gap,i}\ p_u\ \sqrt{\frac{x_i}{R\ T_u}} \tag{5.118}$$

where j corresponds to the downstream volume, c_{bb} is the apparent discharge coefficient to be experimentally adjusted by means of mean flow measurements,

$A_{gap,i}$ is the gap area of the ring, p_u is the upstream pressure, T_u the upstream temperature and x_i is calculated as:

$$x_i = \frac{2\gamma}{(\gamma-1)}\left[\left(\frac{p_d}{p_u}\right)^{\frac{2}{\gamma}} - \left(\frac{p_d}{p_u}\right)^{\frac{\gamma+1}{\gamma}}\right] \tag{5.119}$$

being p_d the downstream pressure and γ the adiabatic index.

Note that Equation (5.118) is calculated for each crank angle in function of the thermodynamic conditions of the volume i. If the pressure drop comply:

$$\frac{p_d}{p_u} < \left(\frac{2}{\gamma+1}\right)^{\frac{\gamma}{\gamma-1}} \tag{5.120}$$

choked flow occurs and the critic pressure p_{cr}:

$$p_{cr} = p_u\left(\frac{2}{\gamma+1}\right)^{\frac{\gamma}{\gamma-1}} \tag{5.121}$$

is used instead of p_d.

During transient operation, specially in cold start where blow-by is an issue, the integrated gas flow through each volume during one thermodynamic cycle changes cycle to cycle and from one volume to another, taking into account that the gas is accumulated or leaked depending on the transient thermodynamic conditions. However, in steady operation, the cumulated blow-by flow (m_{bb}) reaches an equilibrium after the convergence of the calculation in an iterative process, indicating that the net mass flow leakage through each volume is the same and there is no net accumulation along the cycle.

Once the physic model is described, it is necessary to perform some assumptions and initializations in order to apply the model. Firstly, the piston geometry presented in Figure 5.36 is used to determine the volumes between the piston and the liner. The interesting volumes are those between rings, i.e. V_2 and V_3. To estimate those volumes, they are divided in zones as shown in Figure 5.37. The volumes of such zones can be easily calculated as presented in Equation (5.122):

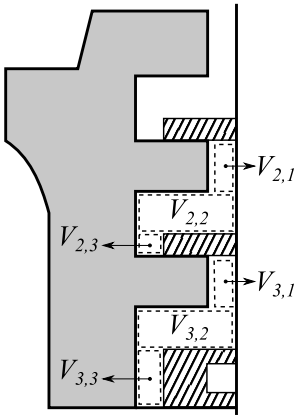

Figure 5.37. *Detail of the volume between piston and liner.*

$$V_{2,1} = \frac{\pi\ h_{p1p2}}{4}\ \left[D^2 - (D - 2x_{cl})^2\right] \tag{5.122}$$

$$V_{2,2} = \frac{\pi\ (h_{p2} - h_{r2})}{4}\ \left[D^2 - (D - 2x_{cl} - 2x_{p2})^2\right] \tag{5.123}$$

$$V_{2,3} = \frac{\pi\ h_{r2}}{4}\ \left[(D - 2x_{r2})^2 - (D - 2x_{cl} - 2x_{p2})^2\right] \tag{5.124}$$

and Equation (5.127):

$$V_{3,1} = \frac{\pi\ h_{p2p3}}{4}\ \left[D^2 - (D - 2x_{cl})^2\right] \tag{5.125}$$

$$V_{3,2} = \frac{\pi\ (h_{p3} - h_{r3})}{4}\ \left[D^2 - (D - 2x_{cl} - 2x_{p3})^2\right] \tag{5.126}$$

$$V_{3,3} = \frac{\pi\ h_{r3}}{4}\ \left[(D - 2x_{r3})^2 - (D - 2x_{cl} - 2x_{p3})^2\right] \tag{5.127}$$

thus, V_2 and V_3 are calculated as the addition of each volume as:

$$V_2 = V_{2,1} + V_{2,2} + V_{2,3} \tag{5.128}$$

$$V_3 = V_{3,1} + V_{3,2} + V_{3,3} \tag{5.129}$$

The thermodynamic conditions at each volume are determined through an iterative process. Thus, some initial assumptions have to be done to start the calculations:

– The discharge coefficient of each gap ($c_{bb,i}$) has an initial value of 1. These values are adjusted each iteration as is explained later.

– The pressure in the volumes 2 and 3 (p_{V2} and p_{V3}) are initialized as:

$$p_{V2,0} = \frac{p}{\sqrt{p/p_{crank}}} \tag{5.130}$$

$$p_{V3,0} = \frac{p_{V2}}{\sqrt{p_{V2}/p_{crank}}} \tag{5.131}$$

– The pressure in the 4$^{\text{th}}$ volume is the crankcase pressure, which is assumed to be the atmospheric pressure.

The thermodynamic conditions of volumes 1 and 4 are completely defined, meanwhile the conditions in the volumes 2 and 3 are determined by means of an iterative process. This process converge when the difference between experimental and estimated mass flow ($\varepsilon_{m_{bb}}$) presented in Equation (5.132) is lower than 1%.

$$\varepsilon_{m_{bb}} = \frac{m_{1,2} + m_{2,3} + m_{3,4}}{3\ m_{bb,exp}} - 1 \tag{5.132}$$

where $m_{bb,exp}$ is the mean value of the experimental blow-by mass flow.

In Figure 5.38, the modelled instantaneous blow-by mass flow for the extreme points of the **Engine A** map are presented. As shown in the detail (upper corner of Figure 5.38), this model is able to detect the blow-back phenomena, which corresponds to the zones with negative blow-by mass flow around 90° and 300° ATDC.

Along with the instantaneous blow-by mass flow, the instantaneous pressure in the rings grooves shown in Figure 5.39 are also obtained. These pressures are key inputs for the piston friction model described in Section 5.4.2.

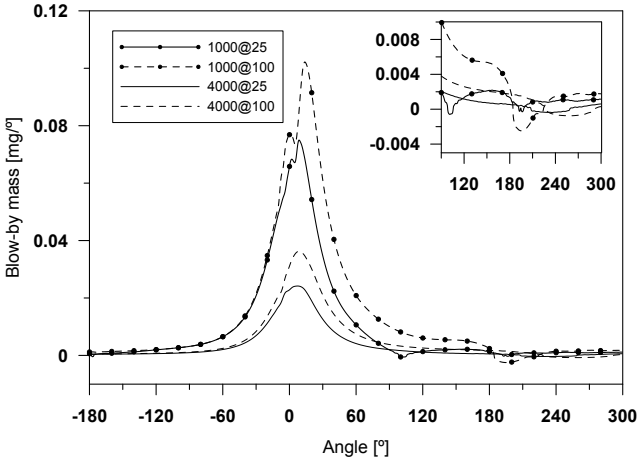

Figure 5.38. *Blow-by mass flow.*

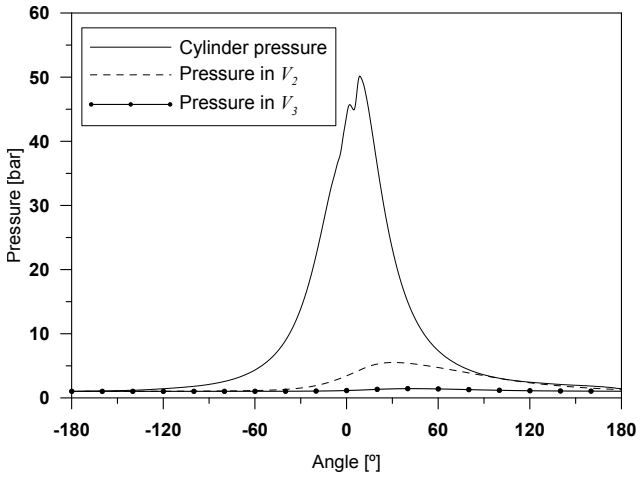

Figure 5.39. *Pressure in the rings grooves.*

5.C Appendix: piston rings mounting force determination

The relationship between the tangential ($F_{t,ri}$) and diametral ($F_{d,ri}$) forces with the contact pressure ($p_{c,ri}$) can be obtained taking into account that the bending moment (M_{ri}) produced by $F_{t,ri}$ and the $p_{c,ri}$ must be the same. Thus, considering the scheme shown in Figure 5.40, the momentum produced by the pressure applied in a differential ring slide is [36]:

$$\mathrm{d}M_{ri} = p_{c,ri}\ h_{ri}\ (D/2)^2\ sin(\beta - \varphi)\ \mathrm{d}\beta \tag{5.133}$$

and by integration:

$$M_{ri} = p_{c,ri}\ h_{ri}\ (D/2)^2\ \ (1 + cos\varphi) \tag{5.134}$$

where h_{ri} and D are the ring height and the ring external diameter after mounting (equal to the cylinder bore).

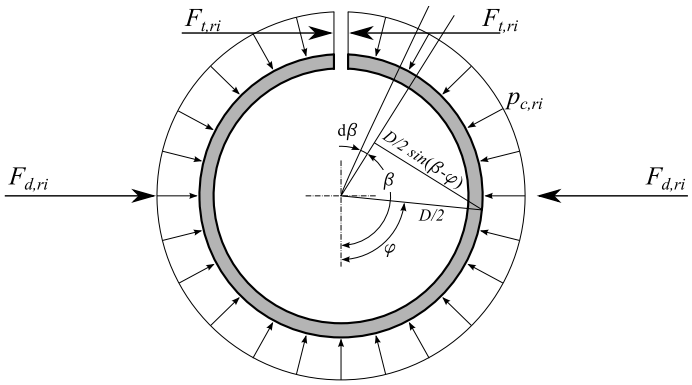

Figure 5.40. *Equivalent forces acting on a ring.*

On the other hand, M_{ri} can be also expressed in terms of $F_{t,ri}$ as follows:

$$M_{ri} = F_{t,ri}\ (D/2)\ \ (1 + cos\varphi) \tag{5.135}$$

Combining Equations (5.134) and (5.135) and solving for $p_{c,ri}$, the following expression is obtained:

$$p_{c,ri} = \frac{2\ F_{t,ri}}{D\ h_{ri}} \tag{5.136}$$

The mounting load on the ring can be also characterized by means of the diametral force ($F_{d,ri}$), which is the force acting diametrically at 90° to the gap that is necessary to compress the ring to its nominal diameter. To correlate $F_{d,ri}$ and $F_{t,ri}$, the mathematical expression proposed in reference [36] can be used:

$$F_{d,ri} = 2.2667 \left(1 - 0.33\ k_{ri} - 7.8\ \frac{u_{ri}}{D} - 24\ \frac{x_{ri}^2}{D^2}\right)\ F_{t,ri} \tag{5.137}$$

where u_{ri} is the ovality and k_{ri} is a piston ring parameter.

Since the terms required to solve Equation (5.137) are not always available, the simplified form presented in Equation (5.138) can alternatively be used [36]:

$$F_{d,ri} = 2.2\ F_{t,ri} \tag{5.138}$$

Once $p_{c,ri}$ is determined as a function of $F_{t,ri}$ or $F_{d,ri}$, the mounting force of each ring ($F_{m,ri}$) can be directly calculated by knowing the ring surface in contact with the liner ($A_{c,ri}$). Therefore, combining Equations (5.136) and (5.138), the following relations are obtained:

$$\begin{aligned} F_{m,ri} = p_{c,ri}\ A_{ri} &= \left(\frac{2\ F_{t,ri}}{D\ h_{ri}}\right)(\pi\ D\ h_{ri}) \\ &= 2\ \pi\ F_{t,ri} && (5.139) \\ &= 0.9\ \pi\ F_{d,ri} && (5.140) \end{aligned}$$

Note that $F_{m,ri}$ is a key parameter to determine the normal force between each ring and liner ($F_{N,ri}$) as described in Section 5.4.2.1, and hence, to determine the friction between piston pack and liner as shown in Section 5.4.2.2.

5.D Appendix: kinematic and dynamic analysis of the engine mechanism

5.D.1 Engine kinematics

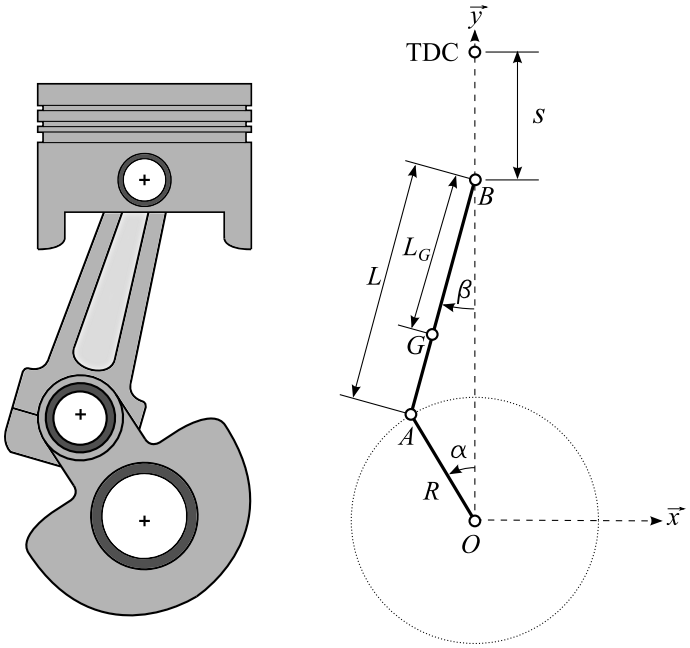

Figure 5.41. *Engine mechanism.*

The engine mechanism (Figure 5.41) consists on the crankshaft ($\bar{OA}$), the connecting rod ($\bar{AB}$), the piston pack (B) and the bearings (A and O). Usually, the piston pin is not located in the cylinder axis; however, this eccentricity is small and wont be considered in the following analysis.

Starting the kinematic study in the connecting rod, and through the geometrical relations shown in Figure 5.41, the Equation (5.141) can be written:

$$R\ sin\ \alpha = L\ sin\beta \tag{5.141}$$

thus, β can be expressed as function of α as:

$$\beta = sin^{-1}\left(\frac{R}{L}\ sin\ \alpha\right) \tag{5.142}$$

Assuming uniform angular speed ($\mathrm{d}\alpha/\mathrm{d}t = \omega$ and $\mathrm{d}^2\alpha/\mathrm{d}t^2 = 0$) and by deriving twice Equation (5.141), the connecting rod angular speed and acceleration are obtained:

$$\frac{\mathrm{d}\beta}{\mathrm{d}t} = \frac{R\ cos\ \alpha}{L\ cos\ \beta}\ \omega \tag{5.143}$$

$$\frac{\mathrm{d}^2\beta}{\mathrm{d}t^2} = \left[\left(\frac{\mathrm{d}\beta}{\mathrm{d}t}\right)^2 - \omega^2\right] tan\ \beta \tag{5.144}$$

It is also interesting to determine the kinematics of the connecting rod centre of mass G, whose position, speed and acceleration are:

$$x_{_G} = -L_{_G}\ sin\beta\ \ ;\ \ y_{_G} = R\ cos\ \alpha + (L - L_{_G})\ cos\ \beta \tag{5.145}$$

$$\begin{aligned} v_{x,_G} &= \frac{-L_{_G} R\ \omega}{L}\ cos\alpha\ \ ; \\ v_{y,_G} &= -R\omega\ sin\ \alpha\left(1 + \frac{(L - L_{_G})tan\ \beta}{L\ tan\ \alpha}\right) \end{aligned} \tag{5.146}$$

$$\begin{aligned} a_{x,_G} &= \frac{L_{_G} R\ \omega^2}{L}\ sin\ \alpha\ \ ; \\ a_{y,_G} &= -R\omega^2\left[cos\ \alpha + \frac{(L - L_{_G})}{L}\left(\frac{R\ cos^2\alpha}{L\ cos^3\beta} - sin\ \alpha\ tan\ \beta\right)\right] \end{aligned} \tag{5.147}$$

The crankshaft follows a rotational movement with centre in O and radius $R = \bar{OA}$. Therefore, the position, speed and acceleration of the point A referred to the coordinate system $(\vec{x}, \vec{y})$ describe the crankshaft kinematics:

$$x_{_A} = -R\ sin\ \alpha\ \ ;\ y_{_A} = R\ cos\ \alpha \tag{5.148}$$

$$v_{x,_A} = -R\omega\ cos\ \alpha\ \ ;\ v_{y,_A} = -R\omega\ sin\ \alpha \tag{5.149}$$

$$a_{x,_A} = R\omega^2\ sin\ \alpha\ \ ;\ a_{y,_A} = -R\omega^2\ cos\ \alpha \tag{5.150}$$

The piston kinematics is represented by the point B, whose position, speed and acceleration with respect to the coordinate system $(\vec{x}, \vec{y})$ are:

$$x_{_B} = 0 \;\; ; \;\; y_{_B} = R\ cos\ \alpha + L\ cos\ \beta \tag{5.151}$$

$$v_{x,_B} = 0 \;\; ; \;\; v_{y,_B} = -R\omega\ \frac{sin(\alpha+\beta)}{cos\ \beta} \tag{5.152}$$

$$a_{x,_B} = 0 \;\; ; \;\; a_{y,_B} = -R\omega^2\ \left[\frac{cos(\alpha+\beta)}{cos\ \beta} + \frac{R\ cos^2\alpha}{L\ cos^3\beta}\right] \tag{5.153}$$

The piston position is more commonly referenced to the TDC. Thus, the distance between the point B and the TDC is known as the engine displacement (s), and can be determined as:

$$s = R + L - (R\ cos\ \alpha + L\ cos\ \beta) \tag{5.154}$$

5.D.2 Engine dynamics

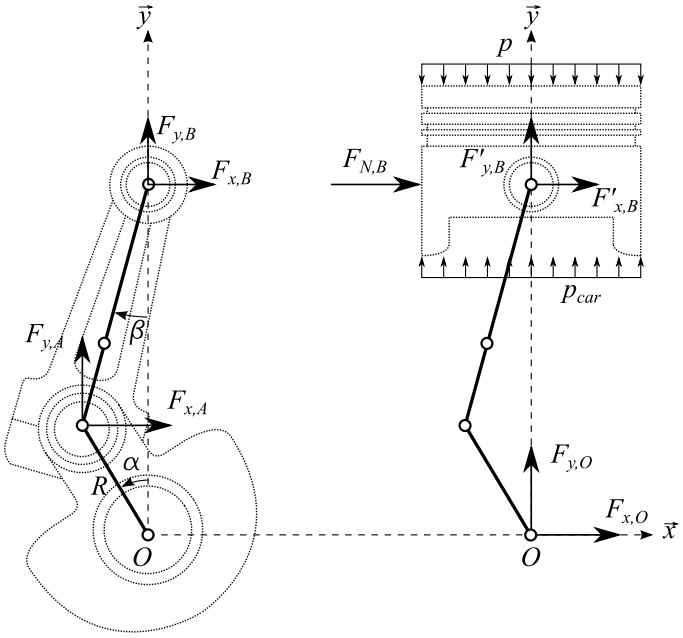

Figure 5.42. *Forces acting on the engine mechanism.*

In this analysis, the weight of the engine components as well as the friction between pieces have not been considered, taking into account that the main load is the gas pressure (p). The scheme of the forces applied on the engine mechanism are presented in Figure 5.42. By analysing the forces applied on the connecting rod, the Equations (5.155) and (5.156) can be obtained:

$$F_{x,A} + F_{x,B} = m_c \; a_{x,G} \tag{5.155}$$

$$F_{y,A} + F_{y,B} = m_c \; a_{y,G} \tag{5.156}$$

where m_c is the connecting rod mass. This mass can be decomposed in three punctual masses m_A, m_B and m_G located at A, B and G respectively. In practice, $m_G \approx 0$, thus it can be neglected. Therefore, to correctly perform the mass decomposition, the following conditions have to be accomplished:

$$m_c = m_A + m_B \tag{5.157}$$

$$m_A(L - L_G) = m_B \; L_G \tag{5.158}$$

$$I_c = m_A(L - L_G)^2 + m_B \; L_G^2 \tag{5.159}$$

where I_c is the connecting rod moment of inertia.

The force exerted by the connecting rod on the piston is equal and opposite to that exerted by the piston on the connecting rod ($F'_{x,B} = -F_{x,B}$ and $F'_{y,B} = -F_{y,B}$); therefore, the result of the forces applied on the piston can be expressed as:

$$F_{x,B} - F_{N,B} = 0 \tag{5.160}$$

$$F_{y,B} = -m_p \; a_{y,B} - \left[\frac{\pi \; D^2}{4}(p - p_{crank})\right] \tag{5.161}$$

where $F_{N,B}$ is the normal force between piston and liner, and the crankcase pressure (p_{crank}) is applied over an area equal to the piston surface.

To solve the dynamic system an additional equation is required. This is achieved by performing the sum of moments in the centre of masses G:

$$\begin{aligned} &-(L - L_G)cos\ \beta \; F_{x,A} + L_G cos\ \beta \; F_{x,B} + \\ &+(L - L_G)sin\ \beta \; F_{y,B} - L_G sin\ \beta \; F_{y,B} = I_c \frac{\mathrm{d}^2\beta}{\mathrm{d}t^2} \end{aligned} \tag{5.162}$$

Equation (5.162) can be solved by knowing the position of the centre of mass. Since it is not usually known, an accurate assumption is that it is located at $L/3$ of point A.

By combining Equations (5.155), (5.156), (5.160), (5.161) and (5.162), the following equation system is obtained:

$$\begin{bmatrix} 1 & 0 & 1 & 0 & 0 \\ 0 & 1 & 0 & 1 & 0 \\ 0 & 0 & 1 & 0 & -1 \\ 0 & 0 & 0 & 1 & 0 \\ -(L-L_G)cos\beta & (L-L_G)sin\beta & L_G cos\beta & -L_G sin\beta & 0 \end{bmatrix} \begin{bmatrix} F_{x,A} \\ F_{y,A} \\ F_{x,B} \\ F_{y,B} \\ F_{N,B} \end{bmatrix} =$$

$$= \begin{bmatrix} m_c\ a_{x,G} \\ m_c\ a_{y,G} \\ 0 \\ -m_p\ a_{y,B} - \left[\frac{\pi\ D^2}{4}(p - p_{crank})\right] \\ I_c \frac{\mathrm{d}^2\beta}{\mathrm{d}t^2} \end{bmatrix} \tag{5.163}$$

The solution of Equation (5.163) allows determining the dynamics of the engine mechanism at each crank angle.

Finally, to calculate the friction in the crankshaft bearing (see Section 5.4.3), the force applied in the point O is assumed to be equal but opposite to that in point B, thus:

$$F_O = \sqrt{F_{x,B}^2 + F_{y,B}^2} \tag{5.164}$$

5.E Appendix: kinematic and dynamic analysis of the valve train

5.E.1 Cam/follower kinematics

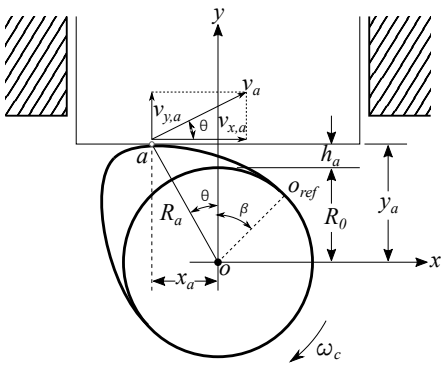

Figure 5.43. *Cam/tappet kinematic scheme.*

In Figure 5.43, a schematic of the cam/tappet contact is presented. The speed of the contact point between the cam and tappet (point a), is determined as [48]:

$$v_a = \omega_c R_a = \sqrt{v_{x,a}^2 + v_{y,a}^2} \tag{5.165}$$

where ω_c is the angular speed of the cam whose value is one half of the engine speed ($\omega_c = 0.5\ \omega$) and v_a is the speed of the point a, whose components ($v_{x,a}$ and $v_{y,a}$) are geometrically determined as follows:

$$\begin{aligned} v_{x,a} &= \omega_c\ R_a\ cos\ \theta \\ &= \omega_c\ (R_0 + h_a) \end{aligned} \tag{5.166}$$

$$\begin{aligned} v_{y,a} &= \omega_c\ R_a\ sin\ \theta \\ &= \omega_c\ x_a \end{aligned} \tag{5.167}$$

where θ is the angle between the line $\bar{oa}$ and the y axis, R_0 is the cam base radius, h_a is the tappet lift and R_a is the distance between the contact point and the cam centre. Through derivation the instantaneous tappet lift, the acceleration of the follower (a_v) is obtained:

$$a_v = \frac{\mathrm{d}^2 h_a}{\mathrm{d}t^2} = \omega_c^2 \, \frac{\mathrm{d}^2 h_a}{\mathrm{d}\beta^2} \tag{5.168}$$

where β is the angular position of the cam with respect to the reference line (oo_{ref}^{-}), called also *cam rotation angle*.

Solving for x_a in Equation (5.167), the following expression can be obtained:

$$x_a = \frac{v_{y,a}}{\omega_c} = \frac{\mathrm{d}h_a/\mathrm{d}t}{\mathrm{d}\beta/\mathrm{d}t} = \frac{\mathrm{d}h_a}{\mathrm{d}\beta} \tag{5.169}$$

therefore, the velocity of the cam/tappet contact point relative to the tappet (v_t) can be determined through derivation of Equation (5.169) as follows:

$$v_t = \frac{\mathrm{d}x_a}{\mathrm{d}t} = \omega_c \frac{\mathrm{d}x_a}{\mathrm{d}\beta} = \omega_c \frac{\mathrm{d}^2 h_a}{\mathrm{d}\beta^2} \tag{5.170}$$

where $\mathrm{d}^2 h_a/\mathrm{d}\beta^2$ is known as the *geometrical acceleration* of the follower, caused by the cam lift movement pattern.

The sliding velocity (v_s) corresponds to the horizontal velocity of point a observed by a static point in the tappet. Therefore, for a flat-tappet follower without tappet spin $v_s = v_{x,a}$. Taking this into account, the resultant contact velocity of the cam/tappet (v_c) is expressed as the addition of v_s and v_t as follows [48]:

$$v_c = v_s + v_t = \omega_c \left(R_0 + h_a + \frac{\mathrm{d}^2 h_a}{\mathrm{d}\beta^2} \right) \tag{5.171}$$

Note that the term in brackets correspond to the instantaneous radius of curvature of the cam (R_c) [56]:

$$R_c = R_0 + h_a + \frac{\mathrm{d}^2 h_a}{\mathrm{d}\beta^2} \tag{5.172}$$

Finally, to determine the tribological conditions between the cam and the tappet, it is necessary to calculate the instantaneous velocity of lubricant entrainment into the cam/tappet contact (v_e), which is done as proposed in [48]:

$$v_e = \frac{v_c + v_t}{2} = \frac{\omega_c}{2}\left(R_0 + h_a + 2\,\frac{\mathrm{d}^2 h_a}{\mathrm{d}\beta^2}\right) \tag{5.173}$$

As rolling followers are often preferred over tappet ones, the kinematic analysis is also provided. The optimal design and kinematic analysis of cam/roller followers mechanisms can be found in [57].

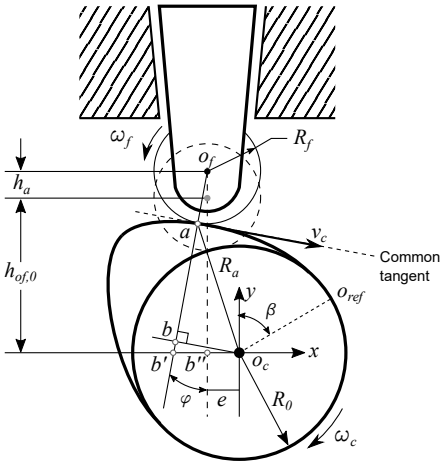

Figure 5.44. *Cam/rolling follower kinematic scheme.*

In Figure 5.44, a schematic of the cam/rolling follower contact is presented. The contact velocity (v_c) can be expressed in terms of the follower roller angular speed (ω_f) and radius (R_f) as [57]:

$$v_c = \omega_f \; R_f \tag{5.174}$$

Since the cam angular speed (ω_c) can be directly correlated with the engine angular speed, it is interesting to express v_c in terms of ω_c as:

$$v_c = \omega_c \; \bar{ab} \tag{5.175}$$

where $\bar{ab}$ is the distance between the contact pole (b) and the contact point (a), which are continuously changing during the cam rotation. This line can be determined through the geometrical correlation $\bar{ab} = \bar{ab'} - \bar{bb'}$, where $\bar{ab'}$ is calculated by means of the analysis of the triangle $o_f - b' - b''$ as:

$$\bar{ab'} = \frac{(h_{o_f,0} + h_a)}{cos\ \varphi} - R_f \tag{5.176}$$

where $h_{o_f,0}$ is the minimum height between the cam and follower centres when the valve is closed, which is determined from the R_f, R_c and the eccentricity between cam and rolling follower centres (e). h_a is the valve lifting and φ is the pressure angle. Similarly, $\bar{bb'}$ is obtained by analysing the triangle $o_c - b - b'$ as:

$$\bar{bb'} = \bar{o_c b}\ tan\ \varphi \tag{5.177}$$

where $\bar{o_c b}$ is determined through the following trigonometric expression:

$$\bar{o_c b} = \bar{o_c b'}\ cos\ \varphi \tag{5.178}$$

and $\bar{o_c b'}$ is obtained by means of the triangle $o_f - b' - b''$ as follows:

$$\begin{aligned} \bar{o_c b'} &= e + \bar{b'b''} \\ &= e + (h_{o_f,0} + h_a)\ tan\ \varphi \end{aligned} \tag{5.179}$$

Consequently, the following $\bar{o_c b}$ expression is attained by replacing Equation (5.179) in (5.178) as:

$$\begin{aligned} \bar{o_c b} &= [e + (h_{o_f,0} + h_a)\ tan\ \varphi]\ cos\varphi \\ &= e\ cos\ \varphi + (h_{o_f,0} + h_a)\ sin\ \varphi \end{aligned} \tag{5.180}$$

and finally, $\bar{bb'}$ is obtained by replacing Equation (5.180) in (5.177):

$$\bar{bb'} = e\ sin\ \varphi + (h_{o_f,0} + h_a)\ sin\ \varphi\ tan\ \varphi \tag{5.181}$$

Therefore, $\bar{ab} = \bar{ab'} - \bar{bb'}$ can be rewritten as a function of more convenient geometrical parameters by considering Equations (5.176) and (5.181) as:

$$\bar{ab} = \frac{(h_{o_f,0} + h_a)}{cos\ \varphi} - R_f - e\ sin\ \varphi - (h_{o_f,0} + h_a)\ sin\ \varphi\ tan\ \varphi \tag{5.182}$$

This last expression can be substituted in Equation (5.175) to obtain v_c. To solve this equation, it is also necessary to determine φ (the rest of the parameters can be obtained from geometry).

In Figure 5.44, it can be observed that the normal to the common tangent (line $\bar{ab}$) intersects the x axis in the point b', which corresponds to the instantaneous centre of rotation between cam and follower. Since the follower describes a translational motion along the y axis, the *lifting velocity* can be determined as point b' velocity ($v_{b'}$) as:

$$v_{b'} = \omega_c \; \bar{o_c b'} \tag{5.183}$$

For convenience, Equation (5.183) can be rewritten as:

$$\bar{o_c b'} = \frac{v_{b'}}{\omega_c} = \frac{\mathrm{d}h_a/\mathrm{d}t}{\mathrm{d}\beta/\mathrm{d}t} = \frac{\mathrm{d}h_a}{\mathrm{d}\beta} \tag{5.184}$$

Then, by combining Equations (5.179) and (5.184), the following expression can be obtained:

$$\frac{\mathrm{d}h_a}{\mathrm{d}\beta} = e + (h_{o_f,0} + h_a) \; tan \; \varphi \tag{5.185}$$

from which the pressure angle is attained as:

$$\varphi = tan^{-1} \left(\frac{\mathrm{d}h_a/\mathrm{d}\beta - e}{h_{o_f,0} + h_a} \right) \tag{5.186}$$

From a tribological point of view, it is interesting to determine the instantaneous velocity of lubricant entrainment into the cam/tappet contact (v_e). This velocity can be obtained as the average between the cam (v_c) and the follower (v_f) contact velocities [58]. Assuming that the roller follower rolls without slipping, v_c must be equal as v_f, therefore the following relation can be obtained:

$$\begin{aligned} v_e &= 0.5 \; (v_c + v_f) \\ v_e &= v_c \end{aligned} \tag{5.187}$$

Note that the model is written as a function of the cam rotation angle β which can be expressed in terms of the crank angle α, considering that

the cam have twice the angular speed of the crankshaft in 4-stroke engines, and the same angular speed in 2-stroke engines. This relationship is useful to determine the friction over an engine cycle.

5.E.2 Cam/follower dynamics

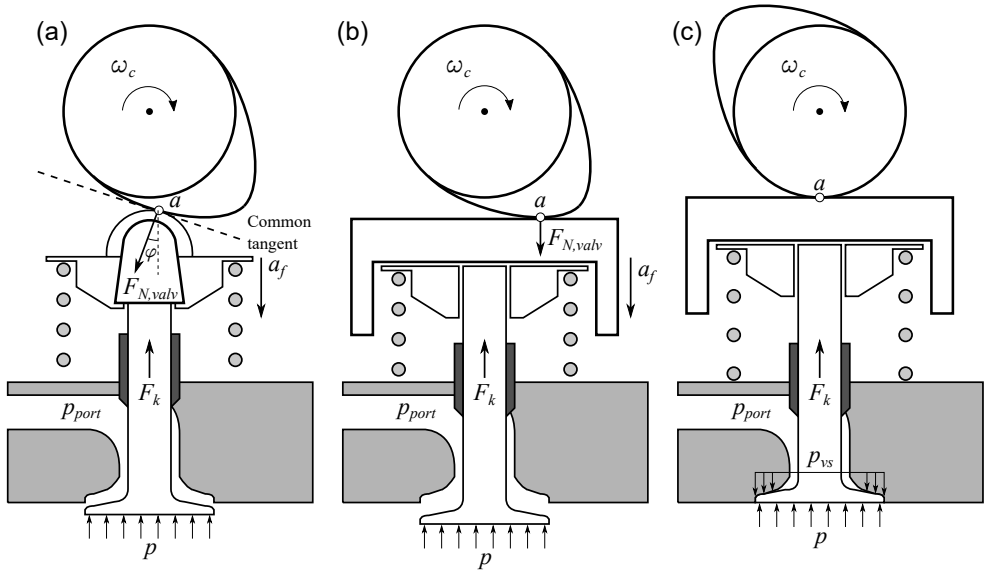

Figure 5.45. *Cam/follower dynamic scheme.*

Despite several valve train mechanism configurations could be used in automotive applications [44], in this work it is assumed that the follower rod is the valve rod itself, which is the case of **Engine A** and **Engine B**. In Figure 5.45, the forces acting in a rolling follower and in a bucket tappet follower are presented.

In the more general case of a roller follower (Figure 5.45 (a)), when the valve is open, the force normal to the common tangent ($F_{N,valv}$) can be determined through $\sum F_y = ma$ as:

$$F_{N,valv}\ cos\ \varphi = A_v\ (p - p_{port}) + F_k - (m_v\ a_v + m_s\ a_s)$$

$$F_{N,valv} = \frac{1}{cos\ \varphi}\left[A_v\ (p - p_{port}) + F_k - (m_v\ a_v + m_s\ a_s)\right] \qquad (5.188)$$

where a_v and $a_s = a_v/2$ are the valve and the spring centre of mass accelerations, m_v and m_s are the valve and spring masses, p is the in-cylinder pressure, p_{port} is the port pressure[17] (which is equal to the intake or exhaust pressure depending on the valve analysed) and F_k is the spring force, which is calculated as:

$$F_k = F_{k,0} + k_s \; h_a \tag{5.189}$$

being $F_{k,0}$ the spring pre-load, k_s the spring constant[18] and h_a the spring displacement from the initial position.

In the case of tappet followers (Figure 5.45 (b)), the common tangent is parallel to the tappet surface, thus $\varphi = 0$ and hence Equation (5.188) becomes:

$$F_{N,valv} = A_v \; (p - p_{port}) + F_k - (m_v \; a_v + m_s \; a_s) \tag{5.190}$$

As the instantaneous pressure at intake and exhausts ports are not always available, their mean values can be also used. Figure 5.46 shows a comparison of the normal force estimation without considering the pressure loads and using either the instantaneous or mean exhaust pressures. As can be seen, considering the pressure loads is important at the beginning of the valve lifting, since the in-cylinder pressure is high and tends to impede the valve opening. However, when the pressures get closer (about 200°), the net pressure load becomes negligible. As the mean exhaust pressure does not follow the initial in-cylinder pressure trend, there is an overestimation of the normal force few degrees after the valve closing.

When the valve is closed (Figure 5.45 (c)), three main observations have to be made[19]:

- The valve and spring masses are stopped, thus no inertial loads are exerted.
- The force due to the chamber and port pressures ($A_v \; (p - p_{port})$) is supported in the valve seat.

[17] Taking into account that there is some load due to the atmospheric pressure, p_{port} is assumed to be applied on an area equal to A_v to account for the atmospheric load.

[18] In **Engine A**, $F_{k,0} = 30$ N and $k_s = 15000$ N/m according to the manufacturer.

[19] Despite Figure 5.45 (c) shows a bucket tappet follower, these comments are also valid to rolling followers.

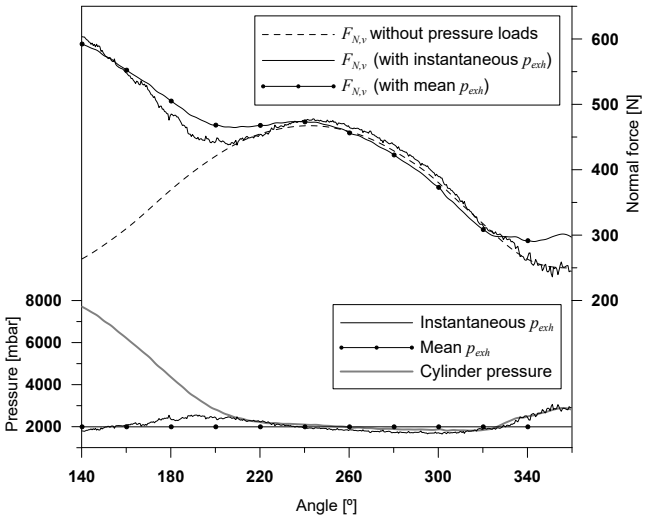

Figure 5.46. *Exhaust valve loads considering instantaneous and mean exhaust pressure.*

– The contact between cam and follower should be minimum, thus a very low normal force is exerted in this contact point.

Taking these comments into account, it can be assumed that when the valve is in contact with the valve seat, there is no normal force exerted between cam and follower and the friction is negligible.

Once the normal force is determined for both rolling and tappet followers, the friction in the cam/follower contact can be determined. In the following appendix, the lubrication details for the case of the rolling follower contact is comprehensive analysed. The analysis of the friction in a tappet follower contact was presented in Section 5.4.4.

5.F Appendix: rolling follower friction force determination

Similarly as for the cam/tappet follower contact, the friction in the cam/rolling follower contact ($F_{fr,valv}$) has two components, the boundary friction ($F_{b,valv}$) and the viscous friction ($F_{v,valv}$) [47, 48]:

$$F_{fr,valv} = F_{b,valv} + F_{v,valv} \tag{5.191}$$

The boundary component is determine as for the cam/tappet follower [49]:

$$F_{b,valv} = \tau_0 \; A_a + k_m \; P_a \tag{5.192}$$

being τ_0 the Eyring shear stress, k_m the pressure coefficient of the boundary shear strength, P_a the load carried by the asperities and A_a the asperity area [49]:

$$A_a = \pi^2 (\varrho \; \zeta \; \sigma)^2 A \; F_2 \tag{5.193}$$

and P_a can be determined as:

$$P_a = \frac{16\sqrt{2}}{15} \; \pi (\varrho \; \zeta \; \sigma)^2 \; \sqrt{\frac{\sigma}{\zeta}} \; E_c \; A \; F_{5/2} \tag{5.194}$$

being ϱ the asperity density, ζ the asperities radius of curvature, σ the composite surface roughness parameter, F_2 and $F_{5/2}$ statistical functions[20] and A the Hertzian contact area calculated as:

$$A = 2 \; b \; L_{cam} \tag{5.195}$$

being b determined as [45]:

$$b = \sqrt{\frac{8 \; F_{N,valv} \; R'_c}{\pi \; E_c}} \tag{5.196}$$

[20] The definition of these functions and the simplified expressions provided in Section 5.4.4 can be also used in this model.

where R'_c is the combined radius of curvature defined as [47, 51]:

$$\frac{1}{R'_c} = \frac{1}{R_c} + \frac{1}{R_f} \tag{5.197}$$

where R_c is the instantaneous radius of curvature of the cam (calculated as shown in Equation (5.172)) and R_f is the follower radius.

To determine the viscous friction component, the tribological features of a cam/rolling follower contact must be considered. Therefore, $F_{v,valv}$ is determined as proposed by Goksem and Hargreaves [51], which provide a simplified expression for the case of isothermal fully flooded rolling traction (i.e. not including shear heating):

$$F_{v,valv} = \frac{4.318}{\alpha_c} \, (G \, U)^{0.658} \, W^{0.0126} \, R'_c \, L_{cam} \tag{5.198}$$

where G, U and W are determined as[21]:

$$U = \frac{\mu \, v_e}{E_c \, R'_c} \tag{5.199}$$

$$G = \alpha_c \, E_c \tag{5.200}$$

$$W = \frac{F_{N,valv}}{E_c \, R'_c \, L_{cam}} \tag{5.201}$$

[21] The terms included in these equations are defined in Section 5.4.4.

Bibliography

[1] Pastor J.M. *Análisis del proceso de barrido en motores de dos tiempos de pequeña cilindrada.* Reverté, ISBN 978-84-291-4713-1, Barcelona, 2009.

[2] Heywood J.B. and Sher E. *The Two-Stroke Cycle Engine: It's Development, Operation and Design.* Taylor and Francis, ISBN 978-1560328315, Pennsylvania, 1th edition, 1999.

[3] Huang R.F., Huang C.W., Chang S.B., Yang H.S., Lin T.W. and Hsu W.Y. "Topological flow evolutions in cylinder of a motored engine during intake and compression strokes". *Journal of Fluids and Structures*, Vol. 20 n^o 1, pp. 105–127, January 2005.

[4] Kim M., Lee S. and Kim W. "Tumble Flow Measurements UsingThree Different Methods and its Effects on Fuel Economy and Emissions". *SAE Technical paper 2006-01-3345*, 2006.

[5] Micklow G.J. and Gong W.D. "Investigation of the grid and intake-generated tumble on the in-cylinder flow in a compression ignition direct-injection engine". *Journal of Automobile Engineering*, Vol. 222 n^o 5, pp. 775–788, May 2008.

[6] Grover Jr R.O. and Cleary D. "Correlating Measured Combustion Performance with CFD Predicted In-Cylinder Flows for a Spark-Ignition Direct-Injection (SIDI) Engine with Enhanced Charge Motion". *SAE Technical paper 2013-01-1090*, April 2013.

[7] Benajes J., Olmeda P., Martín J. and Carreño R. "A new methodology for uncertainties characterization in combustion diagnosis and thermodynamic modelling". *Applied Thermal Engineering*, Vol. 71, pp. 389–399, 2014.

[8] Payri F., Martín J., Garcia A. and Carreño R. "Experimental and Theoretical Analysis of the Energy Balance in a DI Diesel Engine". *SAE Technical Paper 2015-01-1651*, 2015.

[9] Dolz V. *Transmisión de calor en motores alternativos : aplicación al aprovechamiento energético de los gases de escape.* Reverté, ISBN 978-84-291-4715-5, Barcelona, 2011.

[10] Depcik C. and Assanis D. "A Universal Heat Transfer Correlation for Intake and Exhaust Flows in an Spark-Ignition Internal Combustion Engine". *SAE Technical Paper 2002-01-0372*, mar 2002.

[11] Caton J.A. "Comparisons of Thermocouple, Time-Averaged and Mass-Averaged Exhaust Gas Temperatures for a Spark-Ignited Engine". *SAE Techinical Paper 820050*, 1982.

[12] Sieder E.N. and Tate G.E. "Heat Transfer and Pressure Drop of Liquids in Tubes". *Industrial and Engineering Chemistry*, Vol. 28 n^o 12, 1936.

[13] Lee K., Yoon M. and Sunwoo M. "A study on pegging methods for noisy cylinder pressure signal". *Control Engineering Practice*, Vol. 16 n^o 8, pp. 922–929, 2008.

[14] Payri F., Luján J.M., Martín J. and Abbad A. "Digital signal processing of in-cylinder pressure for combustion diagnosis of internal combustion engines". *Mechanical Systems and Signal Processing*, Vol. 24 n^o 6, pp. 1767–1784, 2010.

[15] Martín J. *Diagnóstico de la combustión en motores de Diesel de inyección directa*. Reverté, ISBN 978-84-291-4717-9, Barcelona, 2012.

[16] Payri F., Molina S., Martín J. and Armas O. "Influence of measurement errors and estimated parameters on combustion diagnosis". *Applied Thermal Engineering*, Vol. 26 n^o 2-3, pp. 226–236, February 2006.

[17] Klein M., Eriksson L. and Åslund J. "Compression ratio estimation based on cylinder pressure data". *Control Engineering Practice*, Vol. 14 n^o 3, pp. 197–211, March 2005.

[18] Stricker K., Kocher L., Koeberlein E., Alstine D.V. and Shaver G.M. "Estimation of Effective Compression Ratio for Engines Utilizing Flexible Intake Valve Actuation". *Journal of Automobile Engineering*, 2011.

[19] Lapuerta M., Armas O. and Molina S. "Study of the compression cycle of a reciprocating engine through the polytropic coefficient". *Applied Thermal Engineering*, Vol. 23 n^o 3, pp. 313–323, February 2003.

[20] Payri F., Olmeda P., Martín J. and García A. "A complete 0D thermodynamic predictive model for direct injection diesel engines". *Applied Energy*, Vol. 88 n^o 12, pp. 4632–4641, December 2011.

[21] Aronsson U., Solaka H., Chartier C., Andersson O. and Johansson B. "Impact of Mechanical Deformation Due to Pressure, Mass, and Thermal Forces on the In-Cylinder Volume Trace in Optical Engines of Bowditch Design". *SAE Technical Paper 2011-26-0082*, 2011.

[22] Komninos N.P. and Kosmadakis G.M. "Heat transfer in HCCI multi-zone modeling: Validation of a new wall heat flux correlation under motoring conditions". *Applied Energy*, Vol. 88 n^o 5, pp. 1635–1648, May 2011.

[23] Tunestål P. "Self-tuning gross heat release computation for internal combustion engines". *Control Engineering Practice*, Vol. 17 n^o 4, pp. 518–524, April 2009.

[24] Ångström H. "Cylinder pressure indicating with multiple transducer, accurate TDC evaluating, zero levels and analysis of mechanical vibrations". *3 Internationales Indiziersymposium*, pp. 103–108, 1998.

[25] Tunestål P. "TDC Offset Estimation from Motored Cylinder Pressure Data based on Heat Release Shaping". *Oil & Gas Science and Technology - Revue d'IFP Energies nouvelles*, Vol. 66 n^o 4, pp. 705–716, October 2011.

[26] Tazerout M., Le Corre O. and Rousseau S. "TDC Determination in IC Engines Based on the Thermodynamic Analysis of the Temperature-Entropy Diagram". *SAE paper 1999-01-1489*, 1999.

[27] Hohenberg G. "Definition und Eigenschaften des thermodynamischen Verlustwinkels von Kolbenmaschinen". *Automobil-Industrie*, Vol. 4, pp. 15–21, 1976.

[28] Lapuerta M., Armas O. and Bermúdez V. "Sensitivity of diesel engine thermodynamic cycle calculation to measurement errors and estimated parameters". *Applied Thermal Engineering*, Vol. 20 n^o 9, pp. 843–861, 2000.

[29] Weisberg S. *Applied Linear Regressions*. John Wiley & Sons, ISBN 0-471-66379-4, 3rd edition, 2005.

[30] Woschni G. "A Universally Applicable Equation for the Instantaneous Heat Transfer Coefficient in the Internal Combustion Engine". *SAE Technical Paper 670931*, 1967.

[31] Payri F., Olmeda P., Martín J. and Carreño R. "A New Tool to Perform Global Energy Balances in DI Diesel Engines". *SAE Int. J. Engines*, Vol. 7 n^o 1, pp. 43–59, 2014.

[32] Olmeda P., Martín J., Novella R. and Carreño R. "An adapted heat transfer model for engines with tumble motion". *Applied Energy*, Vol. 158, pp. 190–202, 2015.

[33] Benajes J., Molina S., García A., Belarte E. and Vanvolsem M. "An investigation on RCCI combustion in a heavy duty diesel engine using in-cylinder blending of diesel and gasoline fuels". *Applied Thermal Engineering*, Vol. 63 n^o 1, pp. 66–76, February 2014.

[34] Stanley R., Taraza D. and Henein N. "A Simplified Friction Model of the Piston Ring Assembly". *SAE Technical Paper 1999-01-0974*, 1999.

[35] Tian T. *Modeling the performance of the Piston Ring-Pack in internal combustion engines.* Ph.D. Thesis, Massachusetts Institute of Technology, 1997.

[36] Federal-Mogul. "Goetze Piston Ring Handbook". *online resource*, 2008.

[37] Taraza D. and Henein N. "Friction Losses in Multi-Cylinder Diesel Engines". *SAE Technical Paper 2000-01-0921*, 2000.

[38] Ushijima K., Moteki K., Goto T. and Aoyama S. "A Study on Engine Bearing Performance Focusing on the Viscosity-Pressure Characteristic of the Lubricant and Housing Stiffness". *SAE Technical Paper 961144*, 1996.

[39] Goenka P.K. "Dynamically Loaded Journal Bearings: Finite Element Method Analysis". *ASME Journal of Tribology*, Vol. 106 n^o 4, pp. 429–437, 1984.

[40] Taylor C.M. *Engine Tribology.* Elsevier, ISBN 978-0444897558, 1997.

[41] Payri F. and J.M. Desantes. *Motores de combustión interna alternativos.* Reverté, ISBN 978-84-291-4802-2, Barcelona, 2011.

[42] Cameron A. *Basic Lubrication Theory.* Longman, ISBN 978-0470275542, New York, 1971.

[43] Teodorescu M., Taraza D., Henein N. and Bryzik W. "Experimental Analysis of Dynamics and Friction in Valve Train Systems". *SAE Technical Paper 2002-01-0484*, 2002.

[44] Beloiu D. "Modeling and Analysis of Valve Train , Part I - Conventional Systems". *SAE Technical paper 2010-01-1198*, 2010.

[45] Nayak N., Lakshminarayanan P.A., Babu M.K.G. and Dani A.D. "Predictions of cam follower wear in diesel engines". *Wear*, Vol. 260 n^o 1-2, pp. 181–192, jan 2006.

[46] Dowson D. and Higginson G.R. *Elastohydrodynamic Lubrication, SI Edition*. Pergamon press, ISBN 978-0080213026, Oxford, 1977.

[47] Teodorescu M., Taraza D., Henein N. and Bryzik W. "Simplified Elasto-Hydrodynamic Friction Model of the Cam-Tappet Contact". *SAE Techinical Paper 2003-01-0985*, 2003.

[48] Guo J., Zhang W. and Zou D. "Investigation of dynamic characteristics of a valve train system". *Mechanism and Machine Theory*, Vol. 46 n^o 12, pp. 1950–1969, dec 2011.

[49] Greenwood J.A. and Tripp J.H. "The Contact of Two Nominally Flat Rough Surfaces". *Proc. Instn. Mech. Engrs*, Vol. 185, pp. 625–633, 1970.

[50] Teodorescu M., Kushwaha M., Rahnejat H. and Taraza D. "Elastodynamic transient analysis of a four-cylinder valvetrain system with camshaft flexibility". *Proceedings of the Institution of Mechanical Engineers, Part K: Journal of Multi-body Dynamics*, Vol. 219 n^o 1, pp. 13–25, 2005.

[51] Goksem P.G. and Hargreaves R.A. "The effect of viscous shear heating on both film thickess and rolling traction in a EHL line contact. Part I: Fully flooded conditions". *ASME. J. of Lubrication Tech.*, Vol. 100 n^o 3, pp. 346–352, 1978.

[52] Calabretta M., Cacciatore D. and Carden P. "Valvetrain Friction - Modeling, Analysis and Measurement of a High Performance Engine Valvetrain System". *SAE Int. J. Engines*, Vol. 3 n^o 2, pp. 72–84, 2010.

[53] Moody L.F. "An approximate formula for pipe friction factors". *Trans. ASME*, Vol. 69 n^o 12, pp. 1005–1011, 1947.

[54] Furuhama S. and Tada T. "On the Flow of Gas Through the Piston-Rings (1st Report, The Discharge Coefficient and Temperature of Leakage Gas)". *Bulletin of JSME*, Vol. 4 n^o 16, pp. 684–690, 1961.

[55] Furuhama S. and Tada T. "On the Flow of Gas Through the Piston-Rings (2nd Report, The Character of Gas Leakage)". *Bulletin of JSME*, Vol. 4 n^o 16, pp. 691–698, 1961.

[56] Shigley J.E. and Uicker J.J. *Theory of Machines and Mechanisms.* McGraw-Hill, ISBN 0-07-Y66560-5, Singapore, international edition, 1981.

[57] Pisla D., Ceccarelli M., Husty M. and Corves B. *New Trends in Mechanism Science: Analysis and design.* Springer, ISBN 978-90-481-9689-0, Heidelberg, 2010.

[58] Lee J. and Patterson D. "Analysis of Cam/Roller Follower Friction and Slippage in Valve Train Systems". *SAE Technical paper 951039*, 1995.

Chapter 6

Application of the GEB in direct injection engines

Contents

6.1 Introduction

After the development of the sub-models shown in the previous chapter, the analysis tool is ready to perform the GEB in **Engine A** and **Engine B**, whose experimental installation were comprehensively explained in Chapter 3.2. The main objectives are, on the one hand, to provide a reliable calibration procedure which assures accurate HT estimations, and on the other hand, to perform the comprehensive analysis of the thermal behaviour of different engines technologies, as an example of the tool potential. In Table 6.1, a brief summary of the engines features is presented:

	Engine A	**Engine B**
Strokes per cycle	4	2
Cylinders	4	1
Air motion	Swirl	Tumble
Fuel	Diesel	Gasoline
Injection	DI	DI
Ignition	Compression	Compression
Combustion	CDC	PPC

Table 6.1. *Engines tested.*

On the one hand, most of the experimental work for the development of the tool calibration methodology was performed in **Engine A**. It was selected taking into account that it is more representative of the current engine technologies used in automotive applications. On the other hand, **Engine B** is a research engine with different features from those usual in current automotive engines: it is a single-cylinder, 2-stroke, gasoline CI engine. Moreover, in this case, the experimental information was limited in comparison with **Engine A**. Therefore, this engine was selected to check the performance of the GEB

methodology when applied in a non-conventional engine, taking into account that the GEB is expected to be used for the evaluation of new engine concepts.

Before discussing the results of different parametric studies carried out on each engine, the calibration methodology is presented for each of them. The objective is to provide an optimal set of calibration constants for the different sub-models, along with the comprehensive methodology followed for their determination, taking into account that the available information for each engine is different. Once the calibration is complete, the following studies are presented:

- **Engine A** map analysis. In this study, the GEB is performed in the engine map and the results are analysed using a combination of experimental and modelled information. The objective is to identify the main energy trends observed in current automotive engines, and explain in detail the physical phenomena causing the energy repartition.
- **Engine B** parametric studies. For this engine, two operating points are taken as reference, in which several studies changing the injection setting and the intake/exhaust conditions are performed. The results show how the methodology presented is useful to diagnose new engine concepts.

  In order to determine the potential engine efficiency improvement by reducing the heat rejection to the chamber, a predictive approach is carried out with the predictive tool SiCiclo described in Chapter 3.3.

6.2 GEB in Engine A

The main objective of this section is to analyse the trends of the energy repartition in the whole operation map of **Engine A**, including the previous calibration method required.

To ensure a stable thermal behaviour of the engine, stabilization periods ranging from 20 to 40 min between consecutive measurements were required. It was assumed that the thermal stabilization was reached when the variation rate of the liquids temperatures (coolant, cooling water and oil) was lower to 1°C per minute (the accuracy range of the thermocouples is about ±1.5°C). The gases temperatures (intake air and exhaust gases) were also controlled, but the stabilization was faster than in the case of the liquids, thanks to the lower thermal inertia and the higher convective HT between those fluids and

the thermocouples and RTDs. More stabilization time is required in the case of engine heating at low speed and load, due to the lower heat rejection in comparison with high speed and load conditions, where the fluids are heated and stabilized faster.

Speed [rpm]	**Load** [%]	T_{cool} [°C]	T_{oil} [°C]	p_{int} [bar]	p_{exh} [bar]
1000	25-100	85	90	1.0-1.3	1.0-1.6
1500	25-100	85	90-110	1.0-2.0	1.2-2.2
2000	25-100	85	90-113	1.2-2.5	1.3-2.6
2500	25-100	85	90-120	1.4-2.6	1.7-2.7
3000	25-100	85	95-120	1.5-2.6	1.8-2.9
3500	25-100	85	100-125	1.6-2.5	1.9-3.0
4000	25-100	85	100-125	1.6-2.3	2.0-3.0

Table 6.2. *Experiments performed on* ***Engine A****.*

All the measured points are summarized in Table 6.2. As shown, in the reference conditions the coolant temperature was set at 85°C, the oil between 90-125°C depending on the operating conditions[1] and the fresh air at 30°C (after the intercooler and before the mixing with the EGR). The load was changed with steps of 25% between 25 and 100% of the maximum torque, the rest of parameters were automatically set by the ECU.

6.2.1 Sub-models calibration

Before analysing the GEB of **Engine A**, the calibration methodology depicted in Figure 6.1 has to be followed to ensure accurate results.

As can be seen, the global calibration process is performed in 4 steps:

- **Step 1:** a complete calibration of the HT model to the chamber walls using motoring and combustion tests is firstly performed. The process starts with the *Engine characterization* presented in Chapter 5.3, where the uncertain parameters are adjusted with the criterion of reducing the RoHR residuals in a sweep of engine speed at motoring conditions. This step allows ensuring accurate gas properties calculation, being key

[1]For temperatures higher than 90°C, the oil cooler operates at maximum capacity.

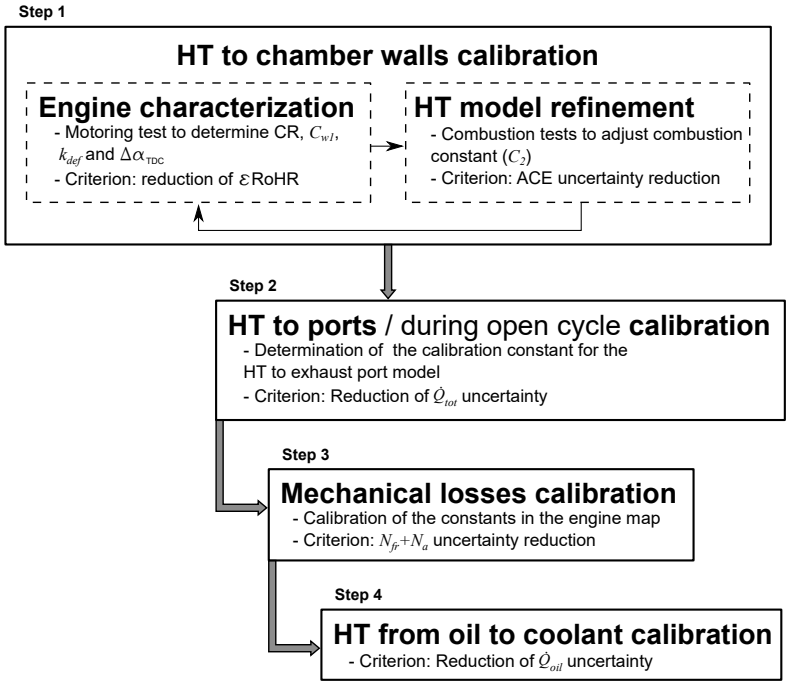

Figure 6.1. *Sub-models calibration procedure.*

parameters for the sub-models, specially the HT model. The process continues with the refinement of the HT model in combustion conditions, using the engine map shown in Table 6.2. In this case, the adjustment criterion consists on reaching an apparent combustion efficiency (ACE) of 100%. Note that the results of the *Engine characterization* and the HT model calibration have cross effects, thus, the optimal set of values is obtained through an iterative process.

- **Step 2:** despite most of the HT from the hot gases to the engine walls occurs in the chamber during the closed cycle, the HT to the ports during open cycle cannot be neglected, specially at the exhaust ports, considering the high temperature and velocity of the exhaust gases. Thus, the convective HT to ports model is adjusted to reduce the difference between the experimental and modelled $\dot{Q}_{tot}$ (See Chapter 4.3.1 for its definition). Note that the calibration of the HT during the open cycle is also included in Figure 6.1; however, the information available for its adjustment is the same as for the ports, and both cannot be simulta-

neously calibrated. For this reason, only the HT to ports is calibrated for **Engine A**, taking into account that it has more weight in the IGEB (about 30% of the total modelled HT) and that the reference model has been adjusted to get accurate results during open cycle [1].

- **Step 3:** to attain a good modelling of the HT to the coolant and the oil, it is necessary to know the detailed auxiliary (N_a) and friction (N_{fr}) losses distribution, since most of them are dissipated in the cooling and lubricating systems. Therefore, the calibration process of the mechanical losses model is described.

- **Step 4:** once the HT and the mechanical losses are calibrated, the experimental and modelled heat rejection to coolant and oil are evaluated separately. At this point, the only interaction that has not been considered is the HT between the oil and the coolant $\dot{Q}_{oil,cool}$. Thus, the model accounting for $\dot{Q}_{oil,cool}$ is adjusted based on the reduction of the difference between the experimental and modelled $\dot{Q}_{oil}$. This criterion was selected taking into account that $\dot{Q}_{oil,cool}$ has higher relative effect on $\dot{Q}_{oil}$ than in $\dot{Q}_{cool}$ ($\dot{Q}_{oil}$ is about 4 times lower than $\dot{Q}_{cool}$).

Once the sub-models are adjusted, they are used to obtain detailed information of all the relevant engine energy terms, combining internal and external points of view, which are useful to understand the energy management in **Engine A**.

6.2.1.1 Heat transfer to chamber walls calibration

The calibration of the HT to chamber walls is performed in a two stages process as presented in Figure 6.2.

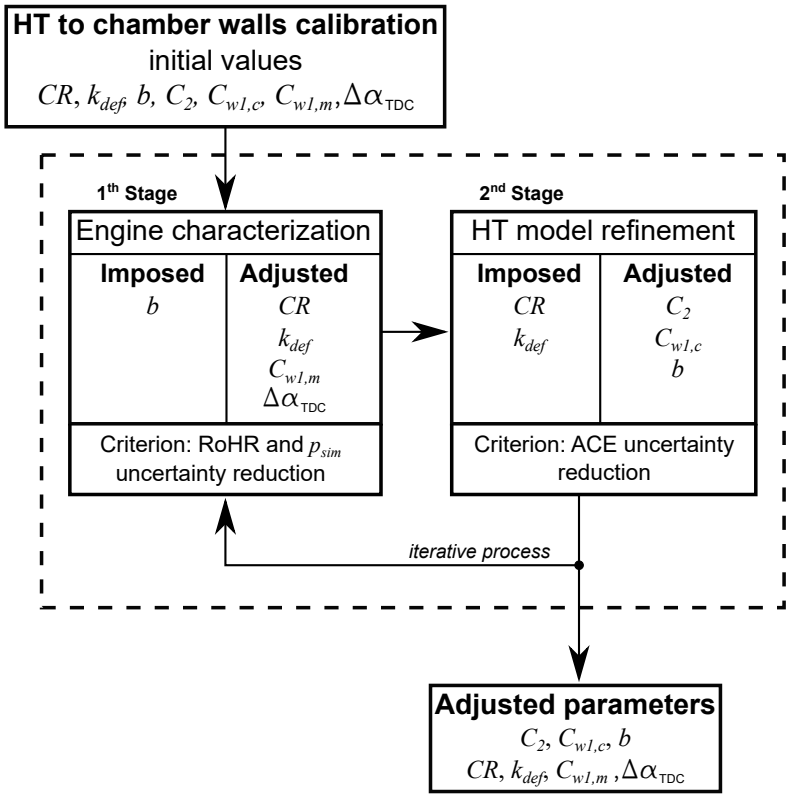

Figure 6.2. *Calibration of heat transfer to chamber walls.*

The **1th stage** consist on the *Engine characterization* in a speed sweep at motoring conditions as described in Chapter 5.3, in which the optimal set of values for the main uncertainties affecting the HT (CR, $\Delta\alpha_{\mathrm{TDC}}$ and k_{def}) are obtained along with the HT calibration constant (C_{w1}). As the *Engine characterization* is performed in a set of motoring tests, the HT differs from that of a combustion as a consequence of the different thermo-fluid-dynamic conditions in the chamber. To ensure the accuracy, different calibration constants are defined to be used either in motoring ($C_{w1,m}$) or combustion ($C_{w1,c}$) conditions respectively.

To get the $C_{w1,c}$ value, the **2nd stage** consist on the calibration procedure with combustion tests, in which the Woschni constants ($C_{w1,c}$, C_2 and b of Equation (3.26)) are determined with the criterion of the ACE optimiza-

tion, whose definition is shown in Equation (6.1), which should equals the combustion efficiency[2] calculated as shown in Equation (6.2).

$$\text{ACE} = \frac{HR_{max}}{\dot{m}_f H_v} \times 100 \tag{6.1}$$

$$\eta_{comb} = \left(1 - \frac{\dot{m}_{HC}}{\dot{m}_f} - \frac{\dot{m}_{CO}}{4\ \dot{m}_f}\right) \times 100 \tag{6.2}$$

Note that the calibration of the constant b in the second stage makes necessary to recalibrate $C_{w1,m}$, thus the calibration of the HT to chamber walls is performed through an iterative process.

The results of the *Engine characterization* and the HT calibration are presented in Table 6.3. Note that the HT constants in motoring conditions slightly differ from those presented in Chapter 5.3.2.1 (see Table 5.8). This is explained by the change in the exponent b from 0.8 to 0.7, which leads to different values of $C_{w1,m}$.

Motoring		Combustion	
$C_{W1,m}$	2,3	$C_{W1,c}$	3,99
CR	15,9:1	b	0,7
k_{def}	1,29	C_2	0,0012
$\Delta\alpha_{\text{TDC}}$	369,9		

Table 6.3. *Results of Engine characterization and calibration of HT to chamber walls.*

In Figure 6.3, the ACE for the complete engine map before and after the adjustment is presented. It is possible to see that the ACE was at first overestimated for almost all the measured points; however, after the calibration in combustion, the ACE has values closer to the target of $100\%\dot{m}_f H_v$.

[2] $\eta_{comb} \approx 100\%\dot{m}_f H_v$ in CDC.

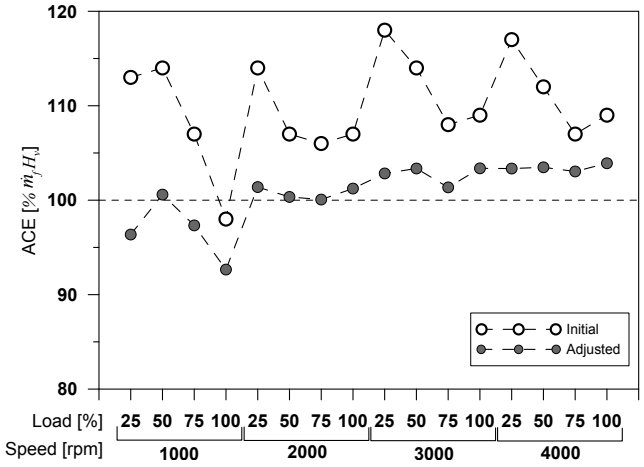

Figure 6.3. *ACE before and after calibration of the heat transfer to chamber.*

6.2.1.2 Heat transfer to ports calibration

As presented in Table 5.6, the HT to the exhaust ports in the open cycle accounts for more than the 90% of the total HT to the ports. After the calibration of the HT to chamber, $\dot{Q}_{ports}$ is the only term that significantly affects $\dot{Q}_{tot,mod}$ (see Equation (4.35)). Thus, the adjustment of the C constant in Equation (5.30) is performed with the criterion of difference minimization between $\dot{Q}_{tot,exp}$ and $\dot{Q}_{tot,mod}$. It is interesting to highlight that $\dot{Q}_{tot,exp}$ is not calculated directly with $\dot{Q}_{cool,exp}$ and $\dot{Q}_{oil,exp}$ to reduce the experimental uncertainty as discussed in Chapter 4.4. Instead, experimental variables with lower uncertainty were used as justified in Chapter 4.3.1. As a result of this calibration process, the value of $C = 1.63$ is obtained.

In Figure 6.4, a comparison between experimental and modelled total HT is presented. The comparison was performed in an extensive experimental database with more than 200 measurements carried out in **Engine A**, which includes the extended engine map starting from low speed (1000 rpm) and low load (about 10%) to high speed (4000 rpm) and maximum load. As shown, there is a good agreement between the terms compared, lying almost all of them on the bisecting line. The mean uncertainty is ±8%, in Section 6.2.1.5, a detailed analysis of this uncertainty is provided

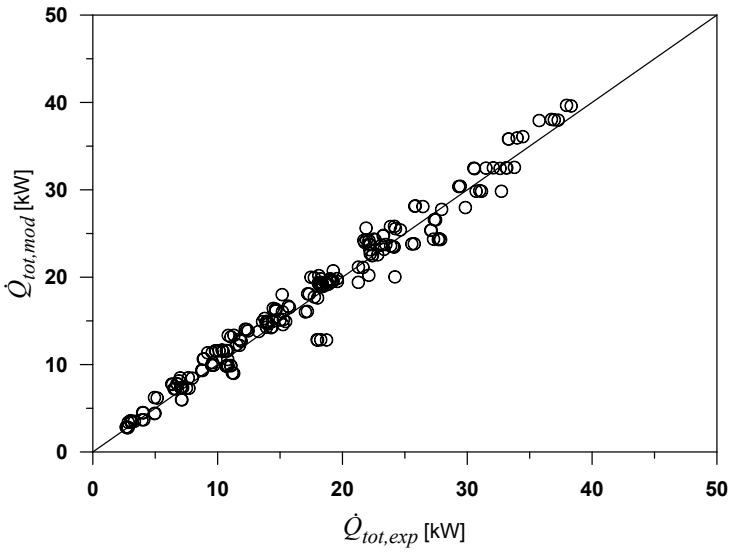

Figure 6.4. *Experimental and modelled $\dot{Q}_{tot}$ comparison after the calibration of $\dot{Q}_{ports}$.*

6.2.1.3 Mechanical losses

To adjust the mechanical losses model, the total modelled losses ($(N_{fr} + N_a)_{mod}$) are compared with the experimental ones ($(N_{fr} + N_a)_{exp}$). The adjustment criterion is then the reduction of the difference between them:

$$\begin{aligned}(N_{fr} + N_a)_{exp} &= (N_{fr} + N_a)_{mod} \\ &= k_{pis}\ N_{fr,pis} + k_{bear}\ N_{fr,bear} + k_{valv}\ N_{fr,valv} + \\ &\quad + k_{cool}\ N_{cool} + k_{oil}\ N_{oil} + k_f\ N_f \end{aligned} \tag{6.3}$$

As shown in Equation (6.3), six calibration constants have to be adjusted. In order to assure the calibration robustness, it is desirable to reduce this amount of parameters. Therefore, the auxiliary (N_{cool}, N_{oil} and N_f) were calibrated based on information provided by manufacturers and by means of dedicated experimental campaigns, as presented in Chapter 5.4. Table 6.4 summarizes the calibration constants obtained to determine the power of the coolant, oil and fuel pumps from Equations (5.103), (5.111) and (5.116) respectively.

Coolant pump		Oil pump		Fuel pump	
$k_{1,cool}$	$5,14x10^{-5}\frac{bar}{(l/min)^2}$	$k_{1,oil}$	$7,9x10^{-3}\frac{l/min}{rpm}$	$k_{1,f}$	$3,43x10^{-9}\frac{m^3/s}{(g/s)^{0.6}}$
$k_{2,cool}$	$5,51x10^{-2}\frac{l/min}{rpm}$	$k_{2,oil}$	$2.03\frac{bar}{(l/min)^2}$	$k_{2,f}$	0,6
		$k_{3,oil}$	0.64		

Table 6.4. *Calibration constants of the auxiliary losses models.*

Since the auxiliary systems were prior calibrated, the terms k_{cool}, k_{oil} and k_f of Equation (6.3) become 1. The adjustment of the friction constants (k_{pis}, k_{bear} and k_{valv}) was performed in the engine map, whose operating conditions are summarized in Table 6.2.

It is important to notice that the accurate estimation of friction components depends on the derivation of suitable values for the empirical coefficients. The discrepancy of the constants with respect to the reference values (i.e. $k_{pis} = k_{bear} = k_{valv} = 1$) is a consequence of uncertainties regarding the elements geometry, load determination and sub-models imperfections. This discrepancy with respect to reference values is also reported in other works [2], which proposed "variable" constants values as a function of the engine speed. As it was found that friction losses were overestimated at low engine speed, this approach was also considered in this work. A linear correlation for the piston constant was finally proposed: $k_{pis} = k_{1,pis} + k_{2,pis}\ n$. In the case of k_{bear} and k_{valv}, no clear improvement was found by applying this approach; therefore, they were maintained constant for all operating conditions. In Table 6.5, the results of the friction models calibration campaign are summarized.

$k_{1,pis}$	$k_{2,pis}$	k_{bear}	k_{valv}	k_{cool}	k_{oil}	k_f
0.498	$2.28\times10^{-3}rpm^{-1}$	3.9	2.5	1	1	1

Table 6.5. *Calibration constants of the friction and auxiliary losses models for* ***Engine A****.*

Figure 6.5 shows the mechanical losses repartition in the engine map. In the upper Figure 6.5, it is possible to see the good agreement between the experimental and modelled total mechanical losses, having a good behaviour for all the operating points. In the bottom of Figure 6.5, it is possible to see the good agreement of $N_a + N_{fr}$ relative distribution when compared with that found in the literature [3–5], being $N_{fr,pis}$ between 40-60% , $N_{fr,bear}$ between

15-25%, $N_{fr,valv}$ between 5 and 15%, N_{cool} about 15%, N_{oil} about 5% and N_f about 20% of the total $N_a + N_{fr}$.

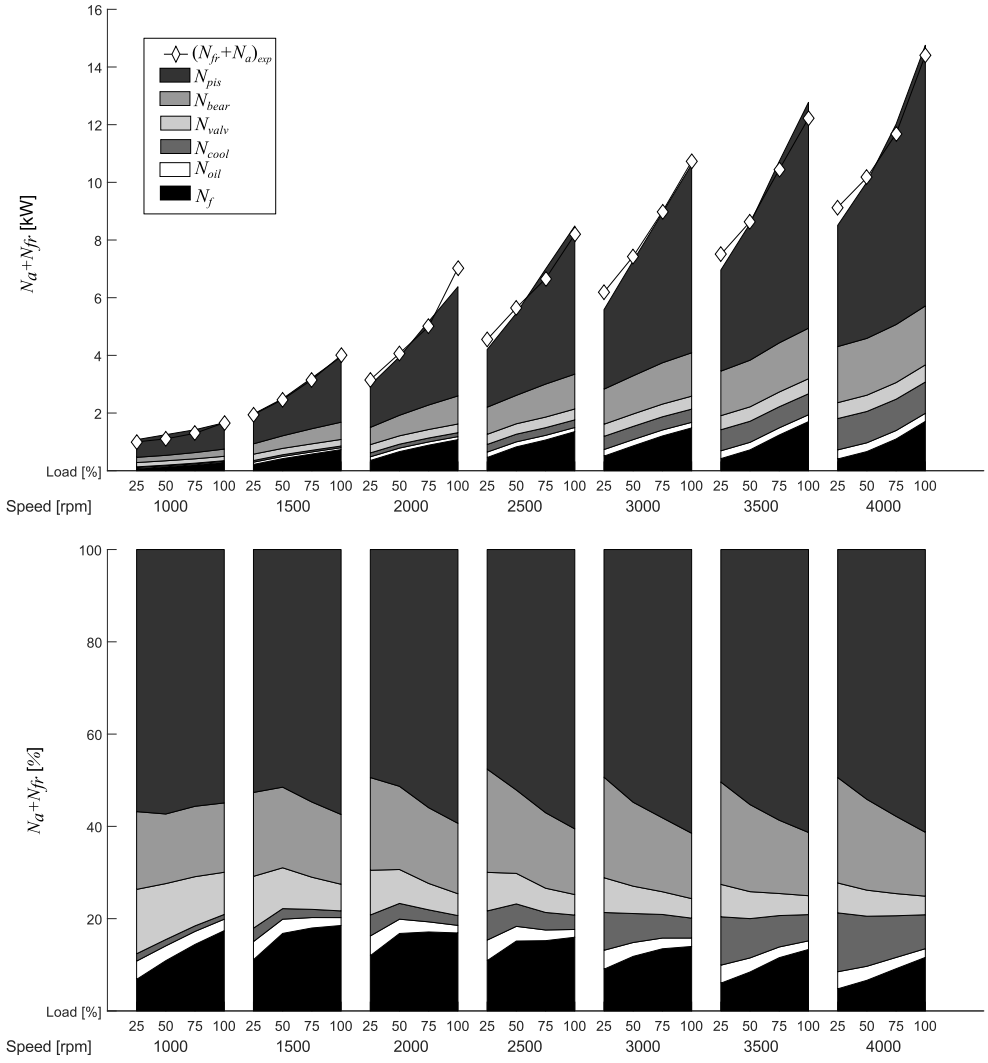

Figure 6.5. *Auxiliary and friction results.*

6.2.1.4 Heat transfer from oil to coolant

The adjustment of $\dot{Q}_{oil,cool}$ is performed through the determination of the constants k_1 and k_2 of Equation (5.42), rewritten below for convenience:

$$\dot{Q}_{oil,cool} = \frac{D^2(T_{oil} - T_{cool})}{\frac{2}{k1\ n} + \frac{D}{k_2\ k_{wall}}} \tag{6.4}$$

The values of k_1 and k_2 are determined with the criterion of difference minimization between $\dot{Q}_{oil,exp}$ and $\dot{Q}_{oil,mod}$. It is important to highlight that this calibration was performed after the mechanical losses adjustment, because part of them (N_{bear}, N_{valv} and N_{oil}) are finally rejected to the oil. The adjustment provides the value of constants $k_1 = 6,42$ and $k_2 = 8,8 \times 10^8$. It is possible to notice that $1/k_2 \approx 0$, and hence the conduction can be considered almost negligible in comparison with the convective heat transfer (see Chapter (5.2.3)).

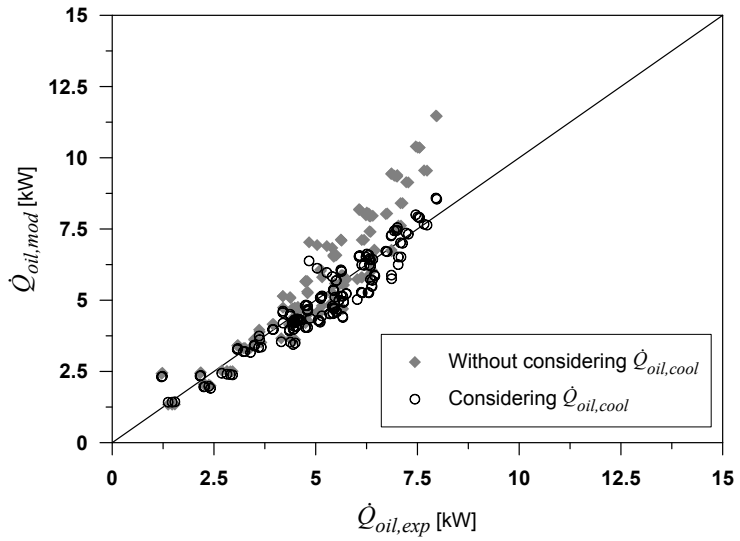

Figure 6.6. *Experimental and modelled $\dot{Q}_{oil}$ comparison after $\dot{Q}_{oil,cool}$ adjustment.*

In Figure 6.6, the comparison between $\dot{Q}_{oil,exp}$ and $\dot{Q}_{oil,mod}$ is presented[3]. It is possible to see how not including heat rejection from oil to coolant leads to overestimation of the HT to the oil, specially at high power, having a mean uncertainty about ±15%. When heat rejection from oil to coolant is included, $\dot{Q}_{oil,exp}$ and $\dot{Q}_{oil,mod}$ are in better agreement, having a mean uncertainty about ±9%. More details of the uncertainty are presented in Section 6.2.1.5.

6.2.1.5 Calibration evaluation

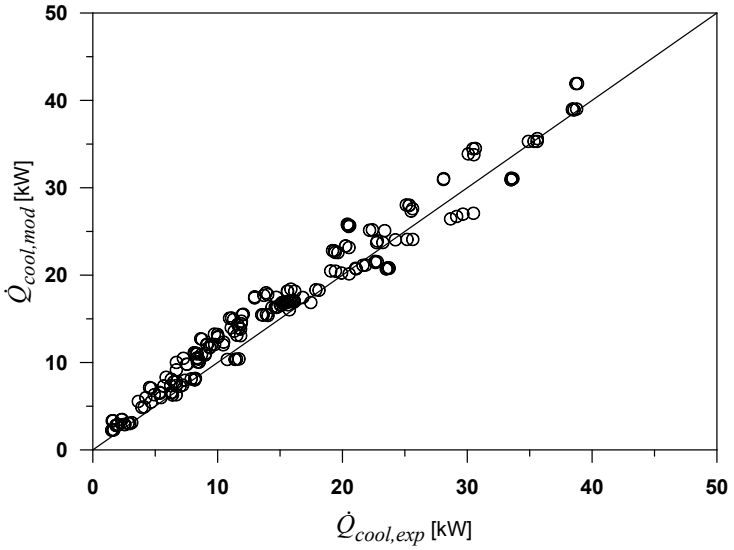

Figure 6.7. *Experimental and modelled $\dot{Q}_{cool}$ comparison.*

As presented in Figures 6.4 and 6.6, the modelled and experimental $\dot{Q}_{tot}$ and $\dot{Q}_{oil}$ depict a good behaviour after the adjustment. In Figure 6.7, it is possible to see that the modelled HT to the coolant is in good agreement with the experimental results, having a mean uncertainty of ±19%. Taking into account the relatively high uncertainty in the experimental estimation of the HT to coolant (up to 12%) as commented in Chapter 4.4.4, it can be concluded that the modelling work matches reasonably with the experiments.

[3]The lowest power operating points have not been included in the graph because the oil cooling system was deactivated due to the low oil temperature.

From Figure 6.8 to 6.10, the difference between modelled and experimental $\dot{Q}_{tot}$, $\dot{Q}_{cool}$ and $\dot{Q}_{oil}$ in terms of fuel energy ($\%\dot{m}_f H_v$) are presented. The following observations can be highlighted:

– The maximum difference between $\dot{Q}_{tot,mod}$ and $\dot{Q}_{tot,exp}$ is observed at low engine speed, ranging between -2$\%\dot{m}_f H_v$ and -10$\%\dot{m}_f H_v$. In the rest of the map the difference is remarkably lower, depicting an average difference lower than $\pm 1\%\dot{m}_f H_v$.

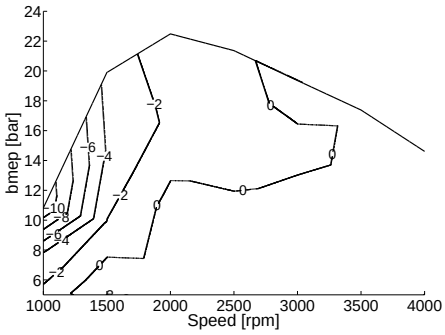

Figure 6.8. *Difference between modelled and experimental $\dot{Q}_{tot}$ in terms of $\%\dot{m}_f H_v$.*

– The HT to the coolant has a maximum uncertainty of about 6$\%\dot{m}_f H_v$ at low load due to the high experimental uncertainty in the determination of $\dot{Q}_{cool,exp}$ at these conditions, as was seen in Figure 4.10; however, in the complete engine map the average difference is about $\pm 2\%\dot{m}_f H_v$.

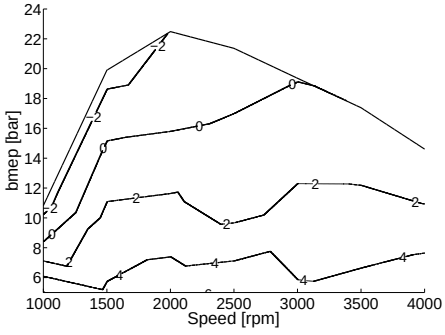

Figure 6.9. *Difference between modelled and experimental $\dot{Q}_{cool}$ in terms of $\%\dot{m}_f H_v$.*

– The HT to the oil shows a maximum variation of about $\pm 1.5\% \dot{m}_f H_v$. This value is higher than that observed in the case of the experimental uncertainty presented in Figure 4.49. Thus, it can be assumed that part of the difference observed in Figure 6.10 is explained by modelling imperfections. Even so, the HT to the oil has the lowest relative uncertainty of the three terms shown in this section, mainly due to its low relative weight as later analysed in Section 6.2.2.3.

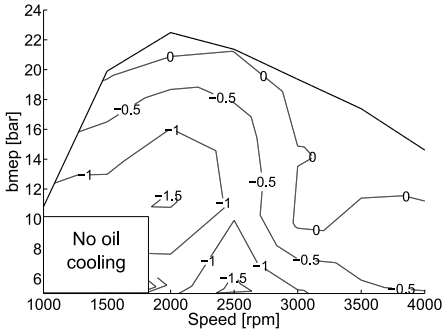

Figure 6.10. *Difference between modelled and experimental $\dot{Q}_{oil}$ in terms of $\% \dot{m}_f H_v$.*

6.2.2 GEB analysis of the engine map

Once the sub-models provided in Chapter 5 were calibrated and their uncertainty was confirmed to be between reasonable limits when compared with the experimental uncertainty presented in Chapter 4.4, the next step is to perform and analyse the GEB in **Engine A**, taking into account the main energy terms involved in the EGEB and IGEB. Consequently, the analysis presented in this section is based on the combination of both, experimental and modelled results. The main objective is then, to assess the importance of each GEB term in different regions of the engine map. For this reason, the complete speed and load sweep presented in Table 6.2 will be evaluated.

The analysis starts with the chemical fuel energy released in the complete engine map, shown in Figure 6.11. As expected, the input fuel energy increases with both, engine speed and load, since the amount of injected fuel must be also higher to achieve the power output required at each point. As the results of the GEB terms will be presented in both, absolute (kW) and relative ($\%\dot{m}_f H_v$) terms, this figure helps to understand the weight of each term depending on the operating condition.

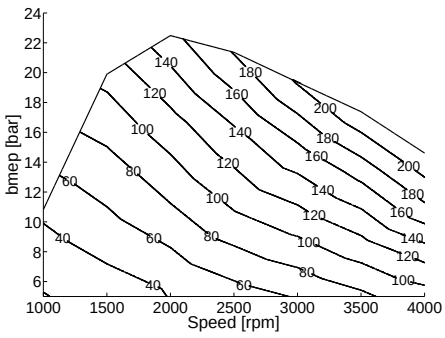

Figure 6.11. *Fuel chemical energy in (kW).*

6.2.2.1 Analysis of engine efficiency

The indicated power and indicated efficiency are plotted in Figure 6.12. As commented in Chapter 2.3, the behaviour of the indicated efficiency is mainly controlled by the RoHR shape and the HT to the combustion chamber

walls during closed cycle (which also depends on the combustion process). In this sense, the following trends can be highlighted:

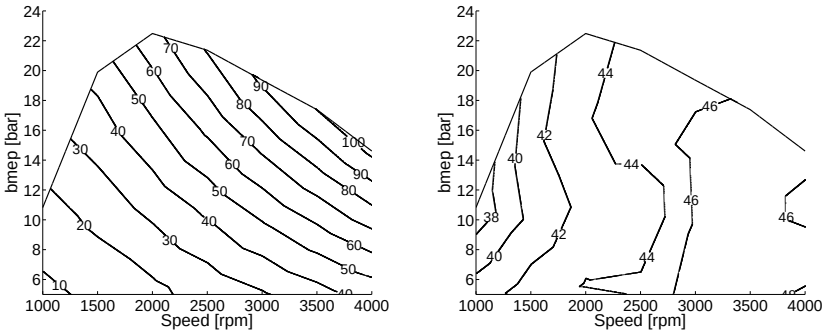

Figure 6.12. *Indicated power (N_i). Left: absolute value (kW). Right: relative value ($\%\dot{m}_f H_v$).*

– There is a global trend to increase η_i from $38\%\dot{m}_f H_v$ to $46\%\dot{m}_f H_v$ when the engine speed increases. It can be justified by the lower weight of HT to the chamber walls during closed cycle ($\dot{Q}_{cham,cc}$), which is about $10\%\dot{m}_f H_v$ lower at high speed as shown in Figure 6.13.

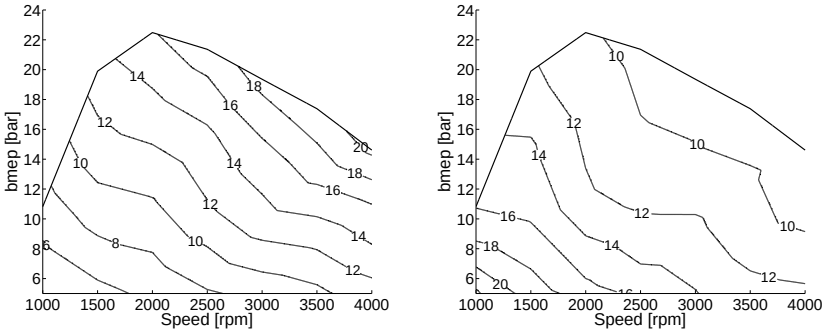

Figure 6.13. *Heat transfer to the chamber walls during closed cycle ($\dot{Q}_{cham,cc}$). Left: absolute value (kW). Right: relative value ($\%\dot{m}_f H_v$).*

– Contrary to $\dot{Q}_{cham,cc}$, the indicated efficiency shows low sensitivity to load changes, as can be seen in Figure 6.12. This behaviour can be justified taking into account that the lower weight of HT at high load observed in Figure 6.13 is compensated by the global trend to increase

the combustion duration at high load, thus η_i has less variation with this parameter. Furthermore, the changes of the number of injection pulses and the effect of EGR, highly dependent on the engine optimization[4], also contribute to the slightly effect of the load.

Starting from η_i, the brake efficiency shown in Figure 6.14 can be explained through the analysis of the mechanical efficiency ($\eta_m = N_b/N_i \times 100$) presented in Figure 6.15. As the increase of η_i with the engine speed is overcome by the lower mechanical efficiency, the maximum η_b is reached at mid speed. On the other hand, η_i shows a poor effect with the load while η_m reaches its maximum value at high load; therefore, the maximum η_b is reached near full load.

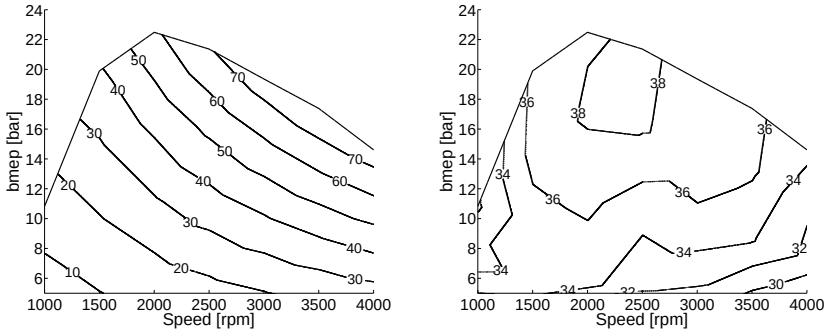

Figure 6.14. *Brake power (N_b). Left: absolute value (kW). Right: relative value ($\%\dot{m}_f H_v$).*

6.2.2.2 Analysis of mechanical losses

In the previous section, the degradation from the indicated efficiency to brake efficiency was briefly analysed to justify the trends. However, to achieve a better insight of this process, the detailed mechanical losses (i.e. pumping, friction and auxiliary) should be analysed. In this regard, the following comments can be made:

– Pumping power: in absolute terms, the pumping power (N_p) shown in Figure 6.16 increases with the speed and is almost insensitive to the

[4]The ECU sets the number of injections and the EGR strategy, according to the manufacturer calibration, in order to attain the best trade-off between consumption and emissions.

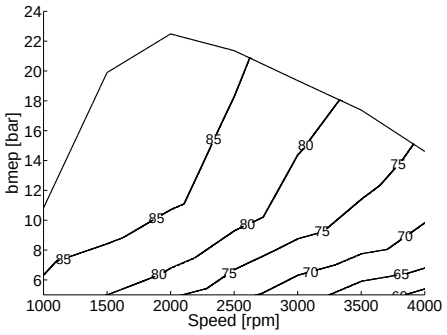

Figure 6.15. *Mechanical efficiency ($N_b/N_i \times 100$).*

load. Similarly, the relative weight of N_p increases with the speed, but in this case, it has a slight trend to diminish with the load. This trend can be justified considering that increasing the speed leads to higher air mass flow, thus increasing the difference between exhaust and intake pressures. Although increasing the load also requires higher air flow, the increase of the exhaust temperature allows to compensate it, thanks to the increase of the gas enthalpy at the turbine inlet.

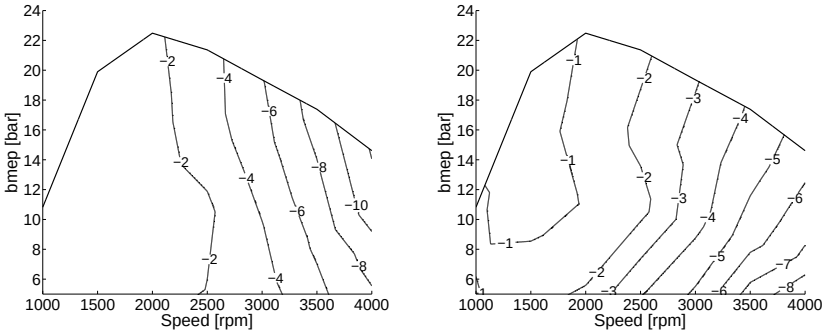

Figure 6.16. *Pumping power (N_p). Left: absolute value (kW). Right: relative value ($\%\dot{m}_f H_v$).*

– Friction: most of the engine friction takes place in the piston pack, the bearings and the valve train, whose values are shown in Figures 6.17, 6.18 and 6.19 respectively. In absolute terms, the friction increases mainly with the speed, except in the piston pack where it increase with both

speed and load. This is explained by the fact that friction power is highly dependent on the engine speed [6], as can be seen in Equations (5.73), (5.79) and (5.99). In addition, the friction coefficient, used to calculate the friction force, also depends on the engine speed. Nevertheless, in relative terms, the friction decreases when increasing the load, which is explained by the higher fuel energy.

As can be seen, $N_{fr,pis}$ is the most important friction term, reaching values up to $5\%\dot{m}_f H_v$ at high speed and low load, followed by $N_{fr,bear}$ with a maximum weight of $2\%\dot{m}_f H_v$ at low load, and finally, the less important term is $N_{fr,valv}$, whose maximum value is $0.7\%\dot{m}_f H_v$ at low load.

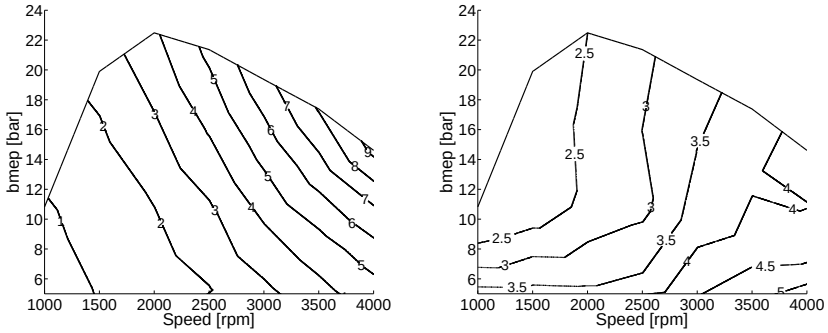

Figure 6.17. *Friction between piston pack and liner ($N_{fr,pis}$). Left: absolute value (kW). Right: relative value ($\%\dot{m}_f H_v$).*

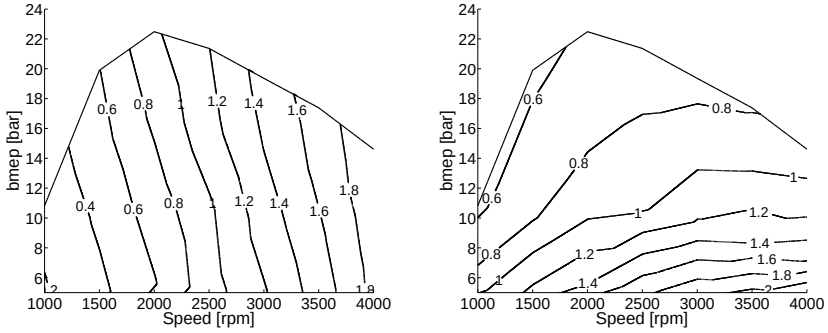

Figure 6.18. *Friction in the bearings ($N_{fr,bear}$). Left: absolute value (kW). Right: relative value ($\%\dot{m}_f H_v$).*

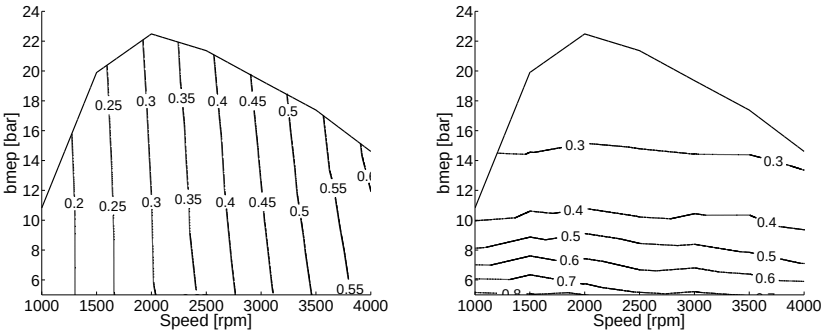

Figure 6.19. *Friction in the valve train ($N_{fr,valv}$). Left: absolute value (kW). Right: relative value ($\%\dot{m}_f H_v$).*

– Auxiliary: the coolant, oil and fuel pumps[5] energy consumption is shown in Figures 6.20, 6.21 and 6.22.

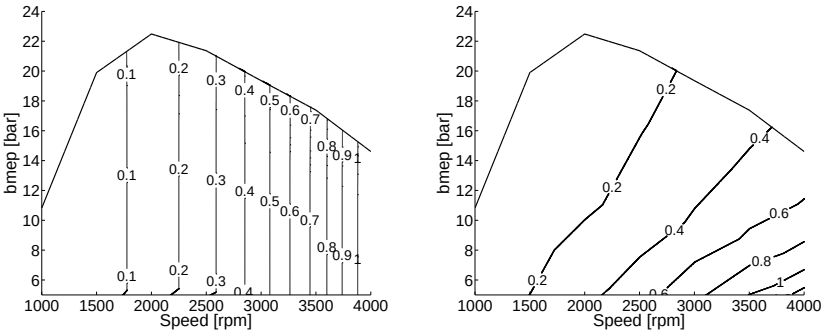

Figure 6.20. *Coolant pump power (N_{cool}). Left: absolute value (kW). Right: relative value ($\%\dot{m}_f H_v$).*

As can be seen, the absolute power of the coolant and oil pumps is proportional to the engine speed. However, their relative weight changes with both, speed and load. On the one hand, the relative weight of N_{cool} ranges between 0.2-1$\%\dot{m}_f H_v$, being specially important at high speed and low load, and on the other hand, N_{oil} weight lies between 0.3-

[5]Some sub-systems such as the air conditioner also consumes part of the fuel energy; however, these systems are not equipped in conventional research test benches and are not included in this work.

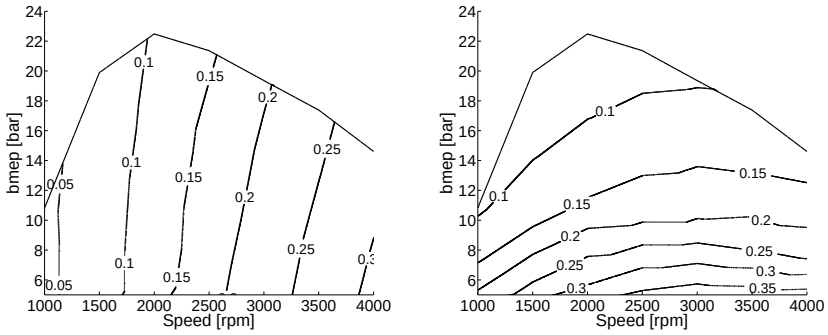

Figure 6.21. *Oil pump power (N_{oil}). Left: absolute value (kW). Right: relative value ($\%\dot{m}_f H_v$).*

$0.4\%\dot{m}_f H_v$ at low load. The general higher weight of N_{cool} is explained by the higher coolant flow requirements.

In the case of the fuel pump, its absolute power increases with both, speed and load, since this pump has a pressure control valve and a volume control valve. Therefore, the compressed fuel is controlled by the ECU at low load to reduce unnecessary fuel pumping. As a consequence, the relative weight of N_f in the complete map is almost constant about $0.7\%\dot{m}_f H_v$.

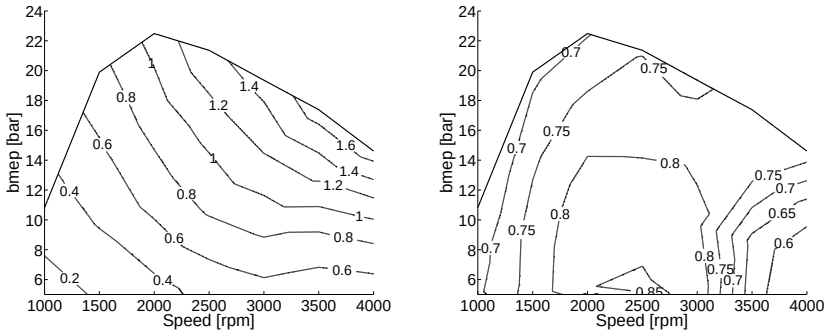

Figure 6.22. *Fuel pump power (N_f). Left: absolute value (kW). Right: relative value ($\%\dot{m}_f H_v$).*

6.2.2.3 Analysis of heat transfer

The HT in the chamber during closed cycle was analysed in Section 6.2.2.1 to explain η_i trends. This section deals with the complete evaluation of the heat rejection to coolant and oil. To explain the heat rejection to the coolant ($\dot{Q}_{cool}$), it is interesting to analyse in detail the HT to chamber walls ($\dot{Q}_{lin}$ and $\dot{Q}_{ch}$)[6] and ports ($\dot{Q}_{ports}$).

As can be seen in Figures 6.23 and 6.24, the absolute values of $\dot{Q}_{lin}$ and $\dot{Q}_{ch}$ increase with the engine speed since the HT to chamber walls is proportional to c_m powered to $b < 1$ (see Equation (3.26))[7]. However, increasing the engine speed also reduces the available time for HT, which is inversely proportional to c_m, being this the key factor as it implies lower residence time of the fluids in the engine. Thus, the relative weight of $\dot{Q}_{lin}$ and $\dot{Q}_{ch}$ is lower at high speed. Additionally, increasing the load leads to higher absolute HT, nevertheless, it is overcome by the increase of fuel energy, thus resulting in lower HT weight.

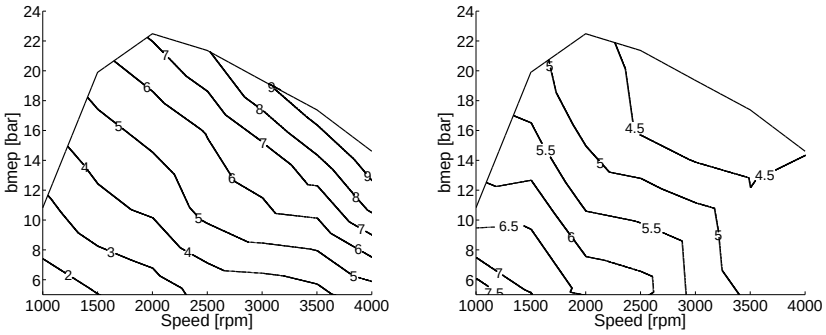

Figure 6.23. *Heat transfer to liner ($\dot{Q}_{lin}$). Left: absolute value (kW). Right: relative value ($\%\dot{m}_f H_v$).*

In the case of the ports, increasing the speed and load leads to higher absolute $\dot{Q}_{ports}$ values. However, in relative terms, it decreases with the speed as a consequence of the lower residence time of the gases in the ports; nevertheless, increasing the load leads to higher exhaust temperature and gas

[6]The HT to liner and cylinder head were assumed to be rejected to the coolant, see Chapter 4.2.2.

[7]The heat transfer coefficient is proportional to v_g^b, being v_g also dependent on the mean piston speed c_m.

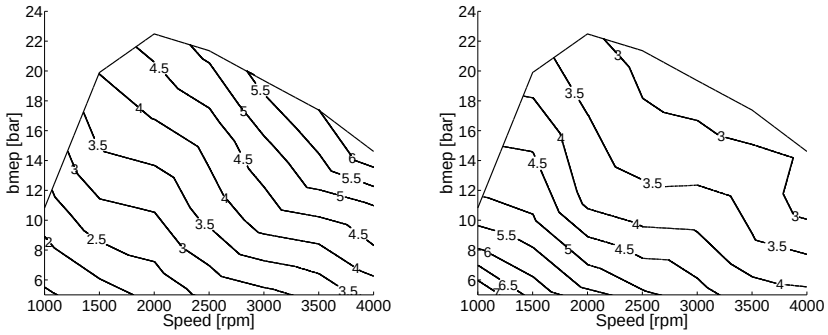

Figure 6.24. *Heat transfer to cylinder head ($\dot{Q}_{ch}$). Left: absolute value (kW). Right: relative value ($\%\dot{m}_f H_v$).*

velocity due to the higher exhaust flow, which results in a $\dot{Q}_{ports}$ increment similar as the relative increase of the fuel energy, thus this term does not change significantly with the load.

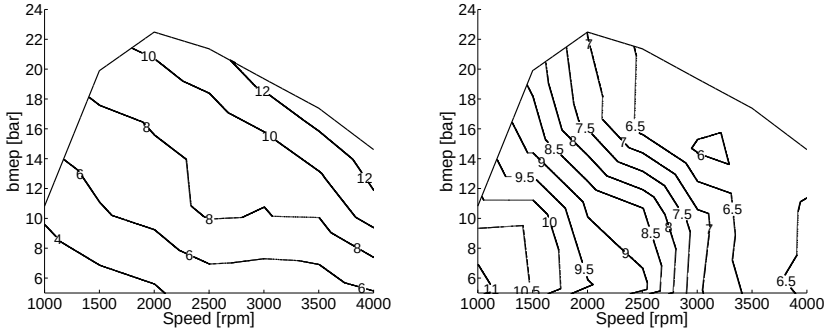

Figure 6.25. *Heat transfer to ports ($\dot{Q}_{ports}$). Left: absolute value (kW). Right: relative value ($\%\dot{m}_f H_v$).*

Taking into consideration the trends described for $\dot{Q}_{lin}$, $\dot{Q}_{ch}$ and $\dot{Q}_{ports}$ (and in lower extent for N_{cool} and $N_{fr,pis}$), the relative weight of $\dot{Q}_{cool}$ shown in Figure 6.26 can be then analysed. As the relative weight of all these terms decreases with the speed, $\dot{Q}_{cool}$ also follows this trend. However, the lower dependency of $\dot{Q}_{ports}$ with the load, and considering that its relative weight is almost the same as the other two heat rejection terms, the dependency of $\dot{Q}_{cool}$ with the load is lower than that of $\dot{Q}_{lin}$ and $\dot{Q}_{ch}$. As a result, the relative

weight of $\dot{Q}_{cool}$ ranges between $18\%\dot{m}_f H_v$ at high speed to $28\%\dot{m}_f H_v$ at low speed.

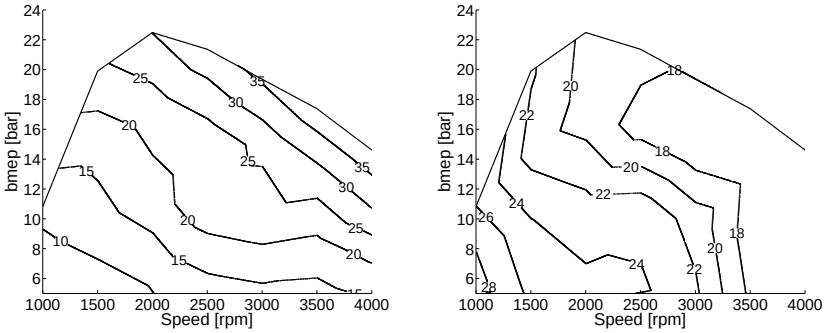

Figure 6.26. *Heat transfer to coolant ($\dot{Q}_{cool}$). Left: absolute value (kW). Right: relative value ($\%\dot{m}_f H_v$).*

Additionally, as commented in Chapter 4.3.2, the friction between piston pack and liner and the coolant pump power are also assumed to be rejected to the coolant. As the relative weight of $N_{fr,pis}$ does not change significantly with the load, specially at high speed as shown in Figure 6.17, it also helps to reduce $\dot{Q}_{cool}$ dependence with the load. In the case of N_{cool} (see Figure 6.20), its low weight has no significant effect on $\dot{Q}_{cool}$ but a slight general increase in the complete engine map.

The HT to the oil ($\dot{Q}_{oil}$) is shown in Figure 6.27. As can be seen, it is clear that $\dot{Q}_{oil}$ is about 4 times lower than $\dot{Q}_{cool}$ (shown in Figure 6.26). In general, the absolute and relative trends observed for $\dot{Q}_{oil}$ are similar as those of the HT to the piston ($\dot{Q}_{pis}$), presented in Figure 6.28. This similarity is reasonable since $\dot{Q}_{pis}$ is mainly dissipated to the oil. It is interesting to highlight that $\dot{Q}_{pis}$ is about $1\%\dot{m}_f H_v$ higher than $\dot{Q}_{oil}$, since part of $\dot{Q}_{oil}$ energy is rejected to the coolant.

It is interesting to highlight some effects due to the mechanical losses energy dissipation to the oil, i.e. the friction from bearings ($N_{fr,bear}$), valve train ($N_{fr,valv}$) and oil pump power (N_{oil}), shown in Figures 6.18, 6.19 and 6.21 respectively. In absolute terms, these mechanical losses depend mainly on the engine speed, thus the trend of $\dot{Q}_{oil}$ becomes more dependent on n than $\dot{Q}_{pis}$. Nevertheless, in relative terms, $N_{fr,bear}$, $N_{fr,valv}$ and N_{oil} do not significantly depend on the speed; therefore, $\dot{Q}_{oil}$ changes slightly less with the speed than $\dot{Q}_{pis}$.

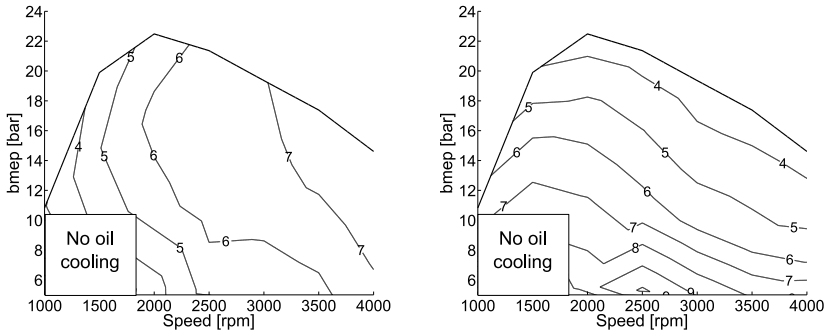

Figure 6.27. *Heat transfer to oil ($\dot{Q}_{oil}$). Left: absolute value (kW). Right: relative value ($\%\dot{m}_f H_v$).*

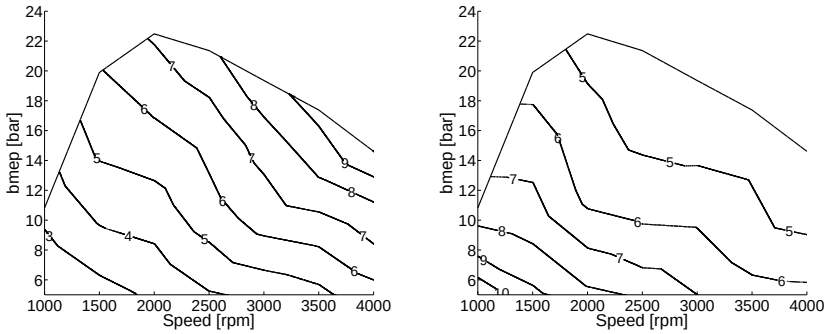

Figure 6.28. *Heat transfer to piston ($\dot{Q}_{pis}$). Left: absolute value (kW). Right: relative value ($\%\dot{m}_f H_v$).*

6.2.2.4 Analysis of exhaust energy losses

The net sensible enthalpies, $\dot{H}_{g,ports}$ (between ports), $\dot{H}_{g,in}$ (between intercooler outlet and turbocharger inlet) and $\dot{H}_{g,ex}$ (between compressor inlet and turbocharger outlet)[8] are shown in Figures 6.29, 6.30 and 6.31. They depict similar trends but at different levels: they depend on both the engine speed and load; thus, the higher the load and speed, the higher the absolute value of the exhaust gases energy. It is worth to highlight that, in relative terms, the net sensible enthalpy shows higher sensitivity to the engine speed than in absolute terms.

[8]Definition of these terms can be found in Chapter 4.2.

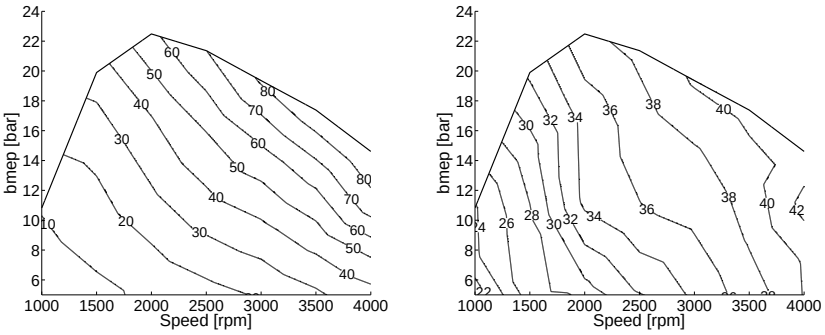

Figure 6.29. *Net sensible enthalpy at ports ($\dot{H}_{g,ports}$). Left: absolute value (kW). Right: relative value ($\%\dot{m}_f H_v$).*

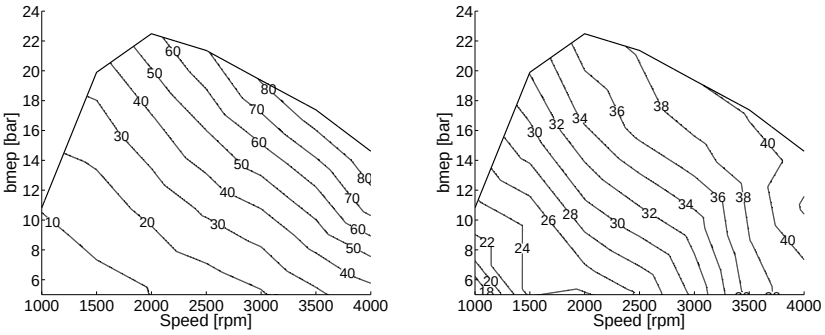

Figure 6.30. *Internal net sensible enthalpy ($\dot{H}_{g,in}$). Left: absolute value (kW). Right: relative value ($\%\dot{m}_f H_v$).*

The relationship between these enthalpies was stablish in Chapter 4.2.2, for convenience, they are rewritten below:

$$\dot{H}_{g,in} = \dot{H}_{g,ex} + \dot{Q}_a + \dot{Q}_{turbo} + \dot{Q}_{ext,turbo} \tag{6.5}$$

$$\dot{H}_{g,ports} = \dot{H}_{g,in} + \dot{Q}_{\mathrm{EGR}} + \dot{Q}_{ext,man} \tag{6.6}$$

The level difference between $\dot{H}_{g,ports}$ and $\dot{H}_{g,in}$ is mainly explained by the HT to the EGR ($\dot{Q}_{\mathrm{EGR}}$), shown in Figure 6.32. Since no EGR strategy was used at high load and speeds above 3500 rpm, no EGR refrigeration was required at these operating conditions and the difference between $\dot{H}_{g,ports}$ and $\dot{H}_{g,in}$ is low, being the small deviation (lower than $1\%\dot{m}_f H_v$) due to $\dot{Q}_{ext,man}$.

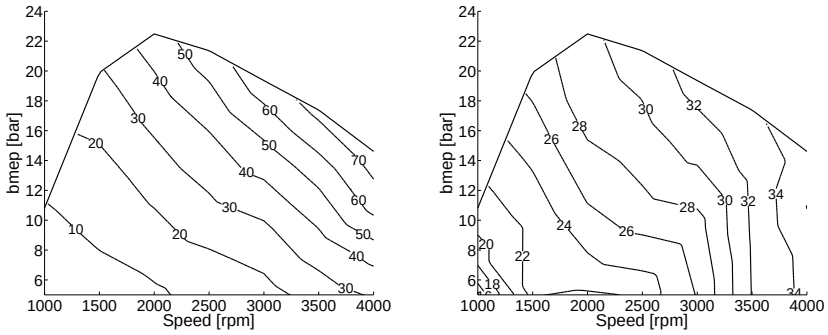

Figure 6.31. *External net sensible enthalpy ($\dot{H}_{g,ex}$). Left: absolute value (kW). Right: relative value ($\%\dot{m}_f H_v$).*

In the low-mid speed and load, the differences become higher, reaching values up to $5\%\dot{m}_f H_v$ at 2500 rpm and low load, where the EGR rate is about 30%, and hence $\dot{Q}_{\mathrm{EGR}}$ reaches its maximum relative weight.

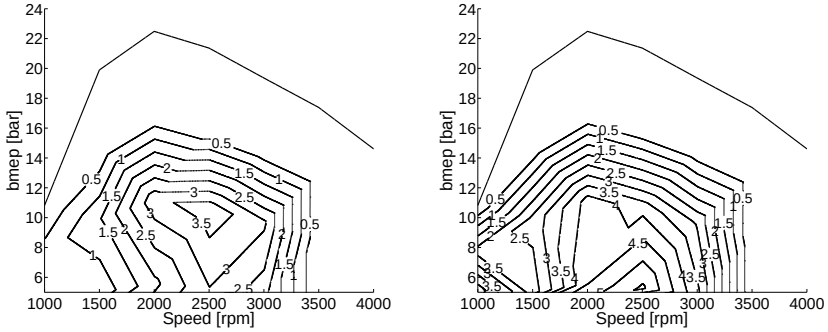

Figure 6.32. *Heat transfer from EGR ($\dot{Q}_{\mathrm{EGR}}$). Left: absolute value (kW). Right: relative value ($\%\dot{m}_f H_v$).*

Similarly, the level difference between $\dot{H}_{g,in}$ and $\dot{H}_{g,ex}$ is explained mainly through the HT to the intercooler ($\dot{Q}_a$). In Figure 6.33, it is possible to see how $\dot{Q}_a$ follows a similar trend as the net sensible enthalpy, i.e. its absolute values are higher at high speed and load operating conditions due to the effect of air compression in the turbocharger. This is reasonable taking into account that the higher $\dot{H}_{g,in}$ is related with the available energy to be used in the turbine, and hence a higher compression work is done in the compressor,

which leads to higher air temperature and higher relative cooling demand in the intercooler.

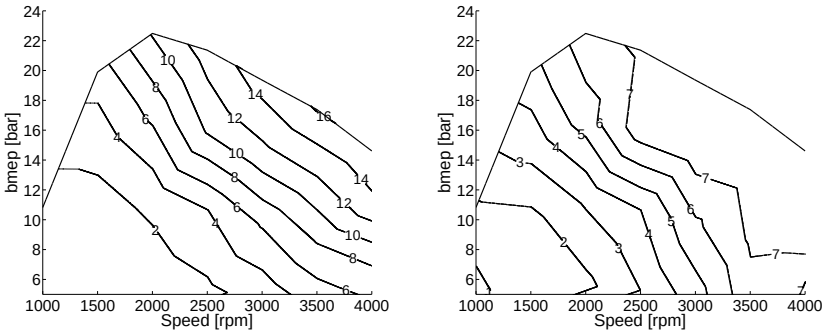

Figure 6.33. *Heat transfer from air ($\dot{Q}_a$). Left: absolute value (kW). Right: relative value ($\%\dot{m}_f H_v$).*

Note that in global relative terms, the net sensible enthalpies have a contrary trend as that observed in $\dot{Q}_{cool}$ and $\dot{Q}_{oil}$ (see Figures 6.26 and 6.27). This is mainly explained by the lower HT weight at high speed and load, where the heat rejection reduction is partially recovered as efficiency, but mostly evacuated as sensible enthalpy at exhaust.

6.2.2.5 Analysis of miscellaneous losses

As explained in Chapter 4.2.1, the miscellaneous term ($\dot{Q}_{misc}$) gathers some terms with relatively low weight in the GEB, as presented in Equation (4.18), recalled here for the sake of clarity.

$$\dot{Q}_{misc} = \dot{Q}_{ext} + \dot{Q}_{turbo} + \dot{Q}_f + \dot{H}_{ic} + \dot{H}_{bb} + \dot{Q}_{unbal,ex} \tag{6.7}$$

As shown in Figure 6.34, the lower the speed and load, the higher the relative weight of $\dot{Q}_{misc}$. This trend can be explained by two main reasons: on the one hand, as shown in Figure 6.35, at low speed and load the relative weight of the HT to the ambient ($\dot{Q}_{ext}$) is higher because the external wall temperature of the engine, mainly dependent on coolant temperature, does not change dramatically with the engine speed and load, contrary to the fuel mass. On the other hand, the uncertainty ($\dot{Q}_{unbal,ex}$) is maximum at low speed

and load due to the small power of all the experimental terms measured, at these conditions, the temperature differences and flow rates are smaller and the relative uncertainty tends to increase as can be seen in Figure 6.36.

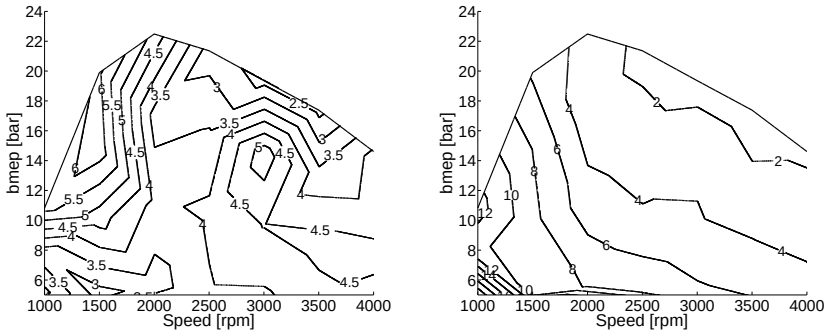

Figure 6.34. *Miscellaneous term ($\dot{Q}_{misc}$). Left: absolute value (kW). Right: relative value ($\%\dot{m}_f H_v$).*

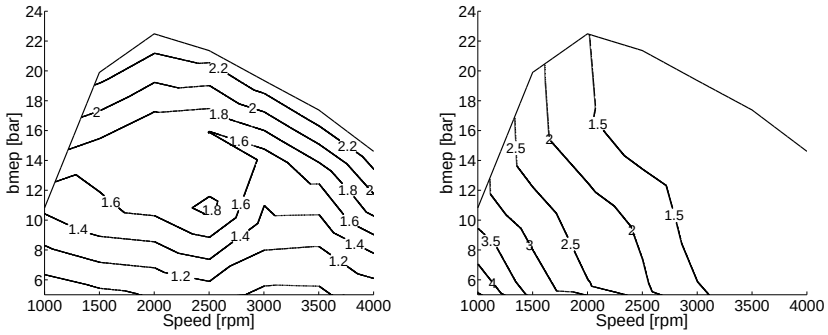

Figure 6.35. *Heat transfer to ambient ($\dot{Q}_{ext}$). Left: absolute value (kW). Right: relative value ($\%\dot{m}_f H_v$).*

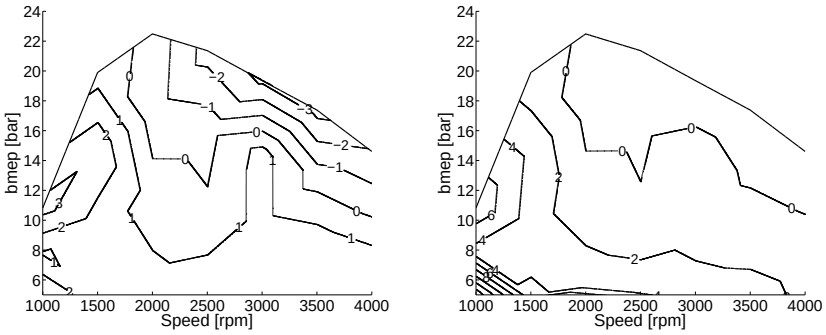

Figure 6.36. *External unbalance term ($\dot{Q}_{unbal,ex}$). Left: absolute value (kW). Right: relative value ($\%\dot{m}_f H_v$).*

6.3 GEB in Engine B

Once the GEB has been analysed in a conventional Diesel engine, the methodology is applied in a new concept engine. For this reason, the single-cylinder, two stroke engine (**Engine B**), described in Chapter 3.2.2 is analysed. The work presented in this section is aimed at obtaining different combustion and thermodynamic conditions as those obtained in CDC. For this reason, gasoline was used as fuel, and a Partially Premixed Combustion (PPC) was tested. The analysis has two main goals:

- Showing how the GEB methodology can be used to perform thermal diagnoses in diverse engines, operating with different fuels and combustion modes.
- After the uncertainties adjustment and the sub-models calibration, a predictive approach is used to assess the effect of the HT in the PPC concept. This study is performed with the thermodynamic predictive tool SiCiclo.

For the experimental work, two operating points at mid-speed have been selected: one at low load and the other at mid load, thus avoiding the high uncertainty zone at low speed (see Chapter 4.4). These loads were chosen because the potential of PPC is fully shown at those regions. In Table 6.6, the base operating settings of the measured points are presented.

	Speed [rpm]	$imep$ [bar]	$\dot{m}_a$ [g/s]	$\dot{m}_f$ [g/s]	Δp * [mbar]	p_{rail} [bar]	**Injections** [-]	τ_{EGR} [%]
L1	2000	3.3	5.6	0.24	250	400	2	24
L2	2000	5.5	6.6	0.38	400	600	3	33

*Δp is defined as $p_{int} - p_{exh}$ in this engine.

Table 6.6. *Base setting of measured points in* ***Engine B****.*

The first step is the tool calibration as performed in **Engine A**. It is important to take into account that the experimental facility of **Engine B** was not intended to determine all the heat fluxes; therefore, the information required to perform the complete EGEB (i.e. by means of a mostly experimental approach) is not available. Nevertheless, the experimental measurements available are enough to calibrate the models presented in this work.

Once the models are calibrated for the selected operating conditions, parametric variations at two levels of some operating variables (i.e. post and main injections and Δp) are performed. Finally, a brief theoretical study with SiCiclo to assess the effect of the HT in the L2 operating point is carried out.

6.3.1 Sub-models calibration

The calibration of **Engine B** was performed following the same procedure as for **Engine A**; however, two comments have to be made:

- As this is a research engine, the optimization work has been focused on the indicated efficiency because the engine design has not been optimized to reduce mechanical losses. Therefore, they will not be analysed and the model is not calibrated.
- As commented, the experimental information in this engine is more reduced than in the case of **Engine A**. As a consequence, the information required to calibrate the HT from oil to coolant is not available.

Taking into account these comments, the calibration procedure followed in **Engine B** is presented in Figure 6.37. The steps followed for the calibration are the following:

- **Step 1:** similarly as for **Engine A**, the calibration of heat transfer to chamber walls is performed in two stages. First, the *Engine characterization* is performed following the methodology described in Chapter 5.3.1. For this specific engine, this process is carried out in a set of skip-fire tests as was discussed in Chapter 5.2.1. Taking into consideration that this engine has tumble motion instead of swirl (see Chapter 5.2.1), the Woschni constant (C_{w1}) is replaced for the equivalent constant C_{t1} of Equation (5.5), recalled below for convenience.

$$v_{g,t} = C_{t1}\ c_m + C_{t2}\ c_t + C_2\ \frac{V_d\ T_{\mathrm{IVC}}}{V_{\mathrm{IVC}}\ p_{\mathrm{IVC}}}\ (p - p_0) \tag{6.8}$$

  Once the *Engine characterization* is performed, the C_2 constant of Equation (6.8) that accounts for the combustion effect on HT is adjusted. The criterion followed is the reduction of ACE uncertainty (as in **Engine A**).

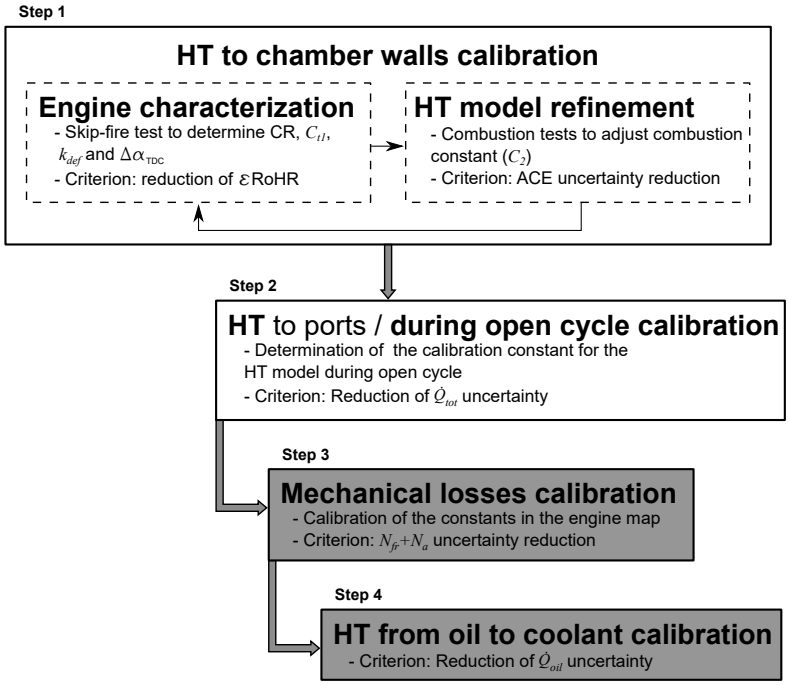

Figure 6.37. *Sub-models calibration procedure.*

This procedure was carried with the set of combustion measurements[9] presented later in Section 6.3.2 (see Table 6.8).

Since the parameters involved in the *Engine characterization* have cross effects [7] with the HT to the chamber, the previously commented stages are carried out simultaneously[10] as shown in Figure 6.37. The results of the *Engine characterization* and the HT model adjustment are presented in Table 6.7.

As the HT model during closed cycle was tuned with skip-fire tests, it was assumed that the difference between η_{comb} and the ACE mainly depends on the combustion component C_2 of the gas velocity in Equation (6.8). Therefore, its value was determined with the criterion of reducing

[9] A sweep of engine speed should be used to cover the complete engine operation range; however, due to the particularities of this engine and the specific objective of this study, this experimental set was considered enough.

[10] This is consistent with the tumble model calibration presented in Chapter 5.2.1.4, which was also simultaneously carried out with the *Engine characterization*.

Parameter	Value
CR	16.5:1
k_{def}	0.99
$\Delta\alpha_{\text{TDC}}$	167.3
C_{t1}	1.05
C_{t2}	0.53
C_2	0.005
$C_{t1,oc}$	22.4

Table 6.7. *Engine characterization and HT model fitting constants.*

ACE-η_{comb}. η_{comb} is determined by means of Equation (6.2), and for the evaluated points, it has a value of 98±1%; therefore, this value was used as reference. The results of this process provides a $C_2 = 0.005$ as shown in Table 6.7.

- **Step 2:** the next step consist on adjusting the HT during open cycle ($C_{t1,oc}$ instead of C_{t1} in Equation (6.8)). As explained in Section 6.2.1, adjusting simultaneously the HT to ports and in the chamber during open cycle is not possible. Thus, differently to **Engine A**, in this case the HT to the chamber during open cycle was adjusted instead of HT to ports. The reason is that in this case the in-cylinder HT has a big uncertainty, while the HT in the ports was previously studied in **Engine A**, thus assuming similar behaviour. As no tumble nor combustion are considered during open cycle ($C_{t2} = 0$ and $C_2 = 0$), $C_{t1,oc}$ value has to be adjusted to account for the air velocity effect on the HT due to the piston movement. This process is similar as the adjustment of the HT to ports performed in **Engine A**; therefore, the criterion is the reduction of $\dot{Q}_{tot}$ uncertainty for the operating conditions shown in Table 6.8. The calibration constant of the HT to exhaust ports obtained in **Engine A** was also used in this engine.

Finally, during the open cycle no tumble is considered by the model presented; however, as commented in Chapter 5.2.1.1, some rotative macro structures start forming during the intake process. Therefore, it is important to adjust the $C_{t1,oc}$ to compensate their effect on HT. As shown in Table 6.7, $C_{t1,oc}$ has a value of 22.4. This high value is consequence of adjusting the gas velocity effect only with the mean piston speed (c_m). To include the tumble

effect during the open cycle, a specific sub-model is required; however, it would not improve the combustion diagnosis and would have just a slightly effect on the IGEB.

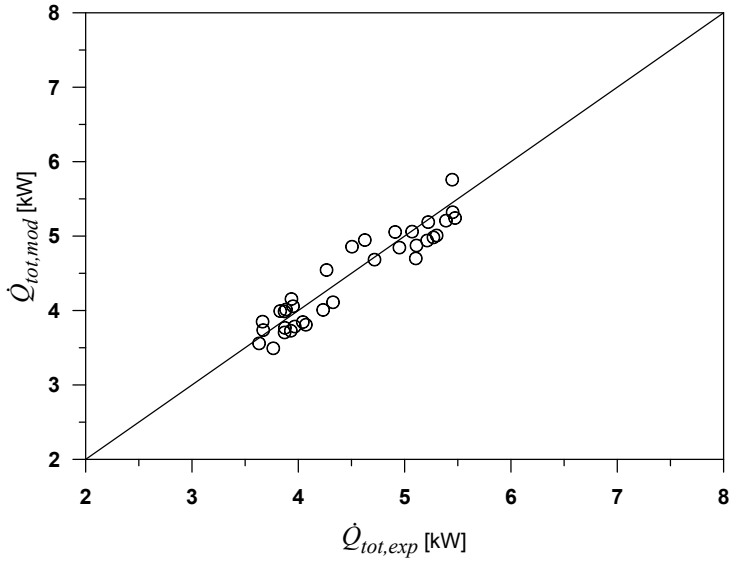

Figure 6.38. *Experimental and modelled $\dot{Q}_{tot}$ comparison after HT adjustment.*

To assess the calibration performance, the comparison of $\dot{Q}_{tot,exp}$ and $\dot{Q}_{tot,mod}$ is presented in Figure 6.38. As can be seen, the modelled values are in good agreement with the experimental ones, having a mean deviation about $\pm 3.5\%$ (about $\pm 1\% \dot{m}_f H_v$).

6.3.2 Parametric studies

Once the HT model is tuned, several parametric studies were carried out. These test were performed using gasoline RON 95 as fuel and a PPC mode. The parametric studies performed are:

- Study 1: Variation of post injection timing.
- Study 2: Variation of main injection timing.

– Study 3: Variation of the intake-exhaust pressure drop (Δp).

The relevant operating conditions of the parametric studies are summarized in Table 6.8. These ranges were the maximum variations possible at which a stable combustion was achieved. Higher variations of these parameters could lead to flame quenching or knocking [8, 9].

	Operating point	SoI pilot [°]	SoI main [°]	SoI post [°]	Δp * [mbar]
Study 1	L1	*n/a*	-42	**-10/0**	250
	L2	-60	-44	**-6/-14**	400
Study 2	L1	*n/a*	**-36/-46**	-10	250
	L2	-60	**-42/-48**	-10	400
Study 3	L1	*n/a*	-42	-4	**210/270**
	L2	-60	-44	-10	**400/480**

*Δp is defined as $p_{int} - p_{exh}$ in **Engine B**.

Table 6.8. *Parametric studies performed on* ***Engine B****.*

In the following sections, $\dot{Q}_{unbal,in}$ is not analysed. The reason is that it is lower than $1\%\dot{m}_f H_v$ in all the analysed points, which is in the range of the fuel measurement uncertainty. It is interesting to clarify that $\dot{Q}_{unbal,ex}$ was considered in the analysis of **Engine A** because it changes importantly in the engine map. Similarly, the blow-by also affects the GEB; however, its effect is always lower than $0.06\%\dot{m}_f H_v$ and it is not considered in the analysis.

6.3.2.1 Post injection timing variation

In this study, the post injection timing was change at two levels: 0 and -10° for the L1 point, and -6 and -14° for the L2 point, as shown in Table 6.8. The rest of the operating parameters were kept constant to assure a clear comparison between results.

Results on L1 point: the injection rate and the RoHR are presented in Figure 6.39. As shown, the advanced post injection leads to faster combustion, evident by the higher RoHR peak. This sharper combustion leads to higher gas temperature peak and hence to higher HT as shown in Figure 6.40. During

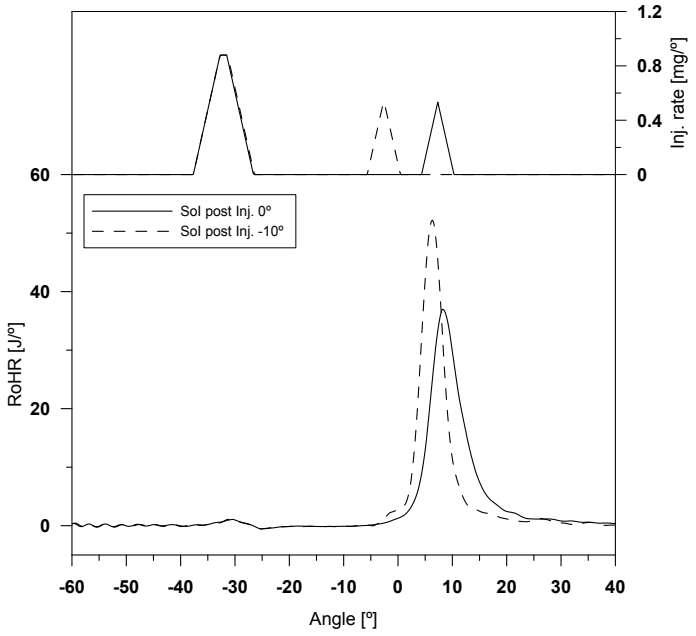

Figure 6.39. *RoHR shape due to post injection variation in L1.*

the expansion stroke the temperature tends to become similar in both cases, being slightly lower for the delayed post injection. This is explained by the longer combustion in this case, in which the combustion process is slower and starts later, thus increasing T and HT during the expansion.

In Figure 6.41, the GEB is presented. As can be seen, the indicated efficiency is almost the same in both cases; however, delaying the post injection reduces $\dot{Q}_{cham,cool}$ and $\dot{Q}_{cham,oil}$ about 0.6 and $0.7\%\dot{m}_f H_v$ respectively. This HT reduction is compensated by two effects: on the one hand, the higher $\dot{H}_{ic}$ due to lower combustion efficiency, and on the other hand, the higher $\dot{H}_{g,in}$ and $\dot{Q}_{\mathrm{EGR}}$ (about $0.5\%\dot{m}_f H_v$ each of them) explained by the slightly higher exhaust temperature because of the late combustion during expansion.

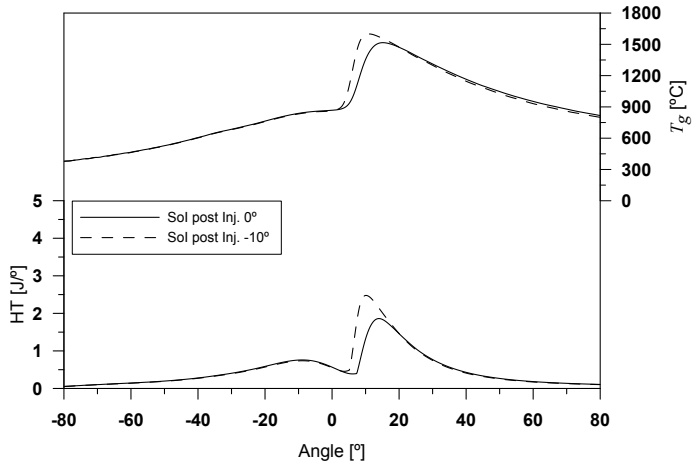

Figure 6.40. *HT and T changes due to post injection variation in L1.*

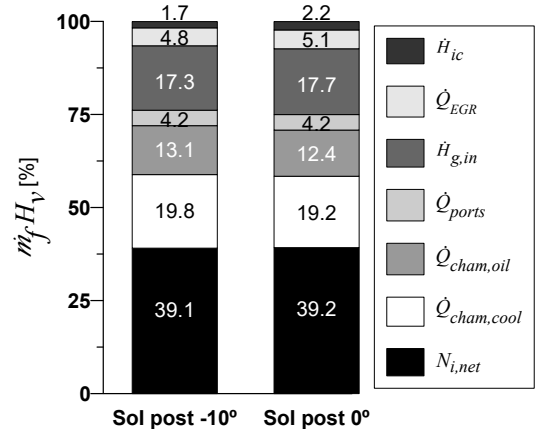

Figure 6.41. *GEB of post injection variation in L1.*

Results on L2 point: contrary to the effect observed in the L1 point, advancing the post injection at higher load leads to lower RoHR peak and delayed combustion, as can be seen in Figure 6.42. In this case, this earlier post injection leads to higher delay time because of the reduction of the local temperature due to the effect of fuel evaporation; however, it seems that in

the second case (delayed post injection), the injection begins after the Start of Combustion (SoC) of the main injection, thus leading to a faster combustion of the post injection, as can be noticed in the sharper shape of the RoHR.

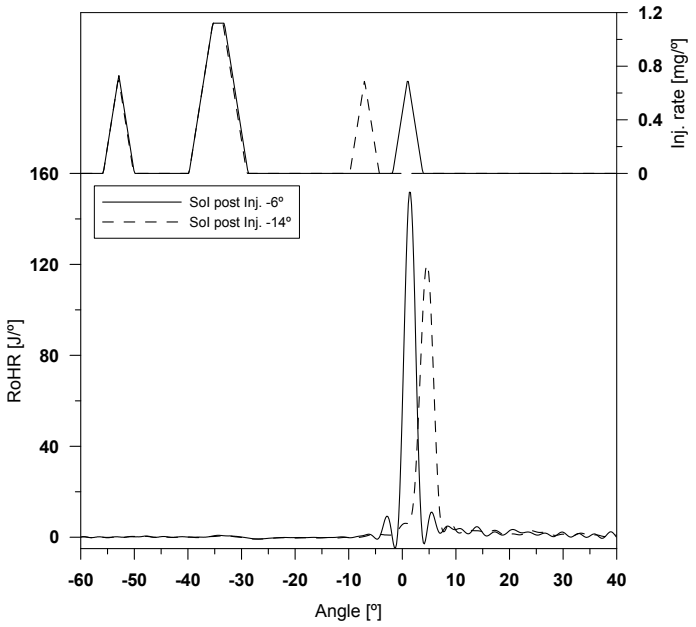

Figure 6.42. *RoHR shape due to post injection variation in L2.*

It is interesting to highlight that the HT in the delayed post injection is higher near to the TDC as shown in Figure 6.43. This higher HT is due to the faster combustion and the faster increase of T. However, the later End of Combustion (EoC) of the advanced post injection leads to increase T during the expansion stroke. Therefore, some degrees after TDC, both T and HT reach similar levels for both post injection cases. However, the effect of the higher T close to TDC leads to increase $\dot{Q}_{cham,cool}$ and $\dot{Q}_{cham,oil}$ about 0.7 and $0.9\%\dot{m}_f H_v$ (see Figure 6.44).

As shown in Figure 6.44, $\eta_{i,net}$ is about $0.8\%\dot{m}_f H_v$ higher in the case of advanced post injection, which is explained by the global reduction of the HT in the chamber about $1.6\%\dot{m}_f H_v$. Regarding $\dot{H}_{g,in}$, it is $0.5\%\dot{m}_f H_v$ higher in the advanced post injection case, whilst $\dot{Q}_{ports}$ and $\dot{Q}_{\mathrm{EGR}}$ have similar values in the GEB as shown in Figure 6.44, (the addition of them is about $0.3\%\dot{m}_f H_v$

higher in the case of advanced post injection). Note that $\dot{H}_{ic}$ is similar in both cases, which means that the combustion efficiency is not importantly affected by the post injection timing at this load.

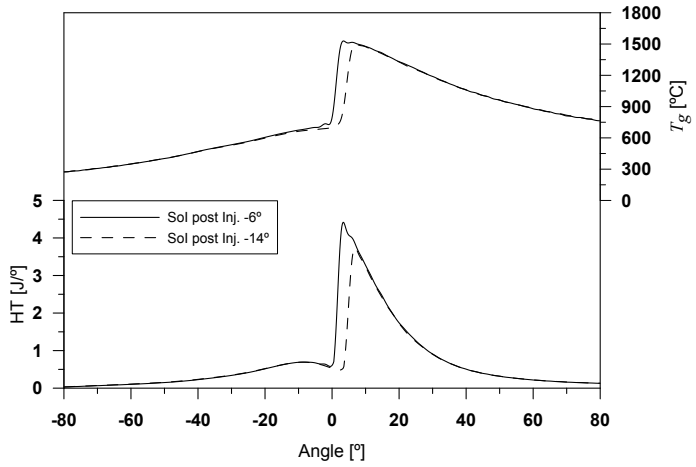

Figure 6.43. *HT and T changes due to post injection variation in L2.*

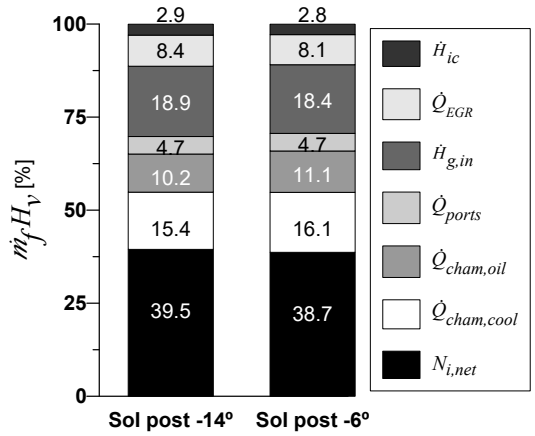

Figure 6.44. *GEB of post injection variation in L2.*

6.3.2.2 Main injection timing variation

The procedure followed in this study is similar as that of the previous study, but this time changing the main injection timing. For L1 point it was varied between -36 and -46°, and for L2 between -42 and -46°, as shown in Table 6.8.

Results on L1 point: advancing the main injection provides more time for the air/fuel mixing process, thus leading to higher premixed combustion and hence a sharp shape of the RoHR as shown in Figure 6.45. Also both SoC and EoC occurs earlier in the case of advancing main injection.

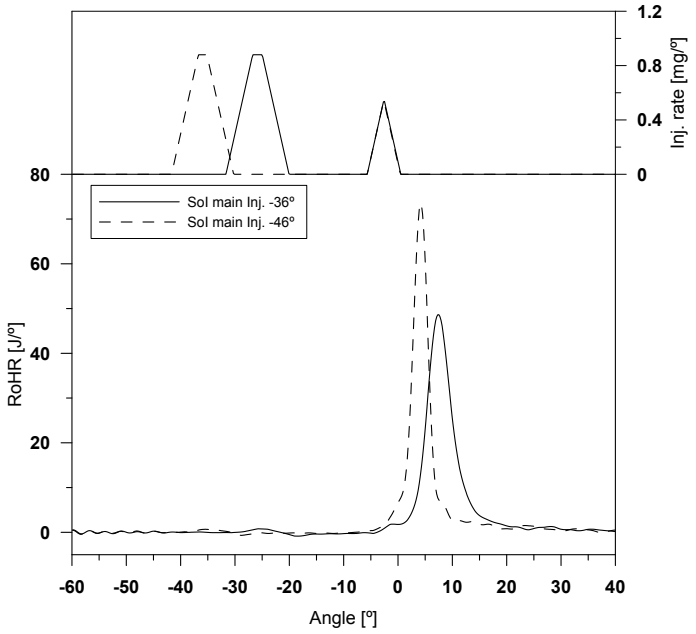

Figure 6.45. *RoHR shape due to main injection variation in L1.*

This faster combustion leads to higher T, and hence higher HT near TDC, where the combustion takes place. However, delaying the main SoI leads to longer and later combustion, and hence to slightly higher exhaust temperature.

As can be observed in Figure 6.47, delaying the main SoI reduces $\dot{Q}_{cham,cool}$ and $\dot{Q}_{cham,oil}$ about 0.6 and $0.7\%\dot{m}_f H_v$ respectively. Moreover, $\dot{H}_{ic}$ is $1.1\%\dot{m}_f H_v$

lower, which indicates a better combustion performance, explained by the lower amount of gasoline near the walls where the temperature is low, and hence the fuel is not completely burned [10]. This global HT reduction and the improved combustion efficiency lead to an increase of $\eta_{i,net}$ about $1.4\%\dot{m}_f H_v$.

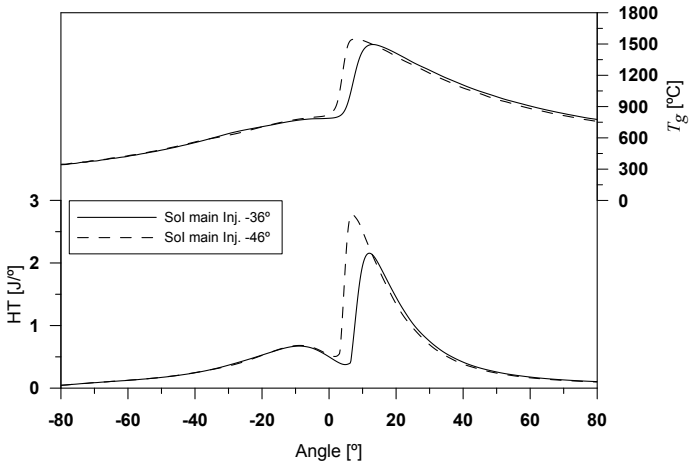

Figure 6.46. *HT and T changes due to main injection variation in L1.*

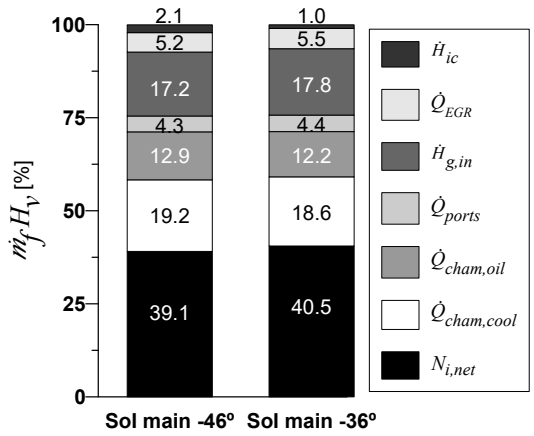

Figure 6.47. *GEB of main injection variation in L1.*

As can be seen in Figure 6.47, $\dot{H}_{g,in}$ is $0.6\%\dot{m}_f H_v$ lower when advancing the main SoI due to lower exhaust temperature. For the same reason, $\dot{Q}_{ports}$ and $\dot{Q}_{\mathrm{EGR}}$ are slightly lower in this case.

Results on L2 point: as shown in Figure 6.48 both main SoIs tested have similar RoHR shape, SoC and EoC. However, advancing the main SoI leads to lower RoHR peak and slightly advanced combustion.

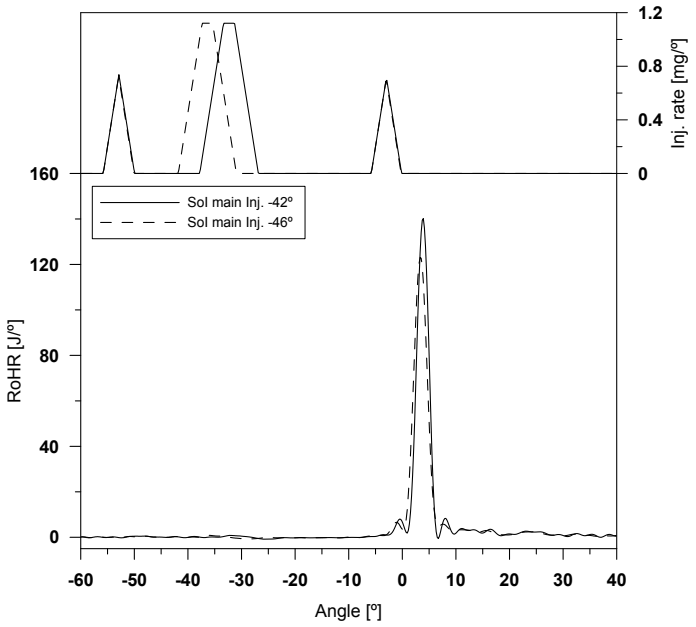

Figure 6.48. *RoHR shape due to main injection variation in L2.*

Since the combustion process is quite similar, both T and HT have similar behaviour during the whole cycle as shown in Figure 6.49. It is only remarkable a slightly lower temperature after TDC for the advanced SoI.

As shown in Figure 6.50, a $\eta_{i,net}$ improvement of $0.5\%\dot{m}_f H_v$ is attained when advancing the main SoI as a consequence of the addition of small favourable processes: a better combustion performance that leads to $0.3\%\dot{m}_f H_v$ lower $\dot{H}_{ic}$, and slightly lower HT.

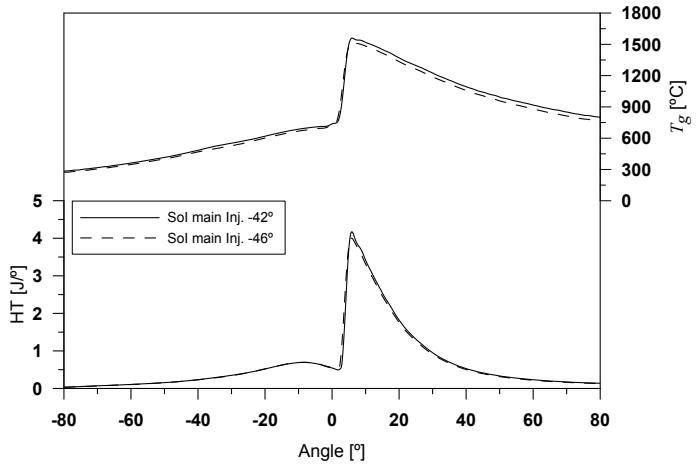

Figure 6.49. *HT and T changes due to main injection variation in L2.*

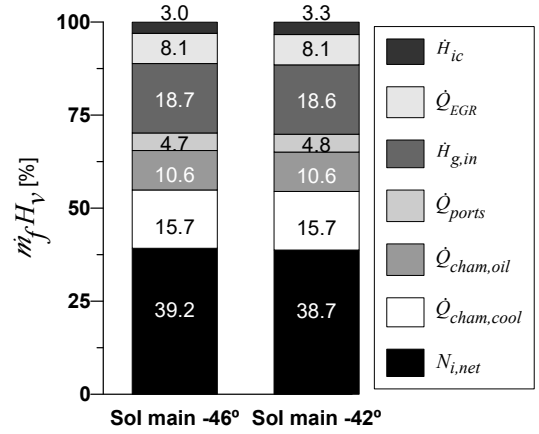

Figure 6.50. *GEB of main injection variation in L2.*

6.3.2.3 Variation of the intake-exhaust pressure drop

Due to the particularities of the Gasoline PPC concept, the air management plays a crucial role, since high IGR rate is key to increase the temperature of the charge and trigger the auto-ignition of the low reactivity mixture. In

2-stroke engines, the sweep of the burned gases is highly sensible to the difference between intake and exhaust pressure ($\Delta p = p_{int} - p_{exh}$). For this reason, a study at two different Δp was carried on as shown in Table 6.8: Δp was swept from 210 to 270 mbar at L1, and from 400 to 480 mbar at L2. These variations were made by changing the exhaust pressure and maintaining the intake pressure values presented in Table 6.6.

Results on L1 point: The increase of Δp enhances both, the intake of fresh air and the sweep of burned gases. As shown in Figure 6.51, the higher Δp delays the SoC. This is explained by the lower T during most of the cycle (see Figure 6.53) due to the lower residual gases fraction, being about 5% lower when increase Δp in the range considered.

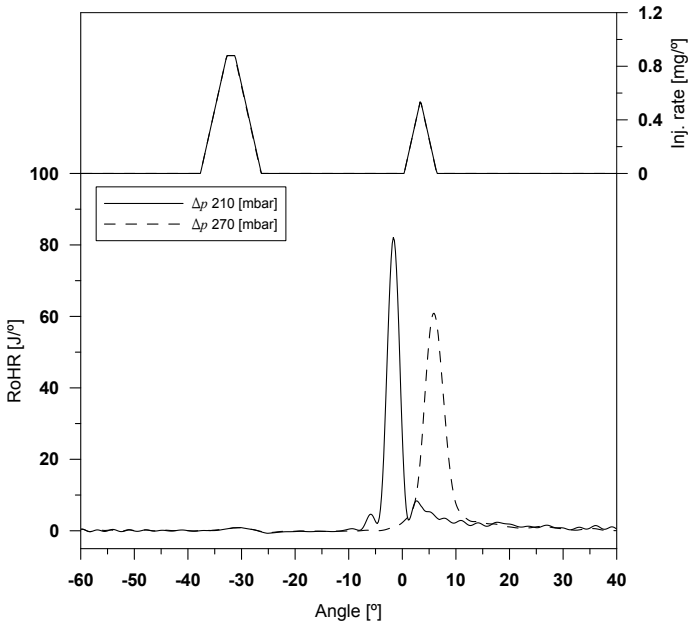

Figure 6.51. *RoHR shape due to Δp variation in L1.*

The lower T at higher Δp also leads to lower HT, as shown in Figure 6.52. Moreover, it can be seen how the temperature is lower during the compression and also becomes increasingly lower during the expansion stroke, thus leading to lower exhaust temperature.

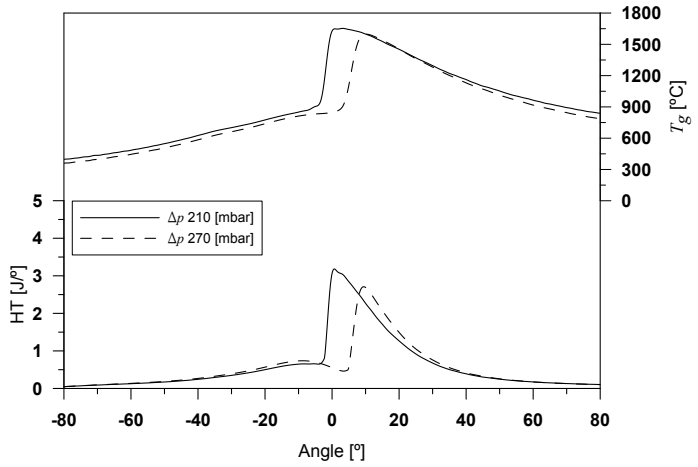

Figure 6.52. *HT and T changes due to Δp variation in L1.*

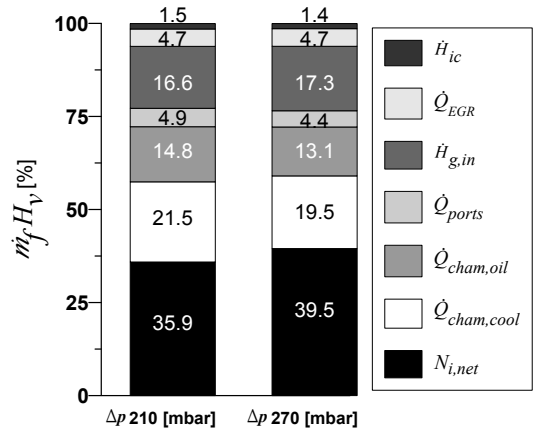

Figure 6.53. *GEB of Δp variation in L1.*

In the high Δp case, the explained in-cylinder HT reduction leads to an important heat rejection diminution in terms of $\dot{Q}_{cham,cool}$ and $\dot{Q}_{cham,oil}$ (about 2 and 1.7%$\dot{m}_f H_v$ respectively), as can be seen in Figure 6.53. This HT reduction, along with the changes in the RoHR, leads to about 3.6%$\dot{m}_f H_v$ higher $\eta_{i,net}$. In the case of $\dot{Q}_{ports}$, the lower exhaust temperature leads to a

reduction of $0.5\%\dot{m}_f H_v$, as shown in Figure 6.53. In spite of the lower exhaust temperature when increasing Δp, $\dot{H}_{g,in}$ is $0.7\%\dot{m}_f H_v$ higher due to the higher fresh mass flow.

It is interesting to highlight that at the measured conditions, $\dot{H}_{ic}$ was constant due to similar combustion efficiency in both cases. It was checked that further increase of Δp leads to lower combustion efficiency, higher combustion instability and misfire due to low temperature and auto-ignition issues [8].

Results on L2 point: similarly as for L1 point, when increasing Δp, the intake of fresh air and the sweep of burned gases are improved. Thus, as shown in Figure 6.54, the increase of Δp delays the combustion process even though at higher load the effect is smaller than in L1. As the scavenging process is enhanced by higher Δp, lower IGR rates are used; therefore, a slightly lower T evolution is observed during the whole cycle as shown in Figure 6.55, which results in a slightly lower HT.

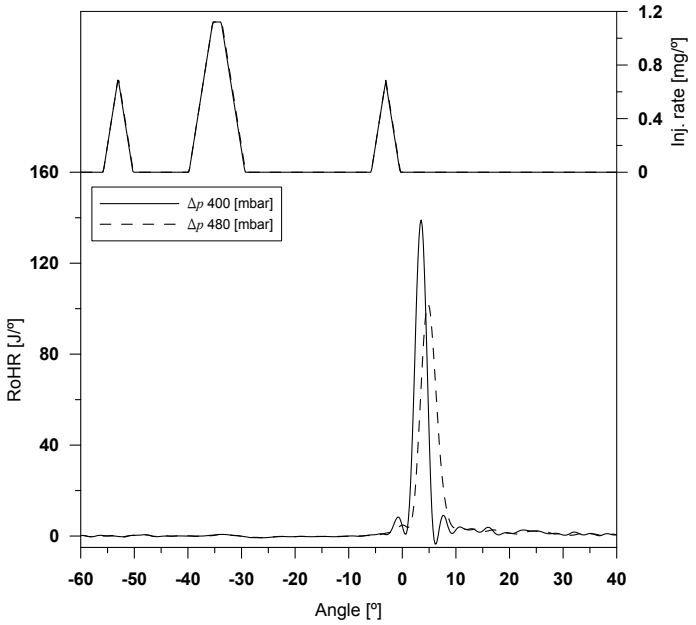

Figure 6.54. *RoHR shape due to Δp variation in L2.*

As can be seen in Figure 6.56, the better air management increases $\eta_{i,net}$ about $1.3\%\dot{m}_f H_v$. This is explained, on the one hand, by the lower HT to the

chamber walls ($\dot{Q}_{cham,cool}$ and $\dot{Q}_{cham,oil}$ about 0.5 and 0.3%$\dot{m}_f H_v$ lower), and on the other hand, by the lower $\dot{H}_{ic}$ about 1%$\dot{m}_f H_v$, which indicates a better combustion performance. Similarly as for L1, $\dot{Q}_{ports}$ is 0.2%$\dot{m}_f H_v$ lower due to lower exhaust temperature, and $\dot{H}_{g,in}$ is 0.4%$\dot{m}_f H_v$ higher due to higher air mass flow at intake.

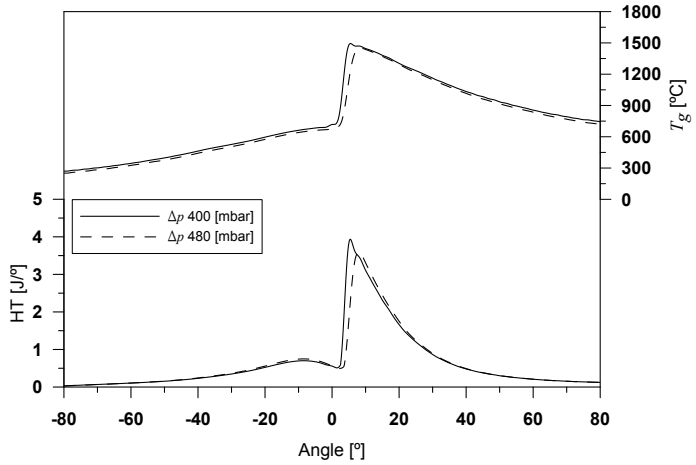

Figure 6.55. *HT and T changes due to Δp variation in L2.*

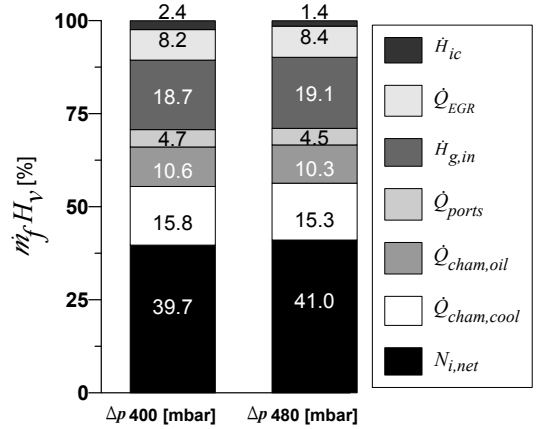

Figure 6.56. *GEB of Δp variation in L2.*

6.3.2.4 Predictive study on heat transfer reduction

After the analysis performed in the previous section, and taking into account that the HT sub-models were exhaustively calibrated for this engine as described in Section 6.3.1, a consequent next step is using the predictive tool SiCiclo to asses the potential of the tuned sub-models to evaluate the effect of HT on the engine efficiency, and the benefits obtained if HT is reduced.

From the analysis presented in the previous section, and bearing in mind that the indicated efficiency is mainly controlled by the RoHR shape and the HT to the chamber walls, the following observations can be highlighted:

- Further improvement of the combustion process in **Engine B** is hardly achievable by changes in the studied parameters (related with the injection setting and air management), which is principally due to the limited variation range.
- The instantaneous HT to the chamber walls reaches the highest values during expansion stroke; therefore, it is well known that reducing the HT during close cycle leads to higher instantaneous pressure evolution, and hence better indicated efficiency.

Attending to these comments, it was considered to evaluate the effect of the HT in the indicated cycle as well as in the GEB terms. For this reason, a predictive study that consists on gradually reduce the HT from the reference case to the ideal adiabatic cycle was performed. This study is carried out in the L2 operating point, whose main operating conditions are provided in Table 6.9 (more information can also be found in Table 6.6).

	SoI pilot [°ATDC]	SoI main [°ATDC]	SoI post [°ATDC]	p_{int} [bar]	p_{exh} [bar]	T_{int} [°C]	T_{exh} [°C]
L2	-60	-42	-10	1.7	1.3	47	414

Table 6.9. *Operation settings of L2 reference point used for the predictive study.*

The comparison between the reference and the adiabatic cycle (extreme conditions) is interesting to determine the upper limit of what can be achieved by reducing the HT. Thus, some simulations were performed with SiCiclo, using the HT constant adjusted in Section 6.3.1, and imposing adiabatic chamber

conditions. In order to take into account only heat rejection effects, the RoHR was assumed to be the same. The comparison of the indicated cycles is shown in Figure 6.57. The simulations confirm the expected improvement on the indicated work in the adiabatic case, as the pressure clearly increases during the expansion stroke as presented in Figure 6.58, and hence the area of the $p-V$ diagram increases. This pressure increase leads to higher gas temperature evolution as shown in Figure 6.57, thus affecting several terms of the GEB (e.g. the sensible enthalpy at exhaust and the HT to ports). Therefore, the analysis of the GEB is interesting to complete the evaluation of the HT reduction outcomes.

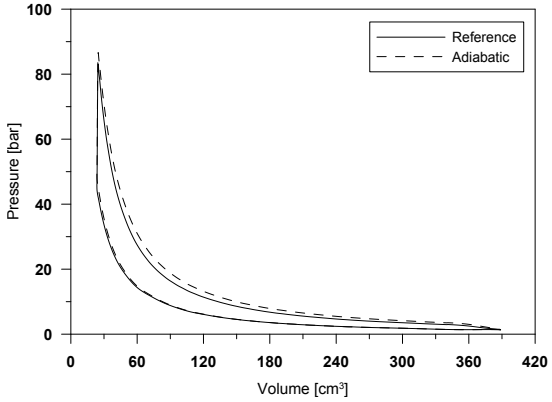

Figure 6.57. *$p-V$ diagramm.*

In order to obtain results in realistic cases, the HT was reduced at two intermediate levels between the reference and the adiabatic cases (33 and 67% of total HT to chamber). As the analysis is centred on the chamber process, some clarifications have to be made: on the one hand, the analysis is focused on the engine block, thus $\dot{H}_{g,ports}$ variation is analysed instead of $\dot{H}_{g,in}$. On the other hand, the combustion efficiency was assumed to be the same for all the simulations because SiCiclo is not able to model the combustion completeness, thus $\dot{H}_{ic}$ cannot be calculated.

The GEB results are presented in Table 6.10. It can be seen that the main terms changing are the indicated efficiency, the heat transfer to chamber ($\dot{Q}_{cham,cool}$ and $\dot{Q}_{cham,oil}$) and the exhaust enthalpy, whilst the HT to ports has a maximum increase about $1\%\dot{m}_f H_v$. The lower sensitivity of $\dot{Q}_{ports}$ in

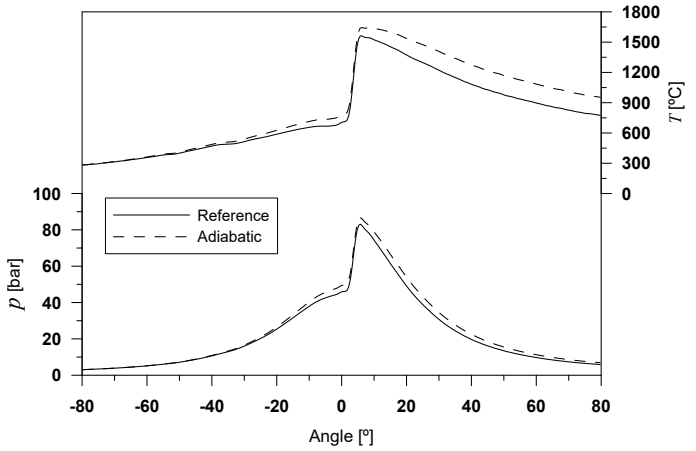

Figure 6.58. *p and T comparison between the reference and adiabatic cases.*

comparison with $\dot{Q}_{cham,cool}$ and $\dot{Q}_{cham,oil}$ is due to the fact that in the case of in-cylinder HT, both gas velocity and temperature are changing, while in the ports only temperature variations are taking place.

In Figure 6.59, the trends of the main terms are presented. As can be seen, in spite of the maximum reduction of $\dot{Q}_{cham}$ about $26\%\dot{m}_f H_v$, a maximum increment on the $\eta_{i,net}$ of $9\%\dot{m}_f H_v$ is achieved. This can be explained, on the one hand, because part of $\dot{Q}_{cham}$ reduction takes place during open cycle, thus only $22\%\dot{m}_f H_v$ corresponds to closed cycle, and on the other hand, assuming a thermal efficiency of the heat to power conversion similar as the indicated efficiency ($39\%\dot{m}_f H_v$), an approximated indicated efficiency improvement of $8.5\%\dot{m}_f H_v$ can be expected; the difference of this value with the simulated results is due to differences between the shape of the HT and the RoHR[11]. In the intermediate points studied, the $\eta_{i,net}$ increment ranges between 3 and $6\%\dot{m}_f H_v$ when reducing the HT between 33 and 66%. Finally, as only part of the HT recovery is converted in work, $\dot{H}_{g,ports}$ increases about $17\%\dot{m}_f H_v$ in the adiabatic case.

Summarizing, a potential improvement of $\eta_{i,net}$ between 3 and $6\%\dot{m}_f H_v$ can be achieved by reducing the HT in this engine. Apart from the gas velocity reduction (as tumble motion is necessary to maintain a suitable combustion

[11]The real benefits of reducing the HT can slightly differ from the results presented as a consequence of changes in the RoHR due to different in-cylinder conditions.

process), the heat rejection diminution can be attained following some of the techniques described in Chapter 2.3.3: through a proper thermal management or by using thermal barrier coatings on the combustion chamber. Moreover, the increase of the available energy at exhaust can be used to enhanced the turbocharging process or in organic regenerative cycles as commented in Chapters 2.3.2 and 2.4.4 respectively.

$\dot{Q}_{cham}$ reduction	$\Delta\eta_{i,net}$ $[\%\dot{m}_f H_v]$	$\Delta\dot{Q}_{cham,cool}$ $[\%\dot{m}_f H_v]$	$\Delta\dot{Q}_{cham,oil}$ $[\%\dot{m}_f H_v]$	$\Delta\dot{Q}_{ports}$ $[\%\dot{m}_f H_v]$	$\Delta\dot{H}_{g,ports}$ $[\%\dot{m}_f H_v]$
33%	2.4	-3.9	-2.6	-0.2	3.9
67%	5.3	-8.8	-6.1	-0.6	9.2
Adiabatic	8.9	-15.4	-10.9	-1.0	16.5

Table 6.10. *Variations of the GEB terms when reducing the HT to the chamber.*

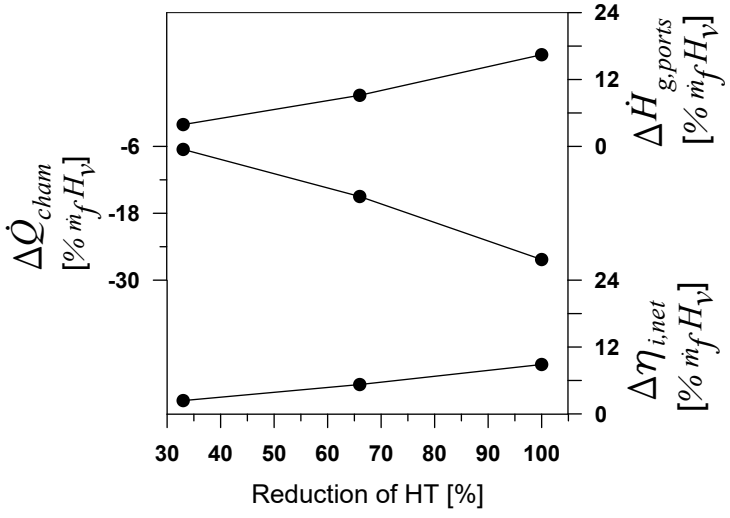

Figure 6.59. *Variation on the GEB parameters due to reduction of the HT.*

6.4 Summary and conclusions

To ensure a suitable HT estimation to perform the GEB, CALMEC and SiCiclo sub-models required calibration prior to be used in a specific engine. For this reason, a global HT calibration methodology has been proposed:

1. **HT to the chamber walls calibration.** In this step, two processes were iteratively performed: on the one hand, the *Engine characterization* (using motoring tests) to obtain some uncertain parameters that affect the in-cylinder conditions calculation[12]. On the other hand, the calibration of the HT to the chamber walls (using combustion tests) with the criterion of reducing the difference between ACE and η_{comb}.

2. **HT to ports / during open cycle calibration.** This step consists on the tuning of the convective HT model to ports (case of **Engine A**) or the HT during open cycle (case of **Engine B**), aimed at reducing the difference between experimental and modelled $\dot{Q}_{tot}$.

3. **Mechanical losses calibration.** The mechanical losses sub-models were adjusted to reduce the deviation from $(N_{fr} + N_a)_{exp}$. This process was only performed for **Engine A**, taking into account that the studies carried out in **Engine B** are aimed at the indicated cycle optimization, thus the analysis of the mechanical losses was not relevant.

4. **HT from oil to coolant calibration.** Once all the models were adjusted, this last term was calibrated with the criterion of reducing the differences between experimental and modelled $\dot{Q}_{oil}$. This step was only carried out in **Engine A**.

After the complete sub-models calibration, the GEB was performed and analysed in **Engine A** map. To improve the analysis, a combination of experimental and modelled results was used. Following, the most noticeable results are presented:

– η_i mainly depends on the engine speed (having a limited variation with load) ranging between $38\%\dot{m}_f H_v$ at low speed and $46\%\dot{m}_f H_v$ at high speed. This behaviour is mainly explained by the reduction of the HT

[12] i.e. CR, k_{def}, $\Delta\alpha_{\text{TDC}}$ and C_{w1}, as described in Chapter 5.3.1.

to the chamber with the speed and load; however, the HT reduction is partially compensated by the increase of the combustion duration when the load increases, which is due to changes in the injection settings and air management; therefore, no clear variation of η_i were observed with the load.

- η_b ranges between 30-38%$\dot{m}_f H_v$, reaching its maximum at mid-speed and high load. This is explained as the combination of two main trends: the higher η_i at higher engine speeds and the higher η_m at lower engine speeds and higher loads.

- The relative trends observed in the HT to coolant are mainly explained by the detailed repartition of HT to the chamber walls and ports. $\dot{Q}_{cool}$ tends to decrease with the speed similarly as $\dot{Q}_{lin}$ and $\dot{Q}_{ch}$; however, it is less dependent on the load than these terms due to the lower sensitivity of $\dot{Q}_{ports}$ to load variations. Therefore, $\dot{Q}_{cool}$ variates between 28%$\dot{m}_f H_v$ at low speed and 18%$\dot{m}_f H_v$ at high speed.

- $\dot{Q}_{oil}$ decreases from 9%$\dot{m}_f H_v$ (at low speed and load) to 4%$\dot{m}_f H_v$ (at high speed and load). This trend is explained mainly by $\dot{Q}_{pis}$. The difference between these terms is due to the heat rejection from oil to coolant.

- The difference between $\dot{H}_{g,ports}$ and $\dot{H}_{g,in}$ is explained by $\dot{Q}_{\mathrm{EGR}}$; therefore, up to mid speed and load both reach similar values (as no EGR strategy was used). Similarly, the difference between $\dot{H}_{g,in}$ and $\dot{H}_{g,ex}$ is explained by $\dot{Q}_a$, being specially important at high speed, where the air cooling demand is higher.

  The relative weight of these net sensible enthalpies mainly increase with the engine speed, thus $\dot{H}_{g,ports}$, $\dot{H}_{g,in}$ and $\dot{H}_{g,ex}$ variate between 22-42%$\dot{m}_f H_v$, 18-40%$\dot{m}_f H_v$ and 16-34%$\dot{m}_f H_v$ respectively.

- $\dot{Q}_{misc}$ has values between 2 and 14%$\dot{m}_f H_v$, explained mainly by $\dot{Q}_{ext}$. However, the higher $\dot{Q}_{misc}$ at low speed and load is explained by the higher experimental uncertainty at these conditions.

In the case of **Engine B**, two operating points at a fixed speed and low and mid loads (L1 and L2) were chosen. Variations of the injection settings (post and main injection) as well as in the difference between exhaust and intake pressures (Δp) were performed. Some remarkable results obtained from these parametric studies are:

- Delaying the post injection in L1 reduces the HT but has low effect on η_i because of the changes in the combustion and the increase of $\dot{H}_{ic}$. Hence, the exhaust enthalpy $\dot{H}_{g,in}$ increases. In the case of L2, the reduction of HT is even higher, thus leading to an η_i improvement about $0.8\%\dot{m}_f H_v$.
- Delaying the main injection in L1 reduces the HT and $\dot{H}_{ic}$, thus obtaining $1.4\%\dot{m}_f H_v$ higher η_i. Despite this improvement in L1, delaying the main injection in L2 did not change significantly the combustion process; thus, a $0.5\%\dot{m}_f H_v$ higher η_i was achieved as the addition slightly lower $\dot{H}_{ic}$ and HT.
- Increasing Δp leads to lower HT, which leads to increase η_i about 3.6 and $1.3\%\dot{m}_f H_v$ in points L1 and L2 respectively. In spite of reducing the exhaust temperature, slightly higher levels of $\dot{H}_{g,in}$ were observed as consequence of the higher mass flow at exhaust.

With this analysis, the potential of using the GEB has been shown in diagnosis applications at different engines and parametric studies. Finally, the tuned sub-models and the GEB analysis have been applied in a predictive application on **Engine B**. Considering that improvements in the RoHR or air management are hardly attainable in **Engine B**, and taking into account that the HT sub-models were comprehensively calibrated, a predictive study with SiCiclo to assess the potential increment of η_i by reducing the HT was performed. In this study, variations of the HT from a reference point (L2) to the ideal adiabatic cycle were carried out.

It was observed that, a maximum $\dot{Q}_{cham}$ reduction about $26\%\dot{m}_f H_v$ leads to $9\%\dot{m}_f H_v$ higher $\eta_{i,net}$; thus, about 35% of the HT reduction becomes engine efficiency and the remaining is lost as sensible enthalpy at the exhaust. In more realistic conditions, reducing the HT to chamber about 33 and 67% leads to $\eta_{i,net}$ increments between 3 and $6\%\dot{m}_f H_v$.

As a final conclusion, it can be stated that the GEB and the methodology to adjust the sub-models provide a set of useful tools to characterize and analyse the energy split in different engine hardware and settings configuration, including diagnosis and predictive applications.

Bibliography

[1] Martín J. *Diagnóstico de la combustión en motores de Diesel de inyección directa*. Reverté, ISBN 978-84-291-4717-9, Barcelona, 2012.

[2] Kouremenos D.A., Rakopoulos C.D., Hountalas D.T. and Zannis T.K. "Development of a Detailed Friction Model to Predict Mechanical Losses at Elevated Maximum Combustion Pressures". *SAE Technical Paper 2001-01-0333*, 2001.

[3] Heywood J.B. *Internal Combustion Engines Fundamentals*. McGraw-Hill, ISBN 978-0-07-028637-5, New York, 1988.

[4] Taraza D. and Henein N. "Friction Losses in Multi-Cylinder Diesel Engines". *SAE Technical Paper 2000-01-0921*, 2000.

[5] Comfort A. "An Introduction to Heavy-Duty Diesel Engine Frictional Losses And Lubricant Properties Affecting Fuel Economy - Part I". *SAE Technical Paper 2003-01-3225*, 2003.

[6] Payri F. and J.M. Desantes. *Motores de combustión interna alternativos*. Reverté, ISBN 978-84-291-4802-2, Barcelona, 2011.

[7] Benajes J., Olmeda P., Martín J. and Carreño R. "A new methodology for uncertainties characterization in combustion diagnosis and thermodynamic modelling". *Applied Thermal Engineering*, Vol. 71, pp. 389–399, 2014.

[8] Benajes J., Martín J., Novella R. and De Lima D. "Analysis of the Load Effect on the Partially Premixed Combustion Concept in a 2-Stroke HSDI Diesel Engine Fueled with Conventional Gasoline". *SAE Techinical Paper 2014-01-1291*, 2014.

[9] Benajes J., Martín J., Novella R. and Thein K. "Understanding the performance of the multiple injection gasoline partially premixed combustion concept implemented in a 2-Stroke high speed direct injection compression ignition engine". *Applied Energy*, Vol. 161, pp. 465–475, jan 2016.

[10] Molina S., García A., Pastor J.M., Belarte E. and Balloul I. "Operating range extension of RCCI combustion concept from low to full load in a heavy-duty engine". *Applied Energy*, Vol. 143, pp. 211–227, 2015.

Chapter 7

Conclusions and future works

Contents

7.1 Conclusions

Taking into account the consumption and emissions trade-off, the main strategies developed during last decades to control emissions in RICEs and their effects on engine efficiency have been exhaustively evaluated. As a result of the continuous RICE improvement, the in-cylinder process optimization has

reached a development level in which further emissions reduction is barely attainable through controlling in-cylinder conditions with conventional methods. Therefore, the use of aftertreatment systems has become a common solution. This generalized use of aftertreatment systems along with the climatic change awareness have moved the research interest towards the optimization of the RICE operation to reach the maximum efficiency.

The thermal balances have gained relevance since they are used to evaluate the actual thermo-fluid-dynamic processes and to obtain reliable predictive information regarding the engine thermal behaviour when using a particular strategy. However, the thermal balances found in the literature use a simple approach to analyse the thermal balance, usually taking into account only the brake efficiency, the total heat rejection and the exhaust losses, and in few cases, the unburned fuel. The simplicity of these approaches can be justified considering the complexity of the experimental measurement of the energy terms and the difficulty of developing and calibrating accurate models. From this literature review, two general observations can be highlighted:

1. *There is a lack of works proposing a global methodology to perform and analyse the thermal balance.*

2. *It is necessary to develop a global strategy to perform a comprehensive analysis of the energy balance, taking into account experimental and modelling tools to obtain all the energy terms.*

Therefore, the work presented in this thesis is aimed at **the development of a comprehensive methodology to perform and analyse the energy balance in reciprocating engines**. To accomplish this purpose, the previous works of Tinaut [1], Armas [2], Degraeuwe [3], Martín [4] and García [5] have been used as a starting point. The cited works have provided the reference thermodynamic model that includes the required sub-models to perform the combustion diagnosis (CALMEC) and the cycle simulation (SiCiclo).

To fulfil the main aim of this thesis, 4 particular objectives were stated in Chapter 1.3:

1. *Proposing a comprehensive thermal balance methodology that allows determining and analysing all the energy terms.*

2. *Developing the necessary sub-models to complete a comprehensive thermal balance.*

3. *Proposing a methodology for the calibration of the sub-models.*

4. *Showing the potential of the calibrated sub-models and the energy balance methodology through their application on different engines.*

In the following sections, the most relevant findings made for each objective will be highlighted.

7.1.1 Conclusions regarding the comprehensive thermal balance methodology that allows determining and analysing all the energy terms

A comprehensive methodology to perform and analyse the thermal balance, called **Global Energy Balance** (GEB), has been proposed. The GEB considers two points of view:

- **External Global Energy Balance** (EGEB): it considers the main energy flows through the engine, based mostly on experimental information.

- **Internal Global Energy Balance** (IGEB): a detailed description of the energy split due to engine internal interactions has been presented. It is based mostly on modelling work, but some experimental variables are also used, being the in-cylinder pressure the most important.

Along with these GEB definitions, some equivalent terms between them have been defined through a proper consideration of the energy repartition. In particular, the experimental and modelled total heat transfer ($\dot{Q}_{tot,exp}$ and $\dot{Q}_{tot,mod}$), heat transfer to coolant ($\dot{Q}_{cool,exp}$ and $\dot{Q}_{cool,mod}$) and heat transfer to oil ($\dot{Q}_{oil,exp}$ and $\dot{Q}_{oil,mod}$) have been presented as key terms for the GEB models calibration and results validation.

To determine the reliability of the experimental work, an uncertainty analysis of the most relevant terms has been performed. It has been concluded that the most uncertain parameter in terms of the fuel energy is the heat transfer to the coolant ($\dot{Q}_{cool}$), whose uncertainty reaches values up to

$2\%\dot{m}_f H_v$ at low speed and load. This relative high uncertainty confirmed the importance of defining $\dot{Q}_{tot,exp}$ based on less uncertain experimental parameters. The rest of the terms analysed have lower uncertainty in terms of the fuel energy, showing most of them values lower than $0.5\%\dot{m}_f H_v$.

7.1.2 Conclusions regarding the development of the necessary sub-models to complete a comprehensive thermal balance

To perform the IGEB, the modelling of some energy terms is necessary; therefore, several sub-models of CALMEC and SiCiclo have been improved and new ones developed:

- **HT model for engines with tumble motion:** a model that considers the tumble motion effect on the HT has been developed based on the analysis of CFD simulations. Then, the experimental calibration was performed with skip-fire tests and the model performance was checked in combustion tests, showing a significant improvement in comparison with the reference swirl model.

- **HT to ports:** a new model to determine the HT to ports has been proposed. This model takes into consideration the high gas velocity and temperature variations in the exhaust ports during the open cycle, when about 90% of the total HT to ports takes place. Therefore, a 0D quasi-steady model that considers the instantaneous evolution of the heat transfer coefficient and gas temperature has been developed.

- **Heat transfer from oil to coolant:** to determine the heat transfer between oil and coolant, a simple lumped model that considers the thermal resistances of the oil, coolant and engine material has been proposed.

- **Uncertainties adjustment:** an adjustment methodology to determine some uncertain parameters (i.e. CR, k_{def}, $\Delta\alpha_{\mathrm{TDC}}$ and C_{w1}), called *Engine characterization*, has been developed. This methodology is based on MLR and the sensitivity analysis of each parameter on the RoHR and the simulated pressure.

- **Mechanical losses model:** as the determination of HT to coolant and oil requires detailed friction and auxiliary modelling, specific sub-models

to calculate the friction between piston pack and liner, bearings and valve train have been proposed. Likewise, simple sub-models to estimate the coolant, oil, and fuel pumps power have been provided.

7.1.3 Conclusions regarding the methodology for the calibration of the sub-models

To ensure accurate HT estimation, the sub-models developed and included in CALMEC and SiCiclo have to be calibrated. Thus, an integral methodology has been proposed, which follows the next steps:

1. HT to the chamber walls calibration, which consists on performing the *Engine characterization* and the HT model refinement with combustion tests.
2. HT to the ports calibration or HT during open cycle calibration.
3. Mechanical losses calibration.
4. HT from oil to coolant calibration.

7.1.4 Conclusions regarding the potential of the calibrated sub-models and the energy balance methodology through their application on different engines

After the adjustment of the sub-models, the GEB was performed in the map of **Engine A**, concluding that:

- η_i depends mainly on the engine speed, ranging between $38\%\dot{m}_f H_v$ at low speed and $46\%\dot{m}_f H_v$ and high speed. Its behaviour has been explained by the reduction of $\dot{Q}_{cham,cc}$ and the increase of combustion duration when increasing the load.
- η_b ranges between 30-$38\%\dot{m}_f H_v$, reaching its maximum at mid-speed and high load. Its behaviour has been explained by η_i and the mechanical efficiency.
- The relative trends observed in $\dot{Q}_{cool}$ are explained by $\dot{Q}_{lin}$, $\dot{Q}_{ch}$ and $\dot{Q}_{ports}$. Therefore, $\dot{Q}_{cool}$ mainly depends on the speed, ranging between $28\%\dot{m}_f H_v$ at low speed and $18\%\dot{m}_f H_v$ at high speed.

- The trends of $\dot{Q}_{oil}$ are explained by $\dot{Q}_{pis}$, where the difference between these terms is due to the heat rejection from oil to coolant. Hence, $\dot{Q}_{oil}$ decreases from $9\%\dot{m}_f H_v$ (at low speed and load) to $4\%\dot{m}_f H_v$ (at high speed and load).

- The relative weight of $\dot{H}_{g,ex}$ ranges between 16 and $34\%\dot{m}_f H_v$ depending on the engine speed. This trend is similar as that of $\dot{H}_{g,in}$ and $\dot{H}_{g,ports}$, being their differences explained by $\dot{Q}_{\mathrm{EGR}}$ and $\dot{Q}_a$.

- $\dot{Q}_{misc}$ has values between 2 and $14\%\dot{m}_f H_v$, explained mainly by $\dot{Q}_{ext}$ and the higher experimental uncertainty at low speed and load.

In the case of **Engine B**, parametric studies of post injection, main injection, and Δp were carried out in two operating points (L1 and L2). Starting from the in-cylinder conditions and the RoHR analysis, the changes of the specific energy repartition were justified; thus, analysing how the injection setting and air management affect the HT and efficiency in this 2-stroke engine. In general, the reduction of the HT leads to η_i increase; however, the different thermodynamic conditions at each load and the variations of $\dot{H}_{ic}$ and RoHR made necessary the GEB to explain the behaviour of PPC operation.

As further improvement of the RoHR with the parameters studied is hardly attainable, the potential of increasing η_i by reducing the HT has been assessed by means of a simulation study performed with SiCiclo. It consisted on variations of the HT from a reference point (L2) to the ideal adiabatic cycle.

In the adiabatic case, it was observed that the maximum $\dot{Q}_{cham}$ reduction ($26\%\dot{m}_f H_v$) leads to $9\%\dot{m}_f H_v$ higher $\eta_{i,net}$; thus, about 35% of the HT reduction can be recovered as engine efficiency, being the remaining part lost as sensible enthalpy at exhaust. In more realistic conditions, reducing the HT to chamber about 33 and 67% leads to $\eta_{i,net}$ increments between 3 and $6\%\dot{m}_f H_v$.

With the finalization of the studies in **Engine A** and **Engine B**, **the potential of the methodology to calibrate, perform and analyse the Global Energy Balance has been demonstrated**. The analysis and calibration methodologies described in this thesis are flexible enough to be applied in different types of engines and combustion modes, showing its usefulness for both diagnostic and predictive applications.

7.2 Future works

As final contribution of this work, the potential improvements and future works according to the author point of view are commented. As can be seen, the work done in this thesis was dedicated to the methodological description of *how to perform* and *how to analyse* the GEB. An important effort was made to provide all the sub-models required to determine the IGEB in different types of engines. At the current state of this work, it can be applied to perform complete combustion and thermal diagnosis, providing interesting insights of the engine process.

Notwithstanding, it seems that this thesis is the first step of a deeper development process, taking into account that the strategies to improve the RICE efficiency are not directly derived from the results shown in this work, beyond a brief application in **Engine B**. In this regard, the dual diagnosis-predictive approach can be improved in a next step. Thus, some improvement works for the predictive tool SiCiclo are proposed:

1. The analysis of the effects of different strategies on the engine efficiency should be improved by considering the effect of the in-cylinder conditions on the RoHR. This is highly important, as most of the strategies used to improve the engine efficiency will affect the combustion process (i.e. the RoHR).

2. In this work, emissions have not been considered; however, from the predictive point of view, it would be interesting to combine consumption and emissions for a complete analysis. Thus, including a model in SiCiclo to take into account the NO_x formation within the chamber would be very useful. This would allow establishing boundaries for the simulation studies or multi-objective optimization.

3. Optimization algorithms can be included. The potential of the predictive results would benefit from a mathematical model that allows determining optimum parameters.

As commented in Chapter 2.4, it is interesting to highlight the benefits of using the GEB analysis for the development of the future engine concepts. In particular, the tool presented in this work could allow a comprehensive energy analysis of emerging technologies, like some advanced engine architectures (e.g. variable valve actuation, opposed piston engines, etc.). To use the GEB

methodology, a prior adaptation of the tool is required, as an example, hybrid powertrains require an important modelling work to make this tool suitable for their diagnosis. In this regard, the methodology described in this work could be extended to include the electric parts (battery packs, electric motor, etc.), which would allow performing a complete thermal diagnosis and predictive optimization of this kind of powertrains.

As conclusions, the author's proposals are to extend the GEB methodology to take into account emerging engine technologies, such as hybrid powertrains, and to update the predictive tool SiCiclo regarding the combustion law and NO_x emissions simulation. SiCiclo can be used together with CALMEC to achieve a **complete RICEs diagnosis/predictive analysis tool** with higher potential to determine engine improvement paths.

Bibliography

[1] Tinaut F. *Contribución al estudio del proceso de combustión en motores de encendido por compresión de inyección directa*. Ph.D. Thesis, Universidad Politécnica de Valencia, 1986.

[2] Armas O. *Diagnóstico experimental del proceso de combustión en motores Diesel de inyección directa*. Servicio de Publicaciones UPV, ISBN 84-7721-772-X, Valencia, 1999.

[3] Degraeuwe B. *Contribution to the thermal management of DI Diesel engines*. Ph.D. Thesis, Universidad Politécnica de Valencia, 2007.

[4] Martín J. *Diagnóstico de la combustión en motores de Diesel de inyección directa*. Reverté, ISBN 978-84-291-4717-9, Barcelona, 2012.

[5] García D. *Aportación al modelado de emisiones y consumo basado en la señal de presión en el cilindro en motores Diesel*. Ph.D. Thesis, Universidad Politécnica de Valencia, 2016.

Bibliographic Index

Abd-Alla G.H. and Abdalla G.
Using exhaust gas recirculation in internal combustion engines: a review.
Energy Conversion and Management, Vol. 43 n^o 8, pp. 1027–1042, 2002. (cited in p. 16)

Abedin M.J., Masjuki H.H., Kalam M.A., Sanjid A. and Ashraful A.M.
Combustion, performance, and emission characteristics of low heat rejection engine operating on various biodiesels and vegetable oils.
Energy Conversion and Management, Vol. 85, pp. 173–189, September 2014.
(cited in pp. 31, 32, 43, 44, 50)

Abedin M.J., Masjuki H.H., Kalam M.A., Sanjid A., Rahman S.M. and Masum B.M.
Energy balance of internal combustion engines using alternative fuels.
Renewable and Sustainable Energy Reviews, Vol. 26, pp. 20–33, October 2013.
(cited in p. 43)

Abedin M.J., Masjuki H.H., Kalam M.A., Varman M., Arbab M.I., Fattah I.M. and Masum B.M.
Experimental investigation of a multicylinder unmodified diesel engine performance, emission, and heat loss characteristics using different biodiesel blends: rollout of B10 in Malaysia.
The Scientific World Journal, Vol. 2014 n^o 349858, pp. 9 pages, January 2014.
(cited in p. 44)

Achuth M. and Mehta P.S.
Predictions of tumble and turbulence in four-valve pentroof spark ignition engines.
International Journal of Engine Research, Vol. 2 n^o 3, pp. 209–227, January 2001.
(cited in p. 18)

Agarwal A.K., Srivastava D.K., Dhar A., Maurya R.K., Shukla P.C. and Singh A.P.

Effect of fuel injection timing and pressure on combustion, emissions and performance characteristics of a single cylinder diesel engine.
Fuel, Vol. 111, pp. 374–383, September 2013. (cited in p. 18)

Aghdam E.A. and Kabir M.M.
Validation of a blowby model using experimental results in motoring condition with the change of compression ratio and engine speed.
Experimental Thermal and Fluid Science, Vol. 34 n^o 2, pp. 197–209, February 2010.
(cited in p. 111)

Aichlmayr H.T., Kittelson D.B. and Zachariah M.R.
Miniature free-piston homogeneous charge compression ignition engine-compressor concept-Part I: performance estimation and design considerations unique to small dimensions.
Chemical Engineering Science, Vol. 57 n^o 19, pp. 4161–4171, oct 2002. (cited in p. 36)

Ajav E.A., Singh B. and Bhattacharya T.K.
Thermal balance of a single cylinder diesel engine operating on alternative fuels.
Energy Conversion and Management, Vol. 41 n^o 14, pp. 1533–1541, September 2000. (cited in pp. 44, 50)

Alasfour F.N.
Butanol–A single-cylinder engine study: availability analysis.
Applied Thermal Engineering, Vol. 17 n^o 6, pp. 537–549, June 1997. (cited in pp. 44, 50)

Aleklett K. and Campbell C.
The Peak and Decline of World Oil and Gas Production.
Minerals & Energy - Raw Materials Report, Vol. 18 n^o 1, pp. 5–20, 2003. (cited in p. 2)

Alkidas A.C.
Combustion advancements in gasoline engines.
Energy Conversion and Management, Vol. 48 n^o 11, pp. 2751–2761, November 2007. (cited in p. 23)

Allen D.J. and Lasecki M.P.
Thermal Management Evolution and Controlled Coolant Flow.
SAE Techinical Paper 2001-01-1732, 2001. (cited in pp. 27, 28)

Andrews G., Ounzain A., Li H., Bell M., Tate J. and Ropkins K.
The Use of a Water/Lube Oil Heat Exchanger and Enhanced Cooling Water Heating to Increase Water and Lube Oil Heating Rates in Passenger Cars for Reduced Fuel Consumption and CO2 Emissions During Cold Start.
SAE Techinical Paper 2007-01-2067, 2007. (cited in pp. 28, 29)

Ångström H.
Cylinder pressure indicating with multiple transducer, accurate TDC evaluating, zero levels and analysis of mechanical vibrations.
3 Internationales Indiziersymposium, pp. 103–108, 1998. (cited in p. 205)

Annand W.J.D.
Heat transfer in the cylinders of reciprocating internal combustion engines.
Proc. Inst. Mech. Engrs., Vol. 177, pp. 973–990, 1963. (cited in p. 102)

Aoyama T., Hattori Y., Mizuta J. and Sato Y.
An Experimental Study on Premixed-Charge Compression Ignition Gasoline Engine.
SAE Techinical Paper 960081, 1996. (cited in p. 23)

Arata T., Novi N., Ariga K., Yamashita A. and Armenio G.
Development of a Two-Stage Variable Displacement Vane Oil Pump.
SAE Techinical Paper 2012-01-0408, 2012. (cited in p. 34)

Armas O.
Diagnóstico experimental del proceso de combustión en motores Diesel de inyección directa.
Servicio de Publicaciones UPV, ISBN 84-7721-772-X, Valencia, 1999.
(cited in pp. 5, 78, 89, 93, 102, 112, 334)

Armas O., Rodríguez J., Payri F., Martín J. and Agudelo J.R.
Effect of the trapped mass and its composition on the heat transfer in the compression cycle of a reciprocating engine.
Applied Thermal Engineering, Vol. 25 n^o 17-18, pp. 2842–2853, December 2005. (cited in p. 86)

Aronsson U., Solaka H., Chartier C., Andersson O. and Johansson B.
Impact of Mechanical Deformation Due to Pressure, Mass, and Thermal Forces on the In-Cylinder Volume Trace in Optical Engines of Bowditch Design.
SAE Technical Paper 2011-26-0082, 2011. (cited in pp. 112, 204)

Arrègle J., López J.J., García J.M. and Fenollosa C.
Development of a zero-dimensional Diesel combustion model. Part 1: Analysis of the quasi-steady diffusion combustion phase.
Applied Thermal Engineering, Vol. 23 n^o 11, pp. 1301–1317, August 2003. (cited in p. 108)

Arrègle J., López J.J., García J.M. and Fenollosa C.
Development of a zero-dimensional Diesel combustion model Part 2: Analysis of the transient initial and final diffusion combustion phases.
Applied Thermal Engineering, Vol. 23 n^o 11, pp. 1319–1331, August 2003. (cited in p. 108)

ASTM.
Standard Test Method for Heat of Combustion of Liquid Hydrocarbon Fuels by Bomb Calorimeter.
ASTM Standards D240, 2002. (cited in p. 143)

Babiak Z., Wenz T. and Engl L.
Fundamentals of Thermal Spraying , Flame and Arc Spraying.
In Bach F., Laarmann A. and Thomas W., editors, *Modern Surface Technology*, chapter 8, pp. 119–136. Wiley-VCH Verlag GmbH & Co. KGaA, ISBN 978-3-527-31532-1, Weinheim, 2006. (cited in p. 31)

Badami M., Mallamo F., Millo F. and Rossi E.E.
Influence of Multiple Injection Strategies on Emissions , Combustion Noise and BSFC of a DI Common Rail Diesel Engine.
SAE Technical Paper 2002-01-0503, 2002. (cited in p. 18)

Bari S. and Saad I.
CFD modelling of the effect of guide vane swirl and tumble device to generate better in-cylinder air flow in a CI engine fuelled by biodiesel.
Computers & Fluids, Vol. 84, pp. 262–269, September 2013. (cited in p. 25)

Beatrice C., Di Iorio S., Guido C. and Napolitano P.
Detailed characterization of particulate emissions of an automotive catalyzed DPF using actual regeneration strategies.
Experimental Thermal and Fluid Science, Vol. 39, pp. 45–53, May 2012. (cited in p. 20)

Beck N.J. and Uyehara O.A.
Factors That Affect BSFC and Emissions for Diesel Engines : Part II Experimental Confirmation of Concepts Presented in Part I.
SAE Techinical Paper 870344, 1987. (cited in p. 23)

Bedoya I.D., Saxena S., Cadavid F.J., Dibble R.W. and Wissink M.
Experimental evaluation of strategies to increase the operating range of a biogas-fueled HCCI engine for power generation.
Applied Energy, Vol. 97, pp. 618–629, September 2012. (cited in p. 23)

Belarte E.
Estudio del proceso de combustión premezclada controlada por la reactividad del combustible en un motor de encendido por compresión.
Ph.D. Thesis, Universitat Politècnica de València, 2015. (cited in p. 24)

Beloiu D.
Modeling and Analysis of Valve Train , Part I - Conventional Systems.
SAE Technical paper 2010-01-1198, 2010. (cited in pp. 230, 264)

Benajes J., Martín J., Novella R. and De Lima D.
Analysis of the Load Effect on the Partially Premixed Combustion Concept in a 2-Stroke HSDI Diesel Engine Fueled with Conventional Gasoline.
SAE Techinical Paper 2014-01-1291, 2014. (cited in pp. 312, 323)

Benajes J., Martín J., Novella R. and Thein K.
Understanding the performance of the multiple injection gasoline partially premixed combustion concept implemented in a 2-Stroke high speed direct injection compression ignition engine.
Applied Energy, Vol. 161, pp. 465–475, jan 2016. (cited in pp. 16, 23, 26, 312)

Benajes J., Molina S., García A., Belarte E. and Vanvolsem M.
An investigation on RCCI combustion in a heavy duty diesel engine using in-cylinder blending of diesel and gasoline fuels.
Applied Thermal Engineering, Vol. 63 n^o 1, pp. 66–76, feb 2014. (cited in p. 24)

Benajes J., Molina S., García A., Belarte E. and Vanvolsem M.
An investigation on RCCI combustion in a heavy duty diesel engine using in-cylinder blending of diesel and gasoline fuels.
Applied Thermal Engineering, Vol. 63 n^o 1, pp. 66–76, February 2014. (cited in p. 217)

Benajes J., Molina S., García A. and Monsalve-Serrano J.
Effects of direct injection timing and blending ratio on RCCI combustion with different low reactivity fuels.
Energy Conversion and Management, Vol. 99, pp. 193–209, jul 2015. (cited in p. 24)

Benajes J., Molina S., García A. and Monsalve-Serrano J.
Effects of low reactivity fuel characteristics and blending ratio on low load RCCI (reactivity controlled compression ignition) performance and emissions in a heavy-duty diesel engine.
Energy, Vol. 90, pp. 1261–1271, oct 2015. (cited in pp. 24, 44, 50)

Benajes J., Molina S., Garcia J.M. and Riesco J.M.
The effect of swirl on combustion and exhaust emissions in heavy-duty diesel engines.
Proceedings of the Institution of Mechanical Engineers, Part D: Journal of Automobile Engineering, Vol. 218 n^o 10, pp. 1141–1148, 2004. (cited in p. 25)

Benajes J., Molina S., Novella R. and De Lima D.
Implementation of the Partially Premixed Combustion concept in a 2-stroke HSDI diesel engine fueled with gasoline.
Applied Energy, Vol. 122, pp. 94–111, jun 2014. (cited in p. 23)

Benajes J., Novella R., De Lima D., Tribotté P., Quechon N., Obernesser P. and Dugue V.
Analysis of the combustion process, pollutant emissions and efficiency of an innovative 2-stroke HSDI engine designed for automotive applications.
Applied Thermal Engineering, Vol. 58 n^o 1-2, pp. 181–193, September 2013.
(cited in pp. 16, 18, 25, 26)

Benajes J., Olmeda P., Martín J. and Carreño R.
A new methodology for uncertainties characterization in combustion diagnosis and thermodynamic modelling.
Applied Thermal Engineering, Vol. 71, pp. 389–399, 2014. (cited in pp. 112, 182, 309)

Benajes J., Pastor J.V., García A. and Monsalve-Serrano J.
An experimental investigation on the influence of piston bowl geometry on RCCI performance and emissions in a heavy-duty engine.
Energy Conversion and Management, Vol. 103, pp. 1019–1030, oct 2015.
(cited in pp. 24, 44)

Benajes J., Pastor J.V., García A. and Monsalve-Serrano J.
The potential of RCCI concept to meet EURO VI NOx limitation and ultra-low soot emissions in a heavy-duty engine over the whole engine map.
Fuel, Vol. 159, pp. 952–961, nov 2015. (cited in p. 24)

Bendu H. and Murugan S.
Homogeneous charge compression ignition (HCCI) combustion: Mixture preparation and control strategies in diesel engines.
Renewable and Sustainable Energy Reviews, Vol. 38, pp. 732–746, October 2014.
(cited in p. 23)

Bermúdez V., Luján J.M., Climent H. and Campos D.
Assessment of pollutants emission and aftertreatment efficiency in a GTDi engine including cooled LP-EGR system under different steady-state operating conditions.
Applied Energy, Vol. 158, pp. 459–473, nov 2015. (cited in p. 42)

Bermúdez V., Luján J.M., Piqueras P. and Campos D.
Pollutants emission and particle behavior in a pre-turbo aftertreatment light-duty diesel engine.
Energy, Vol. 66, pp. 509–522, March 2014. (cited in p. 20)

Bermúdez V., Lujan J.M., Pla B. and Linares W.G.
Effects of low pressure exhaust gas recirculation on regulated and unregulated gaseous emissions during NEDC in a light-duty diesel engine.
Energy, Vol. 36 n^o 9, pp. 5655–5665, 2011. (cited in p. 82)

Boulahlib M.S., Boukebbab S., Gaci F. and Kholai O.
Experimental Study of Energy Balance for Air-Cooled DI Diesel Engines Operating in Hot Climates.
SAE Techinical Paper 2009-01-1974, 2009. (cited in pp. 38, 42, 50)

Bourhis G., Chauvin J., Gautrot X. and de Francqueville L.
LP EGR and IGR Compromise on a GDI Engine at Middle Load.
SAE Int. J. Engines, Vol. 6 n^o 1, pp. 67–77, 2013. (cited in p. 16)

Brandl S., Graf B. and Rust A.
NVH Challenges and Solutions for Vehicles with Low CO2 Emission.
SAE Int. J. Passeng. Cars - Mech. Syst., Vol. 5 n^o 3, pp. 1084–1090, 2012.
(cited in p. 36)

Bression G., Soleri D., Savy S., Dehoux S., Azoulay D., Hamouda H., Doradoux L., Guerrassi N. and Lawrence N.
A Study of Methods to Lower HC and CO Emissions in Diesel HCCI.
SAE Int. J. Fuels Lubr., Vol. 1 n^o 1, pp. 37–49, 2009. (cited in pp. 16, 26)

Calabretta M., Cacciatore D. and Carden P.
Valvetrain Friction - Modeling, Analysis and Measurement of a High Performance Engine Valvetrain System.
SAE Int. J. Engines, Vol. 3 n^o 2, pp. 72–84, 2010. (cited in p. 234)

Cameron A.
Basic Lubrication Theory.
Longman, ISBN 978-0470275542, New York, 1971. (cited in p. 229)

Canakci M.
Combustion characteristics of a DI-HCCI gasoline engine running at different boost pressures.
Fuel, Vol. 96, pp. 546–555, June 2012. (cited in pp. 15, 16)

Cao X.Q., Vassen R. and Stoever D.
Ceramic materials for thermal barrier coatings.
Journal of the European Ceramic Society, Vol. 24 n^o 1, pp. 1–10, January 2004.
(cited in p. 30)

Caton J.A.
Comparisons of Thermocouple, Time-Averaged and Mass-Averaged Exhaust Gas Temperatures for a Spark-Ignited Engine.
SAE Techinical Paper 820050, 1982. (cited in p. 196)

Caton J.A.
Operating Characteristics of a Spark-Ignition Engine Using the Second Law of Thermodynamics : Effects of Speed and Load.
SAE Techinical Paper 2000-01-0952, 2000. (cited in pp. 38, 39, 41, 42, 50)

Caton J.A.
Implications of fuel selection for an SI engine: Results from the first and second laws of thermodynamics.
Fuel, Vol. 89 n^o 11, pp. 3157–3166, November 2010. (cited in pp. 44, 46, 50)

Caton J.A.
Thermodynamic Advantages of Low Temperature Combustion (LTC) Engines Using Low Heat Rejection (LHR) Concepts.
SAE Techinical Paper 2011-01-0312, 2011. (cited in p. 23)

Cernuschi F., Bianchi P., Leoni M. and Scardi P.
Thermal Diffusivity/Microstructure Relationship in Y-PSZ Thermal Barrier Coatings.
Journal of Thermal Spray Technology, Vol. 8 n^o 1, pp. 102–109, 1999. (cited in p. 30)

Chan S.H.
Performance and emissions characteristics of a partially insulated gasoline engine.
International Journal of Thermal Sciences, Vol. 40 n^o 3, pp. 255–261, March 2001. (cited in p. 31)

Chastain J.H. and Wagner J.R.
Advanced Thermal Management for Internal Combustion Engines - Valve Design , Component Testing and Block Redesign.
SAE Techinical Paper 2006-01-1232, 2006. (cited in p. 27)

Chau K.T., Wong Y.S. and Chan C.C.
An overview of energy sources for electric vehicles.
Energy Conversion and Management, Vol. 40 n^o 10, pp. 1021–1039, July 1999. (cited in p. 36)

Cheng W., Wong V. and Gao F.
Heat Transfer Measurement Comparisons in Insulated and Non-Insulated Diesel Engines.
SAE Technical Paper 890570, 1989. (cited in p. 32)

Choukroun A. and Chanfreau M.
Automatic Control of Electronic Actuators for an Optimized Engine Cooling Thermal Management.
SAE Techinical Paper 2001-01-1758, 2001. (cited in pp. 28, 29)

Comfort A.
An Introduction to Heavy-Duty Diesel Engine Frictional Losses And Lubricant Properties Affecting Fuel Economy - Part I.
SAE Technical Paper 2003-01-3225, 2003. (cited in p. 285)

Davies R., Foulger G., Bindley A. and Styles P.
Induced seismicity and hydraulic fracturing for the recovery of hydrocarbons.
Marine and Petroleum Geology, Vol. 45, pp. 171–185, aug 2013. (cited in p. 2)

De Bellis V.
Performance optimization of a spark-ignition turbocharged VVA engine under knock limited operation.
Applied Energy, Vol. 164, pp. 162–174, feb 2016. (cited in p. 16)

De Carvalho M.J., Seidl P., Belchior C. and Sodré J.R.
Lubricant viscosity and viscosity improver additive effects on diesel fuel economy.
Tribology International, Vol. 43 n^o 12, pp. 2298–2302, December 2010. (cited in p. 33)

De Cesare M., Parotto M., Covassin F. and Sgatti S.
Electric Low Pressure Fuel Pump Control for Fuel Saving.
SAE Techinical Paper 2013-01-0339, 2013. (cited in p. 35)

Dec J.E. and Yang Y.
Boosted HCCI for High Power without Engine Knock and with Ultra-Low NOx Emissions - using Conventional Gasoline.
SAE Int. J. Engines, Vol. 3 n^o 1, pp. 750–767, 2010. (cited in p. 23)

Degraeuwe B.
Contribution to the thermal management of DI Diesel engines.
Ph.D. Thesis, Universidad Politécnica de Valencia, 2007. (cited in pp. 5, 27, 105, 334)

Deligant M., Podevin P. and Descombes G.
Experimental identification of turbocharger mechanical friction losses.
Energy, Vol. 39 n^o 1, pp. 388–394, March 2012. (cited in p. 34)

Dempsey A.B., Walker N.R. and Reitz R.D.
Effect of Piston Bowl Geometry on Dual Fuel Reactivity Controlled Compression Ignition (RCCI) in a Light-Duty Engine Operated with Gasoline/Diesel and Methanol/Diesel.
SAE Int. J. Engines, Vol. 6 n^o 1, pp. 78–100, 2013. (cited in p. 24)

Depcik C. and Assanis D.
A Universal Heat Transfer Correlation for Intake and Exhaust Flows in an Spark-Ignition Internal Combustion Engine.
SAE Technical Paper 2002-01-0372, mar 2002. (cited in p. 194)

Desantes J.M., Benajes J., García A. and Monsalve-Serrano J.
The role of the in-cylinder gas temperature and oxygen concentration over low load reactivity controlled compression ignition combustion efficiency.
Energy, Vol. 78, pp. 854–868, dec 2014. (cited in p. 24)

Desantes J.M., Benajes J., Molina S. and González C.A.
The modification of the fuel injection rate in heavy-duty diesel engines. Part 1: Effects on engine performance and emissions.
Applied Thermal Engineering, Vol. 24 n^o 17-18, pp. 2701–2714, December 2004. (cited in p. 19)

Desantes J.M., Benajes J., Molina S. and González C.A.
The modification of the fuel injection rate in heavy-duty diesel engines. Part 2: Effects on combustion.
Applied Thermal Engineering, Vol. 24 n^o 17-18, pp. 2715–2726, December 2004. (cited in p. 19)

Dickey D.
The Effect of Insulated Combustion Chamber Surfaces on Direct-Injected Diesel Engine Performance, Emissions and Combustion.
SAE Technical Paper 890292, 1989. (cited in p. 32)

Dimopoulos P., Bach C., Soltic P. and Boulouchos K.
Hydrogen-natural gas blends fuelling passenger car engines: Combustion, emissions and well-to-wheels assessment.
International Journal of Hydrogen Energy, Vol. 33 n^o 23, pp. 7224–7236, December 2008. (cited in p. 45)

Dogde L.G., Simescu S., Neely G.D., Maymar M.J., Dickey D.W. and Savonen C.L.
Effect of Small Holes and High Injection Pressures on Diesel Engine Combustion.
SAE Technical Paper 2002-01-0494, 2002. (cited in p. 17)

Dolz V.
Transmisión de calor en motores alternativos : aplicación al aprovechamiento energético de los gases de escape.
Reverté, ISBN 978-84-291-4715-5, Barcelona, 2011. (cited in pp. 191, 192, 196, 197)

Donn C., Zulehner W., Ghebru D., Spicher U. and Honzen M.
Experimental Heat Flux Analysis of an Automotive Diesel Engine in Steady-State Operation and During Warm-Up.
SAE Techinical Paper 2011-24-0067, 2011. (cited in pp. 42, 43, 50)

Dowson D. and Higginson G.R.
Elastohydrodynamic Lubrication, SI Edition.
Pergamon press, ISBN 978-0080213026, Oxford, 1977. (cited in p. 231)

Durgun O. and Şahin Z.
Theoretical investigation of heat balance in direct injection (DI) diesel engines for neat diesel fuel and gasoline fumigation.
Energy Conversion and Management, Vol. 50 n^o 1, pp. 43–51, January 2009. (cited in pp. 38, 42, 50)

Edwards K.D., Wagner R. and Briggs T.
Investigating Potential Light-duty Efficiency Improvements through Simulation of Turbo-compounding and Waste-heat Recovery Systems.
SAE Techinical Paper 2010-01-2209, 2010. (cited in pp. 38, 47, 48, 50)

Edwards K.D., Wagner R.M. and Graves R.L.
Identification of Potential Efficiency Opportunities in Internal Combustion Engines Using a Detailed Thermodynamic Analysis of Engine Simulation Results.
SAE Technical Paper 2008-01-0293, 2008. (cited in pp. 38, 41, 47, 48, 50)

Etsion I. and Sher E.
Improving fuel efficiency with laser surface textured piston rings.
Tribology International, Vol. 42 n^o 4, pp. 542–547, April 2009. (cited in p. 33)

European Parliament.
Regulation (EU) No 333/2014 of the European Parliament and of the Council of 11 March 2014 amending Regulation (EC) No 443/2009 to define the modalities for reaching the 2020 target to reduce CO2 emissions from new passenger cars.
Official Journal of the European Union, Vol. L103 Vol 5, pp. 15–21, 2014. (cited in p. 4)

Farrell J.T., Stevens J.G. and Weissman W.
A Second Law Analysis of High Efficiency Low Emission Gasoline Engine Concepts.
SAE Techinical Paper 2006-01-0491, 2006. (cited in p. 48)

Federal-Mogul.
Goetze Piston Ring Handbook.
online resource, 2008. (cited in pp. 225, 252, 253)

Flierl R., Lauer F., Breuer M. and Hannibal W.
Cylinder Deactivation with Mechanically Fully Variable Valve Train.
SAE Int. J. Engines, Vol. 5 n^o 2, pp. 207–215, 2012. (cited in p. 23)

Franco A. and Martorano L.
Methods to Evaluate In-Cylinder Heat Transfer and Thermal Load in the Small Internal Combustion Engines.
SAE Techinical Paper 1999-01-1252, 1999. (cited in p. 47)

Fridriksson H.S., Tuner M., Andersson O., Sunden B., Persson H. and Ljungqvist M.

Effect of Piston Bowl Shape and Swirl Ratio on Engine Heat Transfer in a Light-Duty Diesel Engine.
SAE Techinical Paper 2014-01-1141, 2014. (cited in p. 25)

Fu J., Liu J., Feng R., Yang Y., Wang L. and Wang Y.
Energy and exergy analysis on gasoline engine based on mapping characteristics experiment.
Applied Energy, Vol. 102, pp. 622–630, February 2013. (cited in pp. 38, 41, 48, 50)

Furuhama S. and Tada T.
On the Flow of Gas Through the Piston-Rings (1st Report, The Discharge Coefficient and Temperature of Leakage Gas).
Bulletin of JSME, Vol. 4 n^o 16, pp. 684–690, 1961. (cited in p. 246)

Furuhama S. and Tada T.
On the Flow of Gas Through the Piston-Rings (2nd Report, The Character of Gas Leakage).
Bulletin of JSME, Vol. 4 n^o 16, pp. 691–698, 1961. (cited in p. 246)

Galindo J., Serrano J.R., Climent H. and Varnier O.
Impact of two-stage turbocharging architectures on pumping losses of automotive engines based on an analytical model.
Energy Conversion and Management, Vol. 51 n^o 10, pp. 1958–1969, October 2010. (cited in p. 25)

Galloni E., Fontana G. and Staccone S.
Numerical and experimental characterization of knock occurrence in a turbo-charged spark-ignition engine.
Energy Conversion and Management, Vol. 85, pp. 417–424, sep 2014. (cited in p. 16)

García D.
Aportación al modelado de emisiones y consumo basado en la señal de presión en el cilindro en motores Diesel.
Ph.D. Thesis, Universidad Politécnica de Valencia, 2016. (cited in pp. 5, 334)

García J.M.
Aportaciones al estudio del proceso de combustión turbulenta de chorros en motores Diesel de inyección directa.
Reverté, ISBN 978-84-291-4709-4, Barcelona, 2005. (cited in p. 111)

Gharehghani A., Mirsalim M. and Yusaf T.
Experimental investigation of thermal balance of a turbocharged SI engine operating on natural gas.
Applied Thermal Engineering, Vol. 60 n^o 1-2, pp. 200–207, October 2013. (cited in pp. 45, 50)

Gil A.
Modelado tridimensional del flujo de aire en el cilindro de motores Diesel de inyección directa.
Reverté, ISBN 978-84-291-4711-7, Barcelona, 2007. (cited in p. 24)

Goenka P.K.
Dynamically Loaded Journal Bearings: Finite Element Method Analysis.
ASME Journal of Tribology, Vol. 106 n^o 4, pp. 429–437, 1984. (cited in p. 227)

Goksem P.G. and Hargreaves R.A.
The effect of viscous shear heating on both film thickess and rolling traction in a EHL line contact. Part I: Fully flooded conditions.
ASME. J. of Lubrication Tech., Vol. 100 n^o 3, pp. 346–352, 1978. (cited in pp. 234, 268)

Goodman P., Galatioto F., Thorpe N., Namdeo A., Davies R. and Bird R.
Investigating the traffic-related environmental impacts of hydraulic-fracturing (fracking) operations.
Environment international, Vol. 89, pp. 248–260, feb 2016. (cited in p. 2)

Grandin B. and Ångström H.
Replacing Fuel Enrichment in a Turbo Charged SI Engine: Lean Burn or Cooled EGR.
SAE Technical Paper 1999-01-3505, 1999. (cited in p. 42)

Greenwood J.A. and Tripp J.H.
The Contact of Two Nominally Flat Rough Surfaces.
Proc. Instn. Mech. Engrs, Vol. 185, pp. 625–633, 1970. (cited in pp. 232, 267)

Grover Jr R.O. and Cleary D.
Correlating Measured Combustion Performance with CFD Predicted In-Cylinder Flows for a Spark-Ignition Direct-Injection (SIDI) Engine with Enhanced Charge Motion.
SAE Technical paper 2013-01-1090, April 2013. (cited in p. 173)

Guo J., Zhang W. and Zou D.
Investigation of dynamic characteristics of a valve train system.
Mechanism and Machine Theory, Vol. 46 n^o 12, pp. 1950–1969, dec 2011.
(cited in pp. 232, 233, 234, 259, 260, 267)

Hardy A.J. J. and Heywood J.B.
Fuel economy benefits and aftertreatment requirements of a naturally aspirated HCCI-SI engine system.
SAE International Journal of Engines, Vol. 1 n^o 1, pp. 1263–1277, 2009. (cited in p. 23)

Harrison H.
Evaporative Cooling.
SAE Techinical Paper 260015, 1926. (cited in p. 30)

Hazar H.
Effects of biodiesel on a low heat loss diesel engine.
Renewable Energy, Vol. 34 n^o 6, pp. 1533–1537, June 2009. (cited in pp. 31, 44)

He M., Zhang X., Zeng K. and Gao K.
A combined thermodynamic cycle used for waste heat recovery of internal combustion engine.
Energy, Vol. 36 n^o 12, pp. 6821–6829, December 2011. (cited in pp. 38, 48, 50)

He Y., Selamet A., Reese R.A., Vick R.K. and Amer A.A.
Impact of Tumble on Combustion in SI Engines: Correlation between Flow and Engine Experiments.
SAE paper 2007-01-4003, 2007. (cited in p. 25)

Health Effects Institute.
Diesel Exhaust: A Critical Analysis of Emissions, Exposure, and Health Effects.
A Special Report of the Institute's Diesel Working Group, 1995. (cited in p. 2)

Hejwowski T.
Comparative study of thermal barrier coatings for internal combustion engine.
Vacuum, Vol. 85 n^o 5, pp. 610–616, November 2010. (cited in p. 30)

Heuser B., Kremer F., Pischinger S., Rohs H., Holderbaum B. and Körfer T.
An experimental investigation of dual-fuel combustion in a light duty Diesel engine by in-cylinder blending of ethanol and Diesel.
SAE Int. J. Engines, Vol. 9 n^o 1, pp. 11–25, 2015. (cited in pp. 24, 43, 44)

Heywood J.B.
Internal Combustion Engines Fundamentals.
McGraw-Hill, ISBN 978-0-07-028637-5, New York, 1988.
(cited in pp. 15, 18, 22, 25, 30, 42, 50, 103, 133, 285)

Heywood J.B. and Sher E.
The Two-Stroke Cycle Engine: It's Development, Operation and Design.
Taylor and Francis, ISBN 978-1560328315, Pennsylvania, 1th edition, 1999.
(cited in pp. 87, 173)

Hiwase S.D., Moorthy S., Prasad H., Dumpa M. and Metkar R.M.
Multidimensional Modeling of Direct Injection Diesel Engine with Split Multiple Stage Fuel Injections.
Procedia Engineering, Vol. 51, pp. 670–675, January 2013. (cited in p. 18)

Hohenberg G.
Definition und Eigenschaften des thermodynamischen Verlustwinkels von Kolbenmaschinen.
Automobil-Industrie, Vol. 4, pp. 15–21, 1976. (cited in pp. 111, 205, 206, 211, 215)

Holmberg K., Andersson P. and Erdemir A.
Global energy consumption due to friction in passenger cars.
Tribology International, Vol. 47, pp. 221–234, March 2012. (cited in p. 32)

Hoshi M.
Reducing friction losses in automobile engines.
Tribology International, Vol. 17 n^o 4, pp. 185–189, August 1984. (cited in p. 33)

Huang R.F., Huang C.W., Chang S.B., Yang H.S., Lin T.W. and Hsu W.Y.
Topological flow evolutions in cylinder of a motored engine during intake and compression strokes.
Journal of Fluids and Structures, Vol. 20 n^o 1, pp. 105–127, January 2005.
(cited in pp. 18, 173, 177)

Hughes C.A.V. and Wiseman M.W.
Feasibility of Intelligent Control Strategies to Reduce Cooling System Size.
SAE Techinical Paper 2001-01-1759, 2001. (cited in p. 29)

İşcan B. and Aydın H.
Improving the usability of vegetable oils as a fuel in a low heat rejection diesel engine.
Fuel Processing Technology, Vol. 98, pp. 59–64, June 2012. (cited in p. 31)

Imran A., Varman M., Masjuki H.H. and Kalam M.A.
Review on alcohol fumigation on diesel engine: A viable alternative dual fuel technology for satisfactory engine performance and reduction of environment concerning emission.
Renewable and Sustainable Energy Reviews, Vol. 26, pp. 739–751, October 2013. (cited in p. 43)

Ishibashi Y. and Asai M.
Improving the Exhaust Emissions of Two-Stroke Engines by Applying the Activated Radical Combustion.
SAE Techinical Paper 960742, 1996. (cited in p. 23)

Jaichandar S. and Tamilporai P.
Low Heat Rejection Engines - An Overview.
SAE Technical Paper 2003-01-0405, 2003. (cited in pp. 31, 32)

Jarrier L., Champoussin J.C., Yu R. and Gentile D.
Warm-Up of a D.I. Diesel Engine : Experiment and Modeling.
SAE Technical Paper 2000-01-0299, 2000. (cited in pp. 42, 43)

Javaheri A., Esfahanian V., Salavati-Zadeh A. and Darzi M.
Energetic and exergetic analyses of a variable compression ratio spark ignition gas engine.
Energy Conversion and Management, Vol. 88, pp. 739–748, December 2014. (cited in pp. 45, 50)

Jung D., Yong J., Choi H., Song H. and Min K.
Analysis of engine temperature and energy flow in diesel engine using engine thermal management.
Journal of Mechanical Science and Technology, Vol. 27 n^o 2, pp. 583–592, March 2013. (cited in pp. 42, 43, 50)

Kakaee A.H., Paykani A. and Ghajar M.
The influence of fuel composition on the combustion and emission characteristics of natural gas fueled engines.
Renewable and Sustainable Energy Reviews, Vol. 38, pp. 64–78, October 2014. (cited in p. 43)

Kang H., Ahn H. and Min K.
Smart cooling system of the double loop coolant structure with engine thermal management modeling.
Applied Thermal Engineering, Vol. 79, pp. 124–131, 2015. (cited in pp. 28, 41, 47, 50)

Karabektas M.
The effects of turbocharger on the performance and exhaust emissions of a diesel engine fuelled with biodiesel.
Renewable Energy, Vol. 34 n^o 4, pp. 989–993, apr 2009. (cited in p. 15)

Karaoglanli A.C., Dikici H. and Kucuk Y.
Effects of heat treatment on adhesion strength of thermal barrier coating systems.
Engineering Failure Analysis, Vol. 32, pp. 16–22, September 2013. (cited in p. 30)

Kawashima J.
Research on a variable swirl intake port for high-speed 4-valve DI diesel engine.
JSAE Review, Vol. 20 n^o 3, pp. 421–424, July 1999. (cited in p. 25)

Kim M., Lee S. and Kim W.
Tumble Flow Measurements UsingThree Different Methods and its Effects on Fuel Economy and Emissions.
SAE Technical paper 2006-01-3345, 2006. (cited in p. 173)

Kimura S., Aoki O., Kitahara Y. and Aiyoshizawa E.
Ultra-Clean Combustion Technology Combining a Low-Temperature and Premixed Combustion Concept for Meeting Future Emission Standards.
SAE Technical Paper 2001-01-0200, 2001. (cited in p. 23)

Klein M., Eriksson L. and Åslund J.
Compression ratio estimation based on cylinder pressure data.
Control Engineering Practice, Vol. 14 n^o 3, pp. 197–211, March 2005.
(cited in pp. 204, 205)

Kohketsu S., Tanabe K. and Mori K.
Flexibly controlled injection rate shape with next generation common rail system for heavy duty DI diesel engines.
SAE Technical Paper 2000-01-0705, 2000. (cited in p. 19)

Kokjohn S.L., Hanson R.M., Splitter D.A. and Reitz R.D.
Fuel reactivity controlled compression ignition (RCCI): a pathway to controlled high-efficiency clean combustion.
International Journal of Engine Research, Vol. 12 n^o 3, pp. 209–226, 2011.
(cited in pp. 24, 43, 44, 50, 141)

Kokjohn S.L. and Reitz R.D.
Reactivity Controlled Compression Ignition and Conventional Diesel Combustion: A Comparison of Methods to Meet Light-Duty NOx and Fuel Economy Targets.
International Journal of Engine Research, Vol. 0 n^o 0, pp. 1–17, 2013. (cited in p. 24)

Komninos N.P. and Kosmadakis G.M.
Heat transfer in HCCI multi-zone modeling: Validation of a new wall heat flux correlation under motoring conditions.
Applied Energy, Vol. 88 n^o 5, pp. 1635–1648, May 2011. (cited in p. 205)

Konstandopoulos A.G., Kostoglou M., Vlachos N. and Kladopoulou E.
Advances in the science and technology of diesel particulate filter simulation.
Advances in Chemical Engineering, Vol. 33, pp. 213–275,284–294, 2007. (cited in p. 20)

Körfer T., Lamping M., Kolbeck A., Pischinger S., Adolph D. and Busch H.
Potential of Modern Diesel Engines with Lowest Raw Emissions - a Key Factor for Future CO2 Reduction.
SAE Technical Paper 2009-26-0025, 2009. (cited in p. 35)

Korte V., Glas T., Lettmann M., Krepulat W. and Steinmetz C.
Cam Roller Follower Design for Heavy Duty Diesel Engines.
SAE Technical Paper 2000-01-0525, 2000. (cited in p. 33)

Kouremenos D.A., Rakopoulos C.D., Hountalas D.T. and Zannis T.K.
Development of a Detailed Friction Model to Predict Mechanical Losses at Elevated Maximum Combustion Pressures.
SAE Technical Paper 2001-01-0333, 2001. (cited in p. 285)

Krishna M.V.S.M., Rao V.V.R.S., Reddy T.K.K. and Murthy P.V.K.
Comparative studies on performance evaluation of DI diesel engine with high grade low heat rejection combustion chamber with carbureted alcohols and crude jatropha oil.
Renewable and Sustainable Energy Reviews, Vol. 36, pp. 1–19, August 2014.
(cited in p. 31)

Kumar S., Cho J.H., Park J. and Moon I.
Advances in diesel-alcohol blends and their effects on the performance and emissions of diesel engines.
Renewable and Sustainable Energy Reviews, Vol. 22, pp. 46–72, June 2013.
(cited in p. 43)

Lapuerta M., Armas O. and Bermúdez V.
Sensitivity of diesel engine thermodynamic cycle calculation to measurement errors and estimated parameters.
Applied Thermal Engineering, Vol. 20 n^o 9, pp. 843–861, 2000. (cited in pp. 205, 206)

Lapuerta M., Armas O. and Hernandez J.J.
Diagnosis of DI Diesel combustion from in-cylinder pressure signal by estimation of mean thermodynamic properties of the gas.
Applied Thermal Engineering, Vol. c, pp. 513–529, 1999. (cited in p. 97)

Lapuerta M., Armas O. and Molina S.
Study of the compression cycle of a reciprocating engine through the polytropic coefficient.
Applied Thermal Engineering, Vol. 23 n^o 3, pp. 313–323, February 2003.
(cited in p. 204)

Lapuerta M., Armas O. and Rodríguez-Fernández J.
Effect of biodiesel fuels on diesel engine emissions.
Progress in Energy and Combustion Science, Vol. 34 n^o 2, pp. 198–223, 2008.
(cited in pp. 20, 43)

Lapuerta M., Ballesteros R. and Agudelo J.
Effect of the gas state equation on the thermodynamic diagnostic of diesel combustion.
Applied Thermal Engineering, Vol. 26 n^o 14-15, pp. 1492–1499, October 2006.
(cited in p. 90)

Lasecki M.P. and Cousineau J.M.
Controllable Electric Oil Pumps in Heavy Duty Diesel Engines.
SAE Techinical Paper 2003-01-3421, 2003. (cited in p. 34)

Lee J. and Patterson D.
Analysis of Cam/Roller Follower Friction and Slippage in Valve Train Systems.
SAE Technical paper 951039, 1995. (cited in p. 263)

Lee K., Yoon M. and Sunwoo M.
A study on pegging methods for noisy cylinder pressure signal.
Control Engineering Practice, Vol. 16 n^o 8, pp. 922–929, 2008. (cited in p. 204)

Lima C.R.C. and Guilemany J.M.
Adhesion improvements of Thermal Barrier Coatings with HVOF thermally sprayed bond coats.
Surface and Coatings Technology, Vol. 201 n^o 8, pp. 4694–4701, January 2007.
(cited in p. 30)

López J.J.
Estudio teórico-experimental del chorro Diesel no evaporativo y de su interacción con el movimiento del aire.
Reverté, ISBN 978-84-291-4703-2, Barcelona, 2003. (cited in p. 111)

López J.J., García-Oliver J.M., Martín J., Chemisky J.P. and Bouet A.
A Soot Radiation Model for Diesel Sprays.
SAE Techinical Paper 2012-01-1069, 2012. (cited in p. 103)

Macián V., Serrano J.R., Dolz V. and Sánchez J.P.
Methodology to design a bottoming Rankine cycle, as a waste energy recovering system in vehicles. Study in a HDD engine.
Applied Energy, Vol. 104, pp. 758–771, apr 2013. (cited in p. 31)

Macián V., Tormos B., Bermúdez V. and Ramírez L.
Assessment of the effect of low viscosity oils usage on a light duty diesel engine fuel consumption in stationary and transient conditions.
Tribology International, Vol. 79, pp. 132–139, November 2014. (cited in p. 33)

Magno A., Mancaruso E. and Vaglieco B.
Effects of a biodiesel blend on energy distribution and exhaust emissions of a small CI engine.
Energy Conversion and Management, Vol. 96, pp. 72–80, May 2015. (cited in pp. 44, 47)

Maharudrppa Mallikarjuna J.
Effect of Manifold Orientation on Non-Reacting In-Cylinder Tumble Flows in an IC Engine with Pentroof Piston - An Investigation Using PIV.
SAE Technical Paper 2010-01-0956, 2010. (cited in p. 18)

Maiboom A. and Tauzia X.
NOx and PM emissions reduction on an automotive HSDI Diesel engine with water-in-diesel emulsion and EGR: An experimental study.
Fuel, Vol. 90 n^o 11, pp. 3179–3192, November 2011. (cited in p. 16)

Malkhede D.N. and Khalane H.
Maximizing Volumetric Efficiency of IC Engine through Intake Manifold Tuning.
SAE Techinical Paper 2015-01-1738, 2015. (cited in p. 24)

Martín J.
Diagnóstico de la combustión en motores de Diesel de inyección directa.
Reverté, ISBN 978-84-291-4717-9, Barcelona, 2012.
(cited in pp. 5, 78, 89, 91, 95, 97, 100, 102, 104, 111, 112, 204, 209, 212, 215, 280, 334)

Meira J., Ribeiro E., Filho A. and Melo W.
Strategies for energy savings with use of constant and variable oil pump systems.
SAE Techinical Paper 2011-36-0150, 2011. (cited in p. 34)

Mendoza M.C. and Woon P.V.
E-diesel Effects on Engine Component Cummins C8 . 3 Engine.
SAE Techinical Paper 2002-01-2847, 2002. (cited in pp. 44, 50)

Michel P., Charlet A., Colin G., Chamaillard Y., Bloch G. and Nouillant C.
Optimizing fuel consumption and pollutant emissions of gasoline-HEV with catalytic converter.
Control Engineering Practice, dec 2015. (cited in p. 19)

Micklow G.J. and Gong W.D.
Investigation of the grid and intake-generated tumble on the in-cylinder flow in a compression ignition direct-injection engine.
Journal of Automobile Engineering, Vol. 222 n^o 5, pp. 775–788, May 2008. (cited in p. 173)

Miles P.C.
The Influence of Swirl on HSDI Diesel Combustion at Moderate Speed and Load.
SAE Techinical Paper 2000-01-1829, 2000. (cited in p. 25)

Millo F., Giacominetto P.F. and Bernardi M.G.
Analysis of different exhaust gas recirculation architectures for passenger car Diesel engines.
Applied Energy, Vol. 98, pp. 79–91, October 2012. (cited in p. 26)

Mistry C.S.
Comparative Assessment on Performance of Multi cylinder Engine Using CNG , LPG and Petrol as a Fuel.
SAE Techinical Paper 2005-01-1056, 2005. (cited in p. 46)

Mitroglou N., Nouri J.M., Gavaises M. and Arcoumanis C.
Spray Characteristics of a Multi-hole Injector for Direct-Injection Gasoline Engines.
International Journal of Engine Research, Vol. 7 n^o 3, pp. 255–270, 2006. (cited in pp. 17, 40)

Modi A.J.
Experimental Study of Energy Balance in Thermal Barrier Coated Diesel Engine.
SAE Techinical Paper 2012-01-0389, 2012. (cited in p. 50)

Modi A.J. and Gosai D.C.
Experimental study on Thermal Barrier coated diesel engine performance with Blends of diesel and Palm biodiesel.
SAE Int. J. Fuels Lubr., Vol. 3 n^o 2, pp. 1–16, 2010. (cited in pp. 44, 46, 47)

MohamedMusthafa M., Sivapirakasam S.P. and Udayakumar M.
Comparative studies on fly ash coated low heat rejection diesel engine on performance and emission characteristics fueled by rice bran and pongamia methyl ester and their blend with diesel.
Energy, Vol. 36 n^o 5, pp. 2343–2351, May 2011. (cited in pp. 31, 32)

Mohan B., Yang W. and Chou S.K.
Fuel injection strategies for performance improvement and emissions reduction in compression ignition engines - A Review.
Renewable and Sustainable Energy Reviews, Vol. 28, pp. 664–676, December 2013. (cited in pp. 17, 18, 23)

Molina S., García A., Pastor J.M., Belarte E. and Balloul I.
Operating range extension of RCCI combustion concept from low to full load in a heavy-duty engine.
Applied Energy, Vol. 143, pp. 211–227, 2015. (cited in p. 318)

Moody L.F.
An approximate formula for pipe friction factors.
Trans. ASME, Vol. 69 n^o 12, pp. 1005–1011, 1947. (cited in p. 237)

Morawitz U., Mehring J. and Schramm L.
Benefits of Thermal Spray Coatings in Internal Combustion Engines, with Specific View on Friction Reduction and Thermal Management.
SAE Technical Paper 2013-01-0292, April 2013. (cited in p. 33)

Morel T. and Keribar R.
Heat radiation in DI Diesel engines.
SAE Technical Paper 860445, 1986. (cited in p. 103)

Muhr T.H.
New Technologies for Engine Valve Springs.
SAE Techinical Paper 930912, 1993. (cited in p. 33)

Nayak N., Lakshminarayanan P.A., Babu M.K.G. and Dani A.D.
Predictions of cam follower wear in diesel engines.
Wear, Vol. 260 n^o 1-2, pp. 181–192, jan 2006. (cited in pp. 231, 233, 267)

Neely G.D., Sasaki S. and Leet J.A.
Experimental Investigation of PCCI-DI Combustion on Emissions in a Light-Duty Diesel Engine.
SAE Techinical Paper 2004-01-0121, 2004. (cited in p. 23)

Nishimura T., Satoh K., Takahashi S. and Yokota K.
Effects of Fuel Injection Rate on Combustion and Emission in a DI Diesel Engine.
SAE Technical Paper 981929, 1998. (cited in p. 18)

Nitta J., Minato A. and Shimazaki N.
Performance Evaluation of Three-Stage Turbocharging System for Heavy-Duty Diesel Engine.
SAE Technical Paper 2011-01-0374, 2011. (cited in p. 25)

Nose H., Inoue T., Katagiri S., Sakai A., Kawasaki T. and Okamura M.
Fuel Enrichment Control System by Catalyst Temperature Estimation to Enable Frequent Stoichiometric Operation at High Engine Speed/Load Condition.
SAE Technical Paper 2013-01-0341, 2013. (cited in p. 42)

Oberdörster G. and Utell M.J.
Ultrafine particles in the urban air: to the respiratory tract–and beyond?
Environmental health perspectives, Vol. 110 n^o 8, pp. A440–A441, 2002. (cited in p. 2)

Okamoto M. and Sakai I.
Contact Pressure Distribution of Piston Rings -Calculation Based on Piston Ring Contour -.
SAE Techinical Paper 2001-01-0571, 2001. (cited in p. 33)

Olmeda P., Martín J., Novella R. and Carreño R.
An adapted heat transfer model for engines with tumble motion.
Applied Energy, Vol. 158, pp. 190–202, 2015. (cited in p. 217)

Olsen D., Hutcherson G., Willson B. and Mitchell C.
Development of the tracer gas method for large bore natural gas engines: part 1 - method validation.
J. Eng. Gas Turbines Power, Vol. 124 n^o 3, pp. 678–685, 2002. (cited in p. 85)

Olsen D., Hutcherson G., Willson B. and Mitchell C.
Development of the tracer gas method for large bore natural gas engines: part 2 - measurement of scavenging parameters.
J. Eng. Gas Turbines Power, Vol. 124 n^o 3, pp. 686–694, 2002. (cited in p. 85)

Orbaiz P. and Brear M.
Energy Balance of a Spark Ignition Engine Running on Hydrogen, Synthesis Gas and Natural Gas.
SAE Techinical Paper 2014-01-1337, 2014. (cited in pp. 46, 50)

Orbaiz P., Brear M.J., Abbasi P. and Dennis P.A.
A Comparative Study of a Spark Ignition Engine Running on Hydrogen, Synthesis Gas and Natural Gas.
SAE Int. J. Engines, Vol. 6 n^o 1, pp. 23–44, 2013. (cited in p. 46)

Osada H., Uchida N., Shimada K. and Aoyagi Y.
Reexamination of Multiple Fuel Injections for Improving the Thermal Efficiency of a Heavy-Duty Diesel Engine.
SAE Technical Paper 2013-01-0909, apr 2013. (cited in p. 22)

Özcan H. and Söylemez M.S.
Thermal balance of a LPG fuelled, four stroke SI engine with water addition.
Energy Conversion and Management, Vol. 47 n^o 5, pp. 570–581, March 2006. (cited in pp. 45, 50)

Palma A., Del Core D. and Esposito C.
The HCCI Concept and Control , Performed with MultiAir Technology on Gasoline Engines.
SAE Techinical Paper 2011-24-0026, 2011. (cited in p. 23)

Pang H.H. and Brace C.J.
Review of engine cooling technologies for modern engines.
Proc. Inst. Mech. Engrs., Vol. 218 n^o 11, pp. 1209–1215, 2004. (cited in pp. 22, 29)

Park Y. and Bae C.
Experimental study on the effects of high/low pressure EGR proportion in a passenger car diesel engine.
Applied Energy, Vol. 133, pp. 308–316, November 2014. (cited in pp. 22, 26)

Parlak A.
The effect of heat transfer on performance of the Diesel cycle and exergy of the exhaust gas stream in a LHR Diesel engine at the optimum injection timing.
Energy Conversion and Management, Vol. 46 n^o 2, pp. 167–179, January 2005. (cited in p. 31)

Parlak A., Yasar H. and Sahin B.
Performance and exhaust emission characteristics of a lower compression ratio LHR Diesel engine.
Energy Conversion and Management, Vol. 44 n^o 1, pp. 163–175, January 2003. (cited in pp. 22, 32)

Parvate-Patil G.B., Hong H. and Gordon B.
An assessment of intake and exhaust philosophies for variable valve timing.
SAE Technical Paper 2003-32-0078, 2003. (cited in pp. 22, 24)

Pastor J.M.
Análisis del proceso de barrido en motores de dos tiempos de pequeña cilindrada.
Reverté, ISBN 978-84-291-4713-1, Barcelona, 2009. (cited in p. 173)

Páv K., Václav R. and Václav V.
Heat balance in modern automotive engines.
Journal of Middle European Construction and Design of Cars, Vol. 10 n^o 2, pp. 6–13, 2013. (cited in p. 42)

Payri F., Benajes J., Galindo J. and Serrano J.R.
Modelling of turbocharged diesel engines in transient operation. Part 2: Wave action models for calculating the transient operation in a high speed direct injection engine.
Proc. IMechE, Part D: Journal of Automobile Engineering, Vol. 216 n^o 6, pp. 479–493, 2002. (cited in p. 24)

Payri F., Broatch A., Serrano J.R., Rodríguez L.F. and Esmorís A.
Study of the Potential of Intake Air Heating in Automotive DI Diesel Engines.
SAE Techinical Paper 2006-01-1233, 2006. (cited in p. 101)

Payri F., Galindo J., Martín J. and Arnau F.J.
A Simple Model for Predicting the Trapped Mass in a DI Diesel Engine.
SAE Techinical Paper 2007-01-0494, 2007. (cited in pp. 86, 93)

Payri F. and J.M. Desantes.
Motores de combustión interna alternativos.
Reverté, ISBN 978-84-291-4802-2, Barcelona, 2011.
(cited in pp. 16, 19, 24, 25, 27, 29, 228, 295)

Payri F., Luján J.M., Martín J. and Abbad A.
Digital signal processing of in-cylinder pressure for combustion diagnosis of internal combustion engines.
Mechanical Systems and Signal Processing, Vol. 24 n^o 6, pp. 1767–1784, 2010.
(cited in pp. 82, 144, 204, 208)

Payri F., Margot X., Gil A. and Martín J.
Computational Study of Heat Transfer to the Walls of a DI Diesel Engine.
SAE Technical paper 2005-01-0210, April 2005. (cited in p. 104)

Payri F., Martín J., Garcia A. and Carreño R.
Experimental and Theoretical Analysis of the Energy Balance in a DI Diesel Engine.
SAE Technical Paper 2015-01-1651, 2015. (cited in pp. 16, 25, 191)

Payri F., Molina S., Martín J. and Armas O.
Influence of measurement errors and estimated parameters on combustion diagnosis.
Applied Thermal Engineering, Vol. 26 n^o 2-3, pp. 226–236, February 2006.
(cited in pp. 112, 204, 205, 215)

Payri F., Olmeda P., Arnau F.J., Dombrovsky A. and Smith L.
External heat losses in small turbochargers: Model and experiments.
Energy, Vol. 71, pp. 534–546, July 2014. (cited in p. 128)

Payri F., Olmeda P., Martín J. and Carreño R.
A New Tool to Perform Global Energy Balances in DI Diesel Engines.
SAE Int. J. Engines, Vol. 7 n^o 1, pp. 43–59, 2014.
(cited in pp. 26, 102, 105, 108, 216, 222, 227, 230)

Payri F., Olmeda P., Martín J. and Carreño R.
Experimental analysis of the global energy balance in a DI diesel engine.
Applied Thermal Engineering, Vol. 89, pp. 545–557, October 2015.
(cited in pp. 18, 25, 32, 35, 128, 138, 142, 146)

Payri F., Olmeda P., Martín J. and García A.
A complete 0D thermodynamic predictive model for direct injection diesel engines.
Applied Energy, Vol. 88 n^o 12, pp. 4632–4641, December 2011.
(cited in pp. 89, 101, 102, 113, 204)

Payri F., Serrano J.R., Fajardo P., Reyes-Belmonte M.A. and Gozalbo-Belles R.
A physically based methodology to extrapolate performance maps of radial turbines.
Energy Conversion and Management, Vol. 55, pp. 149–163, mar 2012. (cited in p. 35)

Pearson R.J., Eisaman M.D., Turner J., Edwards P.P., Jiang Z., Kuznetsov V.L., Littau K.A., Di Marco L. and Taylor S.R.G.
Energy storage via carbon-neutral fuels made from CO 2, Water, and Renewable Energy.
Proceedings of the IEEE, Vol. 100 n^o 2, pp. 440–460, 2012. (cited in p. 43)

Petitjean D., Bernardini L., Middlemass C. and Shahed S.M.
Advanced gasoline engine turbocharging technology for fuel economy improvements.
SAE Technical Paper 2004-01-0988, 2004. (cited in pp. 25, 36)

Pickett L.M. and Siebers D.L.
An investigation of diesel soot formation processes using micro-orifices.
Proceedings of the Combustion Institute, Vol. 29 n^o 1, pp. 655–662, jan 2002.
(cited in p. 35)

Pickett L.M. and Siebers D.L.
Soot in diesel fuel jets: effects of ambient temperature, ambient density, and injection pressure.
Combustion and Flame, Vol. 138 n^o 1-2, pp. 114–135, July 2004. (cited in pp. 17, 23)

Pietikäinen M., Väliheikki A., Oravisjärvi K., Kolli T., Huuhtanen M., Niemi S., Virtanen S., Karhu T. and Keiski R.L.
Particle and NOx emissions of a non-road diesel engine with an SCR unit: The effect of fuel.
Renewable Energy, Vol. 77, pp. 377–385, may 2015. (cited in p. 20)

Pisla D., Ceccarelli M., Husty M. and Corves B.
New Trends in Mechanism Science: Analysis and design.
Springer, ISBN 978-90-481-9689-0, Heidelberg, 2010. (cited in p. 261)

Pope C. and Dockery D.
Health Effects of Fine Particulate Air Pollution: Lines that Connect.
Journal of the Air & Waste Management Association, Vol. 56 n^o 6, pp. 709–742, 2006.
(cited in p. 2)

Porot P.A., Ménégazzi P. and Ap N.S.
Understanding and Improving Evaporative Engine Cooling at High Load , High Speed by Engine Tests and 3D Calculations.
SAE Techinical Paper 971792, 1997. (cited in p. 30)

Rabeau F. and Magand S.
Modeling of a Thermal Management Platform of an Automotive D . I Diesel Engine to Predict the Impact of Downsizing and Hybridization during a Cold Start.
SAE Techinical Paper 2014-01-0657, 2014. (cited in pp. 47, 50)

Rakopoulos C.D., Dimaratos A.M., Giakoumis E.G. and Rakopoulos D.C.
Evaluation of the effect of engine, load and turbocharger parameters on transient emissions of diesel engine.
Energy Conversion and Management, Vol. 50 n^o 9, pp. 2381–2393, September 2009. (cited in pp. 15, 16)

Rakopoulos C.D. and Giakoumis E.G.
Speed and load effects on the availability balances and irreversibilities production in a multi-cylinder turbocharged diesel engine.
Applied Thermal Engineering, Vol. 17 n^o 3, pp. 299–313, March 1997. (cited in p. 50)

Rakopoulos C.D. and Giakoumis E.G.
Second-law analyses applied to internal combustion engines operation.
Progress in Energy and Combustion Science, Vol. 32 n^o 1, pp. 2–47, 2006. (cited in p. 47)

Rakopoulos C.D., Hountalas D.T., Zannis T.C. and Levendis Y.A.
Operational and Environmental Evaluation of Diesel Engine Burning Oxygan-Enriched Intake Air or Oxygen-Enriched Fuels: A Review.
SAE Techinical Paper 2004-01-2924, 2004. (cited in p. 20)

Rakopoulos C.D., Kosmadakis G.M., Dimaratos A.M. and Pariotis E.G.
Investigating the effect of crevice flow on internal combustion engines using a new simple crevice model implemented in a CFD code.
Applied Energy, Vol. 88 n^o 1, pp. 111–126, 2011. (cited in p. 101)

Rakopoulos C.D., Kosmadakis G.M. and Pariotis E.G.
Critical evaluation of current heat transfer models used in CFD in-cylinder engine simulations and establishment of a comprehensive wall-function formulation.
Applied Energy, Vol. 87 n^o 5, pp. 1612–1630, May 2010. (cited in p. 101)

Rao Z. and Wang S.
A review of power battery thermal energy management.
Renewable and Sustainable Energy Reviews, Vol. 15 n^o 9, pp. 4554–4571, December 2011. (cited in p. 36)

Roberts A., Brooks R. and Shipway P.
Internal combustion engine cold-start efficiency: A review of the problem, causes and potential solutions.
Energy Conversion and Management, Vol. 82, pp. 327–350, June 2014. (cited in p. 28)

Robinson K., Hawley J.G., Campbell N.A.F. and Tilley D.G.
A Review of Precision Engine Cooling.
SAE Techinical Paper 1999-01-0578, 1999. (cited in p. 29)

Romero C.A., Torregrosa A.J., Olmeda P. and Martín J.
Energy Balance During the Warm-Up of a Diesel Engine.
SAE Techinical Paper 2014-01-0676, 2014. (cited in pp. 42, 43)

Schell A., Peng H., Tran D., Stamos E., Lin C.C. and Kim M.J.
Modelling and control strategy development for fuel cell electric vehicles.
Annual Reviews in Control, Vol. 29 n^o 1, pp. 159–168, January 2005. (cited in p. 36)

Senatore A., Cardone M., Rocco V. and Prati M.V.
A Comparative Analysis of Combustion Process in D.I. Diesel Engine Fueled with Biodiesel and Diesel Fuel.
SAE Techinical Paper 2000-01-0691, 2000. (cited in pp. 20, 44)

Serrano J.R., Olmeda P., Tiseira A., García-Cuevas L.M. and Lefebvre A.
Importance of Mechanical Losses Modeling in the Performance Prediction of Radial Turbochargers under Pulsating Flow Conditions.
SAE Int. J. Engines, Vol. 6 n^o 2, pp. 729–738, April 2013. (cited in p. 34)

Shelef M. and Kukkonen C.A.
Prospects of hydrogen-fueled vehicles.
Progress in Energy and Combustion Science, Vol. 20 n^o 2, pp. 139–148, January 1994. (cited in p. 20)

Shigley J.E. and Uicker J.J.
Theory of Machines and Mechanisms.
McGraw-Hill, ISBN 0-07-Y66560-5, Singapore, international edition, 1981. (cited in p. 260)

Sieder E.N. and Tate G.E.
Heat Transfer and Pressure Drop of Liquids in Tubes.
Industrial and Engineering Chemistry, Vol. 28 n^o 12, 1936. (cited in p. 197)

Singh S., Garg A., Gupta A. and Permude A.
Analysis of Thermal Balance of Diesel Engine and Identification of Scope for Waste Heat Recovery.
SAE Techinical Paper 2013-01-2744, 2013. (cited in pp. 38, 47, 50)

Smith L.A., Preston W.H., Dowd G., Taylor O. and Wilkinson K.M.
Application of a First Law Heat Balance Method to a Turbocharged Automotive Diesel Engine.
SAE Technical Paper 2009-01-2744, 2009. (cited in pp. 38, 39, 41, 42, 50, 128)

Stanglmaier R.H. and Roberts C.E.
(HCCI): Benefits , Compromises , and Future Engine Applications.
SAE Techinical Paper 1999-01-3682, 1999. (cited in p. 23)

Stanley R., Taraza D. and Henein N.
A Simplified Friction Model of the Piston Ring Assembly.
SAE Technical Paper 1999-01-0974, 1999. (cited in pp. 222, 225, 226)

Stricker K., Kocher L., Koeberlein E., Alstine D.V. and Shaver G.M.
Estimation of Effective Compression Ratio for Engines Utilizing Flexible Intake Valve Actuation.
Journal of Automobile Engineering, 2011. (cited in p. 204)

Su T., Chang C., Reitz R., Farrell P., Pierpont A. and Tow T.
Effects of Injection Pressure and Nozzle Geometry on Spray SMD and D.I. Emissions.
SAE Technical Paper 952360, 1995. (cited in p. 17)

Sun X., Wang W.G., Bata R.M. and Gao X.
Performance Evaluation of Low Heat Rejection Engines.
ASME. J. Eng. Gas Turbines Power, Vol. 116 n^o 4, pp. 758–764, 1994. (cited in p. 31)

Taraza D. and Henein N.
Friction Losses in Multi-Cylinder Diesel Engines.
SAE Technical Paper 2000-01-0921, 2000. (cited in pp. 32, 225, 226, 227, 229, 285)

Tauzia X. and Maiboom A.
Experimental study of an automotive Diesel engine efficiency when running under stoichiometric conditions.
Applied Energy, Vol. 105, pp. 116–124, May 2013. (cited in pp. 22, 41, 42, 50)

Taylor C.M.
Engine Tribology.
Elsevier, ISBN 978-0444897558, 1997. (cited in pp. 227, 228, 229)

Taylor J.R.
An Introduction to Error Analysis: The Study of Uncertainties in Physical Measurements.
University Science Books, ISBN 978-0-935702-75-0, Colorado, 2nd edition, 1997.
(cited in p. 141)

Taymaz I.
An experimental study of energy balance in low heat rejection diesel engine.
Energy, Vol. 31 n^o 2-3, pp. 364–371, February 2006. (cited in pp. 31, 46, 47, 50)

Taymaz I., Cakir K., Gur M. and Mimaroglu A.
Experimental investigation of heat losses in a ceramic coated diesel engine.
Surface and Coatings Technology, Vol. 169-170, pp. 168–170, June 2003.
(cited in pp. 46, 47)

Tazerout M., Le Corre O. and Rousseau S.
TDC Determination in IC Engines Based on the Thermodynamic Analysis of the Temperature-Entropy Diagram.
SAE paper 1999-01-1489, 1999. (cited in p. 205)

Teng H.
Waste Heat Recovery Concept to Reduce Fuel Consumption and Heat Rejection from a Diesel Engine.
SAE Int. J. Commer. Veh., Vol. 3 n^o 1, pp. 60–68, 2010. (cited in pp. 38, 41, 50)

Teng H. and McCandless J.
Performance analysis of rail-pressure supply pumps of common-rail fuel systems for diesel engines.
SAE Technical Paper 2005-01-0909, 2005. (cited in p. 34)

Teng H., Regner G. and Cowland C.
Waste Heat Recovery of Heavy-Duty Diesel Engines by Organic Rankine Cycle Part I: Hybrid System of Diesel and Rankine Engines.
SAE Technical Paper 2007-01-0537, 2007. (cited in pp. 38, 47, 50)

Teodorescu M., Kushwaha M., Rahnejat H. and Taraza D.
Elastodynamic transient analysis of a four-cylinder valvetrain system with camshaft flexibility.
Proceedings of the Institution of Mechanical Engineers, Part K: Journal of Multi-body Dynamics, Vol. 219 n^o 1, pp. 13–25, 2005. (cited in p. 234)

Teodorescu M., Taraza D., Henein N. and Bryzik W.
Experimental Analysis of Dynamics and Friction in Valve Train Systems.
SAE Technical Paper 2002-01-0484, 2002. (cited in p. 230)

Teodorescu M., Taraza D., Henein N. and Bryzik W.
Simplified Elasto-Hydrodynamic Friction Model of the Cam-Tappet Contact.
SAE Techinical Paper 2003-01-0985, 2003. (cited in pp. 232, 233, 234, 267, 268)

Thirouard M., Mendez S., Pacaud P., Chmielarczyk V., Ambrazas D., Lavoisier F., Garsi C. and Barbeau B.
Potential to Improve Specific Power Using Very High Injection Pressure In HSDI Diesel Engines.
SAE Technical Paper 2009-01-1524, 2009. (cited in p. 36)

Thirouard M. and Pacaud P.
Increasing power density in hsdi engines as an approach for engine downsizing.
SAE Int. J. Engines, Vol. 3 n^o 2, pp. 56–71, 2010. (cited in p. 35)

Tian T.
Modeling the performance of the Piston Ring-Pack in internal combustion engines.
Ph.D. Thesis, Massachusetts Institute of Technology, 1997. (cited in p. 223)

Tichý J. and Gautschi G.
Piezoelektrische Meßtechnik.
Springer, ISBN 978-3-642-52202-4, Berlin, 1980. (cited in pp. 82, 144)

Tinaut F.
Contribución al estudio del proceso de combustión en motores de encendido por compresión de inyección directa.
Ph.D. Thesis, Universidad Politécnica de Valencia, 1986. (cited in pp. 5, 89, 334)

Torregrosa A.J., Broatch A., Olmeda P. and Cornejo O.
Experiments on subcooled flow boiling in I.C. engine-like conditions at low flow velocities.
Experimental Thermal and Fluid Science, Vol. 52, pp. 347–354, jan 2014. (cited in p. 36)

Torregrosa A.J., Broatch A., Olmeda P. and Martín J.
A contribution to film coefficient estimation in piston cooling galleries.
Experimental Thermal and Fluid Science, Vol. 34 n^o 2, pp. 142–151, February 2010.
(cited in p. 105)

Torregrosa A.J., Broatch A., Olmeda P. and Romero C.
Assessment of the influence of different cooling system configurations on engine warm-up, emissions and fuel consumption.
International Journal of Automotive Technology, Vol. 9 n^o 4, pp. 447–458, 2008.
(cited in pp. 27, 28)

Torregrosa A.J., Olmeda P., Degraeuwe B. and Reyes M.
A concise wall temperature model for DI Diesel engines.
Applied Thermal Engineering, Vol. 26 n^o 11-12, pp. 1320–1327, August 2006.
(cited in pp. 105, 106)

Torregrosa A.J., Olmeda P., Martín J. and Degraeuwe B.
Experiments on the influence of inlet charge and coolant temperature on performance and emissions of a DI Diesel engine.
Experimental Thermal and Fluid Science, Vol. 30 n^o 7, pp. 633–641, 2006.
(cited in p. 80)

Tribotte P., Ravet F., Dugue V., Obernesser P., Quechon N., Benajes J., Novella R. and De Lima D.
Two Strokes Diesel Engine - Promising Solution to Reduce CO2 Emissions.
Procedia - Social and Behavioral Sciences, Vol. 48, pp. 2295–2314, January 2012.
(cited in pp. 84, 85)

Tsumagari I., Hirabayashi H., Takenaka Y., Hosoya M. and Shimoda M.
Study of 2-LEG NOx Storage-Reduction Catalyst System for HD Diesel Engine.
SAE Techinical Paper 2006-01-0211, 2006. (cited in p. 20)

Tunestål P.
Self-tuning gross heat release computation for internal combustion engines.
Control Engineering Practice, Vol. 17 n^o 4, pp. 518–524, April 2009. (cited in p. 205)

Tunestål P.
TDC Offset Estimation from Motored Cylinder Pressure Data based on Heat Release Shaping.
Oil & Gas Science and Technology - Revue d'IFP Energies nouvelles, Vol. 66 n^o 4, pp. 705–716, October 2011. (cited in p. 205)

Turner J., Blake D., Moore J., Burke P., Pearson R., Patel R., Blundell D., Chandrashekar R., Matteucci L., Barker P. and Card C.
The Lotus Range Extender Engine.
SAE Int. J. Engines, Vol. 3 n^o 2, pp. 318–351, 2010. (cited in p. 35)

Turner J., Popplewell A., Marshall D.J., Johnson T.R., Barker L., King J., Martin J., Lewis A.G.J., Akehurst S., Brace C.J. and Copeland C.D.
SuperGen on Ultraboost: Variable-Speed Centrifugal Supercharging as an Enabling Technology for Extreme Engine Downsizing.
SAE Int. J. Engines, Vol. 8 n^o 4, 2015. (cited in p. 36)

Ummel D. and Price K.
Performance and Sulfur Effect Evaluation of Tier 4 DOC+SCR Systems for Vanadia, Iron, and Copper SCR.
SAE International J. Engines, Vol. 7 n^o 3, pp. 1244–1251, 2014. (cited in p. 19)

UNEP.
Gas fracking: can we safely squeeze the rocks?
Environmental Development, Vol. 6, pp. 86–99, apr 2013. (cited in p. 2)

Ushijima K., Moteki K., Goto T. and Aoyama S.
A Study on Engine Bearing Performance Focusing on the Viscosity-Pressure Characteristic of the Lubricant and Housing Stiffness.
SAE Technical Paper 961144, 1996. (cited in p. 227)

Uyehara O.A.
Factors that Affect BSFC and Emissions for Diesel Engines : Part 1 - Presentation of Concepts.
SAE Techinical Paper 870343, 1987. (cited in p. 23)

Verhelst S.
Recent progress in the use of hydrogen as a fuel for internal combustion engines.
International Journal of Hydrogen Energy, Vol. 39 n^o 2, pp. 1071–1085, 2014.
(cited in pp. 20, 43)

Vítek O., Macek J., Polášek M., Schmerbeck S. and Kammerdiener T.
Comparison of Different EGR Solutions.
SAE Techinical Paper 2008-01-0206, 2008. (cited in p. 26)

Waki H., Nishikawa I., Kobayashi A. and Ishii N.
Sensitivity to experimental errors in evaluating the thermal expansion coefficient of a thermal barrier coating by using coating system specimens.
Vacuum, Vol. 88, pp. 93–97, February 2013. (cited in p. 30)

Wang C., Xu H., Herreros J.M., Wang J. and Cracknell R.
Impact of fuel and injection system on particle emissions from a GDI engine.
Applied Energy, Vol. 132, pp. 178–191, November 2014. (cited in p. 23)

Wang X., Huang Z., Zhang W., Kuti O.A. and Nishida K.
Effects of ultra-high injection pressure and micro-hole nozzle on flame structure and soot formation of impinging diesel spray.
Applied Energy, Vol. 88 n^o 5, pp. 1620–1628, May 2011. (cited in pp. 17, 40)

Wei S., Wang F., Leng X., Liu X. and Ji K.
Numerical analysis on the effect of swirl ratios on swirl chamber combustion system of DI diesel engines.
Energy Conversion and Management, Vol. 75, pp. 184–190, November 2013.
(cited in p. 18)

Weisberg S.
Applied Linear Regressions.
John Wiley & Sons, ISBN 0-471-66379-4, 3rd edition, 2005. (cited in p. 207)

Williams F.
Combustion Theory.
The Benjamin/Cummings Publishing Co, ISBN 978-0201407778, 1985. (cited in p. 89)

Wloka J.A., Pflaum S. and Wachtmeister G.
Potential and Challenges of a 3000 Bar Common-Rail Injection System Considering Engine Behavior and Emission Level.
SAE Int. J. Engines, Vol. 3 n^o 1, pp. 801–813, 2010. (cited in p. 17)

Woods M., Bryzik W. and Schwarz E.
Heat Rejection from High Output Adiabatic Diesel Engine.
SAE Techinical Paper 920541, 1992. (cited in pp. 46, 50)

Woschni G.
A Universally Applicable Equation for the Instantaneous Heat Transfer Coefficient in the Internal Combustion Engine.
SAE Technical Paper 670931, 1967. (cited in pp. 93, 102, 103, 215)

Woschni G.
Die Berechnung der Wandverluste und der thermischen Belastung der Bauteile von Dieselmotoren.
MTZ, Vol. 31 n^o 12, pp. 491–499, 1970. (cited in pp. 93, 102, 103)

Xin Q. and Zheng J.
Theoretical Analysis of Internal Combustion Engine Miscellaneous Heat Losses.
SAE Techinical Paper 2009-01-2881, 2009. (cited in p. 47)

Yamaguchi T., Aoyagi Y., Uchida N., Fukunaga A., Kobayashi M., Adachi T. and Hashimoto M.
Fundamental Study of Waste Heat Recovery in the High Boosted 6-cylinder Heavy Duty Diesel Engine.
SAE Int. J. Mater. Manf., Vol. 8 n^o 2, 2015. (cited in pp. 38, 47, 48, 50)

Yang Y., Dec J.E., Sjöberg M. and Ji C.
Understanding fuel anti-knock performances in modern SI engines using fundamental HCCI experiments.
Combustion and Flame, Vol. 162 n^o 10, pp. 4008–4015, oct 2015. (cited in p. 16)

Yingjian L., Qi Q., Xiangzhu H. and Jiezhi L.
Energy balance and efficiency analysis for power generation in internal combustion engine sets using biogas.
Sustainable Energy Technologies and Assessments, Vol. 6, pp. 25–33, June 2014.
(cited in pp. 45, 50)

Yüksel F. and Ceviz M.A.
Thermal balance of a four stroke SI engine operating on hydrogen as a supplementary fuel.
Energy, Vol. 28 n^o 11, pp. 1069–1080, September 2003. (cited in pp. 43, 45, 50)

Zhang L., Takatsuki T. and Yokota K.
An Observation and Analysis of the Combustion Under Supercharging on a DI Diesel Engine.
SAE Techinical Paper 940844, 1994. (cited in p. 25)

Zhen X., Wang Y., Xu S., Zhu Y., Tao C., Xu T. and Song M.
The engine knock analysis - An overview.
Applied Energy, Vol. 92, pp. 628–636, apr 2012. (cited in p. 16)

Zheng M., Han X., Asad U. and Wang J.
Investigation of butanol-fuelled HCCI combustion on a high efficiency diesel engine.
Energy Conversion and Management, Vol. 98, pp. 215–224, July 2015.
(cited in pp. 23, 43)

Zhou B., Lan X., Xu X. and Liang X.
Numerical model and control strategies for the advanced thermal management system of diesel engine.
Applied Thermal Engineering, Vol. 82, pp. 368–379, May 2015. (cited in p. 27)